Volatiles as a link between planetary interiors and the environment

by

Benjamin A. Black

A.B., Harvard University (2005)
M.F.A., New York University (2007)

Submitted to the Department of Earth, Atmospheric, and Planetary Sciences
in partial fulfillment of the requirements for the degree of

Doctor of Philosophy

at the

MASSACHUSETTS INSTITUTE OF TECHNOLOGY

September 2013

Author .....
Massachusetts Institute of Technology
July 31, 2013

Certified by. .....
Linda T. Elkins-Tanton
Director, Department of Terrestrial Magnetism, Carnegie Institution for Science
Thesis Supervisor

Accepted by .....
Robert D. van der Hilst
Schlumberger Professor of Earth Sciences
Head, Department of Earth, Atmospheric and Planetary Sciences, MIT

Volatiles as a link between planetary interiors and the environment

by

Benjamin A. Black

Submitted to the Massachusetts Institute of Technology
September 2013, in partial fulfillment of the
requirements for the degree of
Doctor of Philosophy

Abstract

Volatiles derived from planetary interiors influence magma evolution and environmental processes. Over appropriate timescales, Earth's mantle, crust, ocean, and atmosphere constitute coupled systems. The apparently synchronous Siberian Traps eruption and end-Permian mass extinction offer an ideal test case to study the interactions between magmatism and climate. In this thesis, I use experimental petrology, numerical modeling, geochemical measurements, and field observations to investigate the petrologic sources, eruptive transfer, and climatic effects of volatiles released during emplacement of the Siberian large igneous province. In an extreme variation on terrestrial volatile cycling, I also explore the erosional history of Titan as recorded in valley networks carved by rivers of liquid hydrocarbons.

Thesis Supervisor: Linda T. Elkins-Tanton
Title: Director, Department of Terrestrial Magnetism, Carnegie Institution for Science

Table of Contents

Chapter 1. Introduction

The concentric layers of rocky solar system bodies—from core to mantle to crust to atmosphere—have often been compared to the layers of an onion. That is only accurate if the onion were to evolve dynamically over time, transferring mass and energy between its laminae. On Earth, these exchanges between layers control—for example—fundamental features such as volcanic eruptions, plate tectonics, and the composition of the ocean and atmosphere. The mass transferred to and from the mantle includes a small fraction of key compounds known as volatiles, which transition easily to the vapor state at relatively low temperatures. Mid-ocean ridge basalts contain approximately 0.2 weight percent volatile phases, including water, carbon dioxide, sulfur, halogens, and noble gases. In the depleted mantle where mid-ocean ridge basalts originate, total volatile contents may be as low as 0.04 weight percent (Saal et al., 2002). Despite their relative paucity in Earth's mantle, the abundance of volatiles varies widely throughout the solar system, and these labile compounds wield outsize influence over magma evolution and surface environments.

Over the course of the six chapters that follow, I will explore the history of these volatiles and their effects as they transit the crust and atmosphere. In chapters two through five, I will investigate the interplay between the eruption of the Siberian Traps large igneous province, volatile release to the atmosphere, and global ecology. The eruption of the Siberian Traps has been proposed as a possible trigger for the end-Permian mass extinction. Constraints on the volatile budget and climatic consequences of the eruption are therefore a key ingredient for understanding the potential environmental effects of magmatism. In chapter six, I will turn to Titan—a large Saturnian moon with a distinctly extraterrestrial volatile budget and a surprisingly Earth-like landscape—in order to examine a different kind of environmental effect: the importance of hydrocarbon rain and rivers in Titan's erosional history. The final

chapter will summarize my perspective on the role of volatiles in the co-evolution of planetary interiors and surface environments.

While multiple Phanerozoic mass extinctions appear to occur within suspicious temporal proximity to major large igneous province eruptions, a precise link between basaltic flood volcanism and ecological catastrophe has remained elusive. Because of the volume of the Siberian Traps and the unmatched severity of the end-Permian mass extinction, these two events have proved particularly enticing for matchmakers seeking to pair extinctions with volcanic triggers.

In addition to its volume, several other factors make the Siberian large igneous province unique. The thick volcaniclastic deposits at the base of the volcanic sequence may record episodes of widespread, explosive volcanism (White et al., 2009). Magmas erupted through a thick sequence of sedimentary rocks, including carbonates, coals, evaporites, and Proterozoic hydrocarbon reservoirs (Ganino and Arndt, 2009). Field reconnaissance has revealed numerous diatreme-like pipe structures scattered around the Siberian Traps (Svensen et al., 2009). The eruption occurred at high latitude where the tropopause is lower (Grise et al., 2010), relatively rapidly (Kamo et al., 2003), with episodic pulses of activity (Pavlov et al., 2011).

Since the seminal work of Sepkoski et al. (1981), countless theories have been put forward to explain the end-Permian mass extinction, ranging from bolide impact (Becker et al., 2001) to supernova (Ellis and Schramm, 1995) to a periodic passage of a solar companion star known as Nemesis (Davis et al., 1984; Whitmire and Jackson, 1984). After Renne and Basu (1991) and Campbell et al. (1992) demonstrated that the eruption and the extinction were approximately the same age, the Siberian Traps entered as a critical component of many of these models.

At present, the major hypotheses to explain the mass extinction include: ocean anoxia (Hotinski et al., 2001); CO_2 release and global warming from the Siberian Traps (Campbell et al., 1992); ocean acidification from elevated CO_2 (Knoll et al., 2007); H_2S release from euxinic deep waters following chemocline upwards excursion (Kump et al., 2005); ozone destruction and ultraviolet poisoning from halogen and halocarbon emissions (Beerling et al., 2007); collapse of primary productivity and a

Strangelove ocean (Kump, 1991; Rampino and Caldeira, 2005); catastrophic methane clathrate destabilization (Erwin, 1994); global wildfires (Shen et al., 2011); acid rain (Maruoka et al., 2003); or some combination of the foregoing. Many of these ideas are not mutually exclusive.

In this thesis, I set out to evaluate the unique features of the Siberian Traps in the context of proposed extinction mechanisms. I examine evidence ranging from the microscopic scale—in the form of melt inclusions, tiny bits of frozen magma trapped inside ancient crystals from the Siberian Traps—up to the global scale, in the form of a 3-D climate-chemistry model. Data from Titan offers an entirely different perspective on the past evolution of climate.

Chapter 2. Magnitude and consequences of volatile release from the Siberian Traps

Abstract: The eruption of the Siberian Traps flood basalts has been invoked as a trigger for the catastrophic end-Permian mass extinction. Quantitative constraints on volatile degassing are critical to understanding the environmental consequences of volcanism. We measured sulfur, chlorine, and fluorine in melt inclusions from the Siberian Traps and found that concentrations of these volatiles in some magmas were anomalously high compared to other continental flood basalts. For the ten samples for which we present data, volatile concentrations in individual melt inclusions range from less than the detection limit to 0.51 wt % S, 0.94 wt % Cl, and 1.95 wt % F. Degassing from the Siberian Traps released approximately ~6300-7800 Gt S, ~3400-8700 Gt Cl, and ~7100-13600 Gt F. These large volatile loads, if injected into the stratosphere, may have contributed to a drastic deterioration in global environmental conditions during the end-Permian.

1. Introduction

Almost two decades have passed since the eruption of the Siberian Traps was first proposed as a trigger for the end-Permian mass extinction (Campbell et al., 1992; Renne and Basu, 1991), the largest loss of floral and faunal diversity in Earth's history (Erwin, 1994; Sepkoski et al., 1981). The Permian-Triassic boundary was preceded by an ~1.5 Myr episode of ocean euxinia (Cao et al., 2009) and followed by ~5 Myr of suppressed biological diversity and large fluctuations in the $\delta^{13}C$ record (Lehrmann et al., 2006; Payne et al., 2004). Degassing and atmospheric loading of volatiles is one of the critical mechanisms that links mafic volcanic eruptions with global environmental change (Devine et al., 1984; Thordarson et al., 1996). We seek to quantify volatile flux throughout the evolution of the Siberian Traps large igneous province and to evaluate the potential climatic impact.

The Siberian Traps magmas were erupted through the Tunguska sedimentary sequence, which reaches 12.5 km in thickness (Meyerhoff, 1980). The thickness of Cambrian evaporitic sequences alone can exceed 2.5 km (Figure 1); Zharkov (1984) estimates that the East Siberian Basin hosts a total volume of ~585,000 km^3 of rock salt. Additional Siberian salt deposits are found in Ordovician through Carboniferous strata (Zharkov, 1984).

Evidence from trace elements (Lightfoot et al., 1990; Wooden et al., 1993), $\delta^{34}S$ (Li et al., 2009c; Ripley et al., 2003), ε_{Nd} (Arndt and Christensen, 1992), magmatic sulfides (Li et al., 2009b), and drill cores through pipe structures (Svensen et al., 2009) provides strong support for widespread interaction between crustal rocks (including evaporites and carbonates) and magmas. Contact heating and metamorphism related to sill intrusion may have led to direct, potentially explosive gas release from the Tunguska sediments (Svensen et al., 2009). In addition to this direct degassing, we suggest that Siberian Traps magmas may have extensively assimilated these volatile-rich sedimentary rocks, increasing their concentrations of dissolved volatiles.

Outcrops of the Siberian Traps stretch from the Taimyr Peninsula in the north of Russia as far south as Bratsk (Figure 1). With an estimated volume of ~4×10^6 km^3 (Fedorenko et al., 2000), the Siberian

large igneous province ranks among the largest known continental flood basalts. Volumetrically, it is roughly three times as large as the Deccan Traps (Jay and Widdowson, 2008), and twenty times as large as the Columbia River flood basalts (Coffin and Eldholm, 1994). Although mafic lava flows are most abundant, volcaniclastic and intrusive units also account for large fractions of the total volume. The maximum cumulative thickness of the dolerite sills, which most frequently intrude the Paleozoic sedimentary rocks, has been estimated as 1200 meters (Kontorovich et al., 1997).

The precise temporal relationship between the onset of eruption and the main pulse of extinction remains unclear, despite geochronological advances (Bowring et al., 1998; Kamo et al., 2003). Zircon-bearing rocks are rare at the base of all exposed Traps sections, making ultra high-precision dating of these flows and pyroclastic deposits difficult. U-Pb dating of perovskites in a stratigraphically early Arydzhangsky flow and zircons from a late Delkansky silicic tuff (Figure 2) suggest that in the Maymecha-Kotuy region the bulk of the eruption occurred in <1 Myr, with onset prior to 251.7±0.4 Ma (Kamo et al., 2003).

Ar-Ar geochronology on plagioclase and biotite has also been used to evaluate the timing of the eruption and the extinction (Renne et al., 1995). However, it is difficult to directly compare Ar-Ar dates with U-Pb dates because of, among other factors, uncertainty in the absolute age of the fluence monitor used during Ar-Ar sample irradiation. Reichow et al. (2009) obtained an Ar-Ar date of 250.3 ± 1.1 Ma for the final stages of extrusive volcanism at Noril'sk, within error of their high precision sanidine Ar-Ar date for the main pulse of the extinction at 249.25 ± 0.14 Ma. Because these dates were produced in the same lab using the same fluence monitor age, they should be directly comparable, suggesting that within uncertainty the eruption overlaps with the main pulse of the extinction.

2. The End-Permian Mass Extinction

The end-Permian mass extinction was a period characterized by sudden loss of >90% of marine species and >70% of terrestrial species; even insect diversity suffered (Erwin, 1994). Unlike the

Cretaceous-Tertiary extinction, which was most likely triggered by the bolide impact that formed the Chicxulub impact crater, no major impact event has been generally accepted as the cause of the end-Permian mass extinction (Farley et al., 2005).

Fossil size and diversity did not begin to recover until ~5 Myr after the beginning of the extinction (Lehrmann et al., 2006; Payne et al., 2004), suggesting that environmental conditions could have been inhospitable for a prolonged period. This paleontological observation is matched by an extended period of large amplitude (up to 8 ‰) carbon isotope fluctuations following the first pulse of the extinction (Payne et al., 2004). The observed carbon isotopic instability could result either from perturbations in organic carbon burial associated with a damaged ecosystem, or directly from the environmental disturbances driving the extinction (Payne and Kump, 2007; Payne et al., 2004). Carbon cycle modeling suggests that episodic fluxes of magmatic and organic carbon could produce the late Permian and early Triassic carbon isotopic pattern (Payne and Kump, 2007). However, given the size of the oceanic and atmospheric carbon reservoirs and the probable timescale of eruption, the direct climatic warming due to magmatic CO_2 emissions alone was most likely small (Caldeira and Rampino, 1990).

End-Permian and early Triassic deep-sea cherts are preserved in accretionary sections in Japan and British Columbia, and contain pyrite and lack hematite, implying that anoxic conditions prevailed at the time of deposition (Isozaki, 1997). Huey and Ward (2005) cite these anoxic markers and high background extinction rates in the late Permian as evidence that environmental conditions had deteriorated well before the main pulse of the extinction, suggesting that the Permian-Triassic transition occurred in the midst of an extended period of ecological stress.

Knoll et al. (2007) divide the potential explanations for the end-Permian extinction into two categories: kill mechanisms and trigger mechanisms. A kill mechanism is the actual environmental condition that leads to death of an organism, and a trigger mechanism is a perturbation that initiates reactions that lead to that environmental condition. Many kill mechanisms have been proposed for the end-Permian mass extinction, including: ocean anoxia, euxinia, and/or sulfide release driven by global warming and decreased ocean circulation (Kump et al., 2005), ozone depletion and mutagenesis (Beerling

et al., 2007; Visscher et al., 2004), and elevated carbon dioxide levels (Knoll et al., 2007). Heavily calcified organisms were much more vulnerable to extinction during the end-Permian (Knoll et al., 2007). This suggests that high carbon dioxide levels, also known as hypercapnia, played a significant role in the marine extinction. The Siberian Traps have often been invoked (e.g. Campbell et al., 1992; Payne and Kump, 2007; Svensen et al., 2009) as a trigger mechanism for one or more of the kill mechanisms mentioned above. In particular, the Siberian Traps might have triggered environmental change as a result of degassing related to contact metamorphism of Tunguska sedimentary rocks (Ganino and Arndt, 2009; Kontorovich et al., 1997; Svensen et al., 2009) or as a result of degassing from the magma upon eruption. For example, volcanic sulfur forms sulfate aerosol particles, which can generate global cooling with an e-folding decay time in the atmosphere of ~1 year after the end of the eruption (Barnes and Hofmann, 1997). Cl and other halogens can contribute to ozone destruction in the stratosphere (Beerling et al., 2007; Johnston, 1980; Molina, 1996); sulfate aerosols can provide surfaces for these reactions to proceed (Robock, 2000; Textor et al., 2003).

We investigate the concentrations of dissolved sulfur, chlorine, and fluorine in Siberian Traps melt inclusions in order to assess which kill mechanisms, if any, might have been triggered by degassing from Siberian Traps magmas.

3. Materials and Methods

The micrometer-sized enclaves of trapped magma known as melt inclusions can provide a record of pre-eruptive volatile contents such as S, Cl, F, H_2O, and CO_2 (Anderson, 1974; Devine et al., 1984; Metrich and Wallace, 2008). Before melt inclusions are trapped in crystals, degassing may release volatiles, or crystal fractionation may enrich them in the remaining liquid. After entrapment, volatiles (particularly hydrogen) may diffuse out of or into melt inclusions (Qin et al., 1992). Here we assume that no volatiles diffused from the nominally volatile-free host minerals into inclusions, and any diffusion out would make our measurements minimums. Therefore, these volatile measurements are reasonable

minimums for the original concentrations in the magmas. Major elements and compatible trace elements may also be affected by post-entrapment diffusive re-equilibration and Fe-loss (Cottrell et al., 2002; Danyushevsky et al., 2000; Danyushevsky et al., 2002). This process strongly depends on diffusivities through the host crystal and partition coefficients between the crystal and melt (Qin et al., 1992). Fe-loss will primarily influence Fe and Mg concentrations in olivine-hosted inclusions, and therefore its effect on incompatible volatile elements is likely to be small (Danyushevsky et al., 2000). Because we are primarily interested in pre-eruptive volatile contents, any re-equilibration of the inclusions prior to eruption does not affect our interpretations.

We analyzed by electron microprobe >150 melt inclusions from the Siberian Traps, and we present results from 70 volatile-bearing inclusions. These inclusions were selected on the basis of oxide totals (from 98-101.5 wt %); statistically significant detection of S, Cl, or F; and absence of visible cracks, large spinel crystals, or quench textures. A large fraction of the inclusions we analyzed in samples K08-3.4 and K08-7.10 contained no detectable S, Cl, or F and were probably breached as a result of the strong cleavage in clinopyroxene. We obtained melt inclusions from ten field samples that include dolerite sills near Bratsk and Ust-Ilimsk, crystalline Onkuchaksky and Maymechinsky lava flows, and mafic Arydzhangsky tuffs that are among the earliest erupted Siberian Traps deposits (Figure 1-2, Table 1). The basalts in the Maymecha and Kotuy basins include both high-alkali and tholeiitic flows (Arndt et al., 1998). The mafic tuffs and the unusual MgO-rich (>18 wt %) maymechites belong to the alkaline group; the Onkuchaksky flow is tholeiitic. The Maymecha Kotuy section has been described as a more complete section than Noril'sk (Fedorenko and Czamanske, 1997), which is arguably the most studied region of the flood basalts. While correlation among different areas of the Siberian Traps is difficult, according to the stratigraphy proposed by Fedorenko and Czamanske (1997) and reproduced in Figure 2 our sample set represents close to the full time-span of Traps emplacement. Recent paleomagnetic results (Pavlov et al., 2011) support this interpretation; virtual paleomagnetic poles are statistically identical between the two sections, but an additional reversed interval is recorded in the upper part of the Maymecha-Kotuy section.

We handpicked olivine, plagioclase, and clinopyroxene grains from crushed and sieved samples. To counteract the effects of post-entrapment crystallization, we reheated our mineral grains in oxygen-fugacity controlled 1-atm furnaces at the University of Iowa and MIT at conditions at or slightly below the quartz-fayalite-magnetite buffer. We maintained the appropriate oxygen fugacity with a CO_2:H_2 gas mixture. Target heating temperatures were estimated using COMAGMAT (Ariskin et al., 1993). Samples were held at target temperatures for only ten minutes in order to reduce potential H diffusion (Hauri, 2002), and were then rapidly quenched resulting in homogeneous glassy inclusions. We mounted and polished individual quenched grains until our melt inclusions were exposed at the surface.

For olivine-hosted melt inclusions, we performed olivine addition and subtraction (e.g. Rowe and Lassiter, 2009) to correct for post-entrapment crystallization and over- or under-heating. For plagioclase, the ratio of mineral-melt partition coefficients for calcium and sodium is sensitive to water content (Sisson and Grove, 1993). For melt inclusions from R06-09, the ratio $K_D^{Ca\text{-}Na}=(Ca/Na)_{plagioclase}/(Ca/Na)_{liquid}$ ranges from 0.52 to 0.97, with an average $K_D^{Ca\text{-}Na}$ of 0.74. Sisson and Grove (1993) report an experimental $K_D^{Ca\text{-}Na} = 0.95$ at 8 kbars in an anhydrous magma; the *Ca/Na* for plagioclase versus the whole rock composition of R06-09 averages 0.60. Because these values of $K_D^{Ca\text{-}Na}$ are all ~1, it is difficult to employ measurements of $K_D^{Ca\text{-}Na}$ to detect post-entrapment crystallization and consequent disequilibrium between the host crystal and inclusion. For clinopyroxene-hosted inclusions, equilibrium models for calcium, magnesium, and iron compositions require estimates of pressure and temperature (e.g. Putirka, 1999); as a result, correction on the basis of modeled clinopyroxene-liquid equilibrium might introduce additional uncertainties. Volatiles and other incompatibles not present in the crystal should be minimally affected by any over- or under-heating. The plagioclase- and clinopyroxene-hosted inclusions are therefore presented as measured values, without further correction. However, given the large observed variation in volatile concentrations, this does not significantly affect our results.

Sulfur, chlorine, and fluorine microprobe analyses were performed with the JEOL-JXA-8200 Superprobe at the MIT Microprobe Facility in Cambridge, MA. We employed a 15 kV voltage, and a 10 nA current. The beam diameter was 10 μm for glass analyses and 1 μm for analyses of host crystals. All

counting times were 40 seconds, except for Na and F, which were 5 and 10 seconds respectively. Nominal detection limits are approximately 0.13 wt % for F and 0.017 wt % for S and Cl, although generally consistent repeat measurements for F (Table A.1) suggest that the actual detection limits for F may be lower. Additional S, Cl, F, carbon, and water measurements were performed at the WHOI National SIMS Facility with a Cs- beam on a Cameca 1280 SIMS. Carbon and water analyses are in progress. Initial results show a range of carbon concentrations between ~0.02 wt % and ~0.33 wt % C. These maximum C contents, which occur even in samples not carbon-coated prior to ion probe analysis, are higher than we might reasonably expect on the basis of CO_2 solubility (Newman and Lowenstern, 2002). We cannot exclude the possibility that, despite careful sample selection, a minor amount of C-rich exogenic material might have been incorporated into some glasses during the homogenization process.

Electron microprobe and SIMS analyses were calibrated using a combination of natural and synthetic standards. We discarded electron microprobe glass analyses with totals outside the range of 98 to 101.5 wt %. A complete listing of the whole rock, microprobe and ion probe results for melt inclusions presented here is shown in supplementary Appendix A, Table A.1.

4. Results: Degassing from the Siberian Traps

Our melt inclusions display significant variability in volatile concentrations, and occasionally in major element compositions. Figure 4 shows a ternary olivine-clinopyroxene-plagioclase diagram of the whole rock compositions of the ten samples for which we present data. The Siberian Traps are vast and complex, with a surprising variety of magma compositions. Although not all these varieties have been included in this study, the whole rock data in Figure 4 show that our samples span a large portion of the compositional space occupied by Siberian Traps magmas, as previously reported by Arndt et al. (1995), Dalrymple et al. (1995), Fedorenko and Czamanske (1997), Fedorenko et al. (1996a), Hawkesworth et al. (1995), Lightfoot et al. (1990),Ryabov et al. (1985), Sharma et al. (1991), Sobolev et al. (2009), Wooden et al. (1993) and Zolotukhin and Almukhamedov (1988). Our maymechite melt inclusions follow an

olivine-control line similar to that of the ten inclusions reported in Sobolev (1991). The olivine-rich whole rock compositions imply that these samples may be olivine cumulates.

Aside from the maymechites, most melt inclusions cluster tightly around their whole rock host compositions, suggesting that those inclusions are representative of their host rocks and that rehomogenization temperatures were close to the temperatures of entrapment. The exceptions are the inclusions from Arydzhangsky tuff K08-3.4 and the Bratsk sill sample R06-07 (Figure 4, Table A.1). The inclusions in K08-3.4 are significantly more MgO-rich than their host rock and may therefore be samples of a parental magma. The three inclusions in R06-07 are more silicic than their basaltic host rock. They may have experienced post-entrapment crystallization, or they may be sampling a more evolved magma. Regardless, these inclusions have lower Cl and F concentrations than the plagioclase-hosted inclusions from A10-23.1, and consequently our estimates of volatile contents are not significantly skewed by any incompatible fractionation.

For the ten samples for which we present data, volatile concentrations in melt inclusions range from below the detection limit to 0.51 wt % S, 0.94 wt % Cl, and 1.95 wt % F. We present the maximum and mean S, Cl, and F concentrations for each set of samples in Table 1. Maximum concentrations may be more useful than averages or ranges because of the wide spread in values for many samples and because the lowest concentrations may represent partial degassing.

As shown in Table 1, maximum concentrations of S are more consistent than Cl or F across tuff, sill, and lava samples (except the maymechites), with a range between 0.06 wt % and 0.17 wt %. Melt inclusions from the high MgO maymechite lavas contain S concentrations up to 0.51 wt %. Chlorine ranges from 0.01 wt % in a columnar basalt flow up to 0.94 wt % in a dolerite sill. Fluorine ranges from 0.16 wt % in the columnar basalt flow up to 1.95 wt % in a second dolerite sill. Aside from the sills, Cl ranges from 0.01 wt % to 0.15 wt %, and F ranges from 0.16 wt % to 0.30 wt %.

In addition to the high sulfur maymechites, some of our melt inclusions are substantially enriched in Cl and F compared to maximum concentrations measured in Deccan Traps, Columbia River Flood Basalts, and Laki melt inclusions (Blake et al., 2010; Self et al., 2008; Thordarson and Self, 1996;

Thordarson et al., 1996) (Table 1, Figure 4). In particular, the two massive sills mentioned above contain high concentrations of Cl and/or F. While it is difficult to precisely constrain sill volumes, where these two sills have outcrops along the Angara River they reach 80-120 meters in thickness, and stretch for tens to hundreds of kilometers laterally. Melt inclusions from Noril'sk have also been reported to show moderate enrichments in Cl (Sobolev et al., 2009; Figure 5).

On the basis of our own field work and previous mapping and stratigraphic efforts (Fedorenko et al., 2000; Fedorenko and Czamanske, 1997; Malitch et al., 1999), we calculate approximate present-day volumes of individual flows and tuffs from the Maymecha-Kotuy area for which we have melt inclusion data. Because of erosion, these volume estimates probably represent lower bounds. Using the maximum volatile contents of each unit in Table 1, we find that individual flows and tuffs each contained on the order of a combined 10^2 to 10^3 Mt of dissolved S, Cl, and F prior to degassing (Table 3). Estimated eruption times for individual lava flows within the Roza member of the Columbia River Flood Basalts range from 0.3-4.5 years based on the thickness of lava inflation crusts (Thordarson and Self, 1998a). If the style and timing of Siberian volcanism was similar, episodes of magmatism may have delivered highly concentrated pulses of volatiles to the atmosphere. Paleomagnetic secular variation suggests these pulses may have been very compressed—possibly totaling $< 10^4$ years (Pavlov et al., 2011).The climate effects of volcanic gases other than CO_2 last ~1-10 years (Timmreck et al., 2010; Wignall, 2001). If periods of quiescence between eruptive events were longer than this, emissions from individual eruptive events may be crucial to understanding environmental consequences. However, the currently available volume and timing constraints are less robust for individual eruptions, as shown by the range in our volume estimates. We therefore focus on an estimate of overall degassing from the Siberian Traps.

Groundmass glass was absent or altered in our samples. In order to estimate degassing behavior for the Siberian Traps, we compared degassing data from the other flood basalt provinces and eruptions for which melt inclusion and groundmass glass measurements have been published (Table 2). Large differences in scale and duration of magmatism exist between the Siberian Traps and Laki, the Deccan Traps, and the Columbia River Flood Basalts (Coffin and Eldholm, 1994; Reichow et al., 2009;

Thordarson and Self, 1993a). Nonetheless, because of the parallels in the style of these eruptions, the similar S, Cl, and F contents of many of the lavas (e.g. Thordarson and Self, 1996), and the more extensive information about their structure, they provide the best available analogues for the Siberian Traps. The ratio $(Al_2O_3+CaO+Na_2O+MgO)/SiO_2$ correlates with Cl solubility in basalts (Webster et al., 1999). In Table 2, we calculate this ratio for mean whole rock geochemistry from Laki, the Deccan Traps, and the Columbia River Flood Basalts. The ratio from those three flood basalts is very similar to the ratio from the Siberian Traps, suggesting that they are strong analogs for understanding Cl degassing from our samples.

The degassing efficiencies of S, Cl, and F are relatively consistent for the eruptions presented in Table 2. On average, approximately 64% of magmatic S, 36% Cl, and 30% F were released at vents, and in feeder dikes 44% S, 25% Cl, and 26% F were released (Self et al., 2008; Thordarson and Self, 1996; Thordarson et al., 1996). While degassing efficiencies from feeder dikes—especially feeder dikes involved in phreatomagmatic interactions like the source for these Laki matrix glass samples—are probably substantially different from sills, unfortunately no data are available on degassing of sills related to flood basalt emplacement.

We do not include degassing budgets from non-flood basaltic eruptive centers such as Kilauea, despite the wealth of data, because of the influence that eruptive style and volatile contents may have on degassing efficiencies. It should be noted, however, that Cl and F degassing from Kilauea is significantly lower than what we calculate in Table 2 (Gerlach and Graeber, 1985). Edmonds et al. (2009) find that halogen partition coefficients between fluid and melt are generally low for Kilauea, and that degassing of Cl and F does not begin until shallow depths (~35 meters) in the conduit. Halogen degassing behavior is highly dependent on the partition coefficients for Cl and F; Edmonds et al. (2009) rely on glass data from Kilauea, but experimental data on halogen partitioning in basalts are scarce (Carroll and Webster, 1994; Webster et al., 1999). Chloride solubility in molten basalt is approximately 1.25 to 2.9 wt % (Carroll and Webster, 1994; Webster et al., 1999). As Cl concentrations approach these solubilities, $D_{Cl}^{vapor/melt}$

increases (Webster et al., 1999). Thus for Siberian sills with high Cl, degassing of Cl may be more favorable than at volcanoes like Kilauea, where magmatic Cl concentrations are <0.035 wt % (Hauri, 2002). Cl solubility also decreases with increasing silica content in the melt, such that crystallization in the sills could lead to a Cl-driven 'second boiling' (Webster et al., 1999), which would allow degassing of a Cl-rich vapor after sill emplacement.

The total volume of the Siberian Traps was roughly ~4 × 10^6 km^3 (Fedorenko et al., 2000). Excluding anomalously high S concentrations in the maymechites, we average the maximum and mean concentrations (Table 1) observed in each of our extrusive samples along with the Gudchikhinsky picrites reported in Sobolev (2009) to obtain an estimate of typical volatile contents. Maximum concentrations yield estimates of 0.11 wt % S, 0.09 wt % Cl, and 0.21 wt % F in the extrusive rocks; mean concentrations from each sample yield estimates of 0.10 wt % S, 0.04 wt % Cl, and 0.15 wt % F. Assuming a total extrusive volume of ~3 × 10^6 km^3 and the vent degassing percentages from Table 2, the Siberian Traps tuffs and lavas may conservatively have released ~5300-6100 Gt S, ~1100-2700 Gt Cl, and ~3800-5400 Gt F.

On the basis of our three sill samples (from two sills), we can extrapolate to a rough estimate of degassing potential from ~1 x 10^6 km^3 of intrusives (personal communication, M. Reichow; Vasil'ev et al., 2000). Assuming degassing efficiencies similar to feeder dikes from Table 2, ~1000-1700 Gt S, ~2300-6000 Gt Cl, and ~3300-8200 Gt F could have degassed from intrusive rocks.

The sum of degassing from intrusive and extrusive rocks leads to total magmatic degassing estimates from the Siberian Traps of approximately ~6300-7800 Gt S, ~3400-8700 Gt Cl, and ~7100-13600 Gt F. The range in these estimates represents the difference between averaging mean versus maximum concentrations in melt inclusions from each sample. As mentioned above, intrusion of sills into sedimentary rocks, some of which host petrochemical deposits, has also been proposed as a trigger for gas release related to heating and contact metamorphism of country rock (Svensen et al., 2009). This direct degassing from sedimentary rocks is independent of and would be in addition to our estimates of volatiles degassed from the melts. The presence of immiscible sulfide deposits such as those at Noril'sk (Naldrett

et al., 1992) also suggests that the petrologic estimates of the sulfur budget presented here may be minimums.

Our results highlight the importance of sills and other intrusive rocks, which may represent ~25% of the total volume of the Siberian Traps. The contribution of sills to volatile flux is highly dependent on degassing efficiency; based on the initial results presented here, the sills may have hosted a tremendous reservoir of dissolved halogens, including ~9000-24000 Gt of Cl and ~13000-32000 Gt of F. Because they intrude into sedimentary and igneous rocks ranging in age from Proterozoic to Permian (Kontorovich et al., 1997), and because high-precision U-Pb dates are sparse, little is known about the chronology of sill emplacement.

The maymechites are considered the last extrusive products of Siberian Traps magmatism (Fedorenko and Czamanske, 1997). Our maymechite melt inclusions suggest these lavas may have discharged a large pulse of sulfur (Table 2) during the waning stages of Siberian Traps magmatism.

5. Discussion

5.1 Potential Sources for Magmatic Volatiles

The volatile contents we measure in our melt inclusions may derive, to varying degrees, from a combination of mantle melting, assimilation of volatile-bearing crustal materials, and fractionation.

The share of volatiles contributed by mantle melting may have been significant for magmas originating from very low-degree partial melts. On the basis of primitive melt inclusions from the Siqueiros Fracture Zone, average Cl and F contents of the mantle have been estimated as .0001±0.00005 wt % Cl, and .0016±0.0003 wt % F (Saal et al., 2002). Mid-Ocean Ridge Basalts contain roughly .0002-0.04 wt % Cl (Michael and Cornell, 1998) and .025±0.005 wt % F (Schilling et al., 1980). Recently, Sobolev et al. (2011) have suggested that deep melting of a pyroxenitic source could also contribute to the volatile budget. Arndt et al. (1998) suggest that the alkaline series of Maymecha-Kotuy basalts may result from low-degree melting at great depths (possibly >100 km) in the mantle, whereas the tholeiites may

have been extensively processed in shallow crustal magma chambers. Thus the volatile contents of the alkaline tuffs and the maymechites may derive in part from low-degree melting of the mantle.

For the sills and tholeiites, assimilation and fractionation may have played a greater role. Figure 6 shows the Cl/K_2O ratio plotted against K_2O. Our melt inclusions and those described in Sobolev et al. (2009) demarcate two separate trends, one steep and one shallow. Assuming that the partitioning behavior of Cl is similar to that of K (Kent et al., 1999b), the steep trend is consistent with assimilation of Cl-rich crustal materials such as evaporites, whereas the shallow trend may represent fractionation. In mid-ocean ridge basalts, a steep Cl/K_2O trend may result from assimilation of seawater-derived hydrothermal minerals or brines (e.g. Kent et al., 1999a; Michael and Schilling, 1989). The dolerite sills and some of the Sobolev et al. (2009) picrites trend to particularly high values of Cl/K_2O. The sills were emplaced in the southern part of the Tunguska basin (Figure 1), where evaporite, salt, and other sedimentary layers approach maximum thicknesses. The high Cl/K_2O ratios in these rocks provide support for the hypothesis that some intruding magmas assimilated the sedimentary host rocks.

Lightfoot et al. (1990) and Wooden et al. (1993) suggest that crustal contamination may have been greatest early in the volcanic sequence at Noril'sk, peaking in the Nadezhdinsky Suite, with generally decreasing crustal isotopic and trace element signatures towards the later stages of volcanism. Sulfur isotopes at Noril'sk require assimilation of small amounts of country rock; $\leq$0.5 % assimilation of the S-rich evaporites would be sufficient to explain the observed signatures (Ripley et al., 2003). Such assimilation could also affect the oxygen fugacity and thus the solubility of S (Mavrogenes and O'Neill, 1999; Wallace and Carmichael, 1992) and halogen species (Carroll and Webster, 1994; Webster et al., 1999).

5.2 Consequences of Degassing for the Permian-Triassic Environment

The injection of sulfur, chlorine, and fluorine into the upper atmosphere could have effects ranging from direct toxicity and acid rain to temperature change (Devine et al., 1984) and ozone depletion

(Johnston, 1980). The prevalence of mutant pollen tetrads at the time of the end-Permian extinction has been invoked as evidence for ozone destruction, possibly related to volcanic emissions of chlorine and fluorine compounds (Visscher et al., 2004). The implications for chemical weathering processes and ocean chemistry of volcanic degassing on the scale of the Siberian Traps also deserve further study.

Eruption rates are one important and poorly constrained determinant of the environmental impact of the Siberian Traps. The scale of climatic repercussions from degassing also depends on several additional key factors, including: (1) Will an ascending thermal plume penetrate the tropopause? (2) What percentage of S, Cl, and F will be delivered to the stratosphere and how long will they remain there? (3) What chemical form will the S, Cl, and F take and what are the probable climatic effects, if any, of the introduction of those species to the upper atmosphere? We investigate these questions further in the following sections.

5.3 Plume heights associated with basaltic eruptions

Delivery to the stratosphere is a critical prerequisite for ozone depletion and global climatic effects. In the Permian, Siberia was located at high latitudes, comparable to its present day position (Cocks and Torsvik, 2007). Because convective mixing is less vigorous at high latitudes, the tropopause occurs at a much lower altitude. The altitude of the tropopause is also seasonally variable, but at 60°N, the transition from the troposphere to the stratosphere occurs at an annual-mean altitude of roughly 10 km (Grise et al., 2010). Several processes might have enabled erupted material to reach the stratosphere, including thermal plumes and phreatomagmatic episodes.

Simple early models suggested that large fissure eruptions such as those often associated with flood basalt provinces might produce thermal plumes that could exceed 10 km in height, thereby reaching the high-latitude stratosphere (Stothers et al., 1986). More recent and realistic modeling shows that vent geometry and eruption rate in particular exercise strong control over plume height (Glaze et al., 2011).

The possibility of relatively long lasting individual flood basalt eruptions, with inflated sheet lobes, implies that typical volumetric eruption rates may be on the order of 10^3-10^4 m^3/s, similar to Laki (Bryan et al., 2010; Keszthelyi et al., 2006; Self et al., 1996). Rubbly, broken-up pahoehoe observed at Laki and the Columbia River flood basalts provides evidence for episodes of high-volume eruption that may have reached ~10^6 m^3/s (Keszthelyi et al., 2006). The detection of synchronous Laki-derived sulfates, ash, and trace elements in Greenland ice cores, and witness accounts of eruption columns >9 km high persisting into August 1783, suggest that the Laki plume reached the lower stratosphere (Thordarson and Self, 2003; Wei et al., 2008). If discharge rates and patterns for the Siberian Traps were comparable to those of Laki and the Columbia River flood basalts, some of these intermittent periods of rapid effusion may have generated thermal plumes that breached the high-latitude tropopause.

The presence of tuffs, tuff breccias, and volcaniclastic sequences tens to hundreds of meters thick near the base of the volcanic sequence in the Maymecha-Kotuy and Angara regions may reflect explosive episodes that could have enhanced the potential for volatile addition to the stratosphere, due to more rapid eruption rates (Naumov and Ankudimova, 1995). These volcaniclastic rocks account for ~20-30% of the total volume of the Siberian Traps (Ross et al., 2005). They are characterized by poor sorting, sedimentary and volcanic clasts ranging up to ~1 meter in diameter, and locally abundant accretionary lapilli that are consistent with a phreatomagmatic origin (Gilbert and Lane, 1994; Schumacher and Schmincke, 1995). The sedimentary clasts suggest that a significant proportion of the explosive activity may have been driven by magmatic interaction with deep aquifers, possibly with additional contributions from surface water. The volcaniclastic rocks will be described in greater detail in a separate paper.

Entrainment of atmospheric water vapor may increase the plume height by several kilometers for small mass eruption rates (10^3-10^6 kg/s), through the additional release of latent heat during condensation (Woods, 1993). Walker et al. (1984) estimate a vent exit velocity of 250-350 m/s in the case of the basaltic plinian Tarawera eruption of 1886, which generated a column of ash that ascended an estimated 30 km into the atmosphere. Glaze et al. (2011) assume a vent eruption velocity of 300 m/s, which was probably much higher than that of a typical Siberian Traps eruption based on mass-balance

considerations. Under these conditions, convective plumes from linear vent geometries with fissures longer than 5 km approach the stability of plumes from circular vents. Over a wide range of vent widths, such plumes exceed 10 km in height.

Thus, while introduction of material to the stratosphere by traditional convective plumes was probably sporadic, episodes of higher mass-flux and explosivity during Siberian magmatism may have played an important role in delivering degassing volatiles to greater heights in the atmosphere.

5.4 Effects of S, Cl, and F injection into the atmosphere

The behavior of S in the atmosphere is better known than that of Cl or F. Volcanic SO_2 reacts with the hydroxyl radical and water to form sulfate aerosols, which increase the optical depth of the atmosphere (Devine et al., 1984; Robock, 2000; Sigurdsson, 1990; Sigurdsson et al., 1992; Wignall, 2001). The resultant global cooling may reach 3-4 degrees Kelvin in the case of tropical super-eruptions such as the Younger Toba Tuff (Timmreck et al., 2010). Cooling related to sulfates in the stratosphere lasts on the order of 10 years, with maximum effects in the first 1-2 years (Robock, 2000; Timmreck et al., 2010; Wignall, 2001). On the other hand, flood basalt eruptions can sustain sulfur emissions over much longer periods than those associated with felsic super-eruptions, extending the radiative repercussions (Thordarson et al., 2009). High-latitude eruptions, unlike tropical eruptions, probably generate cooling that is restricted to the hemisphere of the eruption (Oman et al., 2005). The very high sulfate aerosol concentrations associated with super-eruptions may lead to faster removal from the atmosphere; at the same time, larger sulfate particles may form, limiting the potential increase in the optical depth of the atmosphere (Pinto et al., 1989; Timmreck et al., 2010).

Early assessments of Cl degassing concluded that volcanic Cl would be flushed from an ascending thermal plume due to dissolution in supercooled HCl-H_2O droplets and subsequent condensation and precipitation (Pinto et al., 1989; Tabazadeh and Turco, 1993). As a result of this co-condensation effect, water is one of the primary controls on HCl in volcanic plumes. If the mass ratio of

HCl : H_2O in the plume increases significantly compared to the ratio of ~0.007 assumed in Pinto et al. (1989), it becomes more difficult to dissolve HCl. In this study, we document magmatic Cl : H_2O ratios that appear to exceed unity for some magmas.

The translation of our magmatic Cl : H_2O ratios into mixing ratios in the convective plume requires an assumption of degassing efficiencies and an estimate of the surface and atmospheric water that is entrained into the plume. For phreatomagmatic eruptions, the contribution of groundwater may be considerable. This water might help to flush out Cl. However, high-flux episodes of flood lava eruption that would more easily generate stratospheric plumes would entrain relatively less ambient air (Sparks et al., 1997; Woods, 1993), reducing the dilution of magmatic HCl. Our preliminary results and previous measurements of Noril'sk melt inclusions (Sobolev et al., 2009) suggest that Siberian Traps magmas were generally H_2O -poor, ranging from 0.03-0.94 wt % H_2O.

In Figure 7 we extend the vapor pressure curves of HCl in equilibrium with HCl-H_2O solutions as calculated by Nair et al. (1983) to higher HCl concentrations. HCl-H_2O aerosol droplets with 10 mass percent hydrochloric acid have HCl partial pressures significantly above the ambient stratospheric partial pressure of 2×10^{-8} torr (Pinto et al., 1989), even at 215-220 K, the temperature of the high-latitude tropopause in winter (Gill, 1982; Randel and Wu, 2010). Consequently, with an assumption of equilibrium conditions some HCl would remain in the vapor phase and escape condensation. Because the stratosphere is very dry, any aqueous HCl that reaches it may also be subject to evaporation and a return to the gas phase (Pinto et al., 1989).

Thus, Figure 7 suggests that in some cases the removal of Cl through the 'cold-trap' effect may be less efficient, and for a plume that penetrates the tropopause, significant Cl may then reach the stratosphere. This conclusion is consistent with aircraft measurements of the 2000 Hekla plume, which indicate that ~75% of volcanogenic Cl reached the stratosphere where it subsequently led to a reduction in observed ozone levels (Millard et al., 2006; Rose et al., 2006).

Cl can catalyze the destruction of ozone in the stratosphere through cycles that generally resemble:

$$Cl + O_3 \rightarrow ClO + O_2,$$

$$ClO + O \rightarrow Cl + O_2,$$

Net result: $O_3 + O \rightarrow O_2 + O_2$.

Beerling et al. (2007) estimate a total HCl release from the Siberian Traps of 2,200 Gt based on Cl concentrations from the Columbia River Flood Basalts. They find that if released over 100 Kyr, this quantity of HCl would result in between 26 and 55% ozone depletion. The release of HCl in pulses or in conjunction with generation of organohalogen precursors from heating of organic rich rocks would both result in additional ozone destruction.

Our estimate for the total degassing of Cl from the Siberian Traps is ~3400-8700 Gt, 1.5 to 4 times as large as the input used in the Beerling et al. (2007) model. 8700 Gt translates to 8.7×10^{18} g, seven orders of magnitude greater than the 5×10^{11} g Cl that is currently in the stratosphere (Pinto et al., 1989). Even if only a small fraction of volcanic Cl from the Siberian Traps was ultimately delivered to the stratosphere, possibly during pulses of particularly violent eruption, the effect on ozone levels could have been profound.

Fluorine and bromine may also be important chemical constituents of the erupted gas. The direct toxicity of F is well-known. For example, F from the Laki eruption was adsorbed onto tephra grains and resulted in fluorosis poisoning of Icelandic sheep (Thordarson and Self, 2003). While we have not directly measured Br concentrations, it behaves similarly to Cl, with a typical ratio of Cl/Br in the crust of ~273 (Bureau et al., 2000), and approximately 340-400 in the mantle (McDonough and Sun, 1995; Pyle and Mather, 2009). Bureau et al. (2000) use this ratio to estimate Br fluxes for eruptions with known Cl. By this method, we extrapolate to a tentative Br degassing from the Siberian Traps of the order of 10 Gt, or $\sim 10^5$ times the present-day stratospheric reservoir Br may oxidize in volcanic plumes, thereby reducing its solubility and avoiding the effects of co- condensation with water (Bureau et al., 2000). Br is also about two orders of magnitude more effective as a catalyst for the destruction of ozone than Cl (Daniel et al., 1999).

Because sulfate aerosols can also contribute to the activation of halogen compounds (Textor et al., 2003), future modeling of atmospheric chemistry and ozone depletion should investigate the

combined effects of S, Cl, F, and Br based on our new constraints on volcanic emissions from the Siberian Traps.

6. Conclusions

We measure concentrations of S, Cl, and F in melt inclusions from the Siberian Traps. We estimate total magmatic degassing from the large igneous province of ~6300-7800 Gt sulfur, ~3400-8700 Gt chlorine, and ~7100-13600 Gt fluorine. More robust constraints on degassing efficiencies, especially for intrusive rocks, would significantly improve the precision of degassing estimates. These fluxes would be in addition to any direct degassing from heating and contact metamorphism of rocks in the Tunguska sedimentary basin (Svensen et al., 2009). Early episodes of explosive volcanism could have increased the likelihood that volatiles would reach the stratosphere. High Cl concentrations may have allowed some fraction of degassing Cl to escape condensation in order to remain in the ascending plume.

The viability of the Siberian Traps as a trigger for the end-Permian extinction depends heavily on volatile emissions. In order to rigorously assess the effects of volcanic and metamorphic degassing from the Tunguska basin, further atmospheric chemistry and climate modeling is urgently needed. The high volatile contents which we report in this study for many Siberian Traps magmas, and in particular for massive dolerite sills, may have significantly contributed to wholesale deterioration of latest Permian and early Triassic ecosystems.

Acknowledgments

This study was funded by grant EAR-0807585 from NSF Continental Dynamics, and supplemented by the MIT Wade Fund. The American Museum of Natural History graciously provided maymechite samples collected by Valeri Fedorenko. NSF grant EAR-0439888 supported the digital imaging lab, melt inclusion preparation supplies and salary of Ingrid Ukstins Peate. The gas-mixing furnace lab at University of Iowa was established through funds from National Science Foundation grant EAR-0609652 and University of Iowa start-up funds to Ingrid Ukstins Peate. Roman Veselovskiy, Vladimir Pavlov, and Seth Burgess were valued collaborators during field work. The authors gratefully thank Tim Grove, Nilanjan Chatterjee, Nobumichi Shimizu, Chien Wang, and Jay Thompson. Paul Wallace, Stephen Self, Thorvaldur Thordarson, and an anonymous reviewer provided thoughtful comments that greatly improved the quality of this manuscript.

Figures

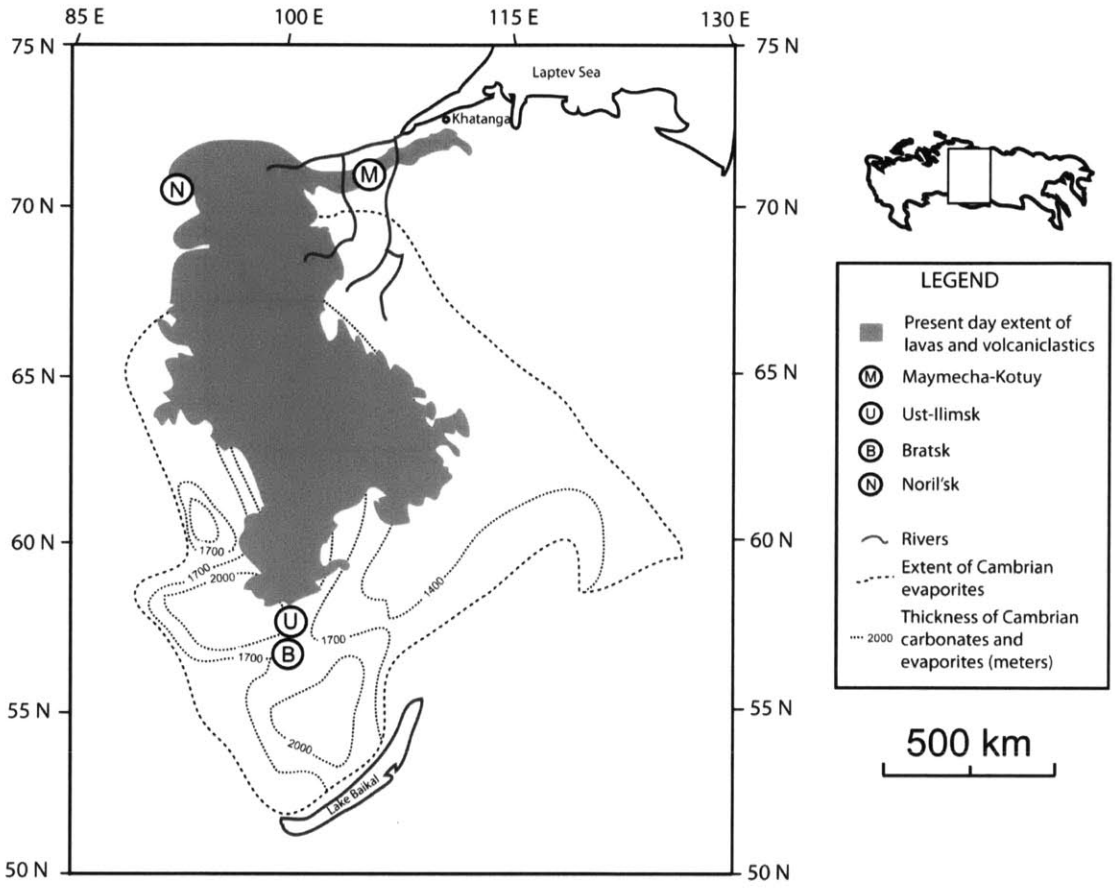

Figure 1: Map showing present day extent of Siberian Traps lavas and volcaniclastics in the Tunguska basin based on Reichow et al. (2005). Thickness and extent of Cambrian evaporites, including limestone, halite, dolomite and anhydrite, are based on Zharkov (1984). As described in the legend, circled letters M, U, and B denote the three areas from which we obtained melt inclusion samples. N marks Noril'sk, the source of the inclusions reported in Sobolev et al. (2009). Reichow et al. (2005) have also argued that the distribution of intrusions and basaltic subcrop supports a much larger original extent of the Siberian Traps, reaching into the adjacent West Siberian Basin (not shown here).

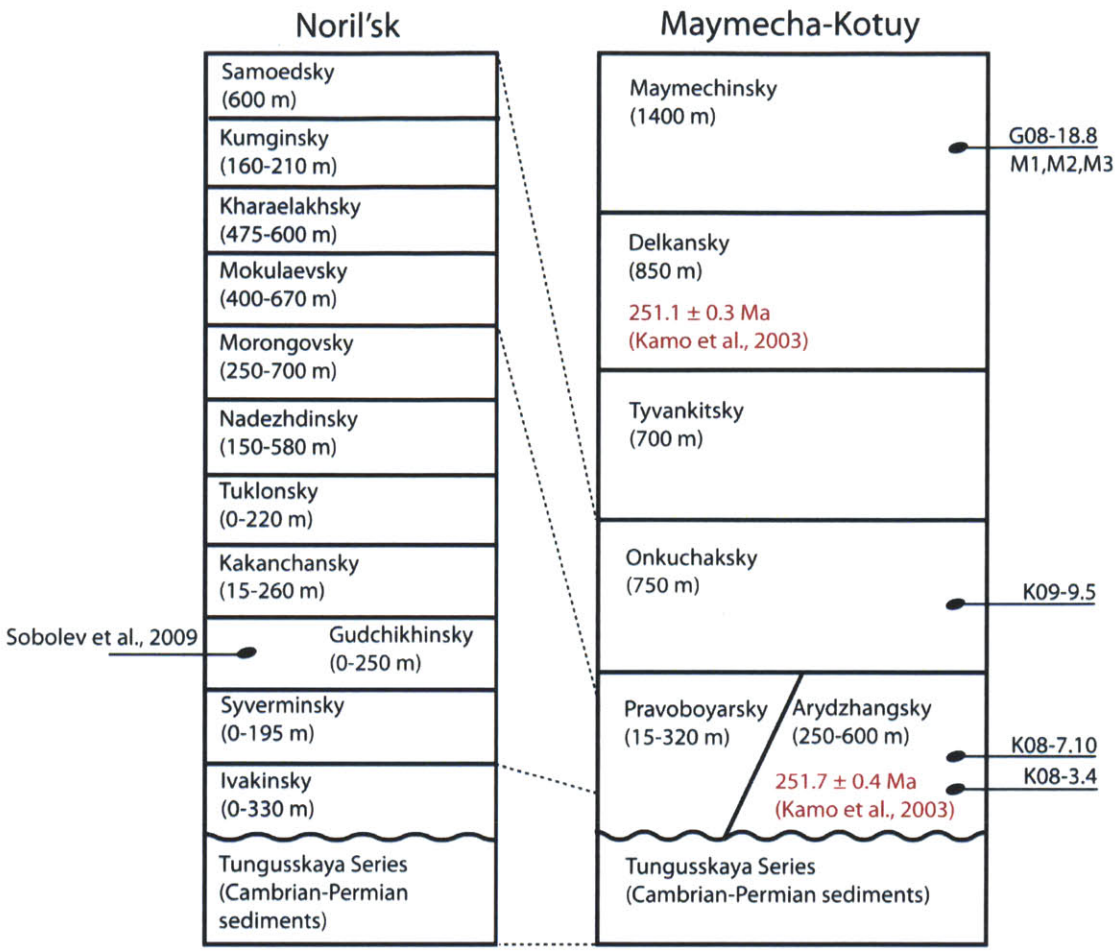

Figure 2: Schematic stratigraphy of the extrusive suites in the Noril'sk and Maymecha-Kotuy regions of the Siberian Traps, marked with an N and M respectively on Figure 1. U-Pb dates from Kamo et al. (2003) are given in red; stratigraphic positions of the samples from the Maymecha-Kotuy presented in this study are denoted on the right. The inclusions reported in Sobolev et al. (2009) come from the Gudchikhinsky picrites, as denoted on the left. Dotted lines show geochemical, paleomagnetic, and paleontological correlations between Noril'sk and Maymecha-Kotuy as proposed by Fedorenko and Czamanske (1997), Fedorenko et al. (2000), Kamo et al. (2003).

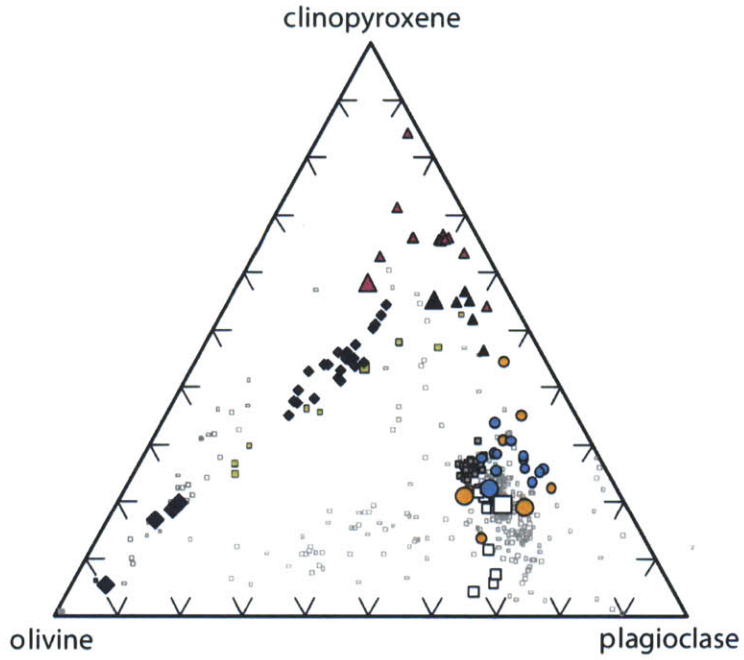

Figure 3: Modal olivine-clinopyroxene-plagioclase ternary diagram showing whole rock and melt inclusion chemistry compared with previous whole rock and melt inclusion studies of the Siberian Traps. Large colored symbols represent whole rock compositions, and small colored symbols represent melt inclusion compositions: R06-07 and A10-23.1, Bratsk dolerite sill (●); R06-09, Ust-Ilimsk dolerite sill (●); K08-3.4, Arydzhangsky tuff (▲); K08-7.10, Arydzhangsky tuff (▲), G08-18.8, M1, M2, and M3, maymechites (◆), and K09-9.5, Onkuchaksky flow (□). Sobolev's (1991) maymechite melt inclusion compositions (■) are consistent with our new maymechite inclusions. Sobolev et al.'s (2009) Gudchikhinsky picrite melt inclusions are shown as small gray squares (■). Whole rock geochemical analyses from Arndt et al. (1995), Dalrymple et al. (1995), Fedorenko and Czamanske (1997), Fedorenko et al. (1996a), Hawkesworth et al. (1995), Lightfoot et al. (1990),Ryabov et al. (1985), Sharma et al. (1991), Wooden et al. (1993) and Zolotukhin and Almukhamedov (1988) are shown in the background (□).

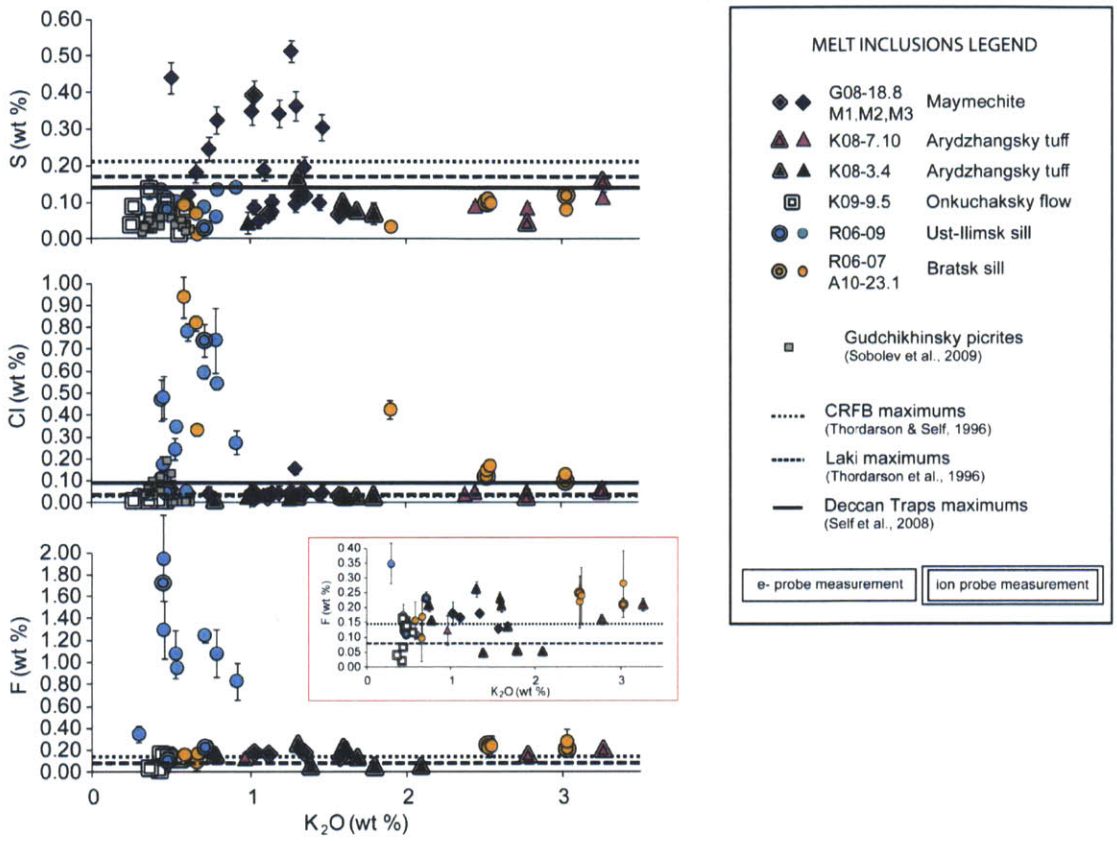

Figure 4: S, Cl, and F in Siberian Traps melt inclusions. Bottom inset (red box) shows an enlargement of F measurements less than 0.40 wt %. Error bars are 2-sigma. Where multiple analyses were available for the same target, error bars represent two standard deviations of the population. Otherwise, for microprobe analyses error bars are derived from counting error divided by the square root of the number of measurement points. For SIMS analyses error was calculated on the basis of the goodness of fit to the standard analyses. Double-outlined data points were obtained with ion-probe analysis; ion probe detection limits for Cl are <0.0045 wt %, and for F are <0.009 wt%.

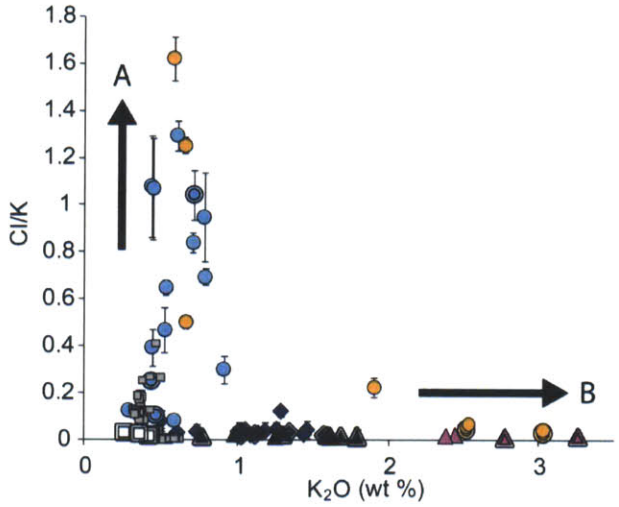

Figure 5: Cl/K_2O ratios for melt inclusions from the Siberian Traps, including Gudchikhinsky picrites reported by Sobolev et al. (2009). Symbols are identical to those in Figure 4 and 5. Two trends are visible. Trend A is a near-vertical increase in Cl/K_2O ratios, which may represent assimilation. Trend B may represent other magmatic processes, in particular fractionation. These trends resemble assimilation and fractionation trends observed in Mid-Ocean Ridge Basalts (Saal et al., 2002). In the case of MORB, assimilation of a hydrothermal brines or Cl-rich minerals may lead to Cl/K_2O ratios >0.3 (Kent et al., 1999a; Michael and Schilling, 1989).

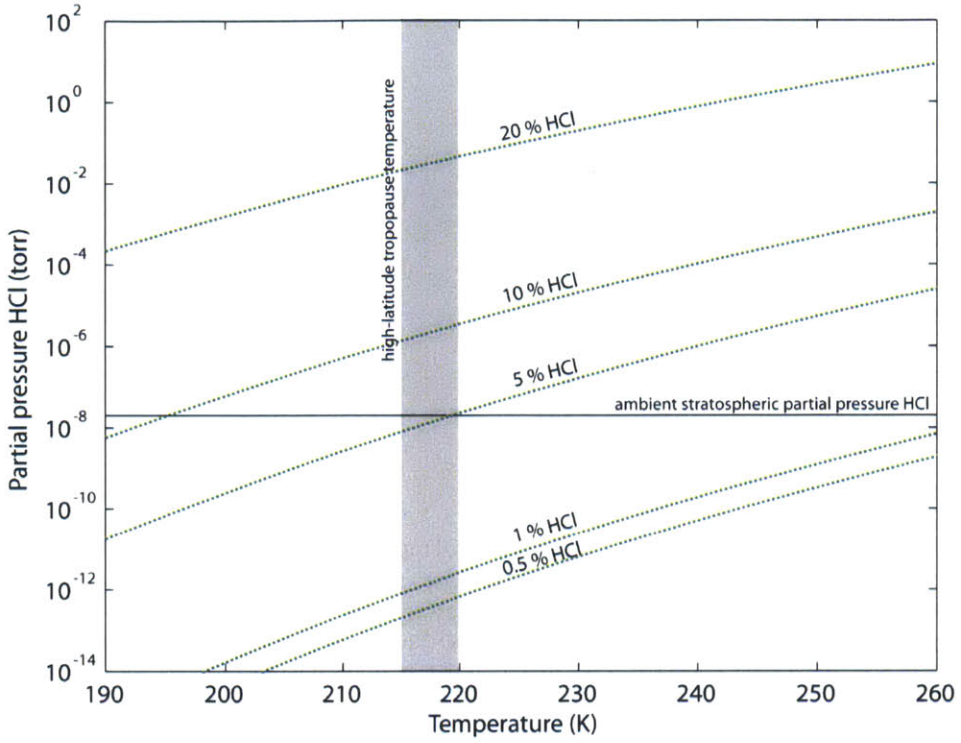

Figure 6: Vapor pressure of HCl in equilibrium with HCl-H_2O solution aerosol of the HCl concentration noted on each curve. The gray vertical box shows the present-day temperature of the high-latitude tropopause (Gill, 1982; Randel and Wu, 2010).The solid horizontal line shows typical stratospheric partial pressure of HCl of 2×10^{-8} torr (Pinto et al., 1989). Where HCl partial pressure curves exceed this threshold, HCl will not completely condense from the ascending plume.

Tables

Sample	Description	Maximum S [Mean S] wt %	Maximum Cl [Mean Cl] wt %	Maximum F [Mean F] wt %
R06-07, A10-23.1	Bratsk dolerite sill	0.13 [0.08]	0.94 [0.33]	0.30 [0.17]
R06-09	Ust-Ilimsk dolerite sill	0.14 [0.09]	0.78 [0.32]	1.95 [0.74]
K08-3.4	Arydzhangsky mafic tuff	0.17 [0.10]	0.03 [0.03]	0.30 [0.19]
K08-7.10	Arydzhangsky mafic tuff	0.16 [0.10]	0.07 [0.05]	0.21 [0.16]
K09-9.5	Onkuchaksky lava flow	0.06 [0.04]	0.01 [0.01]	0.16 [0.09]
G08-18.8, M1, M2, M3	Maymechinsky lava flows	0.51 [0.21]	0.15 [0.05]	0.18 [0.16]
SU50, 4270, KhS51-1 (Sobolev et al., 2009)	Gudchikhinsky picrites	0.061 [0.040]	0.193 [0.042]	—
Deccan Traps	Neral lava flows	0.14 [0.085]	0.09 [0.038]	—
Columbia River Flood Basalts	Wanapum lava flows	0.21 [0.197]	0.035 [0.030]	0.145 [0.131]
Laki	Laki lava flows	0.17 [0.17]	0.035 [0.031]	0.08 [0.065]

Table 1. Maximum and mean measured concentrations of S, Cl, and F from melt inclusions from the Siberian Traps, compared with maximum concentrations from the Deccan Traps (Self et al., 2008), the Columbia River Flood Basalts (Blake et al., 2010; Thordarson and Self, 1996), and Laki (Thordarson et al., 1996). The Bratsk sill is from location B in Figure 1; the Ust-Ilimsk sill is from location U in Figure 1; and the Arydzhangsky, Onkuchaksky, and Maymechinsky samples are from the Maymecha-Kotuy, which is location M in Figure 1. Data from the Gudchikhinsky picrites are from Sobolev (2009).

Eruption	$\frac{Al_2O_3 + CaO + Na_2O + MgO}{SiO_2}$	S (% degassed)		Cl (% degassed)		F (% degassed)		H_2O (% degassed)
		Lava	Feeder Dikes	Lava	Feeder Dikes	Lava	Feeder Dikes	Lava
Laki	0.65	71-88	44	27-51	33	29-52	37	70-90
Deccan Traps	0.69	50-74	N/A	44-72	N/A	N/A	N/A	N/A
Columbia River Flood Basalts	0.58	70-90	44	37-66	17	30-37	15	N/A
Mean	0.64	64-84	44	36-63	25	30-45	26	70-90
Siberian Traps	0.69							

Table 2: Degassing of S, Cl, F, and H_2O, where data is available, from lavas and feeder dikes in flood basaltic eruptions. Estimates of degassing from Laki are from Thordarson et al. (1996), and the ranges represent vent degassing vs. total degassing; feeder dike estimates are based on comparison of melt inclusions with volatiles in groundmass glass from phreatomagmatic tephra clasts. Estimates from the Deccan Traps are from Self et al. (2008), and the ranges represent crystallinity-corrected versus measured results. Estimates from the Columbia River Flood Basalts are from Thordarson and Self (2006) and the ranges represent vent degassing versus total degassing. The ratio $(Al_2O_3+CaO+Na_2O+MgO)/SiO_2$ correlates with Cl solubility in basalts (Webster et al., 1999), and was calculated based on whole rock geochemistry from the studies mentioned above. In the case of the Siberian Traps, the ratio was calculated based on mean whole rock major elements for the samples used in this study, which are shown in Supplementary Table 1.

Extrusive Sample	Individual flow/tuff				Suite in Maymecha-Kotuy			
	Volume (km^3)	**S** (Mt)	**Cl** (Mt)	**F** (Mt)	**Volume** (km^3)	**S** (Gt)	**Cl** (Gt)	**F** (Gt)
K08-7.10	4-112	18-500	8-220	24-660	300-6400	1.4-30	0.4-9	2.1-46
K08-3.4	9-240	42-110	8-200	76-2000				
K09-9.5	16-128	27-220	4-36	72-570	1500-12000	2.5-20	0.4-3.3	6.7-54
G08-18.8 M1, M2, M3	—	—	—	—	90-22400	1.3-320	0.38-94	0.45-110

Table 3: Dissolved volatiles prior to degassing, based on volumetric estimates and maximum concentrations measured in melt inclusions from each sample (Table 1). Data from the Columbia River Flood Basalts suggests that during the Roza eruption of that large igneous province, approximately 70% of magmatic S, 37% of Cl, and 30% of F were released at the vents (Thordarson and Self, 1996). Volumes are based on present-day thickness and areal extent (Fedorenko et al., 2000; Fedorenko and Czamanske, 1997; Malitch et al., 1999). The range represents the current areal extent of individual suites versus the entire area covered by Maymecha-Kotuy lavas (~16,000 km^2). These volume estimates may incorporate additional uncertainty, given the challenges to mapping in the area and the effects of erosion. Note that the thicknesses of individual flows within the maymechite pile (samples G08-18.8, M1, M2, and M3) are generally difficult to distinguish; the volatile contents of individual Maymechinsky flows in the leftmost columns are therefore omitted.

Sample	Host Whole Rock MI	Analysis Method	# of analyses	SiO2 wt %	σ	TiO2 wt %	σ	Al2O3 wt %	σ	FeO wt %	σ	MnO wt %	σ	MgO wt %	σ	CaO wt %	σ	Na2O wt %	σ	K2O wt %	σ	P2O5 wt %	σ	S wt %	σ	Cl wt %	σ	F wt %	σ	Total	Original Total
R0607	**Whole Rock**	ICP-MS	1	48.6		3.32		11.4		20.6		0.34		3.65		7.70		2.80		1.10		0.32		0.10		0.04		0.07		100	
R0607-1	olivine host	microprobe	4	31.5	0.11	0.06	0.02	0.02	0.02	55.2	0.71	0.87	0.01	11.9	0.73	0.36	0.02	0.00	0.00											100	99.84
R0607-2	olivine host	microprobe	5	30.8	1.07	0.07	0.02	1.29	2.61	56.0	1.92	0.89	0.06	10.6	0.28	0.40	0.02	0.00	0.00											100	99.92
R0607-3	olivine host	microprobe	5	31.0	0.06	0.07	0.01	0.02	0.01	57.3	0.26	0.96	0.04	10.3	0.57	0.28	0.02	0.00	0.00											100	100.58
R0607-1	melt inclusion	microprobe	3	57.6	0.88	2.99	0.05	11.2	0.20	14.1	0.31	0.46	0.04	0.82	0.16	6.12	0.06	2.82	1.18	2.52	0.03	0.82	0.05	0.11	0.00	0.15	0.01	0.22	0.09	100	98.61
R0607-1	melt inclusion	ion probe	1																					0.12		14		0.30			
R0607-2	melt inclusion	microprobe	2	56.1	0.33	2.82	0.13	9.75	0.02	18.4	0.30	0.50	0.06	0.95	0.02	4.04	0.01	3.43	0.24	2.54	0.05	0.94	0.06	0.10	0.00	0.17	0.00	0.24	0.04	100	100.20
R0607-3	melt inclusion	microprobe	3	62.8	2.89	2.86	0.41	10.9	0.60	13.6	3.09	0.32	0.03	0.66	0.21	1.52	0.22	3.14	0.62	3.03	0.28	0.69	0.18	0.08	0.03	0.13	0.01	0.28	0.04	100	100.19
R0607-3	melt inclusion	ion probe	1																					0.13		0.11		0.23			
R0609	**Whole Rock**	ICP-MS	1	50.1		3.02		12.2		18.6		0.31		2.92		8.41		2.91		1.02		0.33		0.08		0.01		0.05		100	
R0609-1.2	plag host	microprobe	1	54.6				28.0		0.64				0.09		10.6		5.66		0.22										100	98.55
R0609-1.4	plag host	microprobe	1	53.9				27.1		0.73				0.10		10.1		5.79		0.25										100	99.62
R0609-3.1	plag host	microprobe	1	57.2				27.7		0.71				0.20		10.1		5.47		0.28										100	101.68
R0609-3.2	plag host	microprobe	1	55.5				27.0		0.61				0.15		10.6		5.8		0.37										100	99.67
R0609-4.3	plag host	microprobe	1	56.4				27.3		0.68				0.12		10.1		5.98		0.31										100	101.00
R0609-4.5	plag host	microprobe	1	57.6				27.1		0.60				0		9.14		6.04		0.31										100	100.83
R0609-5.1	plag host	microprobe	6	56.8	0.71			26.7	0.18	0.59	0.05			0.08	0.03	9.63	0.27	5.87	0.12	0.33	0.02									100	100.48
R0609-5.3	plag host	microprobe	6	58.7	1.00			25.6	0.59	0.52	0.13			0.03	0.02	7.98	0.69	6.72	0.39	0.46	0.08									100	100.37
R0609-5.4	plag host	microprobe	5	56.3	0.95			26.9	0.65	0.65	0.04			0.09	0.02	10.0	0.20	5.73	0.17	0.31	0.01									100	100.37
R0609-5.5	plag host	microprobe	5	56.0	0.21			27.2	0.27	0.61	0.03			0.09	0.01	10.3	0.17	5.50	0.06	0.28	0.02									100	100.69
R0609-5.6	plag host	microprobe	6	56.7	0.34			26.6	0.35	0.66	0.05			0.08	0.01	9.69	0.14	5.90	0.10	0.31	0.01									100	100.71
R0609-1.2B	melt inclusion	microprobe	2	49.2		2.14		13.9		15.2		0.21		2.84		9.35		4.87		0.78		0.31		0.06		0.14		1.08		100	98.14
R0609-1.4A	melt inclusion	microprobe	1	44.8		3.39		11.6		21.7		0.32		3.01		9.33		4.15		0.43		0.46		0.13		0.47		0.18		100	98.63
R0609-3.1	melt inclusion	microprobe	3	48.8	1.1	2.56	0.8	12.9	0.7	17.3	1.0	0.29	0.2	2.29	1.1	9.24	1.2	4.41	2.0	0.52	0.2	0.31	0.0	0.10	0.1	0.25	0.1	1.08	0.9	100	100.29
R0609-3.2A	melt inclusion	microprobe	1	47.4		2.93		12.0		19.9		0.35		2.20		9.17		3.18		0.45		0.35		0.12		0.48		1.30		100	99.02
R0609-4.3B	melt inclusion	microprobe	3	48.8	4.8	2.79	0.8	13.9	0.5	16.0	3.0	0.25	0.2	2.34	1.0	9.48	1.0	4.04	2.8	0.44	0.1	0.26	0.0	0.08	0.1	0.18	0.1	1.95	1.7	100	100.44
R0609-4.3B	melt inclusion	ion probe	1																					0.08		0.11		1.73			
R0609-4.3E	melt inclusion	microprobe	1	47.8		2.99		11.5		21.3		0.33		2.50		9.73		3.00		0.29		0.38		0.08		0.04		0.35		100	99.81
R0609-4.5	melt inclusion	microprobe	2	51.6		1.94		13.2		16.30		0.25		0.74		9.11		4.13		0.91		0.51		0.14		0.27		0.83		100	98.36
R0609-5.1	melt inclusion	microprobe	3	49.0	0.13	2.14	0.10	13.2	0.16	16.5	0.13	0.30	0.01	2.19	0.04	9.94	0.04	3.83	0.16	0.71	0.01	0.25	0.02	0.09	0.01	0.59	0.01	1.24	0.16	100	99.07
R0609-5.1	melt inclusion	ion probe	1																					0.02		0.16		0.74			
R0609-5.3A	melt inclusion	microprobe	1	47.0	0.11	2.40	0.07	11.7	0.13	21.5	0.18	0.33	0.03	2.28	0.00	9.64	0.09	4.08	0.09	0.47	0.02	0.31	0.02	0.11	0.00	0.05	0.00	0.12	0.05	100	98.10
R0609-5.3A	melt inclusion	ion probe	1																					0.08		0.03		0.23			
R0609-5.3B	melt inclusion	microprobe	1	46.2		2.27		12.1		21.5		0.44		2.25		9.78		4.24		0.59		0.33		0.08		0.05		0.11		100	98.09
R0609-5.4	melt inclusion	microprobe	4	48.8	0.14	2.27	0.14	12.9	0.11	17.0	0.10	0.29	0.05	2.28	0.02	9.92	0.07	4.24	0.07	0.53	0.01	0.30	0.01	0.10	0.01	0.35	0.01	0.95	0.04	100	98.91
R0609-5.5	melt inclusion	microprobe	2	47.5	0.04	2.52	0.06	11.0	0.01	19.8	0.02	0.31	0.00	2.55	0.02	10.5	0.06	3.88	0.21	0.60	0.02	0.34	0.00	0.09	0.01	0.38	0.03	0.80		100	98.03
R0609-5.6	melt inclusion	microprobe	1	50.1		2.22		11.6		18.0		0.36		2.14		9.51		4.25		0.78		0.34		0.14		0.55		0.90		100	98.42
K08-3.4	**Whole Rock**	ICP-MS	1	51.7		2.96		10.8		9.73		0.14		6.19		8.25		0.68		7.97		0.67		0.02		0.01		0.20		100	
K08-3.4-3.2A	cpx host	microprobe	1	50.4		1.62		5.13		5.83		0.08		14.9		23.2		0.68												100	99.28
K08-3.4-3.3A	cpx host	microprobe	1	51.8		0.95		2.79		4.46		0.09		16.2		23.0		0.70												100	100.11
K08-3.4-5.2B	cpx host	microprobe	1	51.3		1.37		3.75		4.97		0.05		15.4		23.3		0.67												100	99.84
K08-3.4-6.1	cpx host	microprobe	4	51.9	0.79	1.14	0.07	2.61	0.24	4.68	0.20	0.06	0.02	15.7	0.24	23.8	0.21	0.62	0.04											100	100.08
K08-3.4-6.4	cpx host	microprobe	4	51.3	0.57	1.54	0.32	2.75	0.12	5.35	0.24	0.07	0.01	14.8	0.74	23.3	0.18	0.55	0.06											100	99.96
K08-3.4-6.5	cpx host	microprobe	4	51.2	0.61	1.49	0.11	2.91	0.16	5.51	0.24	0.08	0.02	14.9	0.41	23.0	0.27	0.59	0.03											100	100.04
K08-3.4-6.6	cpx host	microprobe	4	51.7	0.60	1.27	0.11	2.69	0.07	5.22	0.18	0.08	0.01	15.3	0.45	23.9	0.20	0.61	0.03											100	100.09
K08-3.4-6.7	cpx host	microprobe	4	51.8	0.71	1.31	0.27	2.58	0.51	4.90	0.50	0.08	0.01	15.4	0.72	23.1	0.18	0.53	0.01											100	100.51
K08-3.4-6.8	cpx host	microprobe	4	51.2	0.40	1.49	0.24	2.83	0.37	5.23	0.18	0.06	0.02	15.3	0.42	23.1	0.16	0.58	0.05											100	100.95
K08-3.4-3.2A	melt inclusion	microprobe	1	45.7		3.45		6.62		9.96		0.10		11.7		18.3		2.83		0.98		0.20		0.05		0.04		n.d.			98.21
K08-3.4-3.3A	melt inclusion	microprobe	1	46.5		3.61		9.02		10.3		0.14		8.95		14.7		4.27		1.79		0.37		0.05		0.07		0.03			98.0
K08-3.4-5.2B	melt inclusion	microprobe	1	46.9		3.51		7.01		9.36		0.11		10.6		17.4		3.35		1.25		0.26		0.01		n.d.		0.02			98.45
K08-3.4-6-1	melt inclusion	microprobe	2	46.4	0.53	2.56	0.10	5.58	0.06	12.2	0.01	0.18	0.03	11.3	0.11	16.1	0.00	1.45	0.04	2.09	0.04	2.02	0.06	n.d.		n.d.		n.d.		100	99.30
K08-3.4-6-1A	melt inclusion	microprobe	3	47.2	0.15	2.96	0.22	6.94	0.02	9.21	0.18	0.15	0.03	11.0	0.10	17.3	0.03	3.05	0.07	1.59	0.02	0.26	0.05	0.09	0.00	0.03	0.00	n.d.			99.49
K08-3.4-6-4A	melt inclusion	ion probe	1																					0.10		0.03		0.23			
K08-3.4-6-4C	melt inclusion	microprobe	1	47.0		3.05		7.12		9.97		0.16		10.8		17.1		2.45		1.68		0.30		0.08		0.03		0.14		100	99.31
K08-3.4-6-5A	melt inclusion	microprobe	4	47.7	0.16	2.89	0.14	6.72	0.05	9.38	0.08	0.13	0.01	11.3	0.15	17.2	0.02	2.69	0.15	1.30	0.01	0.22	0.03	0.13	0.01	0.03	0.01	0.17	0.11	100	98.21
K08-3.4-6-5A	melt inclusion	ion probe	1																					0.17		0.03		0.26			
K08-3.4-6-5B	melt inclusion	microprobe	1	47.7		2.99		7.06		9.25		0.15		10.6		17.0		2.63		1.60		0.29		0.09		0.03		0.30		100	97.98
K08-3.4-6-6B	melt inclusion	microprobe	1	42.1		4.03		4.94		11.9		0.27		11.5		20.7		0.94		0.77		2.68		0.00		0.02				100	99.29
K08-3.4-6-6B	melt inclusion	ion probe	1																					0.00		0.01		0.16			
K08-3.4-6-7	melt inclusion	microprobe	4	44.9	0.23	3.88	0.14	7.23	0.05	11.8	0.11	0.22	0.01	11.3	0.12	17.8	0.06	1.08	0.08	1.38	0.02	0.32	0.01	n.d.		n.d.		n.d.		100	99.54
K08-3.4-6-8	melt inclusion	microprobe	3	41.7	0.45	3.54	0.18	4.69	0.21	12.0	0.06	0.26	0.02	12.2	0.20	23.9	0.19	0.69	0.09	0.74	0.02	0.07	0.01	n.d.		n.d.		0.21	0.02	100	99.17
K08-3.4-6-8	melt inclusion	ion probe	1																									0.21			
K08-7.10	**Whole Rock**	ICP-MS	1	41.1		3.74		8.46		15.5		0.20		9.03		16.2		1.99		1.07		0.58		0.02		0.00		0.45		100	
K08-7.10-2.1	cpx host	microprobe	1	49.9		1.80		2.68		6.25		0.07		14.81		23.9		0.52												100	99.56
K08-7.10-3.1	cpx host	microprobe	1	52.0		1.13		1.83		4.48		0.01		15.82		23.6		0.49												100	99.86
K08-7.10-3.4	cpx host	microprobe	1	49.0		1.92		4.07		6.53		0.07		14.20		23.3		0.69												100	99.52
K08-7.10-5.4.1	melt inclusion	microprobe	1	44.2		3.22		8.49		12.0		0.14		9.43		14.2		5.17		2.38		0.55		n.d.		n.d.		n.d.		100	
K08-7.10-5.4.2	melt inclusion	microprobe	1	43.8		3.15		8.37		12.5		0.16		9.21		14.3		5.17		2.38		0.54		n.d.		0.04		n.d.		100	
K08-7.10-5.4.3	melt inclusion	microprobe	1	44.8		2.49		8.80		11.0		0.16		9.81		13.3		5.55		2.78		0.83		0.09		0.05		n.d.		100	
K08-7.10-5.4.5	melt inclusion	ion probe	1																					0.045		0.025		0.16		100	
K08-7.10-5.4.4	melt inclusion	microprobe	1	43.9		3.19		8.42		12.2		0.19		9.17		14.5		4.89		2.44		0.69		0.09		0.05		n.d.		100	
K08-7.10-2.1.5	melt inclusion	microprobe	1	47.6		2.41		10.36		8.86		0.15		9.32		11.7		5.12		3.26		0.76		0.11		0.07		n.d.		100	
K08-7.10-2.1.5	melt inclusion	ion probe	1																					0.16		0.054		0.21		100	
K08-7.10-5.4H	melt inclusion	microprobe	1	41.7		4.45		6.17		13.4		0.18		8.52		17.5		1.59		0.96		0.30		n.d.		n.d.		0.12		100	
K09-9.5	**Whole Rock**	ICP-MS	1	48.4		1.80		15.7		13.5		0.24		6.26		11.0		2.47		0.31		0.20		0.02		0.02		0.02		100	
K09-9.5.1	plag host	microprobe	*h*	49.6	0.91			31.50	0.86	0.47	0.19			0.19	0.08	15.4	0.68	2.63	0.31	0.07	0.03									100	100.08
K09-9.5.2	plag host	microprobe	*h*	50.1	1.20			31.40	0.84	0.40	0.04			0.16	0.03	14.9	0.98	2.96	0.59	0.08	0.01									100	100.37
K09-9.5.3	plag host	microprobe	*h*	50.0	0.41			31.59	0.32	0.40	0.03			0.16	0.02	15.0	0.31	2.81	0.16	0.08	0.01									100	100.55
K09-9.5.4	plag host	microprobe	*h*	50.0	0.71			31.46	0.50	0.44	0.08			0.17	0.02	14.9	0.42	2.96	0.27	0.09	0.02									100	100.51
K09-9.5.7	plag host	microprobe	*h*	50.2	1.04			31.42	0.63	0.41	0.03			0.16	0.01	14.9	0.59	2.87	0.41	0.08	0.02									100	100.42
K09-9.5.8	plag host	microprobe	*l*	50.2	1.01			29.06	6.57	2.52	5.57			0.94	2.06	14.3	1.73	2.91	0.24	0.12	0.09									100	100.34
K09-9.5.11	plag host	microprobe	*h*	50.1	0.79			31.49	0.83	0.41	0.02			0.16	0.02	14.8	0.38	2.89	0.22	0.08	0.02									100	100.71
K09-9.5.12	plag host	microprobe	*h*	50.0	0.51			31.60	0.36	0.43	0.02			0.16	0.02	15.0	0.47	2.78	0.31	0.08	0.01									100	100.89
K09-9.5.13	plag host	microprobe	*l*	50.0	0.72			31.50	0.68	0.47	0.08			0.15	0.02	15.0	0.46	2.79	0.32	0.08	0.02									100	100.79
K09-9.5.14	plag host	microprobe	*h*	49.4	0.51			31.99	0.34	0.42	0.03			0.14	0.01	15.31	0.23	2.67	0.10	0.08	0.01									100	100.82
K09-9.5.1	melt inclusion	microprobe	1	45.6		0.97		18.3		16.2		0.10		6.69		9.34		2.35		0.26		0.12		0.01		n.d.		n.d.		100	100.15
K09-9.5.1	melt inclusion	ion probe	1																					0.014		n.d.		n.d.			
K09-9.5.2a	melt inclusion	microprobe	1	49.1		1.89		14.4		13.9		0.19		7.00		10.6		2.29		0.45		0.14		0.03		n.d.		0.05		100	98.23
K09-9.5.2a	melt inclusion	ion probe	1																					0.047		n.d.		0.13			
K09-9.5.2c	melt inclusion	microprobe	1	49.1		1.84		14.1		14.0		0.21		7.02		10.7		2.31		0.43		0.18		0.04		n.d.		0.07		100	98.11

Sample	Host Whole Rock MI	Analysis Method	# of analyses	SiO2 wt %	σ	TiO2 wt %	σ	Al2O3 wt %	σ	FeO wt %	σ	MnO wt %	σ	MgO wt %	σ	CaO wt %	σ	Na2O wt %	σ	K2O wt %	σ	P2O5 wt %	σ	S wt %	σ	Cl wt %	σ	F wt %	σ	Total	Original Total
K09-9-5.2c	melt inclusion	ion probe	1																					0.04		n.d.		0.07			
K09-9-5.3	melt inclusion	microprobe	4	49.1	0.13	1.84	0.04	14.6	0.05	13.8	0.10	0.21	0.02	6.84	0.07	10.4	0.06	2.42	0.06	0.45	0.01	0.16	0.01	0.03	0.01	n.d.		0.07	0.04	100	98.64
K09-9-5.3	melt inclusion	ion probe	1																					0.06		0.01		0.13			
K09-9-5.4	melt inclusion	microprobe	1	49.2		1.82		14.5		13.7		0.20		6.86		10.5		2.34		0.46		0.18		0.04		n.d.		0.11		100	98.17
K09-9-5.4	melt inclusion	ion probe	1																					0.06		0.01		0.16			
K09-9-5.7	melt inclusion	microprobe	2	49.2	0.32	1.84	0.09	14.4	0.03	14.1	0.09	0.21	0.00	6.78	0.07	10.5	0.05	2.25	0.15	0.43	0.01	0.16	0.01	0.04	0.01	n.d.		0.11	0.00	100	98.81
K09-9-5.7	melt inclusion	ion probe	1																					0.05		0.01		0.16			
K09-9-5.8A	melt inclusion	microprobe	1	49.2		1.90		14.1		13.9		0.18		7.05		10.8		2.09		0.42		0.16		0.04		0.01		0.05		100	98.22
K09-9-5.8A	melt inclusion	ion probe	1																					0.02		n.d.		0.02			
K09-9-5.8B	melt inclusion	microprobe	1	49.0		1.92		14.2		14.2		0.21		7.06		10.8		2.07		0.36		0.16		n.d.		n.d.		n.d.		100	98.34
K09-9-5.11	melt inclusion	microprobe	3	47.6	0.11	1.77	0.10	15.7	0.05	17.5	0.22	0.22	0.02	5.18	0.01	8.75	0.04	2.54	0.08	0.58	0.03	0.14	0.00	n.d.		n.d.		n.d.		100	99.23
K09-9-5.12A	melt inclusion	microprobe	1	48.1		1.92		16.5		14.9		0.12		6.80		7.96		2.87		0.55		0.13		n.d.		0.01		n.d.		100	99.26
K09-9-5.12B	melt inclusion	microprobe	1	46.3		1.13		16.8		17.8		0.22		6.91		7.74		2.46		0.48		0.02		n.d.		n.d.		0.14		100	99.70
K09-9-5.13A	melt inclusion	microprobe	1	49.5		1.72		14.4		13.8		0.21		6.68		11.0		2.11		0.40		0.17		0.03		0.01		0.02		100	98.43
K09-9-5.14	melt inclusion	microprobe	3	46.9	0.25	2.19	0.12	14.9	0.07	16.3	0.27	0.31	0.01	6.09	0.11	10.5	0.06	2.40	0.04	0.25	0.02	0.21	0.03	n.d.		n.d.		n.d.		100	98.85
A10-23.1	**Whole Rock**	ICP-MS	1	51.6		2.40		14.5		14.2		0.24		3.12		8.66		3.05		1.39		0.29		0.02		0.04		0.03		100	
A10-23.1-2	plag host	microprobe	3	55.4	0.28			27.5	0.17	0.64	0.07			0.09	0.01	10.8	0.18	5.15	0.14	0.29	0.01									100	100.37
A10-23.1-3	plag host	microprobe	6	54.9	1.05			28.0	0.34	0.54	0.03			0.09	0.02	11.1	0.20	5.04	0.11	0.27	0.01									100	100.30
A10-23.1-4	plag host	microprobe	5	54.5	0.40			28.4	0.19	0.57	0.05			0.09	0.02	11.3	0.25	4.86	0.14	0.25	0.01									100	101.03
A10-23.1-6	plag host	microprobe	5	54.9	0.64			27.9	0.22	0.57	0.06			0.09	0.02	11.1	0.11	5.09	0.15	0.26	0.01									100	100.32
A10-23.1-7	melt inclusion	microprobe	2	45.8	0.38	2.32	0.05	12.7	0.32	18.3	0.16	0.38	0.03	2.05	0.01	11.8	0.24	4.65	0.01	0.65	0.00	0.33	0.01	0.07	0.01	0.82	0.02	0.10	0.04	100	98.36
A10-23.1-3	melt inclusion	microprobe	3	45.5	0.29	2.24	0.08	12.7	0.15	20.0	0.21	0.37	0.02	2.28	0.06	10.8	0.03	4.22	0.02	0.66	0.04	0.26	0.03	0.01	0.01	0.33	0.01	0.17	0.03	100	98.32
A10-23.1-4	melt inclusion	microprobe	1	47.2		1.43		16.8		14.8		0.30		2.22		9.26		5.40		1.90		0.22		0.03		0.43		0.01		100	98.13
A10-23.1-6	melt inclusion	microprobe	1	45.9		2.75		11.0		17.9		0.26		2.67		13.7		3.60		0.58		0.31		0.09		0.94		0.16		100	98.32
G08-18.8	**Whole Rock**	ICP-MS	1	40.6		1.43		1.62		12.0		0.19		41.3		2.33		0.10		0.00		0.19		0.05		0.01		0.08		100	
M1	**Whole Rock**	XRF	2	40.97		1.93		2.19		12.82		0.21		36.01		5.30		0.25		0.08		0.24								100	
M2	**Whole Rock**	XRF	2	41.30		2.49		2.92		12.92		0.21		33.33		6.19		0.16		0.14		0.34								100	
M3	**Whole Rock**	XRF	2	41.34		2.60		3.00		13.37		0.22		32.35		6.49		0.17		0.12		0.34								100	
G08-18.8-1.3	olv host	microprobe	1	40.1		0.03		0.01		8.36		0.14		50.6		0.38		0.35												100	101.47
G08-18.8-2.2	olv host	microprobe	1	40.5		0.05		0.02		8.61		0.15		49.7		0.42		0.41												100	100.75
G08-18.8-2.5	olv host	microprobe	1	39.9		0.03		0.03		9.63		0.14		49.4		0.39		0.34												100	100.16
M1A-5	olv host	microprobe	1	40.8		0.03		0.06		8.51		0.12		49.7		0.33														100	99.91
M1A-8	olv host	microprobe	1	40.8		0.02		0.05		9.18		0.15		50.0		0.39														100	100.88
M1B-3	olv host	microprobe	1	40.6		0.01		0.05		9.19		0.13		50.0		0.36														100	100.73
M1B-7	olv host	microprobe	1	41.1		0.05		0.06		8.64		0.13		49.7		0.33														100	99.82
M1A-2	olv host	microprobe	1	39.6		0.05		0.07		11.6		0.19		47.5		0.41														100	99.78
M1A-8	olv host	microprobe	1	40.8		0.02		0.05		9.18		0.15		50.0		0.39														100	100.88
M1A-9	olv host	microprobe	1	40.4		0.03		0.04		8.73		0.11		49.7		0.39														100	99.77
M2A-3	olv host	microprobe	1	40.7		0.03		0.07		8.66		0.13		50.7		0.38														100	101.05
M2A-5	olv host	microprobe	1	40.6		0.02		0.06		11.0		0.14		48.1		0.43														100	100.80
M2B-3	olv host	microprobe	1	40.4		0.05		0.07		8.99		0.11		49.4		0.42														100	99.90
M2B-4	olv host	microprobe	1	40.7		0.05		0.06		8.72		0.15		49.7		0.41														100	100.20
M2B-5	olv host	microprobe	1	40.1		0.04		0.08		9.49		0.13		49.4		0.38														100	100.12
M2A-7	olv host	microprobe	1	40.7		0.02		0.07		8.72		0.11		49.2		0.40														100	99.64
M2A-8	olv host	microprobe	1	41.0		0.04		0.07		8.72		0.13		49.6		0.39														100	100.38
M2A-2	olv host	microprobe	1	40.4		0.01		0.06		10.1		0.14		48.3		0.38														100	100.16
M1B-1	olv host	microprobe	1	40.7		0.04		0.06		11.6		0.18		46.7		0.48														100	98.93
G08-18.8-1.3	melt inclusion	microprobe	1	39.6		5.68		6.07		15.0		0.20		14.5		14.0		2.17		1.28		0.76		0.13		0.04				100	98.37
G08-18.8-2.2	melt inclusion	microprobe	1	39.5		4.54		4.94		17.6		0.25		17.6		11.8		1.64		0.61		0.39		0.05		0.03				100	100.63
G08-18.8-2.7	melt inclusion	microprobe	1	39.7		5.34		5.82		16.4		0.27		13.8		14.0		2.36		1.05		0.16		0.51		0.05				100	98.47
M1A-5.1	melt inclusion	microprobe	1	40.1		4.73		5.73		12.1		0.21		19.1		12.9		2.28		1.26		0.68		0.09		0.15				100	98.28
M1A-8.1	melt inclusion	microprobe	1	39.9		4.45		5.32		13.1		0.21		19.3		12.4		2.41		1.28		0.79		0.19		0.03				100	98.57
M1A-8.2	melt inclusion	microprobe	1	40.0		4.44		4.83		14.1		0.15		20.8		11.6		2.05		1.08		0.48		0.25		0.04				100	98.56
M1B-1.2	melt inclusion	microprobe	1	39.5		5.31		5.58		12.7		0.20		18.6		13.8		2.60		0.74		0.34		0.44		0.06				100	98.83
M1B-7.1	melt inclusion	microprobe	1	40.0		5.12		5.96		11.8		0.17		19.7		13.2		2.39		0.50		0.89		0.18		n.d.				100	98.62
M1B-7.2	melt inclusion	microprobe	1	40.1		5.02		5.49		12.1		0.14		20.2		12.9		2.12		0.66		0.84		0.32		n.d.				100	98.51
M1B-7.3	melt inclusion	microprobe	1	39.9		4.78		5.14		12.1		0.20		20.5		12.7		2.36		0.79		0.72		0.36		n.d.				100	99.07
M1B-2.1	melt inclusion	microprobe	1	40.9		5.13		5.93		14.1		0.24		15.6		13.2		2.30		1.29		0.47		0.09		0.05				100	99.85
M1A-8.3	melt inclusion	microprobe	1	39.7		4.59		5.28		13.6		0.19		19.9		12.6		1.99		1.02		0.54		0.34		0.04				100	98.55
M1A-8.3	melt inclusion	ion probe	1																					0.41		0.03		0.19			
M1A-9.3	melt inclusion	microprobe	1	39.9		5.29		4.76		15.2		0.20		22.3		9.59		1.93		1.18		0.38		0.35		0.04				100	98.02
M2A-1.2	melt inclusion	microprobe	1	41.1		4.93		5.53		14.1		0.20		18.8		11.7		2.29		1.01		0.39		0.30		0.04				100	98.91
M2A-3.1	melt inclusion	microprobe	1	41.5		4.93		6.21		11.7		0.19		18.5		11.7		2.20		1.46		0.76		0.10		0.04				100	98.77
M2A-5.1	melt inclusion	microprobe	1	40.4		3.64		5.22		15.8		0.28		18.6		10.7		2.47		1.14		0.41		0.12		n.d.				100	100.30
M2A-2.1	melt inclusion	microprobe	1	39.6		4.31		4.54		14.5		0.22		21.5		11.1		1.94		1.30		0.58		0.10		0.03				100	98.52
M2A-4.1	melt inclusion	microprobe	1	39.9		3.78		4.80		14.8		0.12		22.6		10.3		1.93		1.44		0.43		0.20		n.d.				100	98.00
M2A-5.1	melt inclusion	microprobe	1	40.7		4.48		5.90		13.7		0.26		18.9		11.0		2.25		1.50		0.70		0.09		0.03				100	100.48
M2A-7.1	melt inclusion	microprobe	1	40.4		3.81		4.90		14.4		0.22		21.9		9.83		1.82		1.34		0.61		0.07		0.04				100	99.10
M2A-7.1	melt inclusion	ion probe	1																					0.13		0.04		0.18			
M2A-8.1	melt inclusion	microprobe	1	40.7		4.77		5.44		13.0		0.26		19.9		11.4		2.28		1.13		0.56		0.07		0.04				100	99.98
M2B-1.1	melt inclusion	microprobe	1	40.2		4.90		5.74		13.6		0.26		18.6		12.2		2.34		1.11		0.60		0.09		0.04				100	99.78
M2B-1.1	melt inclusion	ion probe	1																					0.08		0.04		0.20			
M3A-2.1	melt inclusion	microprobe	1	40.3		4.95		5.81		14.3		0.23		17.9		11.7		2.15		1.57		0.63		0.03		0.05				100	98.64
M3A-2.1	melt inclusion	ion probe	1																					0.04		0.03		0.14			
M1B-1.4	melt inclusion	microprobe	1	40.4		5.30		5.58		16.9		0.24		18.2		10.0		1.93		1.66		0.67		0.02		0.05				100	99.55
M1B-1.5	melt inclusion	microprobe	1	40.2		5.75		4.90		17.9		0.28		19.6		9.7		1.75		1.44		0.47		0.03		0.02				100	98.78

Supplementary Table 1. *Whole rock chemistry, microprobe analyses of host crystals, and ion probe and microprobe analyses of melt inclusions that produce acceptable electron microprobe totals (98.0-101.5) and are not completely degassed.*

Chapter 3. Sulfur isotopic evidence for sources of volatiles in Siberian Traps magmas

Abstract: The Siberian Traps flood basalts transferred a large mass of volatiles from the Earth's mantle and crust to the atmosphere. The eruption of the large igneous province temporally overlapped with the end-Permian mass extinction, and also generated ore deposits of major economic importance. Constraints on the sources of Siberian Traps volatiles are critical for determining the overall volatile budget, the role of assimilation of crustal materials, and genesis of Noril'sk massive sulfide deposits. Sulfur isotopic ratios vary among mantle and crustal materials, with characteristic mantle $\delta^{34}S$ values around 0±2 ‰ Vienna Cañon Diablo Troilite (V-CDT), and crustal $\delta^{34}S$ values between -50 ‰ and +40 ‰. We measure $\delta^{34}S$ ranging from -10.8 ‰ to +25.3 ‰ in melt inclusions from the Siberian Traps. In conjunction with previously published whole rock measurements from Noril'sk, the sulfur isotopic data suggest that crustal assimilation was widespread and heterogeneous—though not universal—during the emplacement of the Siberian Traps. Carbon concentrations constrain minimum entrapment depths of melt inclusions to upper crustal depths. Magmas likely interacted with low-$\delta^{34}S$ sedimentary materials such as shale or coal in addition to high-$\delta^{34}S$ evaporites. These crustal materials may have increased the total volatile budget of the large igneous province, thereby contributing to Permian-Triassic environmental deterioration.

1. Introduction

Early research into the sulfur isotope ratios of Siberian Traps lavas, sills, and country rocks was driven by the need to understand the genesis of the massive Ni-Cu-Platinum Group Elements deposits in the Noril'sk region (Gorbachev and Grinenko, 1973; Grinenko, 1985). These deposits contain enough platinum to satisfy global demand for 10 years or more, and enough palladium for almost half a century (Hageluken, 2006). The mineralized intrusions are characterized by anomalously high $\delta^{34}S$ ratios, possibly as a result of contamination with evaporite (Ripley et al., 2003) or sour gas (Grinenko, 1985).

In addition to the economic importance of the Siberian Traps, the apparent synchronicity of the eruption with the end-Permian mass extinction (Campbell et al., 1992; Renne and Basu, 1991; Renne et al., 1995) provides significant scientific incentive to better understand the details and the effects of magmatism. The end-Permian mass extinction was the largest loss of floral and faunal diversity in Earth's history (Erwin, 1994; Sepkoski et al., 1981).

The end-Permian mass extinction was a period characterized by sudden loss of >90% of marine species and >70% of terrestrial species; even insect diversity suffered (Erwin, 1994). Fossil size and diversity did not begin to recover until ~5 Myr after the beginning of the extinction (Lehrmann et al., 2006; Payne et al., 2004), suggesting that environmental conditions could have been inhospitable for a prolonged period. This paleontological observation is matched by an extended period of large amplitude (up to 8 ‰) carbon isotope fluctuations following the first pulse of the extinction (Payne et al., 2004).

Ar-Ar geochronology suggests that the final stages of extrusive volcanism at Noril'sk occurred at 250.3 ± 1.1 Ma, within error of a high precision sanidine Ar-Ar date for the main pulse of the end-Permian mass extinction at 249.25 ± 0.14 Ma (Reichow et al., 2009). New ultra-high-precision U-Pb dates from zircon and monazite at the Meishan section in China bracket the onset of the mass extinction to just prior to 252.28±0.08 Ma, with a duration of less than 200±100

Kyr (Shen et al., 2011). U-Pb dates from zircon- and perovskite-bearing units in the Maymecha-Kotuy section, near the northeastern corner of the flood basalt province (Figure 1), indicate that early lavas were erupted at 251.7±0.4 Ma, and that the full duration of magmatism lasted less than 1 Myr (Kamo et al., 2003).

The discrepancy between published U-Pb dates for the Siberian Traps and the main pulse of the extinction (Kamo et al., 2003; Shen et al., 2011) may be partially explained by interlaboratory bias between the two studies (Shen et al., 2011), or the close temporal position of the eruption and the extinction may in fact be coincidental. In the latter case, the Siberian Traps may have played an important role during the delayed recovery from ecosystem collapse (Payne et al., 2004).

The climatic potency of the eruption depends on the mass and composition of gases released to the atmosphere. Two related models link gas release from the Siberian Traps to environmental change. In the first model, volatiles were primarily mantle derived (Campbell et al., 1992), possibly from volatile-rich recycled mantle (Sobolev et al., 2011). The second model hypothesizes that assimilation and metamorphism of particularly thick and volatile-rich country rocks produced carbon and halogen compounds, supplementing gases sourced from the mantle and contributing to the deterioration of environmental conditions (Beerling et al., 2007; Ganino and Arndt, 2009; Svensen et al., 2009). This hypothesis is supported by multiple lines of evidence for extensive interaction between magmas and crustal rocks (e.g. Lightfoot et al., 1993; Ripley et al., 2003; Svensen et al., 2009; Wooden et al., 1993). Volatile concentrations measured from the same melt inclusion suite used in this study also record elevated chlorine and fluorine contents, possibly as a result of interaction with crustal rocks (Black et al., 2012).

In order to further evaluate the contributions of crustal contamination to the total magmatic volatile budget—and by implication the contribution of crustal contamination to the environmental consequences of the eruption—we measured $\delta^{34}S$ in melt inclusions from the Siberian Traps. The $\delta^{34}S$ is defined as:

$$\delta^{34}S = 1000 * \frac{\left({}^{34}S/{}^{32}S\right)_{unknown} - \left({}^{34}S/{}^{32}S\right)_{standard}}{\left({}^{34}S/{}^{32}S\right)_{standard}}$$

where the isotopic composition of the unknown is referenced to that of Vienna Cañon Diablo Troilite (V-CDT). Because magmatic isotope ratios can be compared with isotope ratios in country rocks to ascertain the extent of crustal contamination, $\delta^{34}S$ provides a useful tracer for interaction between magmas and crustal rocks. Sulfur isotope ratios are relatively well-known for seawater sulfur (+10 to +35 ‰ V-CDT in the Phanerozoic ocean; Claypool et al., 1980) and mantle sulfur (0±2 ‰ V-CDT; Sakai et al., 1982; Sakai et al., 1984). Sub-arc mantle sulfur is slightly higher (+4.7±1.4 ‰ V-CDT in Indonesia), and may depend on the composition of subducting sediments (de Hoog et al., 2001). Other crustal materials are variable, with reduced sulfur materials tending to have lower $\delta^{34}S$ (Thode, 1991).

Melt inclusions can capture the evolution of magmatic volatile contents through time. Total estimates for volatile release from degassing Siberian Traps magmas range from ~6,300-7,800 Gt S, ~3,400-8,700 Gt Cl, and ~7,100-13,600 Gt F based on melt inclusions (Black et al., 2012). CO_2 degassing may have ranged from 64,000 Gt CO_2 (Beerling et al., 2007) to 170,000 Gt CO_2 (Sobolev et al., 2011). In addition to magmatic degassing, contact heating and metamorphism of sedimentary wall rocks may have produced comparable masses of CO_2 and CH_4, along with organohalogens such as CH_3Cl (Svensen et al., 2009).

The plumbing system of the Siberian Traps was vast; dikes of Permian-Triassic age span ~5 million km^2 (Figure 1; Reichow et al., 2009). The transfer of melts from the mantle to the surface also appears to have been complex and varied, with some magmas ascending rapidly, while others staged and evolved in crustal chambers (Arndt et al., 1998). Deviations of sulfur isotope ratios from mantle values may reflect three main processes: (1) contamination of magmas with crustal materials, (2) mass-dependent fractionation during degassing, and (3) secondary alteration by hydrothermal processes (Ripley et al., 2003). While the third possibility must be carefully evaluated, the first and second signals provide important information about the magmatic

plumbing system. Simple end-member models for degassing include open-system degassing, during which vapor bubbles ascend faster than the magma from which they form, and closed system degassing during in which vapor bubbles ascend together with the magma (Gerlach and Taylor, 1990). Both processes can occur in different magma batches that ascend at different rates.

In addition to our measurements of sulfur isotope ratios, we also report data on carbon concentrations in melt inclusions. We use our sulfur and carbon data in conjunction to explore the degassing systematics and plumbing system of the Siberian Traps, the variability and extent of interaction between magmas and crustal materials, and the implications for ore formation and environmental change near the Permian-Triassic boundary.

2. Geology of the Siberian Traps

The Siberian Traps large igneous province comprises flood basaltic lavas, volcaniclastic deposits, and a complex and only partially exposed system of sills and dikes, with a total volume likely in excess of 4,000,000 km^3 (Reichow et al., 2002). Two of the best studied lava stratigraphies are in Noril'sk and the Maymecha-Kotuy region (Figure 1). The large volume of volcaniclastic deposits associated with the Siberian Traps is unusual among continental large igneous provinces (Ross et al., 2005). The samples we refer to herein as mafic tuffs are from matrix-supported mafic volcaniclastic units with large basaltic fragments. Further work is necessary to determine with certainty whether these rocks are in fact true pyroclastic rocks.

Siberian Traps magmas were erupted through the Tunguska sedimentary sequence, which reaches 12.5 km in thickness (Meyerhoff, 1980). The thickness of Cambrian evaporitic sequences alone can exceed 2.5 km (Figure 1); Zharkov (1984) estimates that the East Siberian Basin hosts a total volume of ~585,000 km^3 of rock salt. Additional Siberian salt deposits are found in Ordovician through Carboniferous strata (Zharkov, 1984). The mineralized intrusions at Noril'sk

are characterized by elevated $\delta^{34}S$ and high bulk sulfur contents, often in the form of sulfides (Grinenko, 1985; Li et al., 2009b; Ripley et al., 2003). The most commercially important intrusions are the Talnakh, Noril'sk-1, and Kharaelakh (Li et al., 2009a). The Kharaelakh sill contains magmatic anhydrite, and intrudes Devonian sedimentary rocks with abundant marine evaporite horizons (Li et al., 2009b). The metamorphism of calc-silicates and pelites produces a fluid rich environment (Aarnes et al., 2011) that could aid in the dissemination of sulfur and other sedimentary volatiles throughout the magmatic system.

3. Materials and Methods

Melt inclusions are micrometer-sized blebs of glass and crystallized silicate material segregated from the parental magma and trapped inside growing crystals. These inclusions provide a record of magma composition at the time of their entrapment. They offer a more privileged geochemical perspective than it is possible to obtain from whole rock analyses. Melt inclusions may preserve pre-eruptive volatile contents and magma compositions isolated from subsequent magmatic processes. Multiple inclusions from a single sample provide a time-series of the evolution of a batch of magma, capturing a more nuanced picture of its history as it crystallizes and degasses. Instead of using whole rock chemistry to approximate a liquid composition, naturally glassy or rehomogenized melt inclusions may be analyzed using in situ techniques to obtain a true liquid composition. Certain fast-diffusing cations can re-equilibrate with an external melt after entrapment (Qin et al., 1992), necessitating careful consideration of the petrologic context of melt inclusion data. Water, which we do not investigate here, is particularly vulnerable to re-equilibration (Gaetani et al., 2012).

This study uses the same suite of melt inclusions described in Black et al. (2012). The homogenization process and its pitfalls are described in that work. In brief summary: inclusion-bearing clinopyroxene, plagioclase, and olivine crystals were heated to estimated liquidus

temperatures to reverse the effects of post-entrapment crystallization. The crystals were then rapidly quenched to produce glassy material, and careful polishing exposed this glass for analysis. Comparison of inclusion chemistry with whole rock compositions suggests that the melt inclusions analyzed here are largely representative of their host rocks (Black et al., 2012).

The primary dataset presented here was collected using the NanoSIMS 50L secondary ion mass spectrometer at the Carnegie Department of Terrestrial Magnetism in Washington, D.C. We conducted simultaneous measurements of ^{12}C, ^{18}O, ^{32}S and ^{34}S in Siberian Traps melt inclusions, utilizing a Cs+ beam and collection of negatively charged secondary ions at a mass resolving power of ~6000, sufficient to resolve oxygen dimers from sulfur masses and $^{32}SH_2$ and ^{33}SH from ^{34}S. The primary beam was rastered over a 10μm x 10μm area, first pre-sputtering for 90 seconds with a 5nA beam, then reducing beam current to 300-600nA (400-500 nanometers diameter) for the analysis, collecting 600 ratios per analyses in order to obtain an in-run precision of 0.5‰ precision (2 mean) on $^{34}S/^{32}S$ and <1% precision on $^{12}C/^{18}O$ and $^{32}S/^{18}O$ ratios used for measurement of inclusion CO_2 and S concentrations. We interspersed analysis of our unknowns with measurements on a suite of natural glasses with known sulfur isotope compositions (Mandeville et al., 2008) and CO_2 and S concentrations (Hauri et al., 2002). Measured sulfur isotope ratios were corrected for drift (where apparent) and instrumental mass fractionation (IMF) using basaltic glass standard ALV892-1 (Mandeville et al., 2008); IMF fractionation factors varied from 1.0389 to 0.9799 from session to session, and were mainly a function of the relative gains of the electron multipliers used to collect ^{32}S and ^{34}S. Measured ratios were then normalized to a $^{34}S/^{32}S$ ratio of 0.0441626 for V-CDT (Ding et al., 2001) to calculate $\delta^{34}S$ values for each analysis. Average reproducibility (2) on ALV892-1 standard was 1‰ while 2 accuracy of $\delta^{34}S$ for this standard is 0.5‰, producing a combined total uncertainty of 1.5‰ (2).

The NanoSIMS provided several advantages over other analytical techniques. The real-time imaging system allowed us to identify and avoid small cracks, pits, and vapor bubbles that capture remnant material from the polishing process (Figure 2). The spatial resolution of the

NanoSIMS also permitted us to analyze smaller inclusions (down to ~10 microns in diameter). Finally, for several maymechite inclusions that contain sub-micron sized sulfides dispersed within the glass, the imaging mode of the NanoSIMS enabled us to extract isotopic information from the glass surrounding the sulfides, using image processing methods as described in Saal et al. (2013).

The melt inclusions analyzed here were extracted from sills, lavas, and mafic tuffs. Though a serious effort was made to capture the diversity of Siberian Traps magmas, many regions and chemical types are inevitably missing from our sample suite. The measurements in Black et al. (2012) were supplemented with published melt inclusion data from Noril'sk (Sobolev et al., 2009) to estimate overall volatile release from Siberian Traps magmas. Many of our inclusions are from the Maymecha-Kotuy region of the Siberian Traps, where silica undersaturated alkaline lavas are intercalated with tholeiitic basalts. The Maymecha-Kotuy section is capped by very high magnesium, olivine-phyric maymechites.

In order to capture a more complete picture of the sulfur isotopic variability within Siberian Traps magmas, we also refer to whole rock sulfur isotope data from Noril'sk (Ripley et al., 2003). These data span the Noril'sk lavas and also the ore-bearing Main Talnakh intrusion. Ripley et al. (2003) report petrographic evidence for hydrothermal alteration of basalts including pyrite stringers and secondary hematite. However, on the basis of internally consistent trace element concentrations and similar $\delta^{34}S$ values between pyrite-rich and chalcopyrite-rich assemblages, they conclude that any hydrothermal redistribution of sulfur was local at most (Ripley et al., 2003). In the case of our melt inclusions, the preservation of distinct sulfur isotopic compositions within the same sample and the apparently degassing-driven correlation of sulfur concentrations with $\delta^{34}S$ (shown in Figure 3 and discussed in Section 5.1) preclude an extensive hydrothermal overprint.

4. Results: Sulfur Isotope Ratios and CO_2 contents

Sulfur isotope ratios in our melt inclusions span a range from -11 to +25‰ V-CDT, in comparison with a range of -5 to +9 ‰ V-CDT for the whole rock analyses of Noril'sk lavas and +10 to +17 for the Main Talnakh Intrusion (Figure 3; Ripley et al., 2003). CO_2 concentrations range from 20 ppm to 657 ppm (Table 1 & 2).

While most inclusions from most samples evince sulfur isotopic ratios close to mantle values of 0±2 ‰ (Sakai et al., 1982; Sakai et al., 1984), several samples show significant positive or negative deviations. One of the dominant features of the overall melt inclusion dataset is a tendency towards lower $\delta^{34}S$ with lower sulfur concentrations (Figures 3 & 4). Sample K08-7.10, a mafic tuff from the early-erupted Arydzhangsky alkaline suite, best exemplifies this pattern.

K09-9.5, a tholeiitic lava from the Onkuchaksky suite, displays $\delta^{34}S$ values from -5.3 to -10.8 ‰. The $\delta^{34}S$ values of sulfide-bearing maymechite inclusions (Figure 5) reach +25 ‰ V-CDT.

Sulfur contents generally decrease with decreasing CO_2 contents, although the correlation is scattered (Figure 6A). Similarly, $\delta^{34}S$ generally trends towards more negative values with decreasing CO_2 contents (Figure 6B). In both cases, the sulfide-bearing maymechite samples include conspicuous outliers.

The primary controls on $\delta^{34}S$ are: 1) initial $\delta^{34}S$ composition of mantle-derived melt, 2) fractionation during degassing, and 3) incorporation of external sulfur from the crust. Data from submarine glasses from the Mariana Arc and Mariana Trough suggest that the isotopic effect of partial melting in the mantle is limited to less than +1.6 ‰ (Alt et al., 1993). The most important factors driving deviations in $\delta^{34}S$ away from mantle values are thus degassing and contamination. In the case of the sulfide-bearing maymechite inclusions, any fractionation between melt and an immiscible sulfide phase must also be considered. In the next section, we will discuss the

potential role of each of these processes in producing the observed array of sulfur isotopes, and the implications for the magmatic plumbing system and degassing budget.

5. Discussion

5.1 Degassing fractionation and degassing style

Sulfur can reside in silicate melts as SO_4^{2-} and S^{2-}; the relative proportion of each species in a magma depends primarily on oxidation state (Nilsson and Peach, 1993; Sakai et al., 1982). Below the Quartz-Fayalite-Magnetite (QFM) buffer, sulfide makes up > 80% of total sulfur, whereas at 1.2 log units above Nickel-Nickel Oxide (NNO), sulfate makes up > 80% of total sulfur. Between QFM and NNO, the speciation of sulfur shifts quickly as a function of fO_2 (Carroll and Rutherford, 1988; Jugo, 2009; Katsura and Nagashima, 1974).

We implement a degassing fractionation model after de Hoog et al. (2001) to simulate the potential range of $\delta^{34}S$ that could be produced through degassing of Siberian Traps magmas, assuming initial MORB-like $\delta^{34}S$ of 0±2 ‰. The sulfur isotopic fractionation between melt and a vapor phase depends on the fractionation factors between and the relative proportions of sulfide and sulfate in the melt, and H_2S and SO_2 in the vapor (Sakai et al., 1982):

$$1000\, ln \propto_{gas-melt} = \delta^{34}S_{gas} - \delta^{34}S_{melt}$$

$$= 1000\, ln \propto_{SO_2-sulfide} - (1-X)1000 ln \propto_{SO_2-H_2S} - (1-Y)1000 ln \propto_{sulfate-sulfide}$$

where X is the fraction of total sulfur in the vapor phase as SO_2 and Y is the fraction of total sulfur in the melt phase dissolved as sulfide (S^{2-}); both X and Y are expressed as mole fractions. The fractionation factor between species m and n is denoted by $\propto_{m-n}$. For example, the fractionation between sulfate and sulfide has $1000 ln \propto_{sulfate-sulfide} \approx 7.5$ ‰ (Sakai et al., 1982). The precise fractionation factors employed in our model are temperature-dependent, following the formulations in Taylor (1986). The mole fraction of sulfide versus sulfate in the melt is a

function of oxygen fugacity, and the mole fraction of SO_2 versus H_2S is a function of pressure, temperature, water contents, and oxygen fugacity (Symonds et al., 1994). We assume fixed fO_2 during degassing, though in reality the magmatic oxidation state may increase or decrease during degassing, depending on magmatic volatile composition (Burgisser and Scaillet, 2007).

Figure 4 shows the fractionation associated with degassing under plausible magmatic conditions for the Siberian Traps. The changing isotopic fractionation associated with degassing (Figure 4A) reflects the dependence of sulfur speciation on fO_2. Sulfur and H_2O are more soluble than CO_2 in basaltic melts, and therefore extensive sulfur exsolution typically occurs only after magmas ascend to pressures of <100 bars (Dixon et al., 1991). At pressures greater than this, sulfur contents in most basaltic magmas will be controlled by sulfide solubility, which increases with decreasing pressure and increasing FeO contents (Mavrogenes and O'Neill, 1999). Fractional degassing drives stronger isotope shifts than equilibrium degassing, and provides a better match to the $\delta^{34}S$ of K08-7.10 and K08-3.4, two mafic tuffs within the same alkaline sequence (Figure 4B). Arndt et al. (1998) have suggested that the interlayered alkaline and tholeiitic lavas in the Maymecha-Kotuy were produced by two separate plumbing systems. They hypothesize that the alkaline rocks originated as deep, volatile-rich melts that erupted rapidly, circumventing crustal magma chambers, whereas the tholeiitic lavas began as shallower melts that ascended in stages through the crust, assimilating crustal material along the way (Arndt et al., 1998). The $^{34}S/^{32}S$ ratios of the alkaline tuffs, which can be almost entirely explained through fractional degassing of magmas with an initially mantle-like sulfur signature, support such a model.

In summary, sulfur isotopic data from melt inclusions from some samples are consistent with shallow exsolution and open-system degassing of sulfur during the final stages of magma transport and eruption. Sulfur concentrations and isotopic ratios from the Ust-Ilimsk sill show few signs of degassing, further corroborating the stability of sulfur in the melt phase until shallow levels in the crust. The consistency between the modeled degassing fractionation curve and

isotopic data suggests that the alkaline rocks in the Maymecha-Kotuy have experienced relatively little contamination with crustal sulfur, and confirms that >90% degassing of initial magmatic sulfur has occurred for some samples.

5.2 Gas-melt segregation and explosive volcanism

The capacity of vapor and melt phases to decouple from each other during an eruption has important implications for both degassing-related fractionation of sulfur isotopes and eruption dynamics. When decompression rates outpace vapor segregation, magmas erupt explosively. The continued association of melt and vapor phases prior to eruption implies closed-system, equilibrium degassing (accompanied by a lower isotopic fractionation factor). Conversely, when decompression is sufficiently slow to allow gases to segregate, open system degassing occurs, and magmas typically erupt effusively (Edmonds and Gerlach, 2007; Head III and Wilson, 1987).

Intriguingly, a significant fraction of early Siberian Traps eruptive activity appears to have been explosive, including two samples analyzed in this study (K08-7.10 and K08-3.4) that record sulfur isotopic trends consistent with open system degassing. The origin and character of early Siberian Traps explosive activity is a standing question (Ross et al., 2005; White et al., 2009). Our sulfur isotopic evidence for effective vapor-melt segregation suggests that magmatic fire-fountaining may not be the dominant process driving pyroclastic fragmentation.

In light of the sulfur isotopic data presented here, we hypothesize that phreatomagmatism was an important process during the initial stages of the Siberian Traps eruption. Because phreatomagmatic fragmentation is independent of internal vapor-melt segregation, it can explain the explosive eruption of low-viscosity mafic Siberian Traps magmas that apparently experienced open-system degassing. The presence of accretionary lapilli and abundant accidental lithic fragments (Black et al., 2011; Black et al., 2012; Campbell et al., 1992) buttresses this interpretation. Deposition of Permian coals in the Tunguska sequence prior to the global coal gap

(Retallack et al., 1996) and regional floral and faunal assemblages suggest that Siberia hosted a swamp-like environment (Czamanske et al., 1998). Phreatomagmatic interaction with plentiful near-surface water may help to explain the thick (locally >200 m) volcaniclastic deposits that mark the onset of Siberian flood volcanism (White et al., 2009).

5.3 The role of crustal contamination

Whole rock sulfur isotopic ratios from Noril'sk record the effects of crustal sulfur contamination, particularly in the case of the Noril'sk 1, Kharaelakh, and Main Talnakh intrusions (Ripley et al., 2003). Within our melt inclusion dataset, an Onkuchaksky lava flow (which is ^{34}S-depleted) and the maymechites (which are ^{34}S-enriched) provide the most convincing evidence for the addition of crustal sulfur.

The most plausible source of ^{34}S-depleted sulfur is from sulfide minerals incorporated during assimilation of shale or coal. Because the sulfur contents of shale and coal are lower than that of evaporites (Table 3), larger quantities of the whole rock must be assimilated to force shifts in δ^{34}S. Given shale with δ^{34}S=-15 ‰ and 1 wt% sulfur in the form of sulfide minerals such as pyrite (Strauss, 1997), and magma with δ^{34}S=-2 ‰ and 0.05 wt % sulfur, incorporation of ~7 wt% shale is required to produce δ^{34}S=-10.8 ‰ in the melt (as in inclusion K09-9.5-7). If the country rocks contain less sulfur, as the samples analyzed in Table 3 do, a proportionately higher total mass must be mined for sulfur through assimilation or fluid transfer. Alternatively, the inclusions from K09-9.5 are uniformly relatively low in sulfur (Table 2), suggesting their δ^{34}S may also be influenced by a prior degassing stage.

NanoSIMS imaging revealed sub-micron scale sulfide grains within some maymechite melt inclusions (Figure 5). The Mg number of the inclusions ranges from 60 to 75, with FeO contents from 12-18 wt % (Black et al., 2012). Many of these melt inclusions contain up to 0.5 wt % sulfur (Table 2), in excess of typical saturation levels even for Fe-rich melts (Blake et al., 2010; Wallace

and Carmichael, 1992) except under highly oxidizing conditions in which sulfur can dissolve as sulfate independent of Fe content (Jugo, 2009). Excess iron contents in melt inclusions have been attributed to dissolution of magnetite during reheating (Rowe et al., 2006); similar remelting of a small amount of co-trapped sulfide may explain the high sulfur concentrations in some maymechite inclusions. However, the need to melt, redistribute, and precipitate this material during the course of a short (~10 minutes) reheating experiment may point to another explanation. Assimilation of sulfate-rich evaporite would increase magmatic fO_2 (Li et al., 2009b), simultaneously elevating sulfur solubility (Jugo, 2009; Wallace and Carmichael, 1992). Later re-equilibration of a trapped inclusion with lower external fO_2—either during passage through a reducing layer such as coal or organic-rich material, or during experimental reheating—may have triggered precipitation of the sulfides shown in Figure 5.

Regardless of the origin of the sulfides, the effect on $\delta^{34}S$ of glass is likely negligible. Any post-entrapment changes in sulfur state will not affect the mean $\delta^{34}S$ of an inclusion. Furthermore, the sulfur isotopic composition of seafloor gabbros containing cumulate sulfides is statistically identical to MORB, suggesting that sulfide-melt isotopic fractionation is minor (Alt et al., 1993).

The $\delta^{34}S$ of the sulfide-bearing maymechite inclusions described here, which ranges from -4.6 to +25.3‰ (Table 2), therefore records a significant departure from mantle sulfur. Enrichment of ^{34}S in the melt during degassing occurs only at low pressures and highly oxidizing conditions (Figure 4A), and even then is insufficient to produce the full $\delta^{34}S$ variation in the maymechite inclusions. Given the isotopic composition of crustal reservoirs (Figure 3), and identification of magmatic anhydrite, indicating oxidized sulfur (Li et al., 2009b), we conclude that ^{34}S-enriched sulfur was likely assimilated or scavenged hydrothermally from evaporites (Li et al., 2009b; Ripley et al., 2003). Because the melting point of gypsum is 1425 °C, well above the temperature of most basaltic magmas, evaporitic sulfur was likely leached and transferred primarily via hydrothermal fluids (Ripley et al., 2003). Paleozoic evaporites vary between +10 and +35 ‰ (Claypool et al., 1980). The single Ordovician gypsum we measured from the Kotuy River

contained sulfur of $\delta^{34}S$=+20.3 ‰ (Table 3). Cambrian evaporites—including the major Irkutsk basin salts in Siberia—are the most ^{34}S-enriched evaporites in the Phanerozoic, with mean $\delta^{34}S$=+30 ‰ V-CDT (Figure 3; Claypool et al., 1980). Two-member mixing curves between maymechite and anhydrite sulfur (with $\delta^{34}S$=+30 ‰) reproduce the observed $\delta^{34}S$ trend reasonably well (Figure 3).

In summary, maymechite melt inclusions (this study) and Noril'sk ore-bearing intrusions (Ripley et al., 2003) provide the best evidence for strong crustal contamination during Siberian Traps magmatism. The multiple samples in this study that bear mantle-like sulfur (Figure 3) suggest that intense crustal processing was not universal. Many magmas, perhaps particularly concentrated among the alkaline, high-Ti lavas of the Maymecha-Kotuy region, may have ascended relatively rapidly, avoiding long residence times in crustal chambers.

5.4 Depths of entrapment and the magmatic plumbing system

Carbon dioxide solubility decreases rapidly as magmas ascend to shallow pressures (e.g. Stolper and Holloway, 1988). Combined CO_2, water, and SiO_2 concentrations in a given melt inclusion allow estimation of minimum depth of entrapment, assuming CO_2 saturation (Lowenstern, 1995). Trends in CO_2 concentration also provide a tracer for degassing (Dixon and Stolper, 1995).

In the case of shallow degassing as described in section 5.1, we expect a positive correlation between S and $\delta^{34}S$ and CO_2 contents. Generally speaking, the data do reflect this correlation (Figure 6). However, some inclusions show relatively high CO_2 contents in conjunction with low sulfur (Figure 6A), indicating a decoupling of sulfur and carbon during the degassing process. Hauri (2002) observed a similar pattern in Hawaiian melt inclusions, and interpreted it as the result of a process known as magma drainback. During eruptions of Kilauea,

magmas occasionally erupt, pool into lava lakes, and then drain back into the vent, presumably returning to the magma storage chamber at ~2 km depth (Wallace and Anderson, 1998).

Both sulfur and carbon would likely degas extensively during an initial eruptive phase. However, because CO_2 is less soluble than sulfur at crustal depths, magmas that return to the storage chamber could be fluxed with exsolved CO_2 from degassing deeper in the conduit, replenishing CO_2 levels (Hauri, 2002). Any deeper assimilation or contact metamorphism would also produce a CO_2-rich gas phase that would dissolve in the undersaturated, degassed melts up to the point of CO_2 saturation at the depth of the magma storage reservoir. This indirect evidence for the presence of a co-existing CO_2-rich gas highlights the fact that any estimate of the magmatic CO_2 budget based on melt inclusions provides a minimum value, limited by CO_2 saturation at the depth of entrapment (Black et al., 2012). Estimates of 64,000-170,000 Gt CO_2, based on present-day observations and hypothesized mantle carbon contents (Beerling et al., 2007; Sobolev et al., 2011), are therefore more reasonable.

Although we have not measured water contents in our melt inclusions, Sobolev et al. (2009) report a range in water concentrations between 300-1900 ppm for their melt inclusions from Noril'sk. Table 1 shows minimum depths of entrapment calculated with PCalc95 (Dixon et al., 1995), using CO_2, mean SiO_2 contents for each sample, and a hypothetical range in water contents between 0.2-1.0 wt%. This range was selected on the basis of the Sobolev et al. (2009) melt inclusions and the observed variation in submarine glasses from Hawaii (Hauri, 2002). The calculated depths, which cluster within the uppermost crust, are collected in Table 1.

5.5 Relevance to Ore Deposits

The relationship between sulfur assimilation, sulfide saturation, and ore formation has been a subject of enduring interest for economic geologists (Li et al., 2009a). Naldrett (1992) postulated that contamination with crustal sulfur triggered the formation and segregation of

immiscible sulfides, which scavenged additional chalcophile elements from undepleted magmas before forming the ore-bearing sulfide deposits. Li et al. (2009a) propose an alternative model, in which the formation of an immiscible sulfide liquid occurred as a result of contamination with granitic lower or middle crust. Although the granitic crustal rocks themselves are PGE-poor, Li et al. (2009a) suggest that an initial sulfide liquid could scavenge chalcophile elements from early magmas, ultimately contributing this PGE-enrichment to later magmas. In this model, these enriched magmas ascended to upper crustal levels where they interacted with evaporites, consequently saturating with a new sulfide phase that ultimately formed the Noril'sk sulfide deposits (Li et al., 2009a).

Our data supports the revised model of Li et al. (2009a), because the maymechites show evidence for contamination with sulfur from evaporites, but they are not known to be associated with economic ore deposits. The maymechite $\varepsilon Nd=+4.65$ value (Fedorenko et al., 2000) suggests that these magmas likely did not interact extensively with granitic crustal rocks. If Li et al. (2009a) are correct, without this interaction an early PGE-scavenging sulfide liquid may not have formed in the roots of the maymechite plumbing system. As a result, although some maymechites may have later saturated with sulfides due to addition of evaporitic sulfur, there was little PGE content available to partition into the sulfide phase.

These observations further underscore the differences between the plumbing system in Noril'sk versus Maymecha-Kotuy. The $\delta^{34}S$ ratios for some maymechite inclusions are comparable to those of the Kharaelakh intrusion, implying that elements of the ore-producing process may have occurred in the Maymecha-Kotuy region and possibly in other locations in addition to Noril'sk.

5.6 Mantle versus crustal sulfur and implications for the end-Permian

As noted in the introduction, volatile degassing forms a key link between the eruption and the potential environmental consequences of the Siberian Traps. Using the sulfur isotopic data presented here, it is possible to estimate the proportions of mantle and crustal sulfur released by the Siberian Traps, which influences the composition and magnitude of emissions.

Given the uncertainty in $\delta^{34}S$ of crustal materials other than evaporites, we model the magmatic sulfur isotope ratios that would result from two-component mixing between sulfur from the mantle and from anhydrite. Li et al. (2009b) average whole rock sulfur isotope measurements from Noril'sk lavas to obtain an overall $\delta^{34}S$=+3.0 ‰, which requires 0.09 wt % anhydrite contamination for magmas initially containing 0.14 wt % sulfur.

To approximate a representative Siberian Traps $\delta^{34}S$ based on our melt inclusion data, we can consider several possible formulations. Black et al. (2012) include melt inclusions from Noril'sk (Sobolev et al., 2009) in order to estimate 9300 Gt dissolved sulfur for the Siberian Traps, but no $\delta^{34}S$ data is available for Noril'sk melt inclusions. Black et al. (2012) also disregarded maymechite data when estimating the sulfur budget, because of the unusual properties of the maymechites and their apparently small relative volume (Fedorenko and Czamanske, 1997). The $\delta^{34}S$ from the inclusion with highest (least-degassed) sulfur contents from each of the remaining samples (R06-09, K09-9.5, K08-3.4, K08-7.10) yields a mean $\delta^{34}S$=+0.1 ‰, with 1500 ppm S (using values from Table 2). Inclusion of the maymechites yields a mean $\delta^{34}S$=+5.1 ‰, with 2300 ppm S.

The $\delta^{34}S$ data presented here suggest that sample K09-9.5 experienced degassing and/or contamination with non-evaporitic crustal material. Exclusion of this sample and of the maymechites yields a mean $\delta^{34}S$=+2.0 ‰, with 1800 ppm S. Admittedly the sample size is small, but this value is consistent with Li et al.'s (2009b) estimate for Noril'sk of $\delta^{34}S$=+3.0 ‰. We assume contamination with anhydrite with bulk $\delta^{34}S$=+20 ‰ and 23.5 wt % sulfur, although the

maymechites appear to have interacted with evaporites containing sulfate $\delta^{34}S$=+30 ‰ to +35 ‰ (Figure 3). Arithmetically, addition of 0.08 wt % anhydrite to a magma that initially contains 1620 ppm S with $\delta^{34}S$=+0.0 ‰ will produce the desired 1800 ppm S with $\delta^{34}S$=+2.0 ‰. Generation of a magma with 1500 ppm S ($\delta^{34}S$=+0.1 ‰) or 2300 ppm S ($\delta^{34}S$=+5.1 ‰), as described above, requires 0.003 wt % or 0.25 wt % anhydrite contamination respectively.

Following from these calculations, our preferred estimate for the fraction of total Siberian Traps sulfur derived from crustal evaporitic material is ~10%. This value could range from 0.5 % to 25 % depending on assumed magmatic sulfur composition. The remaining sulfur is supplied primarily from the mantle.

For comparison, more than 90% of the modern CO_2 flux from Mt. Vesuvius may be sourced from deep-seated carbonate assimilation (Iacono-Marziano et al., 2009). Carbonate assimilation at Mt. Merapi has also been implicated in assisting earthquake-triggered eruptions (Troll et al., 2012), but over the past several decades the bulk of Merapi's CO_2 flux is mantle-derived, and whether or not sedimentary carbon is an important contribution may depend on overall magma flux.

Addition of 0.08-0.25 wt % evaporitic material rich in chlorine or fluorine would be sufficient to explain the higher concentrations of these elements in most Siberian Traps magmas relative to Laki and the Columbia River flood basalts (Black et al., 2012; Thordarson and Self, 1996; Thordarson et al., 1996). Melt inclusions from two sills (R06-09 and A10-23.1) contain much higher Cl and F than the majority of Siberian Traps samples (Black et al., 2012), possibly demanding larger additions of crustal material. However, these sills samples have $\delta^{34}S$ close to mantle values (Figure 3, Table 1). Either halogens have been decoupled from sulfur, or the Cl and F may be mantle-derived.

In brief, the estimated crustal contamination is sufficient to increase volatile loads in specific magmas, but the effect on the overall magmatic degassing budget for the Siberian Traps may be incremental. The more significant effect of the crustal interaction documented in $\delta^{34}S$

ratios, εNd and $^{87}Sr/^{86}Sr$ (Fedorenko et al., 2000; Lightfoot et al., 1993), heating and mobilization of evaporite layers (Melnikov et al., 1997; Svensen et al., 2009), and trace elements (Lightfoot et al., 1990; Wooden et al., 1993) may be increased degassing directly from the heated, metamorphosed, and fluid-fluxed sedimentary rocks rather than degassing of magma that had assimilated such rocks.

Modeling of atmospheric chemistry has shown that CH_3Cl, which can form through heating of hydrocarbon-bearing halites (Svensen et al., 2009), is one of the critical reactive gases that may lead to ozone destruction and ultraviolet-poisoning of terrestrial ecosystems (Beerling et al., 2007).

While attention has occasionally focused on the significance of particular types of sedimentary rocks, such as evaporites or coals (Ganino and Arndt, 2009), our sulfur isotopic data indicate that magmas likely interacted with several varieties of country rock. Pulses of magmatism (Pavlov et al., 2011) would create pulses of direct and indirect degassing, providing a potential episodic trigger for environmental and carbon isotope perturbations, either through injection of isotopically light carbon from heated or assimilated organic-rich Tunguska sedimentary rocks (Payne and Kump, 2007) or through climatic and chemical chain reactions that collaterally disturb global cycles of carbon storage and burial (Kump et al., 2005; Meyer et al., 2011).

6. Summary and Conclusions

We measure the sulfur isotopic composition and carbon contents of melt inclusions from the Siberian Traps large igneous province. The melt inclusions span the volcanic sequence in the northern Maymecha-Kotuy region, and also sample basaltic intrusions from the southern portion of the large igneous province (Black et al., 2012). In conjunction with published whole rock $\delta^{34}S$ data from Noril'sk (Ripley et al., 2003), our results allow us to fingerprint magmatic interaction

with crustal materials over a large area of the Siberian Traps. The $\delta^{34}S$ we measured in melt inclusions ranged from -10.8 to +25.3 ‰ V-CDT.

A combination of degassing-driven fractionation from initially mantle-like sulfur and incorporation of sulfur-bearing crustal materials is sufficient to explain the observed variation in $\delta^{34}S$. Open system degassing produces the best fit for two samples interpreted as pyroclastic deposits. Because open system degassing is often associated with efficient vapor-melt segregation and effusive eruption, we hypothesize that phreatomagmatic interactions provided the driving force for fragmentation. The most likely sources of crustal sulfur are evaporites, with possible additional contributions from shales or coals.

Using thickness estimates from Zharkov (1984), the Cambrian evaporite horizons beneath the Siberian Traps may include on the order of 50,000-270,000 Gt anhydrite and gypsum containing 9,000-63,500 Gt of sulfur. We estimate that around 10% of the ~9300 Gt sulfur (Black et al., 2012) dissolved in Siberian Traps magmas derived from this evaporitic material. The remainder of the magmatic sulfur budget is likely dominated by mantle sulfur.

The sulfur isotopic evidence for prolonged and close association between ascending magmas and potentially hydrocarbon-soaked evaporitic material reinforces the plausibility of thermal production of gases such as CH_4 and CH_3Cl (Svensen et al., 2009). Pulsed emissions of halocarbons from organic-rich sedimentary rocks have been linked with ozone destruction (Beerling et al., 2007); carbon-bearing gases from these sources have also been proposed as the most viable trigger for repeated marine carbon isotopic excursions during the Permian-Triassic transition (Payne and Clapham, 2012a; Payne and Kump, 2007). The crustal contamination documented in $\delta^{34}S$ data points to extensive thermal and hydrothermal perturbation of Tunguska sedimentary rocks. The resulting production of methane, CO_2, and halocarbons from organic material within shales and evaporites (Aarnes et al., 2011) could simultaneously explain the structure of the carbon isotopic record and drive lethal shifts in global atmospheric chemistry at the time of the end-Permian.

Acknowledgments

This study was funded by grant EAR-0807585 from NSF Continental Dynamics, and supplemented by the MIT Wade Fund. The American Museum of Natural History graciously provided maymechite samples collected by Valeri Fedorenko. Roman Veselovskiy, Vladimir Pavlov, Anton Latyshev, Anya Veslovskiy, Sam Bowring, and Seth Burgess were valued collaborators during field work. BB thanks Mike Rowe for educational discussions of sulfur speciation and solubility, and Alexander Polozov for discussion of evaporites. The authors gratefully thank Jianhua Wang and Brenda Carbone.

Figures

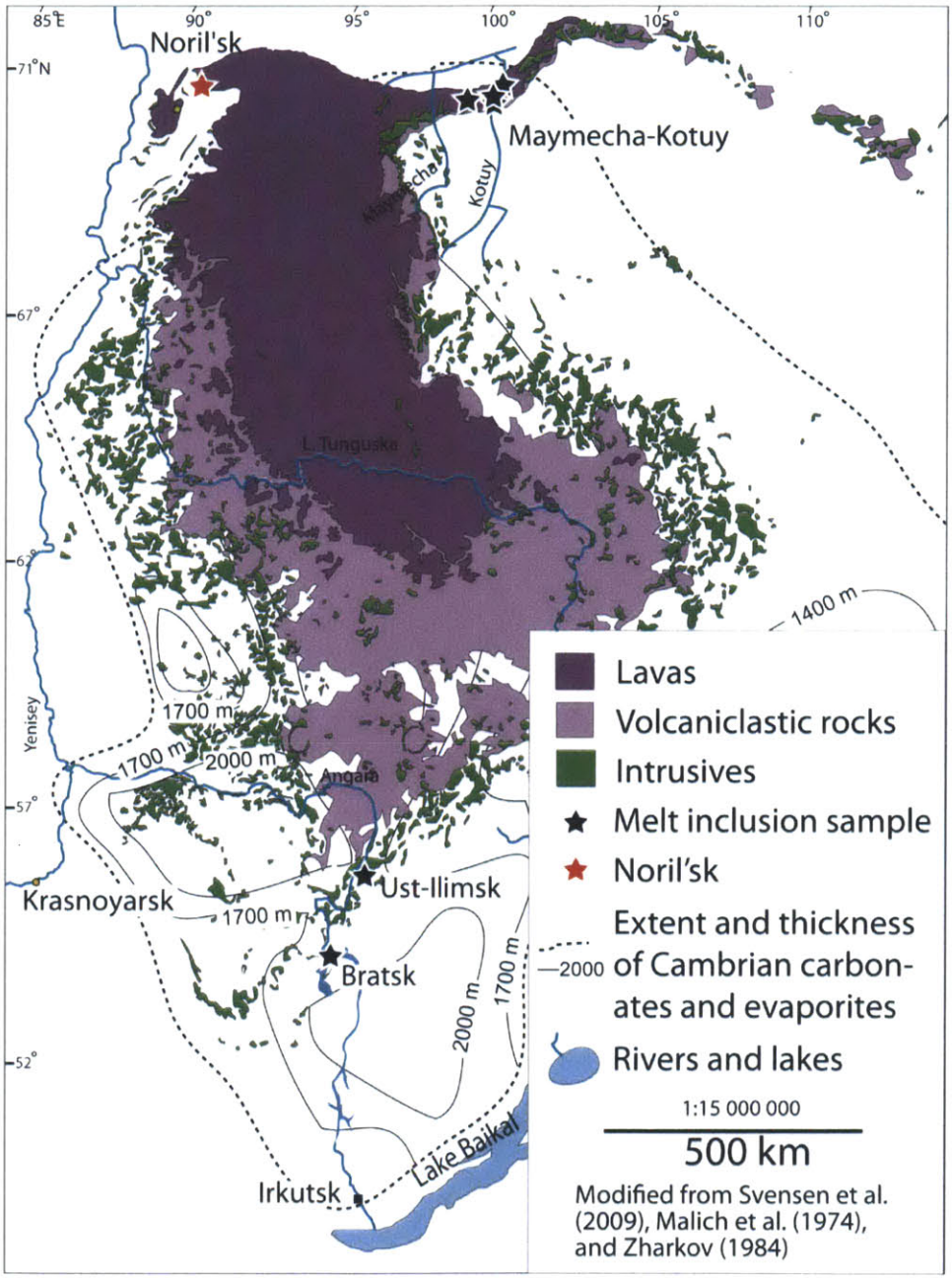

Figure 1: Map showing present day extent of Siberian Traps lavas and volcaniclastics in the Tunguska basin based on Svensen et al. (2009) and Malich et al. (1999). Thickness and extent of Cambrian evaporites, including limestone, halite, dolomite and anhydrite, are based on Zharkov (1984). Maymecha-Kotuy, Bratsk, and Ust-Ilimsk are the three areas from which we obtained melt inclusion samples (starred on the map). Noril'sk is also marked. Reichow et al. (2009) have argued that the distribution of intrusions and basaltic subcrop supports a much larger original extent of the Siberian Traps, reaching into the adjacent West Siberian Basin (not shown here).

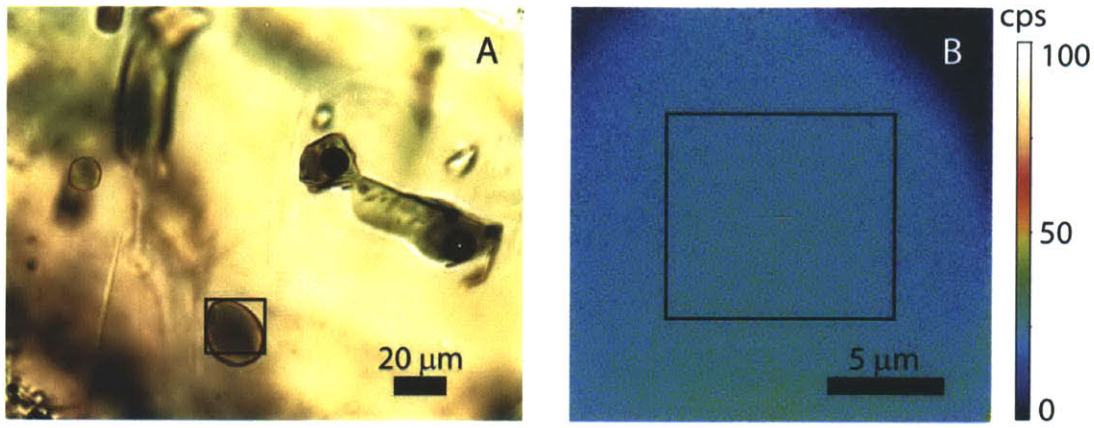

Figure 2A: Plain light microscopic image of melt inclusion K09-9.5-2B. **Figure 2B:** NanoSIMS image of the same melt inclusion, with analysis area outlined in black. The color scale shows ^{32}S counts per second.

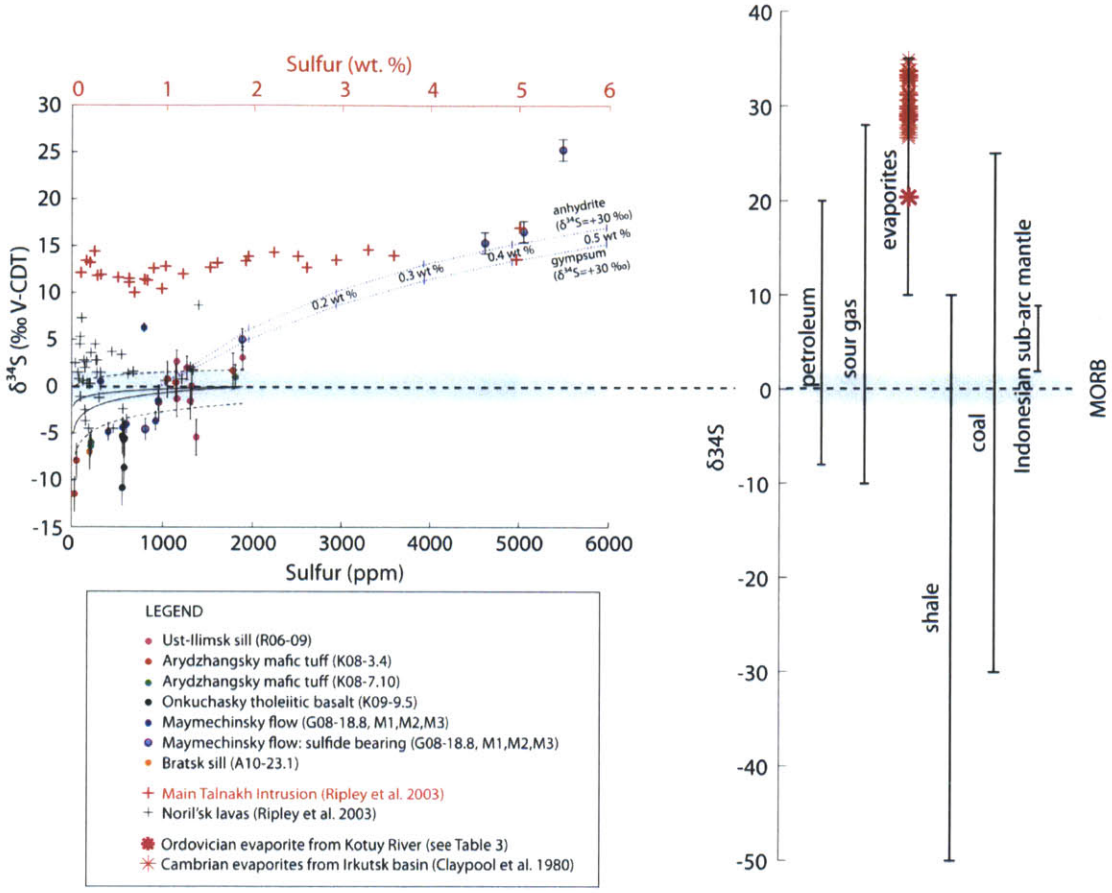

Figure 3: Overview of sulfur isotopic composition of melt inclusions, whole rock data from Noril'sk (Ripley et al., 2003), Ordovician evaporite, Cambrian evaporites from the Irkutsk basin (Claypool et al., 1980), and other crustal sources of sulfur (Thode, 1991). The upper horizontal axis in red applies only to the data points in red (from ore-bearing intrusions), which contain much higher sulfur concentrations. The lower horizontal axis (in ppm) applies to all other points. Indonesian sub-arc mantle range is from de Hoog et al. (2001). The bulk mantle $\delta^{34}S$ value, with associated variation, is shown by the light gray bar (Sakai et al., 1984). Solid curves show fractionation associated with degassing for QFM and NNO oxygen fugacity conditions, assuming water saturation and 30 bars pressure. The dashed black lines show the same curves with initial values shifted to ±2 ‰ V-CDT to encompass variation in initial mantle sulfur values (Sakai et al., 1982). Dashed blue mixing lines describe an initial magma with $\delta^{34}S$=+0 ‰ and 923 ppm S (the maximum value for a maymechite inclusion without sulfides) contaminated with anhydrite or gypsum assumed to contain sulfur with $\delta^{34}S$=+30 ‰.

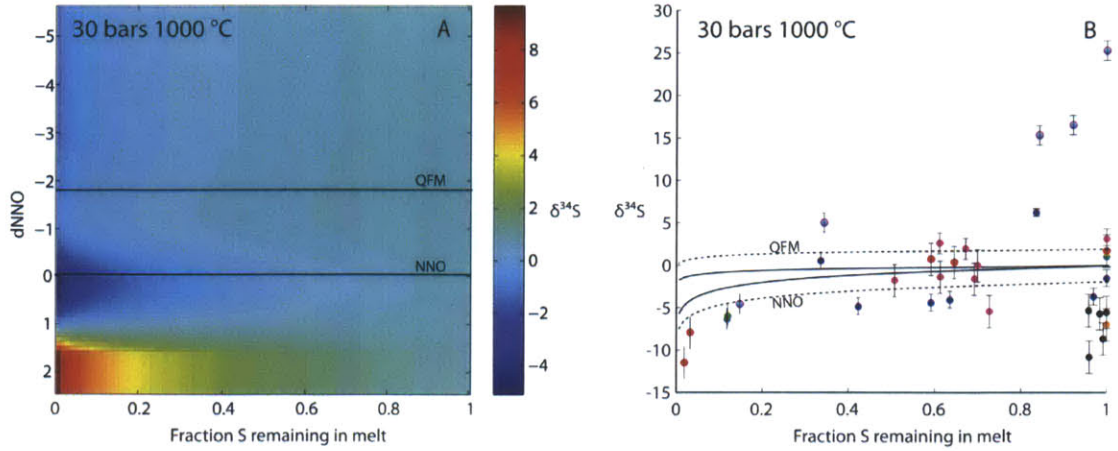

Figure 4A: Relative change in $\delta^{34}S$ for open-system degassing as a function of fraction of sulfur remaining in the melt (1-F, where F is the fraction degassed) and the oxygen fugacity relative to the NNO buffer. At oxygen fugacity more reducing than NNO+1.3, sulfur in the melt is dominantly sulfide and degassing produces a negative shift in sulfur isotopes; at conditions more oxidizing, degassing produces a positive shift in sulfur isotopes. **Figure 4B:** Modeled degassing fractionation curves (after de Hoog et al., 2001) compared with measured melt inclusion data. We employ a fractional degassing scheme; equilibrium degassing results in less pronounced fractionation. All sulfur values are normalized to the maximum sulfur concentration for each sample, as a proxy for undegassed sulfur fraction. 2-sigma error bars represent the reproducibility of interspersed standard measurements. Dashed lines show the dependency on initial $\delta^{34}S$, as in Figure 3. Symbols are as shown in Figure 3.

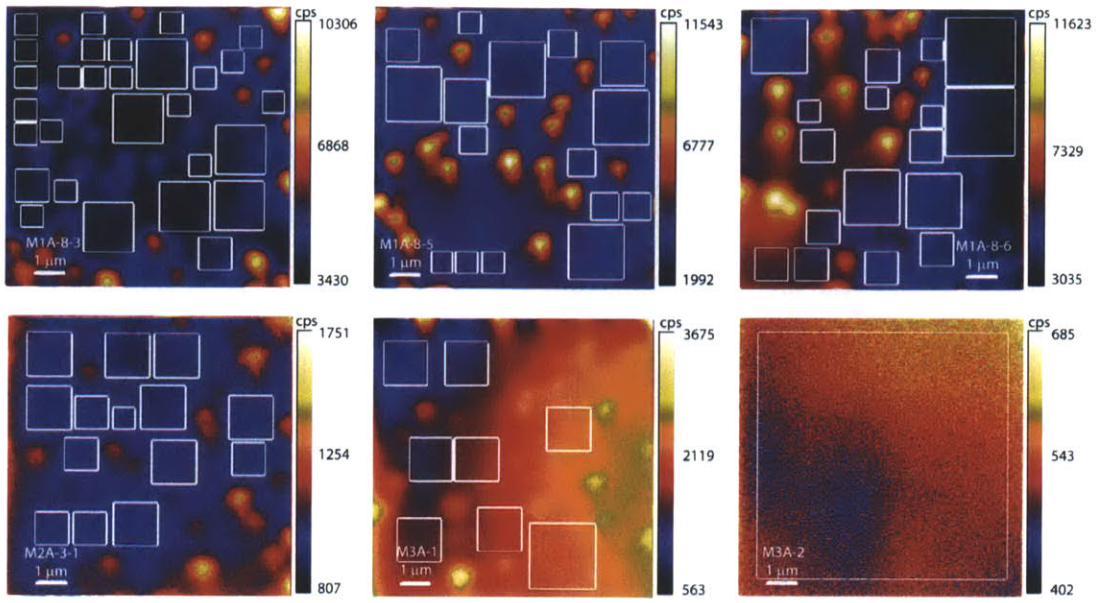

Figure 5: NanoSIMS images of ^{32}S in maymechite melt inclusions. The five inclusions that contain sulfides are shown, along with a sulfide-free inclusion (M3A-2) for comparison. White boxes indicate the areas selected for sulfur isotopic and carbon concentration analysis. Color bar represents mean ^{32}S counts per second.

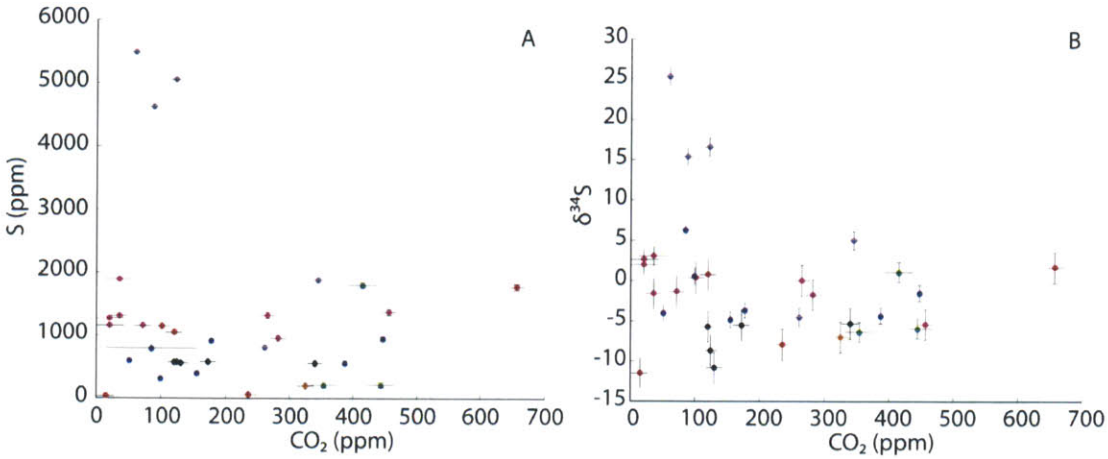

Figure 6A: Sulfur versus carbon concentration. **Figure 6B:** $\delta^{34}S$ versus carbon concentration. Symbols are as shown in Figure 3. 2-sigma error bars represent the reproducibility of interspersed standard measurements. In both plots, the sulfide-bearing, ^{34}S-enriched maymechite inclusions clearly define a distinct and divergent trend.

Tables

Sample	**Description**	**Location (°E, °N)**	**Maximum S** *Mean S* **[ppm]**	**Mean $\delta^{34}S$ [‰ V-CDT]**	**Maximum CO_2** *Mean CO_2* **[ppm]**	**Minimum depth of entrapment [bars]**
A10-23.1	Bratsk dolerite sill	101.799, 56.339	199	-7.01	325	690-790
R06-09	Ust-Ilimsk dolerite sill	102.737, 56.072	1886 *1301*	-0.31	456 *148*	890-980 *300-390*
K08-3.4	Arydzhangsky mafic tuff	102.355, 71.049	1775 *812*	-3.32	657 *152*	610-710 *140-250*
K08-7.10	Arydzhangsky mafic tuff	102.590, 71.181	1802 *744*	-3.71	910 *530*	700-810 *410-530*
K09-9.5	Onkuchaksky lava flow	102.999, 71.547	584 *572*	-4.91	338 *177*	720-1130 380-790
G08-18.8, M1, M2, M3 (no sulfides)	Maymechinsky lava flows	101.14, 70.85	952 *651*	-1.64	447 *200*	200-340 *90-240*
G08-18.8, M1, M2, M3 (with sulfides)	Maymechinsky lava flows	101.14, 70.85	5488 *3571*	+11.55	345 *175*	150-300 *80-230*

Table 1. Mean and maximum sulfur and carbon concentrations and sulfur isotopic variation for each flow, sill, or volcaniclastic unit. The range in each estimate for minimum depth of entrapment is based on a range of H_2O contents from 0.2 to 1.0 wt % H_2O, where the higher H_2O contents correspond to greater minimum depths of entrapment. Italics show mean values.

Inclusion	S [ppm]	$\delta^{34}S$ [‰ V-CDT]	CO_2 [ppm]
R06-09-4.3B	1153	+2.64	20.4
R06-09-4.3C	1266	+1.98	20.2
R06-09-4.5	1886	+3.08	35.5
R06-09-5.1	957	-1.78	282
R06-09-5.3A	1370	-5.43	456
R06-09-5.4	1304	-1.59	35.6
R06-09-5.5	1155	-1.35	71.5
R06-09-5.6	1318	0.0	265
K08-3.4-6-4A	1144	+0.39	101
K08-3.4-6-5A	1775	+1.69	657
K08-3.4-6-5B	1050	+0.76	120
K08-3.4-6-7	34	-11.5	14.9
K08-3.4-6-8	57	-7.96	235
K08-7.10-2-5	1802	+1.10	354
K08-7.10-5-3	216	-5.91	444
K08-7.10-5-4	213	-6.32	415
K09-9.5-2	575	-5.71	120
K09-9.5-3	584	-5.5	172
K09-9.5-4	560	-5.3	340
K09-9.5-7	561	-10.8	130
K09-9.5-8A	579	-8.68	124
M1A-8-3*	4622	+15.39	88
M1A-8-4	795	+6.31	85
M1A-8-5*	5488	+25.32	60
M1A-8-6*	5053	+16.59	122
M2A-3-1*	811	-4.56	261
M2A-7-1	923	-3.66	177
M2B-1-1	604	-4.00	51
M3A-1*	1881	+5.03	345
M3A-2	403	-4.82	155
M3A-4-2	563	-4.35	387
M3B-6-2	319	+0.57	99
G08-18.8-3.2	952	-1.50	447
A10-23.1-3	199	-7.01	325

Table 2. Sulfur and carbon concentrations and sulfur isotopic variation from the full suite of melt inclusions analyzed in this study. Sulfide-bearing maymechite melt inclusions are marked with an asterisk.

Sample	Lithology	Location (°E, ° N)	C [wt %]	S [wt %]	$\delta^{34}S$ [‰ V-CDT]
M09-4.6	Shale	101.239, 70.741	0.35	0.20	
K09-3.2	Shale	102.293, 71.066	2.98	0.06	
K09-7.8	Shale	102.66, 71.131	2.04	0.04	
K08-5.5	Coal	102.675, 71.153	59.4	0.37	
K09-1.3a	Ordovician evaporite	102.61, 71.002			+20.4 ± 0.13

Table 3. Whole rock sulfur contents and sulfur isotopic composition for selected sedimentary rocks from the Tunguska Basin. Carbon and sulfur concentrations were measured with an infrared detector at ACT Laboratories in Ontario; $\delta^{34}S$ was measured at Carnegie.

Chapter 4. Phreatomagmatism during the eruption of the Siberian Traps

Abstract: The Siberian Traps are one of the largest known continental flood basalt provinces, with a total volume of approximately 4,000,000 km^3. The eruption has been invoked as a possible trigger for the end-Permian mass extinction. Up to one quarter of the extrusive volume of the Siberian Traps consists of mafic volcaniclastic deposits. Characterizing the origins of these voluminous deposits is critical to determining the extent of explosive episodes that may have increased the environmental impact of the Siberian Traps. We employ paleomagnetic conglomerate tests in order to investigate the emplacement temperatures of volcaniclastic samples. Observations of petrography and field relationships provide additional perspective on the probable fragmentation mechanisms. We find that phreatomagmatism was likely a key and widespread feature of early Siberian Traps volcanism. Vent-proximal features spread over a wide area provide evidence for multiple spatially distributed eruptive centers. Explosive interaction of magmas with ground or surface waters may have driven scrubbing of soluble gases such as HCl while simultaneously delivering other volatiles to the upper atmosphere, generating global environmental effects.

1. Introduction

The presence of volcaniclastic rocks within the Siberian Traps large igneous province (Ross et al., 2005) is well-known but poorly understood and poorly documented. Detailed accounts of the easily-weathered volcaniclastics vary considerably. The thickness of volcaniclastic material ranges from thin intercalated layers in Putorana (Buchl and Gier, 2003) to hundreds of meters near the base of the volcanic sections in Angara (Naumov and Ankudimova, 1995), the Maymecha-Kotuy (Fedorenko et al., 2000; Fedorenko and Czamanske, 1997) and interlayered with lavas in Noril'sk (Lightfoot et al., 1993). The total volume of mafic volcaniclastic material has been estimated at up to ~1,000,000 km^3 (Ross et al., 2005), equivalent to approximately one quarter of the total volume of the Siberian Traps (Reichow et al., 2009).

The eruption of the Siberian Traps may have been synchronous with the catastrophic end-Permian mass extinction (Reichow et al., 2009). Siberian Traps magmatism has been invoked as a direct or indirect trigger for the extinction, which began just prior to 252.28±0.08 Ma (Shen et al., 2011). While the enormous volume and rich volatile budget of the Siberian Traps (Black et al., 2012) could produce large fluxes of toxic sulfur and halogen gases, explosive delivery of those gases to the stratosphere is a prerequisite for lasting global environmental effects (White, 2002). Flood basalt volcanism has historically been considered predominantly effusive, implying that only long-lived or chemically inert gases such as CO_2 would achieve global climatic significance.

Recently, a more nuanced and complex view of flood basaltic eruptions has emerged, with indications that such volcanism may span the spectrum from effusive to explosive. Proximal scoria falls, clastogenic lava flows, and welded spatter near the Roza vent system of the Columbia River flood basalts denote episodes of pyroclastic activity (Self et al., 1997; Thordarson and Self, 1998b). Similarly, the historic Laki fissure eruption was characterized by episodic explosive convulsions accompanied by ash fall and often followed by a pulse of lava emplacement (Thordarson et al., 2003; Thordarson and Self, 1993b). In a further example that may be particularly relevant to the genesis of Siberian Traps mafic

volcaniclastic deposits, similar rocks in the Transantarctic Mountains associated with the Jurassic Ferrar large igneous province have been interpreted as the products of an extraordinarily large phreatomagmatic vent complex in the Coombs Hills (McClintock and White, 2006; White and McClintock, 2001). The vent complex may consist of multiple overlapping structures analogous to diatremes, and includes large rafts of country rock; rafts of bedded, lapilli, and accretionary-lapilli tuff; late-stage base surge bedforms; irregular intrusions of dolerite with associated peperitic rocks; and abundant heterogeneous clasts of country rock, basalt, and juvenile material (White and McClintock, 2001).Volcaniclastic deposits from some Siberian localities distinctly resemble descriptions from the Coombs Hills, and may represent periods of similarly non-effusive activity during the early phases of the eruption of the Siberian Traps.

Constraints on the extent and style of explosive volcanism during the emplacement of the Siberian Traps could carry far-reaching consequences. If a large fraction of the mafic volcaniclastic deposits were originally fragmented through pyroclastic processes, they could represent one of the largest mafic explosive deposits known in the rock record. Perhaps more importantly, explosive activity governs plume heights—thereby determining the proportion of Siberian Traps sulfur that could have reached the stratosphere and contributed to global acid rain and transient cooling.

The nomenclature of fragmented volcanic rocks is complex and occasionally contradictory. Throughout this article we follow the nomenclature delineated by Fisher and Schmincke (1984) as recently elaborated by White and Houghton (2006). In some cases, White and Houghton (2006) differ significantly from Fisher and Schmincke (1984). For example, we do not use the word 'tuff' in a genetic sense, to indicate pyroclastic origin. Instead, following White and Houghton (2006), among volcaniclastic rocks the terms tuff, lapilli tuff, tuff breccia, and breccia refer to deposit grain-size in ascending order, from ash to lapilli to blocks and bombs. Volcaniclastic rocks are lithified deposits of fragments produced and/or transported during the course of a volcanic eruption, including everything from airfall tuffs to pyroclastic surge and flow deposits to fluvially transported syn-eruptive volcanic materials (White and Houghton, 2006). In contrast, epiclastic deposits include the transported weathering products of volcanic rocks that have been reshaped and resized relative to the original volcanic fragments (White and

Houghton, 2006). Several mechanisms may explain the fragmentation of volcaniclastic rocks. Autoclastic fragmentation occurs as lava cools at its contacts with air and breaks up during flow. Hyaloclastic fragmentation occurs when flowing lava comes into contact with water and freezes. Pyroclastic fragmentation occurs when ascending magmas exsolve volatiles (magmatic fragmentation) or come into contact with ground or surface water (phreatomagmatic fragmentation), in either case resulting in explosive ejection of particles into the air.

Specific volcanic processes and deposits are frequently associated with phreatomagmatic interactions. At the point of contact between the magma and the water, the magma begins to quench (often forming glass with low vesicularity, since internal gases may not be actively exsolving) at the same time as the water flashes to steam (Sheridan and Wohletz, 1983). If the interaction occurs beneath the surface, and the steam is produced rapidly and in large quantities, the overburden may rupture. The resulting explosive eruption ejects a pyroclastic mixture of juvenile magma fragments, earlier magmatic products, pieces of country rock, and steam. Rising magma intersecting with surface water, especially at a vent, may also result in explosive eruption (Sheridan and Wohletz, 1983). Several events may occur next, depending on the energetics and geometry of the eruption (Koyaguchi and Woods, 1996). The pyroclastic mixture of hot particles and water vapor may initiate a buoyant plume that reaches the stratosphere, or the plume may collapse under its own weight, or pyroclastic density currents may transport material laterally away from the vent (Sheridan and Wohletz, 1983). These processes could also occur simultaneously. If the turbulent ash cloud contains sufficient water vapor, aggregates of smaller particles known as accretionary lapilli often form (Schumacher and Schmincke, 1995). Pyroclastic density currents create deposits known as pyroclastic surge and pyroclastic flow deposits, depending on the proportions of vapor and ash in the current (Sheridan and Wohletz, 1981). More vapor-rich currents produce surge deposits, which tend to be distinctly bedded, either with plane-parallel beds or low-angle cross-bedded sandwave bedforms (Cole, 1991; Fisher and Schmincke, 1984). Thus the final geologic deposits record the proportion of vapor involved in the eruption, which in turn is critical to determining the explosive energy (Sheridan and Wohletz, 1981).

In addition to phreatomagmatism, plausible genetic explanations for Siberian mafic volcaniclastic deposits include magmatic fire-fountaining, hyaloclastic effusions, reworking of effusive lavas by mass wasting or fluvial activity, or explosive (possibly phreatomagmatic) ejection through widely distributed Permian-Triassic aged pipe structures (Svensen et al., 2009). To better constrain which of these mechanisms were most important during the early stages of Siberian Traps magmatism, we have undertaken a comprehensive paleomagnetic, petrographic, and field-based investigation into the accessible exposures of the Siberian volcaniclastic deposits. Our methods are described in more detail in the subsequent section.

We find that Siberian Traps volcaniclastic rocks are heterogeneous, varying in thickness from thin layers to several-hundred-meter-thick sections dominated by volcaniclastics. Many spatially separated volcaniclastic rocks show signs of proximal deposition, suggesting a volcanic architecture that included multiple vents spread across hundreds of thousands of square kilometers. While exceptions exist, the volcaniclastic rocks are particularly common in the lowest levels of the volcanic stratigraphy. We present evidence that phreatomagmatic fragmentation accompanied by explosive volcanism was a key process in producing Siberian volcaniclastic rocks. The ejection of lithic blocks deriving from several kilometers depth suggests some eruptions originated with highly energetic flash production of vapor from subsurface magma-fluid interactions. The ubiquity of phreatomagmatism has important consequences for gas delivery to the atmosphere and for magma genesis. Phreatomagmatic explosive eruptions could deliver sulfur to the stratosphere, creating transient global cooling, but soluble gases like HCl would be more easily removed from a water-rich ascending plume (Tabazadeh and Turco, 1993). The implication that Siberia was water-logged at the time of eruption supports reconstructions that position a basin above the magmatic epicenter (Czamanske et al., 1998), placing constraints on the extent of syn-eruptive regional uplift. More detailed physical volcanological study of the large igneous province as a whole is urgently needed to assemble a complete portrait of the magmatic system and a chronology of the eruption.

2. Methods and Geologic Background

Field work is challenging in north-central Siberia, where the remnants of Siberian Traps volcanism are preserved. Sections are exposed primarily along river valleys, making interregional correlations difficult. We visited volcaniclastic sections on the Kotuy, Maymecha, Angara, and Tunguska rivers, as well as at Noril'sk (Figure 1A), in the summers of 2006, 2008, 2009, 2010, and 2012.

Figure 2 compiles several composite stratigraphic sections showing occurrence and characteristics of Siberian volcaniclastic deposits. The volcaniclastic rocks attain maximum reported thicknesses near the center of the Tunguska Basin; drill core suggests that mafic volcaniclastic deposits could reach 700 meters in thickness at the base of the volcanic sequence near Tura (Sharma, 1997; Zolotukhin and Almukhamedov, 1988). The relatively well-studied Noril'sk section hosts intercalated basalts and tuffs (Rudakova and Krivolutskaya, 2009). On the Maymecha River, the basal Pravoboyarsky Suite, which is dominantly composed of volcaniclastic units, reaches ~300 meters in thickness (Fedorenko and Czamanske, 1997), while the corresponding Arydzhangsky Suite on the Kotuy River contains a smaller but still significant proportion of volcaniclastic units (Fedorenko et al., 2000).

In addition to field observations, we examined the petrography and geochemistry of dozens of volcaniclastic samples. Possibly because of their relatively high porosity, the volcaniclastic rocks are particularly vulnerable to secondary alteration (Buchl and Gier, 2003). Grain size distributions are also difficult to interpret in the absence of data about vent architecture and the distance traveled by particles prior to deposition. Nonetheless, many primary volcanic features, including glass shards, accretionary lapilli, and fractured mineral grains, are preserved in thin section.

Hoblitt and Kellogg (1979) pioneered the use of paleomagnetic remanence to deduce emplacement temperatures of volcaniclastic rocks. In the presence of the Earth's magnetic field, the magnetic moments of ferromagnetic grains are statistically more likely to be aligned with that field. If ferromagnetic grains cool through their blocking temperature (between 550-580 °C for magnetite), that bias is locked in as a thermal remanent magnetization (Butler, 1992). The individual clasts within a

volcaniclastic rock will record independent thermal remanent magnetization directions above the emplacement temperature, but grains with blocking temperatures below the emplacement temperature will be uniformly magnetized. Consequently, for volcaniclastic rocks emplaced at temperatures lower than the blocking temperature of magnetite, but higher than any post-emplacement thermal conditions, clasts should contain two magnetic components (Hoblitt and Kellogg, 1979). We extracted mutually oriented clasts from unoriented samples. The samples were subjected to low-amplitude alternating frequency demagnetization (to 100 Gauss) to remove any viscous remanent magnetization associated with exposure to magnetic fields at low temperatures. We then measured the samples with a 2G Enterprises magnetometer during stepwise heating in an oven within a magnetically shielded room.

In total, we measured >100 clasts from 7 samples, searching for a thermal overprint associated with emplacement of the samples. Information about emplacement temperatures can in turn correlate with distance from the vent (McClelland et al., 2004) and can help to differentiate pyroclastic rocks from lahars and debris flows (Hoblitt and Kellogg, 1979).

3. Results

Field evidence

In many localities the volcaniclastic sections are dominated by massive lapilli tuffs or tuff breccias with sporadic, ill-defined layering. Closer study, however, reveals distinctive features including accretionary lapilli, large bombs and lithics (sometimes upended), lithic trains, clastic dikes, plane-parallel bedding and sandwave bedforms, vesicular tuff lenses, hyaloclastite, and diatreme structures. In this section we discuss our field observations and published reports of each of these features. Table 1 organizes these observations geographically.

We find accretionary lapilli in the lowermost reaches of sections on the Kotuy, Angara, and Nizhnyaya Tunguska rivers (Figure 2), as well as in a thick tuff layer in the Morongovsky Suite, which is situated near the midpoint of the Noril'sk stratigraphy (Fedorenko et al., 1996b). They have also been

reported within breccia infilling diatreme structures (Polozov et al., 2010). The accretionary lapilli typically have fine-grained rims, and include armored (Figure 4f), multiply-rimmed (Figure 3f inset), discoidal (Figure 4a) and spherical (Figure 4c) morphologies (Schumacher and Schmincke, 1991). They range in diameter from 1 mm to 3 cm.

On the Angara and Kotuy rivers, the accretionary lapilli occur within well-sorted layers (Figure 3f) with plane-parallel or low-angle cross bedding (Figure 3b). Sandwave bedforms are also present on the Maymecha River (Figure 3i).

The more typical massive deposits include abundant subrounded to angular clasts ranging in size from pebbles to meter-scale boulders (Figure 3g). Clasts occasionally form lithic trains, or occur as upright blocks (Figure 3g). On the Maymecha River (Figure 3f), and locally on the Kotuy River, clasts are angular and dominantly basaltic in composition. A cliff-forming tuff unit that directly overlies Permian sedimentary rocks on the Kotuy River near the town of Kayak (Figure 3d) contains abundant sedimentary lithics, including coal and rounded pebbles. On the Angara River, sedimentary input is even more pronounced; clasts include limestones (Figure 3a) and sandstones. Numerous clastic dikes cut the Angara volcaniclastics. In places the dikes clearly crosscut the entire exposed volcaniclastic section (>100 meters).

Svensen et al. (2009) describe diatreme-like pipe structures near Nepa. The Scholokhovskoie pipe crosscuts at least two large sills—one of which has a U-Pb age of 252.0±0.4 Ma—and extends at least as deep as Cambrian evaporite horizons (Svensen et al., 2009). Several hundred similar pipe structures have been reported in the Russian literature, distributed throughout the Siberian Traps province (Malich, 1974). While the pipe structures at Nepa are large (reaching hundreds of meters in diameter) and are known primarily from magnetite mining and drill cores (Svensen et al., 2009), many pipe structures are much smaller. Wooden et al. (1993) mention a small diatreme associated with the Morongovsky tuff at Noril'sk that has carried fragments of basement and Riphean sedimentary rocks from 9-10 km depth.

In many regions of the Siberian Traps, volcaniclastic rocks are prevalent near the base of the volcanic sequence, but decrease in thickness and occurrence higher in the section. In Noril'sk, however,

tuff layers are intercalated with lavas, and one of the most prominent pyroclastic deposits occurs in the Morongovsky Suite, ~1000 meters above the base of the volcanic section (Rudakova and Krivolutskaya, 2009). Fedorenko et al. (1994; 1996b) suggest that this tuff, which contains abundant accretionary lapilli (Figure 4c,d), may be coeval with the Noril'sk-1 intrusion, which has been dated to 251.2 ± 0.3 Ma (Kamo et al., 2003). On the Kotuy River, thin lenses of highly weathered vesiculated tuff occur within the Onkuchaksky Suite, 500 meters above sample K09-7.7, which rests on top of the Tungusskaya Permian sedimentary rocks. On the Maymecha River, the most silicic known rocks in the entire large igneous province occur in the Delkansky Suite, ~2000 meters above the base of the Pravoboyarsky Suite. These trachytic and rhyolitic tuffs (Figure 5) include welded, glassy groundmass and eutaxitic textures.

In summary, the volcaniclastic rocks vary widely from location to location. Soviet mapping suggests basaltic pipe structures are widespread (Malich, 1974). Volcaniclastic rocks may reach maximum cumulative thicknesses of up to 700 meters in some areas (Zolotukhin and Almukhamedov, 1988); they may also be missing entirely from other central regions of the Siberian Traps (Planke, 2013). Thick volcaniclastic piles dominate the base of the volcanic section in the Maymecha, Tunguska, and Angara river valleys. The deposits on the Maymecha are the most internally diverse, though drill core from the Angara region (Naumov and Ankudimova, 1995) also hints at dozens of distinct tuff layers. In Noril'sk and the Kotuy River valley, tuffs are intercalated with lavas. Even such characterization of sub-regions of the Siberian Traps may simplify the volcaniclastic stratigraphy excessively. As further field work is undertaken to describe the volcanology of the large igneous province in detail, we do not doubt that many more unique localities will be discovered.

Petrography and geochemistry

We examined the volcaniclastic rocks in thin section with a petrographic microscope and the electron microprobe. The shape and vesicularity of glass fragments, each of which can provide information about the fragmentation mechanism (Heiken, 1972; Wohletz, 1983), are listed in Table 1. The

approximate proportion of juvenile, cognate, and accidental particles is also shown. Following Fisher and Schmincke (1984), we define juvenile fragments as particles formed from the erupting magma, whereas cognate fragments originated in a prior eruption and accidental fragments derive from the country rock.

Glass shards vary from deposit to deposit (Table 1), ranging from blocky grains (Heiken, 1972) with mosaic cracks (Büttner et al., 1999) and negligible vesiculation to highly vesicular (Figure 4e), irregularly shaped fragments (Wohletz, 1983). Most of the glass fragments are altered, which may render the cracking patterns apocryphal. Smaller ash particles include moss-like shapes (Wohletz, 1983).

Figure 4f shows fine-grained material that appears to have armored a small, equant, unvesiculated glass fragment. Generally, thin sections of accretionary lapilli revealed fine-grained rims and inwardly increasing grain size. Maximum grain size at the cores of accretionary lapilli (except for armored accretionary lapilli) was ~300 μm. A significant fraction of the accretionary lapilli within the Morongovsky tuff are broken into well-preserved fragments (Figure 4d).

While it can be difficult to differentiate juvenile from cognate fragments, the components of volcaniclastic rocks in Table 1 range from approximately 40-100% juvenile material, 0-40% cognate material, and 0-40% accidental material (excluding the clastic dikes, which include nearly 100% sedimentary precursors).

With the exception of the silicic Delkansky rocks, geochemically the tuffs are largely close to basaltic in composition (Figure 5). In the Maymecha-Kotuy area, many mafic tuffs are also highly alkaline. The whole rock geochemistry of the volcaniclastic rocks also appears to reflect the incorporation of significant country rock material. The tuffs that contain primarily juvenile and cognate clasts are low in silica. Several of the most lithic-rich tuffs have 55-60 wt% SiO_2. We consider this a likely effect of accidental SiO_2-rich components admixed with basaltic juvenile material, though the alteration of juvenile glass hinders an accurate assessment of the liquid composition.

Paleomagnetic remanence

The results from stepwise thermal demagnetization of our samples are shown in Figure 6 and Figure 7. We applied Watson's (1956) test to assess the randomness of the distribution of paleomagnetic directions. For a given number of clasts, Watson (1956) specifies a significance value at the 95% level (R_0), and provides a method for calculating the correlation (called R) within a set of directional vectors. If R exceeds the 95% significance value R_0 for the number of clasts analyzed, the clasts are non-randomly magnetized and the sample fails the conglomerate test. Conversely, if R is less than the 95% significance value R_0 for the number of clasts analyzed, we provisionally conclude that the sample has passed the conglomerate test.

Out of seven samples, A10-3.5, M09-3.3, K08-11.6, and NT12-4.2 fail the conglomerate test at all temperatures ($R/R_0 > 1$) and contain a uniform magnetization (representative Zijderveld diagram for K08-11.6 is shown in Figure 7b), K08-10.3 passes at all temperatures ($R/R_0 < 1$ as noted in Figure 7a), S10-2.5 contains clasts with internally inconsistent magnetization, and K08-11.6 fails the conglomerate test at low temperatures ($R/R_0 > 1$ as noted in Figure 6d) and passes at high temperatures ($R/R_0 < 1$ as noted in Figure 6e). The majority of the clasts from this final sample exhibit a sharp kink in the demagnetization path around 270 °C (Figure 6a-c), though two clasts (9b and 11a) contain only a single component up to the blocking temperature of magnetite. We did not include matrix samples (labeled as m#) in the Watson test calculation.

4. Discussion

The interpretation of paleomagnetic results

Figure 8 summarizes the framework within which we interpreted our paleomagnetic results. Depending on the behavior of clasts from each sample during stepwise thermal demagnetization, we can differentiate the original conditions under which the sample acquired its remanence.

Clasts from sample K08-7.11 contain more uniform directions at low temperature, and less uniform directions at high temperature (Figure 6d-e), with kinked demagnetization paths. Therefore we interpret the paleomagnetic behavior as a record of emplacement at ~270°C, consistent with pyroclastic eruption. Because the samples are unoriented, we could not compare the low temperature direction with the modern field; however preliminary alternating frequency demagnetization to 100 Gauss should remove most viscous overprints.

Sample K08-10.3 passes the conglomerate test at low and high temperature, with consistent intraclast directions. It also discordantly cuts several lava flows. Although we have analyzed a relatively small number of clasts so far (N=6), we conditionally classify K08-10.3 as a debris flow or lahar deposit.

Samples A10-3.5, M09-3.3, K08-11.6, and NT12-4.2 were uniformly magnetized to temperatures above the blocking temperature of magnetite. These samples span virtually the entire breadth of the Siberian Traps (Figure 1). This result allows two possible interpretations. Either the samples were emplaced at temperatures greater than the blocking temperature of the high-temperature magnetic carrier (around 585 °C for magnetite) or they have been thermally or chemically overprinted after emplacement. Oriented samples from these rocks and from adjacent dikes would provide one test to distinguish between these two scenarios. If the dikes are slightly younger, identical magnetic directions in both the volcaniclastic and intrusive rocks implies that both rocks may have been overprinted. M09-3.3 and K08-11.6, from the Maymecha and Kotuy valleys, are particularly well-lithified and may have been sintered, suggesting they could have been emplaced at high temperatures. But the lack of welding or sintering of the Angara and Nizhnyaya Tunguska samples casts doubt on an extremely high emplacement temperature. Because the volcaniclastic rocks are generally relatively porous, they may be more amenable than the lavas to fluid flow and chemical alteration, accompanied by acquisition of a chemical remanence.

The extent of pyroclastic volcanism

The extent of pyroclastic volcanism is a critical determinant of the environmental impact of the Siberian Traps. Because the volcaniclastic deposits are often poorly sorted, with few diagnostic bedding or textural features, positively identifying the products of pyroclastic eruptions is challenging. Field evidence substantiates the presence of hyaloclastic, autoclastic, and epiclastic deposits in addition to pyroclastic rocks, further complicating an estimate of the relative importance of each process.

Our paleomagnetic results (Table 1) offer some additional constraints. As described in the previous section, we find evidence for one pyroclastic sample emplaced at 270-330 °C, one debris flow/lahar sample, one sample with an overprint such that even intraclast directions are inconsistent, and four samples emplaced either at temperatures above 580-600 °C or at unknown temperature and subsequently overprinted with a later thermal or chemical remanence. If these samples are approximately representative, then—depending on whether these uniformly magnetized samples were explosive—on the order of 14-71% of the Siberian Traps volcaniclastic rocks were produced during pyroclastic eruptions. Assuming an original area of volcanic activity spanning ~3,000,000 km^2 (Reichow et al., 2009), and a mean thickness of volcaniclastic rocks of ~300 meters (Zolotukhin and Almukhamedov, 1988), the total pre-erosional volume of volcaniclastic rocks in the large igneous province was around 900,000 km^3. 14 % explosive volcanism would therefore imply a cumulative volume for Siberian Traps pyroclastic deposits of roughly 130,000 km^3.

Given the non-unique interpretation of our paleomagnetic results for the four uniformly magnetized samples, this estimate of the extent of pyroclastic volcanism incorporates considerable uncertainty. However, other lines of evidence also suggest that in some areas pyroclastic fragmentation may have been the major mechanism that produced volcaniclastic deposits. Accretionary lapilli are believed to form in water-rich turbulent ash clouds (Schumacher and Schmincke, 1995). Likewise surge bedforms record dilute, water-rich pyroclastic density currents (Fisher and Schmincke, 1984). Accretionary lapilli and/or surge bedforms are present within one or more tuff layers in five out of the six

localities we visited (Figure 2), indicating that eruptions were at least intermittently pyroclastic in the Kotuy, Angara, Nizhnyaya Tunguska, Maymecha, and Noril'sk regions. In the Kotuy, Angara, Nizhnyaya Tunguska, and Maymecha regions, the lowest exposed units contained accretionary lapilli or surge bedforms, implying that the earliest eruptions were pyroclastic.

The Morongovsky tuff unit includes many broken fragments of accretionary lapilli (Figure 4c), which may indicate particularly violent eruptive conditions. Surge bedforms also document the passage of pyroclastic density currents (Crowe and Fisher, 1973; Fisher and Schmincke, 1984). In Noril'sk and the Kotuy River valley, large fragments of country rock have been excavated from depth (Wooden et al., 1993), as discussed in the next section. Pyroclastic fire-fountaining may also have occurred at vents. Some pyroclasts evince fluidal shapes, and agglomerated tuffs have been reported from the Maymecha River valley (Fedorenko and Czamanske, 1997) and from Noril'sk (Rudakova and Krivolutskaya, 2009).

Basaltic pipe structures infilled with hydrothermally altered breccia provide further evidence of pyroclastic volcanism (Svensen et al., 2009). Although the pipe structures are synchronous with volcanism (Svensen et al., 2009), and at least one pipe actually crosscuts apparently related tuff deposits (Wooden et al., 1993), the largest breccia pipes have not been definitively linked with specific volcaniclastic deposits. Mining near Ust-Ilimsk has exposed a clastic dyke originating from the upper surface of a major sill that reaches several hundred meters in thickness. If the pipe structures, the massive volcaniclastic deposits with locally preserved bedding features, and the clastic dikes in the southern region of the Siberian Traps are in fact all co-genetic, they represent a major explosive province similar in style to that reported in the Transantarctic Mountains (McClintock and White, 2006; White and McClintock, 2001).

The role of phreatomagmatism

Numerous datasets suggest that phreatomagmatism was a critical factor in producing the unusually large volume of volcaniclastic rocks associated with the eruption of the Siberian Traps. The

field evidence includes massive poorly sorted deposits, locally well-defined bedforms, accretionary lapilli, rare vesicular tuffs, and abundant accidental lithic clasts—all of which are consistent with abundant water vapor in the system during deposition (Fisher and Schmincke, 1984). The large size of some lithic clasts further confirms the highly energetic nature of the water-rock interactions. Petrographically, glass fragments typically evince equant, irregular, or fine-grained 'mossy' morphologies, joined with low to intermediate vesicularity and plausible mosaic cracking of some poorly vesicular particles. All of these textures are consistent with a hydrovolcanic origin (Heiken, 1972; Wohletz, 1983), whereas ash produced during basaltic magmatic fragmentation might include larger proportions of fluidal and aerodynamic shapes (Heiken, 1972). In Noril'sk, Fedorenko et al. (1996b) report that the paleontological evidence supports an intermittently subaqueous environment.

The best paleomagnetic estimate we obtained for an emplacement temperature was ~270 °C, which is relatively low for a pyroclastic deposit and is also consistent with phreatomagmatic origin (Fisher and Schmincke, 1984). In the Angara River valley the rocks are poorly consolidated, which may indicate modest emplacement temperatures, though elsewhere agglomerated tuffs have been reported (e.g. Fedorenko and Czamanske, 1997; Rudakova and Krivolutskaya, 2009).

Sulfur isotope fractionation trends for two Kotuy River mafic tuffs are most consistent with open-system degassing (Black et al., submitted-a). Because open-system degassing implies that the vapor phase segregates easily from the melt and provides little explosive impetus (Head and Wilson, 1987), it also favors phreatomagmatic rather than magmatic fragmentation.

The large proportion of accidental material, which is visually apparent in the Angara region and in the tuff unit near Kayak, is characteristic of phreatomagmatic deposits. The incorporation of woody debris into several deposits on the Angara River indicates that at least some of the water-magma interactions likely occurred at shallow levels. However, among many of the Angara volcaniclastic rocks, a white sandstone and a white mottled stromatolitic limestone are two of the most common and distinctive lithic components. Some clasts reach 1 meter in diameter. Based on the distribution of limestones in the underlying sedimentary sequence (Zharkov, 1984), we conjecture that these rocks

originated in strata of Neoproterozoic to Cambrian age. Campbell et al. (1992) similarly report the presence in the tuffs of numerous clasts originating in Devonian and older strata, from depths of 300-1500 or more meters beneath the uppermost Tungusskaya rocks. The initial fragmentation that expelled these clasts therefore occurred at several hundred meters to several kilometers depth, likely indicating that these rocks were expelled and deposited during a highly energetic explosive eruption.

It is possible to use textural features of phreatomagmatic deposits to approximately constrain the vapor-melt ratio and the efficiency with which thermal energy could have been converted to explosive mechanical energy during the eruption that produced the deposits (Sheridan and Wohletz, 1983; Wohletz, 1983). Some caution is required, however, as individual eruptions may have evolved through several phases of magma-water interaction and explosivity (Sheridan and Wohletz, 1983). In Figure 9 we deduce water vapor abundance for some Siberian Traps samples with distinctive textural features. The samples that combine accretionary lapilli with sandwave bedforms (K09-7.7 and A10-13.3) likely achieved highly efficient conversion of thermal to mechanical energy, implying that they could have been erupted during particularly explosive events.

Effects on gas release and environmental consequences

The results presented here shed light on two aspects of magmatic volatile release: the removal of gases from the eruption plume, and the altitude at which gases were released. During phreatomagmatic eruptions, in addition to H_2O released from the magma significant quantities of external water can be vaporized and incorporated into a buoyant eruptive plume (Koyaguchi and Woods, 1996; Woods, 1993). Because HCl is highly soluble in water, and relatively soluble in water ice (Pinto et al., 1989; Tabazadeh and Turco, 1993; Textor et al., 2003), the additional water in the eruption plume would have expedited the rain-out of HCl (Black et al., 2012), thereby diminishing the fraction of HCl that reached the stratosphere. The delivery of HCl to the stratosphere has been proposed to help trigger catalytic destruction of ozone, resulting in increased ultraviolet radiation (Beerling et al., 2007). Our results

suggest that metamorphic CH_3Cl and other less-soluble halogen-bearing compounds (such as BrO) may have been more important for stratospheric chemistry than HCl.

Because CH_3Cl is relatively long-lived in the troposphere, the altitude at which it is released does not significantly affect its ultimate chemical effects (Black et al., submitted-b). In contrast, sulfur rains out of the troposphere within weeks to months, but can remain in the stratosphere for years (Robock, 2000). Whether the volcanic plume penetrates the tropopause therefore partly determines the climate effects of an eruption.

The evidence for explosive volcanism during the eruption of the Siberian Traps increases the likelihood that sulfur emissions reached the stratosphere. Particularly vigorous fire fountains during the historic Laki flood basaltic eruption also produced columns that breached the tropopause (Thordarson and Self, 1993a, 2003). The additional explosivity provided by phreatomagmatic interactions would have increased the scale and frequency of pyroclastic volcanism. Although the vaporization of ground or surface water saps the thermal energy of the magma, that energy is released again in the eruption column, helping to power the buoyancy of the rising plume (Koyaguchi and Woods, 1996). Once in the stratosphere, sulfate particles increase the optical depth of the atmosphere, leading to a transient regional or global cooling (Robock, 2000).

One key question for studies seeking to understand the connection between large igneous provinces and mass extinctions is why some eruptions coincide with extinctions while others do not. The Siberian Traps, Karoo-Ferrar (McClintock and White, 2006; Ross et al., 2005; White et al., 2009; White and McClintock, 2001), and Emeishan (Peate and Bryan, 2008; Ross et al., 2005; White et al., 2009) large igneous provinces all contain significant volumes of mafic volcaniclastic deposits. The Paraná-Etendeka, Central Atlantic Magmatic Province (CAMP), and Columbia River flood basalts were apparently accompanied by less extensive phreatomagmatic explosivity. Of these, the Siberian Traps, the Karoo-Ferrar, Emeishan, and CAMP coincided within uncertainty with mass extinctions, whereas extinction rates were low at the time of the Paraná-Etendeka and Columbia River eruptions (Wignall, 2001). Thus, with the major exception of CAMP, phreatomagmatism may correlate with the environmental

consequences of flood basalt eruptions. Because the climate effects of CO_2 emissions are similar whether the gas is released during explosive or effusive eruptions, this correlation may indicate that sulfur release played a role in some or all of the extinctions that have been linked with the Siberian Traps, Karoo-Ferrar, and Emeishan large igneous provinces.

The overall volcanic architecture of the Siberian Traps and implications for plume-related uplift

While many aspects of the plumbing structure and volcanic architecture of the Siberian Traps remain unknown, the available exposures and geochemical data lead us to hypothesize that a cross section through the lithosphere at the time of the eruption would have resembled the sketch in Figure 10. Large feeder dikes, several hundred meter-thick sills, and vent-proximal pyroclastic features can all be found distributed over hundreds of thousands of square kilometers between the Taimyr Peninsula and Lake Baikal. Vesicular tuffs such as the thin units in the Onkuchaksy Suite near Kayak (103.230 °E, 71.511 °N) rarely occur more than 2-3 km from their source (Fisher and Schmincke, 1984). Likewise the meter-scale blocks in the Angara region (102.371 °E, 58.878 °N) and the Maymecha valley (101.215 °E, 70.753 °N) are also clearly proximal. These features strongly support the existence of numerous vents erupting in concert over a very large area. As shown in Figure 10, depending on the abundance of ground and surface water (and possibly hydrocarbons), a wide variety of volcanic explosions and effusions may have resulted.

White and McClintock (2001) postulate that a 'phreatocauldron' formed in the Coombs Hills of Antarctica from the coalescence of many smaller phreatomagmatic vents. The rarely preserved, laterally disjointed pockets of well-bedded pyroclastic rocks within the mass of poorly sorted volcaniclastic deposits in the Angara region may record a similar environment, wherein successive, overlapping phreatomagmatic episodes disrupted previous bedding features.

The water-rich paleo-environment (Czamanske et al., 1998) may also have encouraged mass-wasting as in the case of sample K08-10.3. However, Fedorenko et al. (1996b) suggest that the general

absence of erosional valleys implies that very little relief existed during magmatism. They conclude that the construction of the volcanic edifice was balanced by subsidence. In this case, post-eruptive mass-wasting and epiclastic re-deposition may have been suppressed.

Early numerical and experimental simulations suggested that mantle plumes would generate broad domal uplifts in overlying crust (Campbell and Griffiths, 1990). Whether such uplifts exist in the rock record, and the implications for the reality of mantle plumes, is the subject of significant controversy (Foulger, 2011; Peate and Bryan, 2008). Recently, more detailed numerical models have shown that dynamic coupling between the crust and delaminating lower lithosphere may generate topographic subsidence (Elkins-Tanton, 2007; Elkins-Tanton and Hager, 2000; Sobolev et al., 2011). The melt injection that triggers density instability and delamination may result either from modest upwellings (Elkins-Tanton and Hager, 2000) or from a mantle plume (Sobolev et al., 2011). In the latter case, dynamic subsidence may entirely negate any plume-related uplift (Sobolev et al., 2011).

In the Kotuy River valley there is an unconformity of unknown duration between the Tungusskaya sedimentary rocks and the volcanic sequence. Overall, however, the evidence for widespread interaction between magmas and both ground and surface waters supports a paleogeography similar to that delineated by Czamanske et al. (1998), in which the eruptive region was relatively low-relief, with abundant swamps and shallow basins. Such a low-relief landscape strongly favors a model for melt generation that does not require broad regional uplift. In the context of existing hypotheses for mantle dynamics during large igneous province eruptions, this requirement implies that density instabilities and sinking lithospheric material (with or without the presence of a mantle plume) were of first-order importance during Siberian Traps magmatism.

5. Conclusions

Eruptions of large igneous provinces are rare but geologically rich events, with potentially cataclysmic environmental consequences. Here we focus on the Siberian Traps, which is one of the most

voluminous continental flood basalt provinces to erupt in the Phanerozoic (Reichow et al., 2009). Intense Siberian magmatism has been linked to the end-Permian mass extinction. Apparent emplacement temperatures in excess of 200 °C for one or more deposits, accretionary lapilli, surge bedforms, typically equant glass fragments, and large blocks and bombs, support the contention that explosive phreatomagmatic interactions contributed to fragmentation and production of the voluminous mafic volcaniclastic deposits that dominate the early Siberian Traps succession in many areas.

Widespread phreatomagmatic activity is consistent with subsiding topography at the time of the eruption. This requirement is best explained by dynamic coupling with a delaminating lower lithosphere (Elkins-Tanton, 2007; Elkins-Tanton and Hager, 2000), possibly triggered by melt injection from an impinging mantle plume (Sobolev et al., 2011).

Intense phreatomagmatism likely produced opposite effects for sulfur and chlorine emissions. Water-rich conditions in the eruptive plume accelerate the removal of soluble chlorine (e.g. Tabazadeh and Turco, 1993). At the same time, explosive eruptions, whether driven by exsolving volatiles or vaporized external water, help to deliver sulfur to the stratosphere. The scale of the Siberian Traps volcaniclastic deposits suggests that transient cooling from sulfur emissions may have been sustained by long-lived episodes of phreatomagmatic activity. Cooling from volcanic sulfur can in some cases trigger sea-ice feedbacks that temporarily shift ocean circulation (Miller et al., 2012). Breccia pipes, which may also be phreatomagmatic in origin (Polozov et al., 2010), provide a release conduit for metamorphic gases such as CH_3Cl (Svensen et al., 2009). These halocarbon gases can catalyze ozone destruction, leading to large increases in biologically effective ultraviolet radiation (Beerling et al., 2007). Thus, phreatomagmatism associated with the early phases of Siberian Traps magmatism may have facilitated environmental shocks in the ocean and on land at the time of the end-Permian mass extinction.

Acknowledgments

This study was funded by grant EAR-0807585 from NSF Continental Dynamics, and supplemented by the MIT Wade Fund. Vladimir Pavlov, Anya Veslovskiy, Sam Bowring, and Seth Burgess were valued collaborators during field work. Bernhard Peucker-Ehrenbrink provided generous assistance with the electric pulse disaggregator at WHOI. The authors also gratefully thank Brenda Carbone.

Figures and Tables

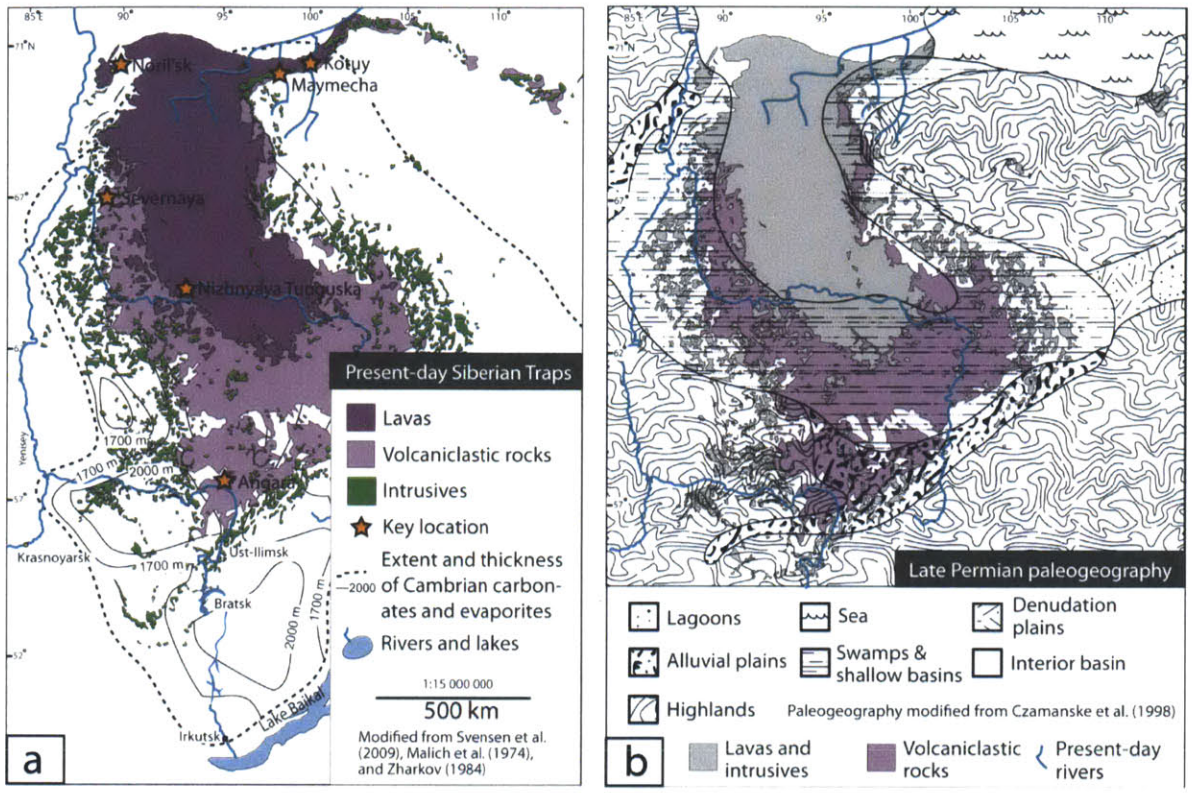

Figure 1. Map of the Siberian Traps, modified from Svensen et al. (2009) and Malich et al. (1974). **a.** Present-day outcrop extent of lavas, volcaniclastic rocks, and intrusives, with Cambrian carbonate and evaporite thicknesses from Zharkov (1984), **b.** overlain with Late Permian paleogeography simplified from Czamanske et al. (1998).

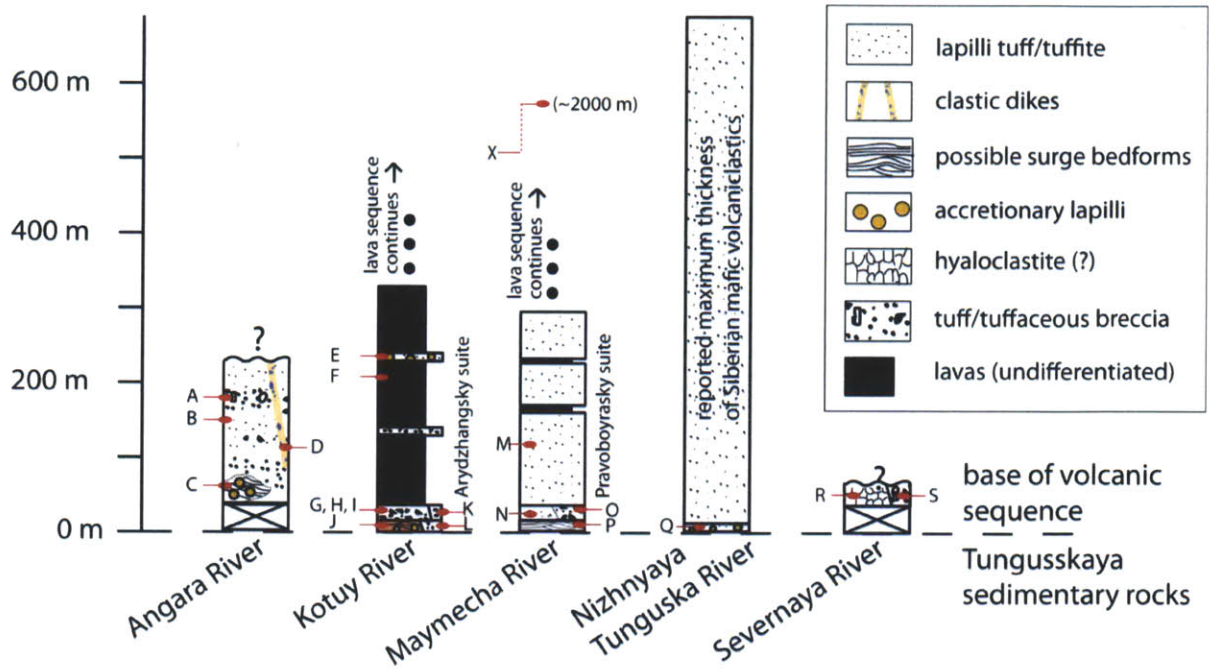

Figure 2. Stratigraphic sections of basal volcaniclastic and lava sequences of the Siberian Traps, based on Fedorenko et al. (2000), White et al. (2009), and our own observations. Thicknesses are laterally variable. Noril'sk is not shown, because tuff layers are intercalated with lava flows. Letters denote units as follows: **A:** A10-7.1 **B**: A10-3.5 **C**: A10-13.3 **D**: A10-10.2 **E**: K08-11.6 **F**: perovskite-bearing flow dated to 251.7 ± 0.4 Ma by Kamo et al. (2003). **G**: K08-7.11 **H**: K08-7.10 **I**: K08-3.4 **J**: K09-7.7. **K**: K08-10.3 **L**: K09-10.4A **M**: Tuff sequence described by Fedorenko et al. (2000), including 'agglomerated tuffs.' **N**: M09-3.3 **O**: Basal tuff breccia shown in Figure 3f. **P:** Surge deposit (just above interface with Tungusskaya sedimentary rocks) shown in Figure 3i. **Q:** NT12-4.2 **R:** Possible hyaloclastite (Planke, personal communication). **S**: S10-2.5 **X**: Welded rhyolitic tuff from Delkansky Suite(~1700 m above top of Pravoboyarsky suite shown here), dated to 251.17 ± 0.3Ma by Kamo et al. (2003). All units are described in more detail in Table 1, except F, M, O, P, and R. The contact with Permian sedimentary rocks at the base of the Angara and Severnaya river sections is covered, and erosion has removed the overlying stratigraphy. The volcaniclastic rocks of the Maymecha and Kotuy rivers are capped by thick lava sequences (not shown here). The reported maximum thickness of the volcaniclastics is based on drill core from near the center of the Tunguska basin (Zolotukhin and Almukhamedov, 1988).

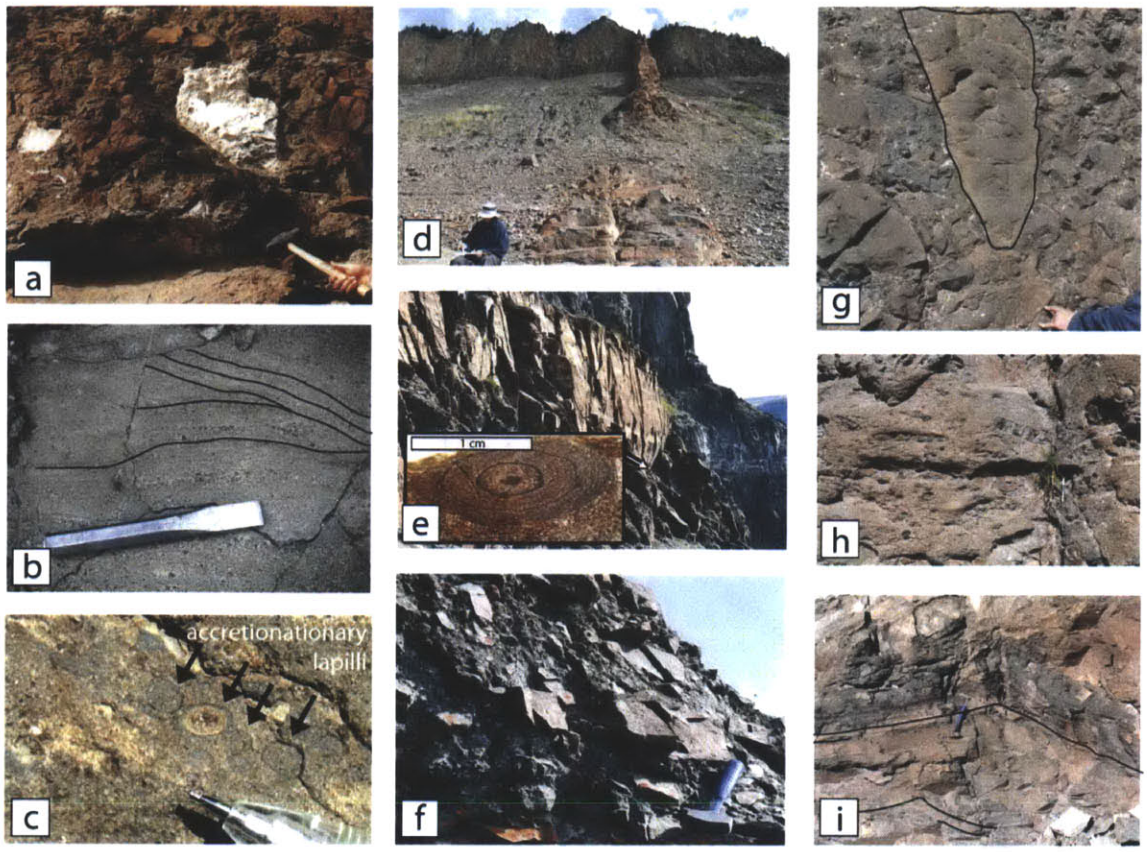

Figure 3. Field photos from the Siberian Traps. **a.** Stromatolitic limestone blocks within poorly sorted tuff (sample A10-7.1). **b.** Low-angle cross-stratification in accretionary lapilli-rich (sample A10-13.3). **c.** accretionary lapilli within sample A10-13.3. **d.** Four meter thick dolerite dike crosscuts both the Tungusskaya sedimentary rocks and a basal 30 meter thick tuff layer (sample K09-10.3) near Kayak. **e.** Plane-parallel bedded surge deposits with multi-layered oblate accretionary lapilli (inset). **f.** Poorly sorted breccia deposit ~30 meters thick with abundant igneous clasts overlying finer-grained tuff (sample M09-4.7). **g.** Meter-scale upright igneous clast with fine-grained rim within Pravoboyarsky tuff. **h.** Possibly imbricated clasts within Pravoboyarsky tuff (pen for scale). **i.** Dune or antidune bedform within lowermost Pravoboyarsky tuff (hammer for scale).

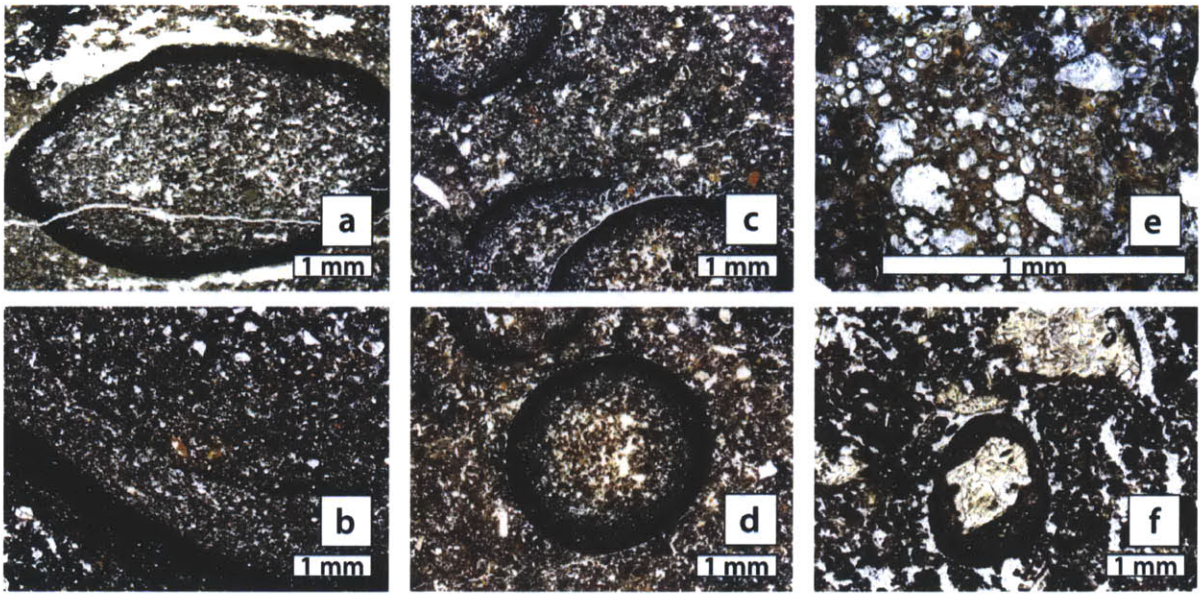

Figure 4. Petrographic images of volcaniclastic rocks in thin section, taken with plane-polarized light source. **a.** Rim-type oblate accretionary lapillus in lowermost Nizhnyaya Tunguska tuff (sample NT12-1). **b.** Multilayered large accretionary lapillus with grain size increasing towards core (sample A10-13.3). **c.** Abundant spherical accretionary lapilli from Morongovsky tuff in Noril'sk (sample N12-8.2). There are numerous broken fragments of accretionary lapilli within this sample, as shown by the partial rim center left. **d.** Well-preserved rim-type spherical accretionary lapilli from Morongovsky tuff (sample N12-8.2). **e.** Small fragment of highly vesicular glass from Pravoboyarsky tuff (sample M09-3.3). **f.** Fine-grained material armoring an equant, poorly vesicular glass fragment (sample K09-11.6).

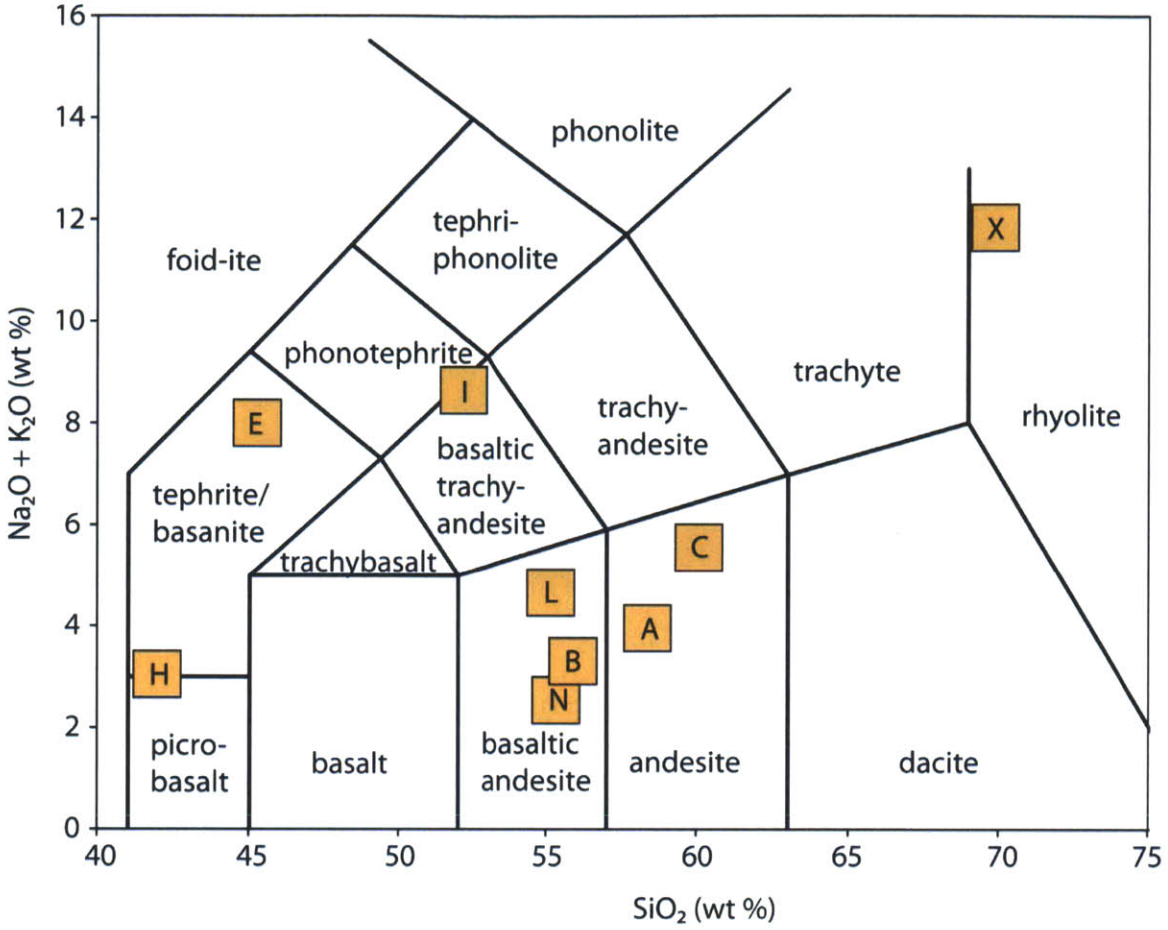

Figure 5. Total Alkali-Silica diagram (Le Bas et al., 1986) for selected volcaniclastic and pyroclastic rocks. Letters in yellow boxes correspond to sample signifiers from Figure 2 and Table 1.

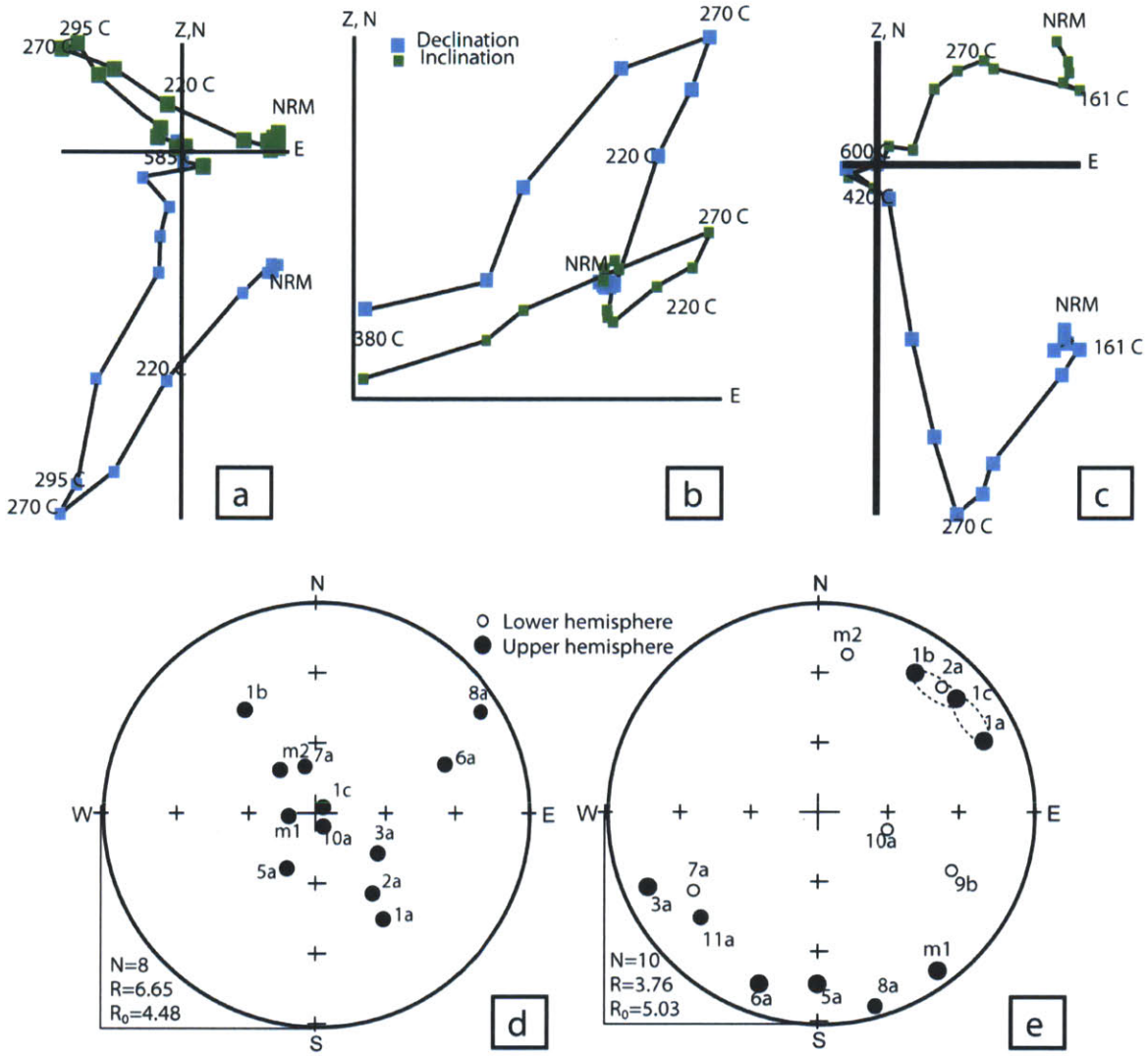

Figure 6. Paleomagnetic results from sample K08-7.11, a mafic tuff from the Kotuy River valley. **a-c.** Zijderveld diagram of the magnetization of selected clasts from K08-7.11 during stepwise thermal heating. Most clasts reveal two components, with a kink between 270-330 °C. **d.** Low temperature (<190-270 °C) least-squares equal area plot for clasts from K08-7.11 showing somewhat consistent magnetization. $R/R_0 > 1$, indicating with 95% confidence that the distribution is non-random. **e.** High temperature (>220-330 °C) least-squares equal area plot for clasts from K08-7.11 showing a significantly more random distribution. $R/R_0 < 1$, indicating that the sample provisionally passes the conglomerate test at high temperature. Individual clasts are labeled. Subsamples from the same clast are linked with dotted circles.

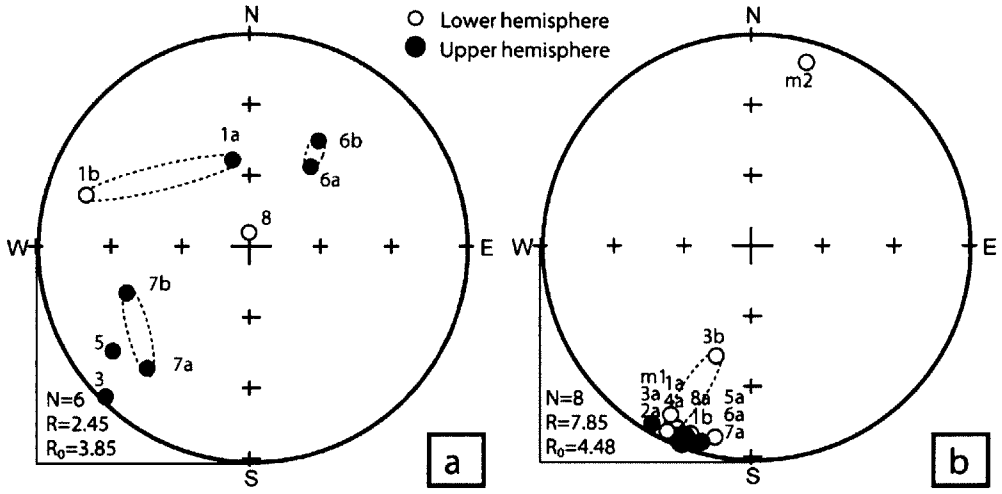

Figure 7. Least-squares equal area stereographic plots. **a.** Sample K08-10.3, which we interpret as a low-temperature conglomerate produced by a lahar or debris flow. **b.** Sample K08-11.6, which is uniformly magnetized at low and high temperatures. Because the sample is unoriented, the directions are valid only relative to one another, and not relative to an external coordinate system. A10-3.5, M09-3.3, and NT12-4.2 exhibit similar behavior.

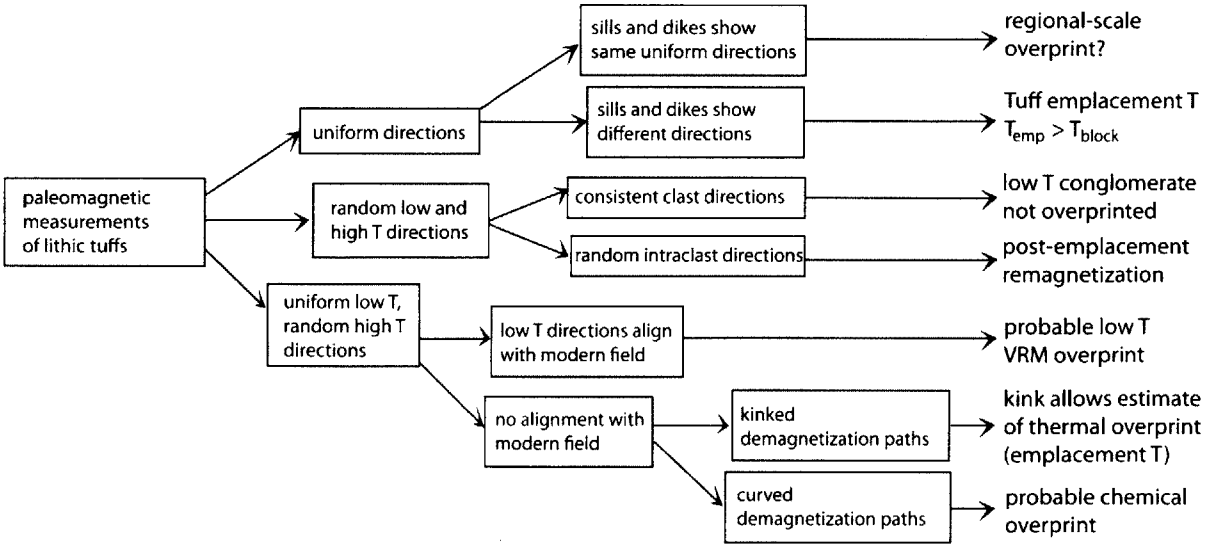

Figure 8. Flow chart showing potential implications of partial thermal demagnetization measurements of lithic tuffs.

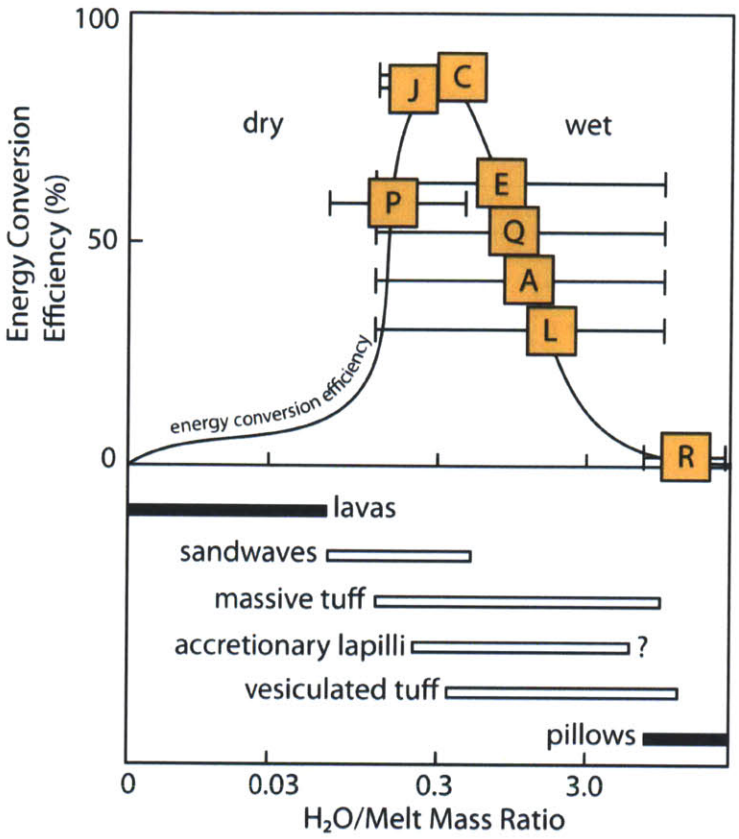

Figure 9. Textural features can pinpoint the vapor/melt ratio and energetics of an eruption. The energy conversion efficiency curve and vapor/melt ratios specific to each textural feature are taken from Sheridan and Wohletz (1983) and Wohletz (1983). The letters follow the shorthand sample conventions from Figure 2 and Table 1, and refer to the following rocks: **A:** A10-7.1 **C**: A10-13.3 **E**: K08-11.6 **J**: K09-7.7. **L**: K09-10.4A **P:** Surge deposit (just above interface with Tungusskaya sedimentary rocks) shown in Figure 3i. **Q:** NT12-4.2 **R:** Possible hyaloclastite (Planke, personal communication). Samples are classified based on their textural attributes as noted in Table 1.

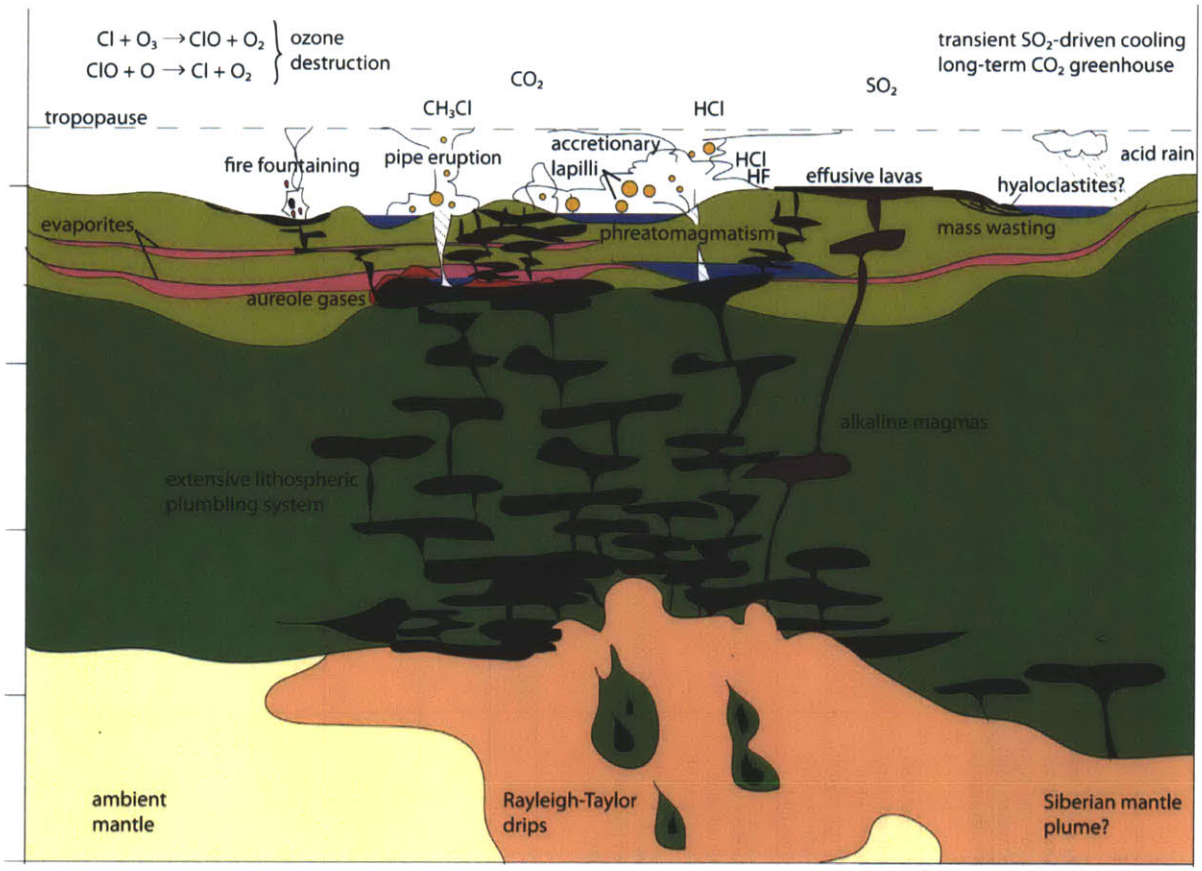

Figure 10. A schematic cross section through the lithosphere and atmosphere during the Siberian Traps eruption. Not to scale.

Region	Sample Signifier	Full Sample ID	GPS	Description	Componentry	Glass fragments	Paleomagnetic results
Angara	A	A10-7.1	102.371 E 58.878 N	Fig. 4a. Poorly sorted clasts include large stromatolitic limestone blocks and small rounded pebbles; rare lenses of well-sorted fine-grained tuff. Outcrop 50 meters high.			N/A
	B	A10-3.5	102.122 E 58.940 N	Poorly sorted lithic-rich tuff with angular igneous clasts.	Feldspars: 25% plagioclase, 75% alkali feldspar. 50% albite.	Weakly to moderately vesicular with scalloped edges and mosaic cracks.	Uniformly magnetized at all T.
	C	A10-13.3	102.723 E 58.738 N	Abundant accretionary lapilli organized into low-angle cross-stratified and plane parallel bedforms. Near base of cliff of volcaniclastic material ~200 meters high.	60 % juvenile, 40 % cognate or accidental. Feldspars 27% plagioclase, 73% alkali feldspar.	Equant unvesiculated glass fragments.	N/A
	D	A10-10.2	102.620 E 58.773 N	Clastic dike cross-cutting relatively fine-grained tuff. Outcrop 10 meters high.			N/A
Kotuy	E	K08-11.6	102.616 E 71.203 N	1 meter thick reddish accretionary lapilli bearing tuff, intercalated with alkaline lavas, approx. 220 meters above base of Arydzhangsky suite.	70% juvenile, 25% cognate, 5% accidental.	See Figure 5X. Poorly vesicular, equant glass fragments.	Uniformly magnetized at all T.
	G	K08-7.11	102.590 E 71.181 N	Mafic breccia from near base of Arydzhangsky suite, sampled from float, 1-2 cm clasts within fine matrix.	100 % juvenile or cognate.		Uniformly magnetized at low T. Non-uniformly magnetized at high T. Emplacement at T=270-340 °C?
	H	K08-7.10	102.590 E 71.181 N	Arydzhangsky Suite.	90% juvenile, 10% cognate.		N/A
	I	K08-3.4	102.355 E 71.049 N	Arydzhangsky Suite.		Weakly to moderately vesicular with scalloped edges.	N/A
	J	K09-7.7	102.663 E 71.131 N	Pravoboyarsky Suite. Cliffy basal breccia capped by fine-grained well-sorted plane-parallel beds 1-3 cm thick, possibly surge deposit. ~8 meters total thickness.			N/A
	K	K08-10.3	102.633 E 71.203 N	Inversely graded, steeply dipping approx 10-12 m thick breccias. Lahar or debris flow?			Randomly magnetized at all T. Cold emplacement?
	L	K09-10.4A	103.105 E 72.497 N	Pravoboyarsky Suite. Cliff-forming 30 meter thick volcaniclastic breccia, unconformable contact with underlying Tungusskaya sedimentary rocks, abundant unsorted 1-50 cm clasts of country rock including coal, limestone, and rounded pebbles.			N/A
Maymecha	N	M09-3.3	101.239 E 70.741 N	Pravoboyarsky Suite. Dense, strongly lithified 8 meter thick lapilli tuff. Glassy	60 % juvenile, 30% cognate, 10 % accidental.	Some glass fragments are highly vesicular, and	Uniformly magnetized at all T.

				fragments. Major, areally extensive deposit.		apparently deformed by flow or compaction. Others fragments are poorly vesicular.	
	O	M09-4.7	101.215 E 70.753 N	Pravoboyarsky Suite. Figure XX. 5 meter thick poorly sorted volcaniclastic breccia. Large (<0.5 m) clasts of igneous and sedimentary material, fine matrix. Very local, variable thickness.			N/A
	X	M09-12.1	100.636 E 70.811 N	Delkansky Suite. Welded rhyolitic tuff. Purple-gray with feldspar laths. 10-20 meters thick.	90% juvenile, 10% cognate.		N/A
Nizhnyaya Tunguska	P	NT12-1	100.505 E 64.172 N	1-meter thick accretionary lapilli bearing basal tuff directly above Tungusskaya sedimentary rocks.		Rare, poorly vesicular, irregular glass fragments.	N/A
Severnaya	R	S10-2-5	90.768 E 66.414 N	Well-lithified gray-and-white tuff with large clasts (up to 3 cm) of heterogeneous igneous and sedimentary rock. Fine ashy matrix.	40% juvenile, 40% cognate, 20% accidental.		Randomly magnetized. Incoherent intraclast directions. Unknown overprint?
Noril'sk		N12-4.2		Clast-rich tuff.			Uniformly magnetized at all T.
		N12-8.2	88.331 E 69.620 N	Morongovsky Suite tuff. 15-30 meters in total thickness. Very abundant spheroidal accretionary lapilli.		Small, equant glass fragments.	N/A

Table 1. Summary of field, petrographic, and paleomagnetic data for selected volcaniclastic rocks from the Siberian Traps.

Sample signifier	Full sample Number	SiO_2 wt %	TiO_2 wt %	Al_2O_3 wt %	FeO wt %	MnO wt %	MgO wt %	CaO wt %	Na_2O wt %	K_2O wt %	P_2O_5 wt %	NiO wt %	Cr_2O_3 wt %	Total
A	A10-7.1	58.28	0.95	14.92	8.21	0.13	4.69	8.59	2.70	1.34	0.12	0.01	0.04	100
B	A10-3.5	55.81	1.01	14.85	9.34	0.32	6.05	9.04	2.54	0.85	0.14	0.01	0.04	100
C	A10-13.3	59.98	0.95	14.96	8.06	0.15	5.24	4.85	4.06	1.58	0.11	0.01	0.04	100
E	K08-11.6	45.17	0.97	12.40	8.55	0.15	5.21	18.79	3.78	4.30	0.63	0.01	0.05	100
G	K08-7.10	41.89	3.81	8.63	15.84	0.20	9.21	16.54	2.03	1.09	0.59	0.02	0.14	100
H	K08-3.4	52.12	2.99	10.90	9.81	0.14	6.25	8.32	0.69	8.04	0.68	0.00	0.07	100
J	K09-10.4A	55.00	1.09	15.51	11.03	0.12	7.16	5.37	3.47	1.07	0.14	0.01	0.04	100
L	M09-3.3	55.25	1.13	15.48	9.85	0.16	6.11	9.20	1.34	1.28	0.15	0.01	0.04	100
X	M09-12.1	69.79	0.74	14.25	2.61	0.08	0.24	0.25	1.04	10.89	0.10	0.00	0.00	100

Table 2. Whole rock major element chemistry for selected Siberian Traps volcaniclastic rocks. Sample signifiers refer to the shorthand employed in Figure 2 and 4 and in Table 1.

Chapter 5. Acid rain and ozone depletion from pulsed Siberian Traps magmatism

Abstract: The Siberian Traps flood basalts have been invoked as a trigger for the catastrophic end-Permian mass extinction. Widespread aberrant plant remains across the Permian-Triassic boundary provide evidence that atmospheric stress contributed to the collapse in terrestrial diversity. Here, we use the first detailed estimates of magmatic degassing from the Siberian Traps to complete the first 3-D global climate modeling of atmospheric chemistry during eruption of a large igneous province. Our results show that both strongly acidic rain and global ozone collapse are possible transient consequences of episodes of pyroclastic volcanism and heating of volatile-rich Siberian country rocks, respectively. In conjunction with abrupt warming from CO_2 release, these repeated, rapidly applied stresses may have contributed to the ecological failure on land. Our modeling depicts the global distribution and severity of ozone depletion and acid rain, providing testable predictions for the geography of end-Permian environmental proxies.

INTRODUCTION

Gas release from Siberian Traps magmatism and thermal metamorphism of hydrocarbon- and evaporite-rich country rocks is a leading candidate to drive end-Permian ecological upheaval (Payne and Clapham, 2012b). We present new results from a comprehensive model of global chemistry and climate (Kiehl and Shields, 2005; Lamarque et al., 2012) that reveal the global patterns of environmental stress that could emanate from pulses of Siberian Traps magmatism.

The end-Permian mass extinction marked the death knell for a vast majority of global species, and set the stage for the rise of the dinosaurs. While the extinction was particularly severe in the oceans—where organisms that were most vulnerable to changes in pCO_2 died preferentially (Knoll et al., 2007) and overall only 10% of species survived into the Triassic (Erwin, 1994)—terrestrial plants and animals also suffered. Numerous reptile, amphibian, and insect genera vanished entirely (Erwin, 1994). An abrupt depositional shift in several locations from meandering to braided river systems has been interpreted as a result of accelerated die-off of terrestrial vegetation (Ward et al., 2000).

The precise onset of Siberian magmatism is geochronologically uncertain, though emplacement of the lava pile was almost complete by 251.4±0.3 Ma (Kamo et al., 2003). The peak marine extinction interval is well-constrained to begin at 252.17±0.06 Ma with a duration of <200±100 Kyr; the global timing of the terrestrial extinction is more tentative, but appears to be synchronous (Shen et al., 2011). Although the coincidence of the marine and terrestrial mass extinctions suggests they were related, perhaps by a common trigger such as the Siberian Traps, the specific environmental conditions that led to declines in diversity may have included distinct elements on land and in the oceans. In this work we investigate two specific kill mechanisms that have been linked (Maruoka et al., 2003; Visscher et al., 2004) to the terrestrial mass extinction: acid rain and ozone depletion.

Here we use the first comprehensive estimates of sulfur release from the Siberian Traps (Black et al., 2012) to carry out the first 3-D global climate modeling of atmospheric chemistry during flood volcanism. The results provide the first data-driven demonstration of the extent and devastating intensity

of acid rain at the end-Permian. We also present results from simulations of ozone chemistry. Previous two-dimensional modeling has shown that emissions of HCl and CH_3Cl related to Siberian magmatism could cause ozone depletion (Beerling et al., 2007). However, the wealth of paleontological data from different Permian-Triassic sections provides a key resource for understanding the patterns of the mass extinction. In particular, palynological data record episodes of high atmospheric stress that produced spikes in abnormal pollen abundance (Visscher et al., 2004). Therefore, in order to produce robust, detailed predictions of the worldwide patterns of magmatism-induced ecological stress for comparison with the paleontological record, three-dimensional modeling of the global severity of both acid rain and ozone depletion is critical.

MODEL DESCRIPTION

We use the Community Earth System Model with the CAM-Chem interactive atmospheric chemistry model (Lamarque et al., 2012) to simulate fully interactive Permian-Triassic atmospheric chemistry with Permian geography, 10x modern CO_2, and prescribed sea surface temperatures (Kiehl and Shields, 2005) (for further details, see Supplementary Table 1). We initialized our atmospheric chemistry simulations with a 1000-year fully coupled equilibration run completed with the Community Climate System Model 4.0 at 3.75° x 3.75° and interpolated to the model resolution. Detailed initial conditions are listed in Supplementary Table 1. Our model atmosphere includes 26 vertical levels and a horizontal resolution of 1.9° x 2.5°, and is coupled to prescribed sea surface temperatures from the initial equilibrium run. Gases are released into the lowermost troposphere (at 0.15 km) or the lower stratosphere (at 14 km).

The environmental effects of volcanism depend on the rates of volatile emission from degassing magmas (Black et al., 2012) and heated and metamorphosed country rocks (Svensen et al., 2009). The lifetimes of sulfate aerosols, methylated halogens, and methane in the Permian stratosphere are on the order of a year, two years, and several decades respectively. U-Pb geochronology suggests that the total emplacement of the ~4,000,000 km^3 Siberian Traps occurred in less than 1 Myr (Kamo et al., 2003), but

paleomagnetic secular variation implies that some large lava suites were erupted in pulses lasting <10 Kyr (Pavlov et al., 2011). In addition to the long-term effects of CO_2 release, these eruptions could have produced severe but geologically short-lived environmental deterioration. We focus on the transient effects of sulfur, halogen, organohalogen, and methane release over timescales of years to tens of years.

We simulated 26 perturbation and recovery scenarios, summarized in Supplementary Table 2. Each was chosen to approximate volatile release from a plausible magmatic episode, including a large pyroclastic eruption (Black et al., 2012), contact heating and metamorphism of hydrocarbon-bearing evaporite salts (Aarnes et al., 2011), and one or more explosive pipes (Svensen et al., 2009). We also considered the effects of stratospheric versus tropospheric release and background emissions of methyl chloride. The gas fluxes in Supplementary Table 2 were selected on the basis of petrologic estimates (Black et al., 2012), experiments and volumetric estimates (Svensen et al., 2009), thermal modeling (Aarnes et al., 2011), and modern volcanological measurements of trace gases (Schwandner et al., 2004).

We track the water contents of each parcel of air, and include the interrelated effects of SO_4, SO_3, HSO_3, NO_3, HCO_3, OH, CO_2, and NH_4 in order to calculate the pH of rain water. Because solubilities depend on pH, we determine the pH iteratively.

Because sulfate deposition is parameterized based on Mount Pinatubo size distribution, estimates of acidity may be conservative. For very large sulfur fluxes, larger sulfate aerosols will form (Timmreck et al., 2009). These larger particles settle more quickly from the atmosphere, potentially translating into a more intense but also shorter-lived pulse of acid rain. We modified CAM-Chem to include the effects of stratospheric sulfate aerosols on polar stratospheric cloud formation, and therefore on the surface area density available to facilitate heterogeneous reactions involving Cl and ozone. For this calculation we use aerosol sizes based on simulations of a 100x Pinatubo sulfur release (Timmreck et al., 2009), which is of a similar order of magnitude to the sulfur release in our y_pt_02 cases (see Supplementary Table 2).

RESULTS

Acid Rain

Our simulations show that both CO_2 and SO_2 release from the Siberian Traps could have strongly affected the acidity of rain. Oxygen isotopic data record a rapid increase in temperatures coincident with the marine extinction interval (Sun et al., 2012), consistent with an order of magnitude increase in atmospheric CO_2. In addition to producing global warming (Kiehl and Shields, 2005), in our model a tenfold increase in CO_2 leads to more acidic rain (pH≈4) globally. Sulfur injected into the stratosphere during a large pyroclastic eruption further shifts pH of rain by one or more log units (Figure 1); pH rebounds quickly after the eruption ceases. Because the Siberian Traps were located around 60°N in the Permian, volcanogenic acid rain is particularly intense in the northern hemisphere. In a broad swath between the equator and 60°N, the annually averaged acidity after a ~200 km^3 eruption drops as low as pH≈2—similar to undiluted lemon juice. Local precipitation on a given day may be significantly more acidic. Furthermore, our model does not include the acidity produced by HCl and HF. Because HCl and HF are preferentially removed proximally to the vent through dissolution or adsorption onto particulates, respectively (Seinfeld and Pandis, 1997), these gases may have intermittently enhanced acidity in the region of the Siberian Traps.

Ozone depletion

Volatile release associated with Siberian Traps magmatism can produce ozone depletion ranging from moderate reduction to near-total collapse in both the northern and southern hemispheres. The fluxes of halogen and halocarbon compounds to the stratosphere critically determine the rate of catalytic ozone loss. In the Tunguska basin, Proterozoic hydrocarbons coexist with halites (Svensen et al., 2009). Depending on the Total Organic Carbon (TOC) contents of Siberian halite layers and conversion efficiency of methane to CH_3Cl, thermal metamorphism related to emplacement of a flat ~5000 km^3 sill

could result in peak annualized production (over 10^2 years) of 0.55 - 0.83 Gt CH_4 and 0.87 - 1.65 Gt CH_3Cl (Aarnes et al., 2011), which may be released passively or through widely dispersed pipe structures (Svensen et al., 2009).

Methane and methyl chloride fluxes in this range produce steady-state ozone depletion of 60-70% globally (Figures 2 & 3). If gases accumulate during the peak production period prior to release through a pipe, ozone depletion can reach 55-60 %, assuming that ~1% of aureole gases mobilize into the pipe. Recovery typically takes approximately 10 years after the cessation of emissions. Because more than 100 pipes are associated with widespread and voluminous Siberian Traps sills (Svensen et al., 2009), ozone levels could have suffered multiple cycles of collapse and recovery. The lifetime of CH_3Cl in the troposphere is sufficiently long (>1 year) that CH_3Cl released in the lower troposphere reaches the stratosphere (Figure 2a). Consequently, the magnitude of ozone depletion is similar for either tropospheric or stratospheric release of CH_3Cl gas (Figure 3).

In the case of magmatic HCl, stratospheric release during an explosive episode is critical, because HCl is soluble and quickly washes out of the troposphere (Textor et al., 2003). The fraction of HCl that reaches the stratosphere after a large Siberian Traps explosive eruption produces only 5-20 % ozone depletion (Figure 3), in contrast to previous results suggesting one-tenth the HCl flux over long timescales would produce ~30% ozone depletion (Beerling et al., 2007). The resilience of the end-Permian ozone layer is consistent with the limited ozone response to hydrogen sulfide emissions observed in global climate-chemistry simulations (Lamarque et al., 2007), and may result from more realistic simulation of polar stratospheric clouds, less severe CO_2-driven stratospheric cooling, and different background O_2 and Cl levels (see Supplementary Table 1).

DISCUSSION

The effects of acid rain on Permian ecosystems are poorly constrained, and depend on species physiology and local buffering capacity. Figure 1b generalizes the pH sensitivity of modern flora and

fauna. Elevated background CO_2 leads to long-term acidification of rain that could have leeched soil nutrients (Likens et al., 1996). During an eruption, sulfur-rich rain with pH≈2 in the northern hemisphere is sufficient to disfigure plants and stunt growth; sustained sulfur release could damage weakly buffered aquatic ecosystems. Paleontological and pollen studies indicate that plant communities in the southern hemisphere also suffered during the end-Permian (Rees, 2002; Visscher et al., 2004). Although increased sulfide concentrations across the Permian-Triassic boundary in the Karoo basin (Figure 1a) have been interpreted as a record of sulfur rainout from volcanic sources (Maruoka et al., 2003), mid-latitude tropospheric folding, sedimentation, and the patterns of stratospheric circulation (Hamill et al., 1997) limit the overall flux of SO_4 from the Siberian Traps to the southern hemisphere.

Whereas sulfuric acid rain is muted in the southern hemisphere—and in contrast to the modest ozone depletion incurred by volcanic HCl—metamorphic CH_3Cl emissions ravage the ozone layer at all latitudes (Figure 2b), with potentially severe consequences for Permian terrestrial biota. The most intense depletion occurs at high latitudes, where the total atmospheric ozone column dwindles to <15% of Permian background levels. Based on power-law scaling of biologically active ultraviolet (UV) radiation with ozone (Madronich et al., 1998), this reduction equates to a maximum 4900% increase in mutagenic UV-B flux (Figure 4). Elevated UV-B fluxes have been shown to produce an increase in genetic recombination rates and stunting of *Arabidopsis* seedlings in laboratory experiments (Ries et al., 2000). Absolute ozone levels are slightly lower in the northern hemisphere (Figure 2b), but the percentage depletion is actually greatest at the south pole (Figure 4). Ozone column density at all latitudes and longitudes is lower than the lowest values associated with the Antarctic ozone hole of the late 20th century (Seinfeld and Pandis, 1997).

Results from our simulations are limited by uncertainties in metamorphic emissions and eruptive timescales, the CO_2 mixing ratio, and pre-eruptive background emissions (Supplementary Table 1). The background concentration of Cl in the stratosphere is governed by emissions of CH_3Cl that oxidize to inorganic Cl, and is one of the key controls on end-Permian ozone stability. In the present day, the most important natural sources of CH_3Cl include biomass burning, tropical vegetation, and fungal digestion of

woody material (Seinfeld and Pandis, 1997). Evidence for widespread wildfires (Shen et al., 2011), warmer temperatures (Sun et al., 2012), and fungal spikes (Visscher et al., 1996) suggests that all three of these sources were likely elevated during the Permian-Triassic, possibly by large factors. As shown in Figure 3, the resultant increase in stratospheric Cl would have decreased ozone levels, both independently and in concert with any thermogenic or volcanic release of Cl-bearing compounds associated with the Siberian Traps.

The rate of environmental change is arguably as important as the magnitude of change. Accelerated shifts in climatic and chemical conditions can outpace the biological capacity for adaptation (Jump and Peñuelas, 2005). Because Siberian Traps magmatism was likely episodic (Pavlov et al., 2011), pulses of deeply acidic rain and/or severe ozone depletion may have accompanied magmatic episodes. In our simulations, acid rain relents within a year after the end of gas emissions, whereas the ozone layer takes around ten years to recover. We suggest that such rapid, drastic fluctuations in pH and ultraviolet flux, coupled with a dramatic increase in global temperatures (Kiehl and Shields, 2005; Sun et al., 2012), contributed to the end-Permian extinction on land.

Figures

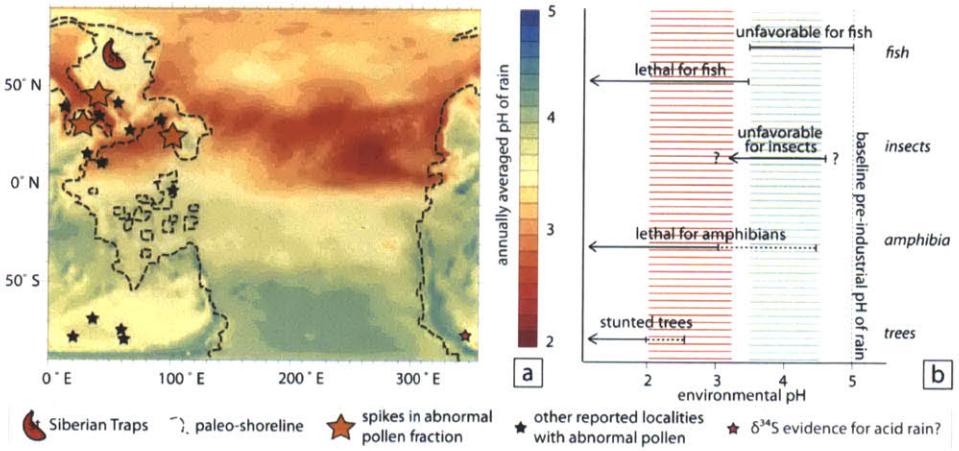

Figure 1. Magnitude and effects of acid rain during Siberian Traps pyroclastic activity. **a.** Annually averaged precipitation-weighted pH of near-surface rain during an explosive eruption (case y_pt_02a_v1, with 1.46 Gt SO_2) that breaches the high-latitude tropopause. Significant spikes in abnormal pollen have been reported in Greenland (Visscher et al., 2004), Russia, and China (Foster and Afonin, 2005); other Permian-Triassic sections where abnormal pollen has been reported are widely distributed (Visscher et al., 2004). Sulfur isotopes in Karoo have been interpreted as evidence for acid rain (Maruoka et al., 2003). **b.** A generalized compilation of the pH sensitivity of modern flora and fauna (Howells, 1990).Green shading indicates the range of acidity observed in high-CO_2 simulations of Permian-Triassic rain; orange shading indicates the acidity in the northern hemisphere during an eruption. Note that pH of aquatic ecosystems will be variably buffered against acid rain (Howells, 1990).

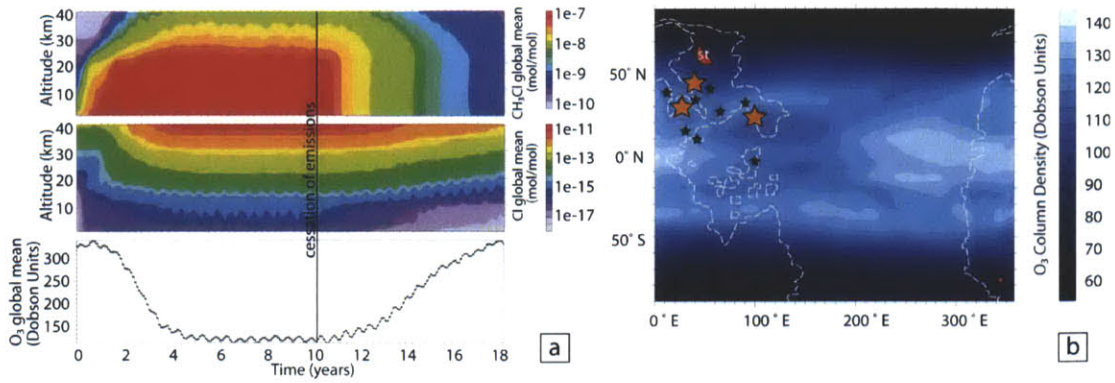

Figure 2. Ozone depletion driven by metamorphic gases. **a.** Sill intrusion into halites (case y_pt_01) results in peak annualized production of 0.87 - 1.65 Gt CH_3Cl (Aarnes et al., 2011). Gas released at the surface (top panel), reaches the stratosphere, where it oxidizes to increase reactive Cl levels (middle panel), ultimately leading to ozone depletion (bottom panel). **b.** Global map of annually averaged ozone column density at year 10 from Figure 2a. Symbols are specified in Figure 1.

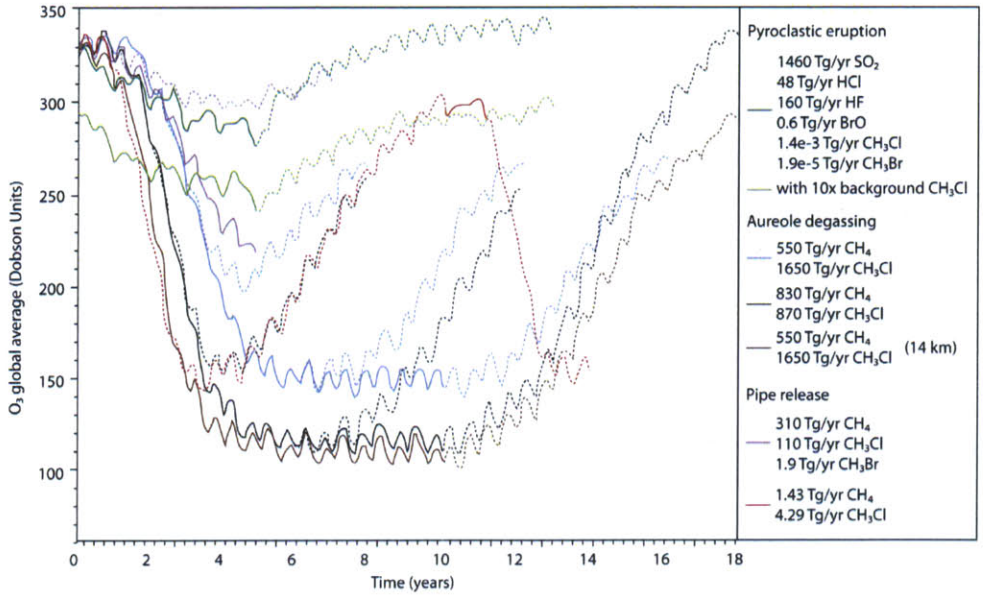

Figure 3. Summary of globally averaged ozone trends for selected simulations of pyroclastic eruptions, sill emissions, and pipe eruptions. Solid lines indicate ongoing release, at rates listed in inset legend. Dashed lines indicate recovery with only background emissions.

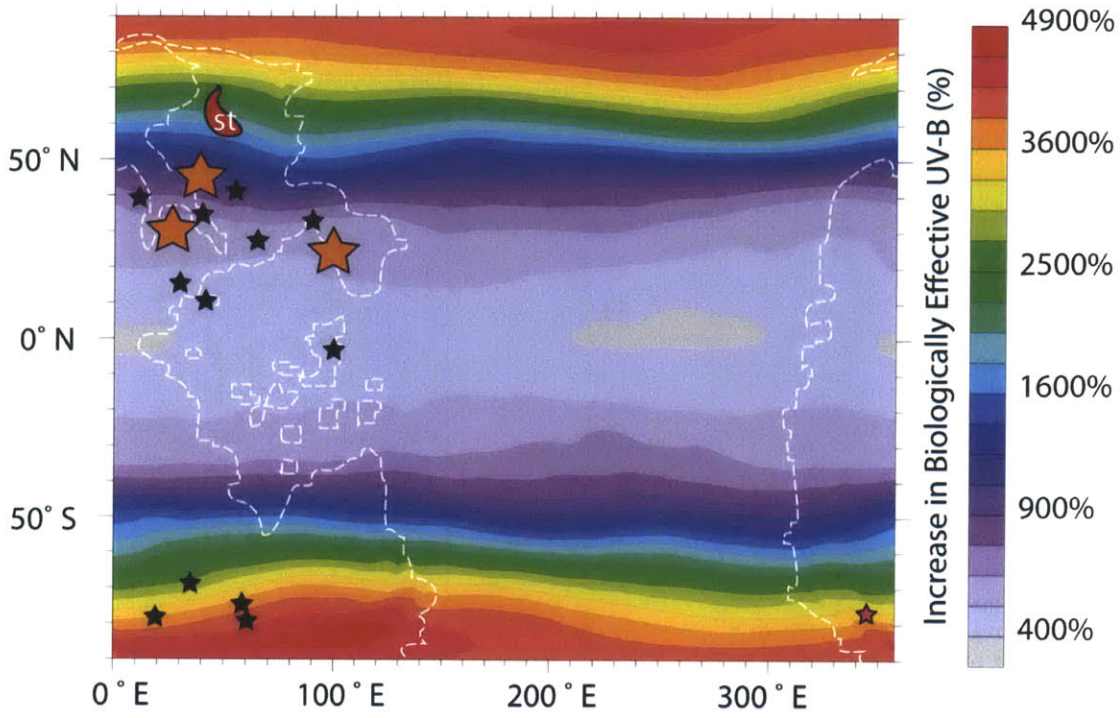

Figure 4. Using the power law relationship UV ~ ozone $^{(-RAF)}$ between biologically active UV flux and ozone, assuming RAF ≈ 2 for mutagenesis and DNA damage (Madronich et al., 1998), we compute the increase in biologically active UV from year 1 to year 10 of simulation y_pt_01b_v1 (shown in Figure 2). Symbols are as defined in Figure 1.

Supplementary Materials

Supplementary Table 1: Initial Conditions

Species	Flux	Fixed Condition	Reference
CH_4	1500 Tg yr^{-1}		(Beerling et al., 2009)
CO	195 Tg yr^{-1}		(Seinfeld and Pandis, 1997)
CH_3Cl	3.5 Tg yr^{-1}		(Seinfeld and Pandis, 1997)
CH_3Br	0.15 Tg yr^{-1}		(Seinfeld and Pandis, 1997)
DMS	30 Tg yr^{-1}		(Elliott, 2009)
NO_x	15 Tg yr^{-1}		(Archibald et al., 2013)
CO_2		3550 ppm	(Kiehl and Shields, 2005)
N_2O		275 ppb	(Kiehl and Shields, 2005)
O_2		21 %	*
S_0		1338 W m^{-2}	(Kiehl and Shields, 2005)

*We use present-day O_2 values because previous WACCM simulations suggested that Permian O_2 of 17% (Berner, 2002) does not strongly alter ozone chemistry (Lamarque et al., 2006). 2-D modeling of Siberian Traps degassing by Beerling et al. (2007) used lower atmospheric O_2 values of 15%, which may partly account for the increased rates of ozone destruction in that model (Beerling et al., 2007). Lower atmospheric O_2 values have been shown to intensify ozone loss at mid- and high-latitudes (Harfoot et al., 2007), implying that our estimates of ozone depletion are conservative. We also observe less intense stratospheric cooling from a CO_2 greenhouse relative to Beerling et al. (2007), which reduces the occurrence of polar stratospheric clouds.

Supplementary Table 2: Simulated Emissions

Case	Run Name	Release Rate	Duration	Notes	References
0: Control	y_pt_00_v3	Background Permian forcing	20 years chemical equilibration	See Supp. Table 1	See Supp. Table 1
	y_pt_00_v4	Background Permian forcing, 10x CH_3Cl background	10 years chemical re-equilibration after y_pt_00_v3	See Supp. Table 1	See Supp. Table 1
	y_pt_00_v5	Background Permian forcing, 20x CH_3Cl	10 years chemical re-equilibration after y_pt_00_v3	See Supp. Table 1	See Supp. Table 1
1: Aureole	y_pt_01b_v1	Aureole degassing: 1.65 Gt/yr CH_3Cl 0.55 Gt/yr CH_4	1-10 years	0.50 CH_4 -> CH_3Cl conversion ratio, lower troposphere release	(Aarnes et al., 2011; Svensen et al., 2009)
	y_pt_01b_v2	Recovery after 10 years			
	y_pt_01b_v3	Recovery after 6 years			
	y_pt_01b_v4	Recovery after 2 years			
	y_pt_01c_v1	Aureole degassing: 0.87 Gt/yr CH_3Cl 0.83 Gt/yr CH_4	1-10 years	0.25 CH_4 -> CH_3Cl conversion ratio, lower troposphere release	(Aarnes et al., 2011; Svensen et al., 2009)
	y_pt_01c_v2	Recovery after 10 years			
	y_pt_01c_v3	Recovery after 6 years			
	y_pt_01c_v4	Recovery after 2 years			
	y_pt_01d_v1	Stratosphere release: 1.65 Gt/yr CH_3Cl 0.55 Gt/yr CH_4	10 years	For comparison with y_pt_01b_v1	
	y_pt_01d_v2	Recovery after 10 years			
2: Pyroclastic	y_pt_02a_v1	Pyroclastic eruption: 1.46 Gt SO_2/year 48 Tg HCl/year 160 Tg HF/year 0.6 Tg BrO/year 0.0014 Tg CH_3Cl/year 1.9e-5 Tg CH_3Br/year	1-5 years	Release at 14 km above Siberian Traps. Assumes that 75% of degassed HCl is removed from plume(Textor et al., 2003). HF is likely removed also.	(Black et al., 2012; Schwandner et al., 2004)
	y_pt_02a_v2	Recovery after 5 years			
	y_pt_02a_v3	Recovery after 1 year			
	y_pt_02b_v1	Pyroclastic eruption, same emissions as	5 years	Background stratospheric Cl	(Beerling et al., 2007;

		y_pt_02a_v1, with 10x background emissions of CH_3Cl		load in Beerling is higher (0.48 Tg)(Beerling et al., 2007).	Black et al., 2012; Schwandner et al., 2004)
	y_pt_02b_v2	Recovery after 5 years			
	y_pt_02c_v1	Pyroclastic eruption, 3x HCl, 10x background CH3Cl: 1.46 Gt SO_2/year 144 Tg HCl/year 160 Tg HF/year 0.6 Tg BrO/year 0.0014 Tg CH_3Cl/year 1.9e-5 Tg CH_3Br/year	5 years	3x Cl release, in case 75% of Cl reaches stratosphere (Rose et al., 2006) rather than 25% (Textor et al., 2003).	(Black et al., 2012; Schwandner et al., 2004)
	y_pt_02c_v2	Recovery after 5 years			
	y_pt_02d_v1	Pyroclastic eruption, 3x HCl, 20x background CH3Cl	5 years	Background stratospheric Cl load in Beerling (2007) is higher (0.48 Tg).	(Beerling et al., 2007; Black et al., 2012; Schwandner et al., 2004)
	y_pt_02d_v2	Recovery after 5 years			
3: Pipes	y_pt_03a_v1	One small pipe per year: 0.31 Gt CH_4 0.11 Gt CH_3Cl 1.9 Tg CH_3Br	1-5 years	Fluxes are not well-constrained. All pipe gases are released to the lower troposphere (although delivery to the stratosphere is possible, it makes a marginal difference)	(Svensen et al., 2009)
	y_pt_03a_v2	Recovery after 5 years			
	y_pt_03a_v3	Recovery after 1 year			
	y_pt_03b_v1	One larger pipe: 4.29 Gt CH_3Cl 1.43 Gt CH_4	1 year	Assumes gases build up during peak production period (~260 years), before ~1% are released via a pipe.	
	y_pt_03b_v2	Recovery after 1 year	9 years		
	y_pt_03b_v3	Second perturbation: 4.29 Gt CH_3Cl 1.43 Gt CH_4	1 year	A second pipe eruption, 10 years later.	
	y_pt_03b_v4	Recovery after second, 1 year perturbation			

Chapter 6. Estimating erosional exhumation on Titan from drainage network morphology

Abstract: Drainage networks on Titan, Earth, and Mars provide the only known examples of non-volcanic fluvial activity in our solar system. The drainage networks on Titan are apparently the result of a methane-ethane cycle similar to Earth's water cycle. The scarcity of impact craters and the uneven distribution of fluvial dissection on Titan suggest that the surface may be relatively young. The purpose of this study is to assess the importance of erosion relative to other plausible mechanisms of resurfacing such as tectonic deformation, cryovolcanism, or deposition of aerosols. We present a new method, based on a measure of drainage network shape known as the width function, to estimate cumulative erosion into an initially rough surface. We calibrate this method with a numerical landscape evolution model, and successfully test the method by applying it to river networks on Earth with different exhumation histories. To estimate erosional exhumation on Titan, we mapped fluvial networks in all Synthetic Aperture Radar swaths obtained by the Cassini spacecraft through T71. Application of our method to the most completely imaged drainage networks indicates that for two of four regions analyzed, Titan's fluvial networks have produced only minor erosional modification of the surface. For the best-constrained region in the northern high latitudes, we find that fluvial networks reflect spatially averaged erosion of more than 0.4% but less than 9% of the initial topographic relief. This result implies either a recent, non-fluvial resurfacing event or long-term fluvial incision rates that are slow relative to the rate of resurfacing.

1. Introduction

Prior to the arrival of the Cassini-Huygens spacecraft in orbit around Saturn in 2004, the surface of Titan was the subject of wide-ranging interest and speculation. Gerard Kuiper was the first scientist to detect methane in Titan's atmosphere (Kuiper, 1944). Methane is near its triple-point (91 K and 0.2 bars) at surface conditions on Titan of ~94 K and 1.47 bars (Fulchignoni et al., 2005). This observation led *Sagan and Dermott* (1982) to envision methane oceans on Titan hundreds of meters deep. *Lunine et al.* (1983) suggested that methane photolysis might instead result in an ocean dominated by ethane, of even greater depth. Other researchers, however, concluded that global methane oceans seemed unlikely (Eshleman et al., 1983).

As a result of the thick organic-rich haze that shrouds Titan, the actual landscape on the surface of the moon remained mysterious until the first spectacular results from the Cassini spacecraft. While Titan does not host a global surface ocean, Synthetic Aperture Radar (SAR) images from the Cassini Titan Radar Mapper (Elachi et al., 2004) show 100 km-scale drainage networks with branching morphologies (Fig. 1). This morphology was revealed in even greater detail and at finer scales for networks imaged by the Huygens Probe Descent Imager/Spectral Radiometer (Tomasko et al., 2005). The negative topographic relief associated with the Huygens networks (that is, they are clearly valleys) (Soderblom et al., 2007; Tomasko et al., 2005) further suggests that they were created by fluvial erosion (Langhans et al., 2012; Moore and Pappalardo, 2011; Perron et al., 2006). These networks were most likely carved by a mixture of liquid methane (Kouvaris and Flasar, 1991) and possibly ethane (Brown et al., 2008; Lunine et al., 1983) as they eroded "bedrock" composed of water ice (Griffith et al., 2003; McCord et al., 2006; Rodriguez et al., 2006), perhaps with a sedimentary veneer of organic atmospheric precipitates (Krasnopolsky, 2009; Lavvas et al., 2008; McKay et al., 2001; Yung et al., 1984). Near the poles, river valleys feed into typically RADAR-dark hydrocarbon lakes; the RADAR-darkness of the lakes most likely corresponds to lower backscatter associated with a smoother surface (Mitri et al., 2007; Stofan et al., 2007). Some lake-shaped features are distinctly brighter and are probably dry lakebeds (Hayes et al.,

2008); possible SAR-bright paleolakes have also been identified in the low-latitude Hotei Regio and Tui Regio basins (Moore and Howard, 2010).

Titan has relatively few visible impact craters, and these are unevenly distributed geographically. Depending on the crater production rate, Titan's globally averaged surface age may be between ~0.2 to ~1 billion years (Lorenz et al., 2007; Neish and Lorenz, 2012); tropical dunefields and the north polar region display a particular dearth of craters (Wood et al., 2010). SAR swaths currently cover ~40% of Titan's surface. These images show abundant fluvial networks at high northern latitudes (Fig. 2), several large networks and numerous fragmentary ones near the tropical region of Xanadu (e.g. Fig. 1) and in the southern high latitudes, and scattered networks elsewhere. If this apparently patchy and uneven fluvial dissection (Drummond et al., 2012) is truly representative of the surface, it further supports the hypothesis that Titan's surface is locally relatively young, and subject to variable amounts of modification. Cryovolcanism (Mitri et al., 2008; Sotin et al., 2005), tectonic deformation (Burr et al., 2009; Radebaugh et al., 2007), deposition of organic aerosols (Khare et al., 1978), possible migration of observed dunes (Lorenz et al., 2006), and erosional exhumation all provide plausible mechanisms for resurfacing, but determining which process has been dominant is a key question for deciphering Titan's geologic history.

The high concentration of methane in Titan's atmosphere provides some clues to the enigma of Titan's youthful surface, but also underscores an additional puzzle. Titan's total atmospheric pressure is ~1.47 bars at the surface, composed of roughly 95% nitrogen and 5% methane (Fulchignoni et al., 2005; Lindal et al., 1983; Niemann et al., 2005). This methane abundance creates the potential for methane saturation, precipitation, and fluvial modification of the surface (Perron et al., 2006; Schneider et al., 2012; Turtle et al., 2011). However, photochemical breakdown and hydrogen loss to space means that the lifetime of methane in Titan's atmosphere is in the range of 10-100 Myr (Niemann et al., 2005). Therefore, in order to maintain the observed methane pressures on Titan, there must be some source of replenishment. Over the course of geologic history, *Yung et al.* (1984) estimate that Titan may have lost a total of 8 bars of methane. This assessment was confirmed by *Niemann et al.* (2005), who find that Titan's primitive atmosphere may have been several times as massive as at present. *Mitri et al.* (2007)

determine that the observed atmospheric concentrations of methane could be supported by evaporation from lakes covering 0.2-2% of Titan's surface. Alternatively, the atmospheric concentrations of methane could provide evidence for transfer of subsurface materials to the surface and atmosphere of Titan (Lunine and Lorenz, 2009). Possible cryovolcanic features are not widespread on Titan's exterior, however (Lopes et al., 2010; Moore and Pappalardo, 2011), suggesting that some of the other processes mentioned above, such as erosional modification, are important in the rejuvenation of the surface.

The history of Titan's surface is thus critical to understanding both its interior processes and hydrocarbon cycle. While erosion of water-ice bedrock or organic sedimentary layers by methane-ethane rivers might seem inconsistent with the conditions of terrestrial erosion, theoretical and experimental results imply that the rates and dominant mechanisms of fluvial erosion may be similar. *Collins* (2005) investigates scaling relationships between Titan and Earth. He argues that mechanical erosion processes can operate on Titan at rates that are not radically different from those for the corresponding processes on Earth. *Burr et al.* (2006) and *Perron et al.* (2006) conclude that it may be slightly easier to transport sediments on Titan than on Earth or Mars, due to the greater buoyancy of sediment and the lower gravitational acceleration. *Tomasko et al.* (2005) report that grains at the Huygens landing site, which are 2-20 cm in diameter (Keller et al., 2008), are rounded, suggesting that they have been transported over a sufficient distance for rounding to occur. Solubility analyses suggest that chemical erosion of water-ice bedrock on Titan is unlikely (Lorenz and Lunine, 1996), and low surface temperatures and the lack of significant daily temperature variation would impede thermal erosion of water ice (Perron et al., 2006), leaving mechanical erosion as the most likely incision and particle shaping mechanism for water ice bedrock. As noted by *Perron et al.* (2006), some of the valley heads imaged during the Huygens descent are located on isolated topographic highs, the networks have many tributaries, and valleys appear to widen downstream, all of which are most consistent with mechanical erosion by runoff. Organic materials that have precipitated from Titan's atmosphere (Krasnopolsky, 2009; Lavvas et al., 2008; McKay et al., 2001; Yung et al., 1984) may be more soluble than water-ice bedrock in hydrocarbon liquids (Malaska et al., 2011). If significant thicknesses of organic fallout layers do mantle areas of Titan, dissolution erosion

may be locally important (Malaska et al., 2011). However, we are not aware of any extensive valley networks on Earth that have formed mostly or entirely through dissolution. Mechanical erosion therefore appears to be the simplest explanation for Titan's valley networks.

In this study, we analyze the planform geometries of Titan's drainage networks in order to quantify erosional exhumation, and thereby describe the evolution of the landscape through time. Metrics of drainage network shape—such as drainage density, the width function, and channel sinuosity—are commonly applied on Earth to understand the way network structure relates to environmental variables such as precipitation or bedrock lithology (e.g. Rodriguez-Iturbe and Rinaldo, 1997). Our measurements of purely planform geometry are unusual by terrestrial standards, however, because analyses of fluvial incision on Earth typically also rely on elevation data to measure landscape characteristics such as slope, drainage area, and valley relief. In the case of Titan the limited available topographic data currently inhibit such measurements. Even on Earth, it is challenging to assess the cumulative erosion that a landscape has experienced without independent knowledge of the initial conditions. The goal of this paper is to develop and apply a method to assess the extent of erosional development of a fluvial landscape, using only features that can be measured in plan view.

We first present a geometrical statistic for quantifying the shape of drainage networks, and demonstrate its usefulness for evaluating the extent of erosional modification of a surface. We calibrate our statistic with a simple landscape evolution model, and we validate it through comparisons with terrestrial drainage networks with constrained exhumation histories. Finally, we map fluvial networks on Titan and apply our method to those networks. Our results suggest that some of Titan's most prominent drainage networks have caused spatially averaged erosion of only a small fraction ($< \sim 10\%$) of the initial topographic relief in the regions where they have formed.

2. A statistic relating drainage network geometries to erosional exhumation

2.1 Evolution of drainage networks

With few impact craters and little ground-based or historical data available, Titan's drainage networks provide one of the best sources of information about past erosion and resurfacing patterns. Over time, we expect the geometry of these networks to evolve. Topographic data that resolve the cross-sectional and longitudinal forms of fluvial valleys on Titan are currently limited. In the absence of widespread topographic data, as discussed above, we must focus our analysis on the planform geometry of drainage networks. Our conceptual model for drainage network development is similar to that outlined by *Horton* (1945). The basic stages in this model are shown schematically in Fig. 3, starting with initial perturbations in a random surface (Fig. 3a). These initial perturbations develop into channels that compete for water and therefore drainage area. Because the erosion rate in channels is proportional to flow discharge (see section 3), incipient channels that have smaller drainage areas and therefore smaller discharge than their neighbors will grow less rapidly than their faster-eroding neighbors. The more rapidly eroding networks will gradually integrate more drainage area and develop simple tributary channels (Fig. 3b). At first, the channel networks will expand mainly through headward growth of the trunk channel, but once they reach the drainage divide, tributaries will grow laterally and capture additional drainage area. As the surviving networks approach a steady form, they develop dendritic drainage networks with evenly spaced trunk channels and less-elongated drainage basins (Fig. 3c).

By devising a method to quantify these trends, we can use planform drainage network morphology to gauge the extent of erosional modification. Although this assessment sounds like a simple task, it has not yet been completed for Earth—in part because elevation data and various lines of geological evidence can often be used to constrain the development of terrestrial networks.

As the geometric sequence described above proceeds, the drainage networks incise through the initial relief (the initial range of elevations in a landscape over a given horizontal area), gradually overprinting the initial topography (Fig. 3d-f). We can define the relative "age" of a fluvial landscape as the extent to which it has modified an initial surface. All else being equal, this sequence will proceed more slowly at larger spatial scales with higher relief. By normalizing the total vertical erosion E

(spatially averaged over the landscape) by the initial relief H_0, we obtain a dimensionless measure of the relative erosional "age" of the landscape. Because landscapes can develop at different rates, the morphologic age does not correspond to an absolute calendar age. Henceforth, we will use the qualitative terms "immature" and "mature" to refer to networks that are in the early stages of fluvial dissection (small E/H_0) and networks that have caused extensive erosion of an initial surface (E/H_0 approaching unity, or exceeding unity if uplift or base level lowering generate additional relief), respectively.

2.2 The cumulative width function

Given these general expectations for how a drainage network should evolve over time, especially the development of dendritic tributaries and the trend towards more equant and integrated basins, we can define a morphologic statistic to quantify the relative maturity of a network. *Rodriguez-Iturbe and Rinaldo* (1997) define the width function as the number of links in a drainage network at a given distance from the drainage basin outlet. The cumulative width function, as demonstrated in Fig. 3g-i, is the integral of the width function: the fraction of the network that lies within a given flow distance from the outlet.

We predict that the cumulative width functions of less mature drainages (such as Fig. 3a) will reflect a uniform distribution of channel segments, because the drainage will not have developed an equant shape with dendritic tributaries. Basins like those in Fig. 3b-c, which are further along in their development, will have sigmoidal or concave cumulative width functions. In order to compare the cumulative width functions of various networks, we calculate the absolute value of the area between each network's cumulative width function and the straight line that represents a uniform width function (Fig. 3g-i), and we define this dimensionless quantity as ΔW. This statistic, which measures the deviation of the measured width function from a uniform width function, is conceptually similar to the Cramér-von Mises criterion, which measures the difference between a theoretical cumulative distribution function and a measured distribution. The ΔW statistic is distinct, however, from the Kolmogorov-Smirnov statistic, which only considers the maximum difference between a measured cumulative distribution and a theoretical one.

In summary, ΔW is a measure of how much the distribution of segments within a fluvial network deviates from a uniform distribution. In order to test our hypothesis that ΔW should increase as drainage networks dissect a surface, and to quantify any such relationship between ΔW and cumulative erosion, we turn to a numerical model of landscape evolution.

3. Landscape evolution model

Numerical modeling provides a clear theoretical framework for both testing and calibrating our predictions for how the ΔW statistic should behave as drainage networks evolve. We identify several processes that are likely to be most important in shaping fluvial landscapes on Titan and include them in our evolution model.

Drainage basins on Titan, like those on Earth, have developed through a combination of fluvial incision, which creates networks of incised channels, and hillslope processes that govern the response of the surrounding topography to channel incision. The limited stereo topography currently available for Titan confirms that many of the networks visible in SAR are incised valleys with steep valley walls, and therefore bedrock erosion must have occurred during their formation (Soderblom et al., 2007; Tomasko et al., 2005). Images from the Huygens probe (Tomasko et al., 2005) show branched networks dissecting the landscape down to a certain scale, but with channels that appear to truncate at a scale coarser than the image resolution. This observation implies that at the finest scales, non-fluvial erosion mechanisms are more important than fluvial incision. However, because we are interested in the shapes of networks which span 20 to 500 kilometers, the relative contribution of hillslope processes to network geometry is likely to be small. Cross sections through valleys near the Huygens landing site show nearly straight hillslope profiles with slopes of roughly 30 degrees (Tomasko et al., 2005), suggesting that hillslope erosion may be modeled with a critical angle, where any hillslopes that steepen beyond this angle experience rapid mass wasting.

We therefore employed a simple model that includes only bedrock river incision and mass wasting. The mass wasting is driven by a slope threshold. When valley side slopes exceed a critical gradient of 0.6 (31°) we assume that failure will occur, transporting material downslope to the channel and then out of the system. We assume that the flow's transport capacity exceeds the supply of landslide-derived sediment, such that the transport of sediment does not limit the rate of channel incision. Channel incision into bedrock is modeled with a stream power equation (Seidl and Dietrich, 1992; Whipple and Tucker, 1999),

$$\left.\frac{\partial z}{\partial t}\right|_{\text{channel}} = -KA^{m}|\nabla z| \qquad (1)$$

which is derived from the assumption that the rate of incision is linearly proportional to the rate of energy expenditure by the flow per unit area of the channel bed, also called the "unit stream power." In Equation (1), z is elevation, t is time, A is drainage area, m is a constant, and $|\nabla z|$ is the channel slope. We assume that there is no change in surface elevation due to uplift or subsidence. K is the stream incision coefficient, which represents the effects of bedrock erodibility, precipitation rates, drainage basin hydrology, and hydraulic geometry on fluvial incision rates. We assume that K is spatially uniform, and therefore that bedrock erodibility, precipitation, and other components of K are also uniform. The coefficient m, which typically has a value of approximately 0.5 (Howard and Kerby, 1983; Whipple and Tucker, 1999), incorporates the relationships between erosion and stream power, channel geometry and discharge, and basin geometry and discharge (Howard, 1994; Whipple and Tucker, 1999). It influences the concavity of the channel longitudinal profile and the relative balance between drainage area and channel slope in shaping the overall geometry of the network. Both theoretical arguments (Howard, 1994; Tucker and Bras, 1998; Willgoose et al., 1991) and empirical observations (e.g. Rosenbloom and Anderson, 1994) support the utility of Equation 1 as a simplified general model for bedrock river incision, and it has been used previously in many models of landscape evolution (e.g. Howard, 1994; Pelletier, 2004; Perron et al., 2008; Perron et al., 2009).

We modeled the evolution of the landscape by solving Equation 1 forward in time on a regular grid using a finite difference method. We began with random, self-affine initial surfaces defined by the variance in elevation and the slope of the surface's power spectrum. We assume there are no structures that would introduce strongly oriented initial topography. The lowest 10% of elevations in the initial surface were set to a fixed elevation of zero to simulate a base level, as might be provided for high-latitude networks by Titan's polar lakes. Initial relief for our model landscapes was approximately 400 meters. The average relief of equatorial mountains reported by *Radebaugh et al.* (2007) was ~400 m over horizontal profiles tens of kilometers long. The grid size is 400 by 400 points, with $\Delta x = \Delta y = 125$ m. We selected K=0.005 yr^{-1} with m=0.5, and ran the model for 25 Myr. Because the magnitude of K is not known for Titan, these model results are not tuned to be specifically applicable to the rate of erosion on Titan. Rather, they form a test set for our general predictions of landscape evolution and the ΔW statistic. There is a tradeoff between initial relief, K, horizontal scale, and the time interval over which the landscape erodes. We are primarily interested in how drainage network form changes as a function of how much of the initial relief has eroded. Because this evolution is independent of the absolute rate of erosion, our results are valid without reference to the value of K or elapsed time.

Our model runs employed a drainage area exponent of m=0.5 and a slope exponent of one, which implies that erosion rate is linearly proportional to stream power (Whipple and Tucker, 1999). Varying these exponents will shift the concavity and response time of the drainage profiles (Whipple and Tucker, 1999), but exploratory model runs not presented here indicate that this has only a minor effect on ΔW. The 50 km by 50 km scale of the model runs is similar to that of most of the networks we analyzed on Titan, though some of the networks are several times larger. In Fig. 4, the imprint of initial topography is clearly visible even after 25 Myr of landscape evolution. The self-affine random surface that we use to initiate the models is qualitatively consistent with available data from Titan, which generally show gentle slopes over long baselines (Zebker et al., 2009), though higher resolution data from the Huygens landing site contain valley side slopes up to 30 degrees over short distances (Tomasko et al., 2005).

Fig. 3d-f shows three stages in a typical run of the landscape evolution model. To investigate our hypothesized relationship between fluvial network morphology and the extent of erosion, we require a criterion for defining fluvial networks in our model topography that is comparable to the visibility of fluvial networks in coarsely resolved Cassini SAR images. As we discuss in section 5, deeper valleys should be much easier to detect in SAR imagery of Titan, and very shallow valleys may be invisible. Therefore, in our model runs, we calculated the ΔW only for those portions of the network that have incised a depth greater than 20% of the initial relief of the landscape. 10-25% thresholds all yield similar trends, but lower thresholds correspond with lower confidence in our upper limits on erosion. We discuss this sensitivity in greater depth in section 6.2. In order to avoid fragmented networks, we included all portions of a network downstream from a segment that has eroded to this depth. This approach is comparable to our procedure for mapping discontinuous but clearly related fluvial features.

Four timesteps from a 25 Myr model run are shown in Fig. 4a-d. In Fig. 4e-h, we isolate a single network and show the portion that we analyzed after applying the "visibility" criterion described above. These frames show how, for the most deeply eroded fluvial features, the evolution of the network generally matches our predictions as shown in Fig. 3. Because stream incision rate is proportional to drainage area, A, in Equation 1, there is a positive feedback between stream incision and drainage area. The more drainage area a given network claims, the faster it incises, which allows it to lengthen or widen, thereby capturing more drainage area. Incision rate is also proportional to land-surface slope, so networks grow more quickly in the upslope direction. As networks begin to form on an initially undissected surface, they will first grow headward, because headward growth is unimpeded by competition with neighboring networks. This growth leads them to become elongated, as in Fig. 4a, b, e, and f. Once networks begin to impinge on one another on opposite sides of a drainage divide, however, they widen and become more equant, as in Fig. 4c, d, g and h.

These trends are reflected in ΔW, as shown in Fig. 4i-l. On the x-axis, instead of time, we express the progressive development of the drainages in terms of E/H_0, the normalized measure of average erosion defined in section 2.1. Very early in the development of the networks, the ΔW is low. It rises

quickly to a nearly steady value that varies from network to network. The precise final configuration of each drainage network depends on initial conditions (Perron and Fagherazzi, 2012); the overall shape of the basin will control the shape of the cumulative width function (of which Fig. 4i-l shows examples), and will therefore also influence the ultimate value of ΔW achieved by each network. In order to better estimate the distribution of possible outcomes, we employed a Monte Carlo procedure in which we performed twenty model runs with twenty different initial surfaces that shared similar statistical characteristics. The largest networks (drainage area > 10 % of the total grid) in these runs were used to construct a calibration dataset for ΔW as a function of E/H_0. We binned these data according to E/H_0. The resulting distributions of ΔW for various values of E/H_0 are plotted in Fig. 5, with the mean trend with increasing E/H_0 shown in Fig 6. Because the distributions for low and high ΔW statistics are associated with different E/H_0, we can use our results to calculate the statistical likelihood of a given erosional exhumation for drainage networks on Titan or Earth.

4. Validation with terrestrial drainage networks

4.1 Glaciated and unglaciated landscapes

To complement the theoretical predictions of landscape evolution provided by numerical modeling, we sought observational validation of our hypotheses. We measured the ΔW for drainage networks in several landscapes in North America. These terrestrial locations are summarized in Table 1. We selected four sites in North America with one of two histories: a long history of fluvial erosion, or a short history of fluvial erosion following resurfacing by glacial processes. The first two sites, in the Allegheny Plateau of Pennsylvania and the Oregon Coast Range, have not been glaciated in Pleistocene time. The other two sites, on the southern edge of Lake Superior in Michigan and near Hudson Bay in northern Québec, were glaciated during the Last Glacial Maximum (Braun et al., 2004; Kobor and Roering, 2004). Because continental ice sheets caused extensive erosion of the landscapes that we categorize as recently glaciated, the onset of Northern Hemisphere deglaciation around 19-20 ka (Clark et al., 2009) serves as the effective surface age for the Michigan and Hudson Bay sites.

We also selected four sites that straddle the line marking the maximum extent of the Wisconsonian glaciation. These sites—in Washington's Puget Sound and northwestern Pennsylvania—provide a range of surface ages while holding erodibility and climate generally constant.

As shown in Table 1, these eight sites all had relatively similar mean ΔW statistics, compared to the broader range observed for individual terrestrial drainage networks and during model simulations. In part, this difference between the terrestrial and model data may be explained by the absence of an incision threshold for the terrestrial data. Because initial relief is not known, we calculated the ΔW for all parts of a network, not only for those parts that had incised more than 20% of the initial relief. The eight terrestrial sites do, however, show a systematic pattern wherein recently glaciated landscapes are biased to lower ΔW statistics and older landscapes are biased to higher ΔW statistics (Fig. 7). This pattern is consistent with the general prediction that drainage networks that have eroded a larger fraction of the initial topographic relief will have a larger fraction of the network concentrated at intermediate distances from the basin outlet (Figs. 3 and 4).

4.2 Drainage networks on Kaua'i

In addition to this qualitative confirmation of the hypothesized relationship between ΔW and E/H_0, we sought to make a quantitative comparison of terrestrial fluvial networks with the landscape evolution model predictions. The western coast of the Hawaiian island of Kaua'i, above the Mana Plain, provides a unique opportunity to measure the ΔW statistic for a landscape with known amount of cumulative erosion. This portion of the island is relatively homogeneous, with a classic shield volcano structure that has been partially eroded by drainage networks (Macdonald et al., 1960). We identified remnants of the original shield surface surrounding each basin and fit these remnants with spline functions in order to reconstruct the initial surface. We then estimated the volume of material that has been removed through erosion, allowing us to calculate E/H_0 for each basin. We calculated ΔW for 20 adjacent drainage networks (Haeleele, Hanakapiai, Hanakoa, Hikimoe, Hoea, Honopu, Hukipo, Kaawaloa, Kaaweiki, Kahelunui, Kahoaloha, Kalalau, Kapilimao, Kauhao, Kaulaula, Kuapaa, Makaha,

Milolii, Nahomalu, Niu, Ohaiula, Paua, Wailao, and Waipao), and obtained a relatively low $\Delta W=0.061\pm0.012$.

In order to compare these measured combinations of E/H_0 and ΔW with data from our model, we performed a Monte Carlo calculation (Fig. 8). In each iteration, we randomly selected twenty networks from the numerical model results (the same as the number of measured Kaua'i networks) for each of eight logarithmically spaced values of E/H_0, and calculated the mean ΔW for each group of twenty model networks. This simulation was performed 100 times. If the mean of the simulated population was separated by at least two standard errors from the mean of the Kaua'i population, then we counted this instance as a statistical difference in the mean. The number of times (out of 100 simulations) that the mean ΔW for the model was two standard errors higher or lower than the mean ΔW for Kaua'i gives an estimate of the likelihood that the Kaua'i drainage basins have eroded less or more, respectively, than each value of E/H_0.

Fig. 8 plots these Monte Carlo percentiles for Kaua'i, along with the E/H_0 value we actually observe there. Based on an approximate initial relief of ~1000 meters in this area of Kaua'i, the Monte Carlo calculation suggests a very high likelihood (95^{th} percentile) that the landscape has experienced more than 4 meters of spatially averaged erosion, and a moderate likelihood (50^{th} percentile) of less than 160 meters. Our best estimate for the actual spatially averaged erosion, based on current topography and the spline-fit initial surface, is ~80 meters. The good agreement between the observed erosion and the constraints based on ΔW suggests that the ΔW value of a drainage network is a robust indicator of the approximate amount of cumulative fluvial erosion in a landscape.

5. Application to fluvial networks on Titan

Analysis of terrestrial and model networks indicates the usefulness of ΔW as a proxy for the cumulative erosion experienced by a landscape. In this section, we discuss the application of this statistic to Titan.

5.1 Mapping and analysis

We produced detailed maps of Titan's fluvial networks using SAR images from the Cassini spacecraft (see Fig. 2 for an example from Titan's North Polar region). SAR images are radar backscatter images. Backscatter intensity is influenced by surface orientation relative to radar incidence and azimuth angles of observation, roughness, dielectric constant, and density of the targeted surface. The resolution of SAR swaths is 350-720 m/pixel at the center of the swaths, and decreases by a factor of ~3 at the two ends. Each SAR swath ranges from 120-450 km wide, and images roughly 1.1% of Titan's surface (Elachi et al., 2004; Elachi et al., 2005). To date, approximately 40% of Titan's surface has SAR coverage.

We mapped all fluvial networks visible in swaths Ta through T71 (Drummond et al., 2011, 2012). We identified networks on the basis of five criteria: light-dark pairings, branching patterns, cross-cutting of other radar features (such as dunes or mountains), connectivity, and orientation with respect to suspected topographic sinks (such as lakes). Light-dark pairings are created by differing illumination conditions on either side of a valley: the slope that is facing the spacecraft is illuminated by the radar and appears bright, whereas the other slope will appear dark. The networks we mapped ranged from first-order networks, which essentially consist of only one visible link, up to fourth-order networks with dozens of tributaries. These orders are apparent orders that describe the features that we have mapped, but because many fine scale features are probably invisible in the SAR imagery, the actual orders of the drainage networks may be much higher. *Drummond et al.* (2011, 2012) provide a more detailed description of the global mapping efforts.

For this paper, we focused on networks from swaths T13, T43, T28, T29, and T39, which include some of the most extensive and most completely imaged networks found on Titan so far. T13 and T43 are equatorial swaths near Xanadu (Fig. 1), T28 and T29 cover the lakes around the north pole (Fig. 2), and T39 is near the south pole. We also designated a probable sink for each large network—a point through which we expect flow from the rest of the network to drain. We identified these sinks based on flow

directions inferred from junction angles and apparent trends in valley width. Starting from the sink in each network, we worked upstream to assign a flow direction to each pixel along the flow path, according to an eight-direction routing scheme.

We calculated ΔW for 52 fluvial networks. These networks were located in four general regions, as shown in Fig. 9 and in the supplementary materials, and we performed our analyses separately for each population. The mean ΔW statistics for each region are weighted according to the lengths of the individual networks; larger networks are therefore weighted more strongly. The results are summarized in Table 1. Below we compare these results with ΔW statistics from numerically simulated landscapes in order to estimate the magnitude of fluvial erosion on Titan.

5.2 Estimating erosion on Titan

In order to place constraints on the amount of erosion that has occurred on Titan, we performed a series of Monte Carlo calculations to compare the distributions of ΔW derived from the landscape evolution model (Fig. 5) against the distributions of ΔW measured for Titan. These Monte Carlo calculations followed the same procedure we applied to terrestrial networks on Kaua'i, as described in section 4.2, except that the number of randomly selected networks in each Monte Carlo iteration was chosen to match the number of mapped networks in each Titan region. Table 1 lists the number of networks we analyzed within each study area on Titan.

Fig. 9 shows percentiles for the upper and lower bounds on E/H_0 for each region, overlain on a map of Titan. Based on our Monte Carlo simulations, we estimate lower limits on erosion on Titan of 0.4% to 0.6% of initial relief in all our study regions. These numbers correspond to the regionally averaged erosion; erosion in fluvial valleys is much larger. As an analogy, for our landscape evolution model runs, $E/H_0 = 0.4\%$ corresponds to erosion within the valleys of ~25-30% of the initial relief, or ~100-120 meters.

For two of our study areas on Titan, the measured ΔW was statistically indistinguishable from the upper values of ΔW obtained during the model runs (Fig. 9), and therefore no upper limit on erosion

could be determined. For the other two study areas, we were able to estimate upper limits on erosion, though with less confidence than for our estimates of the lower limits. Our constraints for an area of Titan's northern lakes region are most robust: we estimate an 85% probability that fluvial erosion in this region is less than 9% of the initial relief. Once again, this value is an average over the entire landscape; within the valleys, the incision may be much deeper.

6. Discussion

6.1 Implications for resurfacing and long-term erosion rates on Titan

In section 1, we reviewed several potential mechanisms for resurfacing on Titan, including cryovolcanism, tectonic deformation, deposition of organic aerosols, possible migration of observed dunes, and erosional exhumation. On the basis of the results presented in section 5.2, we can evaluate the potential effectiveness of fluvial erosion for resurfacing. The maximum relief in Titan's landscapes at low latitudes is approximately 500 to 2000 meters along SAR-based topographic profiles 5 to 20 km long (Radebaugh et al., 2007); much greater relief would trigger flow at the base of Titan's dominantly water ice crust, resulting in orogenic collapse (Perron and de Pater, 2004). *Elachi et al.* (2006) also estimate maximum relief of ~1000 m. Assuming that relief in landscapes on Titan does not generally exceed ~1000 meters, we can calculate an order-of-magnitude estimate of erosion. For NP2 drainages near Ligeia Mare the mean ΔW is 0.05±0.012 (Table 1). This relatively uniform distribution of network segments, in conjunction with numerical model results (Fig. 4 and Fig. 9) and an assumed H_0 of ~1000 m, implies an upper limit on areally averaged erosion of ~100 meters. Fluvial erosion of <9% of the initial relief (our estimate for the region of the NP2 drainages), may have produced a significant modification of the initial landscape, in particular in valleys where incision may be much deeper than 9% of the initial topography.

Impactors smaller than 1 km in diameter may fail to penetrate Titan's thick atmosphere, producing a dearth of microcraters (Artemieva and Lunine, 2003). Erosional exhumation of the magnitude that we predict might be sufficient to erase some of the small craters that are created, especially those that have also experienced viscous relaxation (Artemieva and Lunine, 2003; Parmentier

and Head, 1981). However, as is evident from the persistence of topographically prominent features (e.g. Radebaugh et al., 2007), the magnitude of fluvial erosion has been insufficient to entirely level Titan's surface.

If crater counting surface ages for Titan of 10^8-10^9 years (Lorenz et al., 2007; Neish and Lorenz, 2012; Wood et al., 2010) are accurate, we can use our constraints on maximum exhumation to estimate a long-term erosion rate. A maximum of order 100 m of erosion in 10^8 years provides an upper limit on fluvial erosion rates of $\sim 10^{-6}$ m yr^{-1} for the NP2 area of Titan's northern high latitudes. The calculated long term erosion rates are even slower if we consider an initial relief in the landscape of less than order 10^3 meters, or surface ages of more than 10^8 years. In contrast, the typical range of fluvial erosion rates on Earth's continents is $\sim 10^{-5}$ to 10^{-3} m yr^{-1} (Portenga and Bierman, 2011). In other words, in order to be consistent with our results and with the surface age predicted from crater counting, erosion rates for some areas on Titan would have to be far slower than typical terrestrial rates, despite the fact that rapid surface changes provide signs of present-day methane precipitation at low latitudes on Titan (Turtle et al., 2011).

There are several possible explanations for the apparently slow erosion rates on Titan. *Collins* (2005) has previously suggested that during bedrock incision on Titan, the lower kinetic energy of saltating grains is offset by the lower abrasion resistance of water ice at Titan surface temperatures. Assuming similar discharge rates, the erosion rates on Titan and Earth would then be comparable (Collins, 2005). However, recent experimental evidence shows that ice on Titan may in fact be much stronger than originally thought (Collins et al., 2012), with a tensile strength similar to welded tuff or quartzite, among the strongest of terrestrial continental materials (Sklar and Dietrich, 2001). As a result, river incision on Titan could be slower than on Earth, given similar discharge rates.

On the other hand, typical discharge rates and the frequency of high flow events on Titan may be very different from those on Earth. Additional data on the intensity and duration of precipitation events, and also on the long-term frequency of those events, would significantly improve our knowledge of likely runoff discharge (Perron et al., 2006). If mechanical erosion also occurs through fallout deposits of

organic aerosols from the atmosphere, then additional data on the strength of such materials would be important for understanding their erosional behavior.

A further possible explanation is that the surface age for some regions is in fact much younger than crater counting seems to suggest. Surface ages on Titan may be heterogeneous; in Fig. 2 there are both mottled, slightly darker areas and smooth, light-toned areas, each incised by drainage networks. These different surface appearances may correspond to different ages of resurfacing. If the northern polar region is younger than 10^8 years, then our estimates for erosion rates on Titan would increase proportionally.

Finally, some fluvial networks may be relics, either from an earlier period with higher atmospheric methane concentrations or from a previous topographic state that has been altered tectonically or resurfaced. Methane photolysis (Yung et al., 1984) could engender gradual decreases in methane concentration and precipitation over time, despite reports of present day precipitation (Turtle et al., 2011). Examination of SAR imagery provides some localized indications that changes in flow paths appear to have outpaced the rate at which fluvial erosion erases previous drainage patterns. Fig. 10 shows possible inconsistencies in the flow paths of fluvial features near Ligeia Mare that may reflect relict earlier drainage patterns. Junction angles are ambiguous, raising the possibility that the drainages in Fig. 10 do not terminate into the lake, which we assume is currently a local topographic minimum. The diffuse dark band in Fig. 10, which does connect to the lake, seems to crosscut the narrower branching networks.

Depending on the dominant tectonic style on Titan, our upper bounds on areally averaged erosion hint at more speculative implications for Titan's surface geology. In the case where uplift of bedrock is driven purely by isostatic response to erosional exhumation, that uplift of bedrock cannot exceed the areally averaged erosion (England and Molnar, 1990). Assuming <100 meters of areally averaged erosion in the NP2 area, we conclude that fluvial erosion alone has probably been insufficient to exhume material from deeper in Titan's crust and to expose it at the surface, at least during the formation of the current landscape. Such unroofing would require tectonic processes.

Given the apparent lack of waves on Titan's lakes (Lorenz et al., 2010; Stofan et al., 2007; Wye et al., 2009), the rarity of obvious deltas where fluvial systems drain into hydrocarbon lakes may provide additional evidence that erosion and sediment transport are relatively slow compared to changes in lake level. Over geologic timescales, sediment transport and deposition will gradually fill in topographic sinks. On the southwestern edge of Ontario Lacus, one feature has been interpreted as a delta (Wall et al., 2010). While comparisons are problematic between terrestrial river widths and the widths of valley features visible in SAR data (Burr et al., submitted),*Wall et al.* (2010) cite the small relative size of the Ontario Lacus delta as evidence for low sediment discharge. The shorelines of many of the lakes near the north pole evoke drowned drainage networks (Stofan et al., 2007), even when downstream of existing fluvial networks (e.g. Fig. 2). This observation suggests that sediment deposition during current lake levels has been insufficient to allow significant delta progradation into the standing liquid that fills the drowned lower reaches of the networks. A digital elevation model for the western edge of Kraken Mare, the largest of the northern polar lakes, does reveal a topographic bench that may have been produced by depositional processes (Aharonson et al., 2012). *Aharonson et al. (2012)* estimate that the volume of material required to form this bench translates to ~1 m of areally averaged erosion within Mayda Insula. This value is consistent with the areally averaged erosion of between 0.4 % to 9 % of initial relief that we infer in this study for the areas near to Kraken Mare (Figure 11).

The few available topographic profiles based on stereo Descent Imager/Spectral Radiometer imagery also confirm that our erosion constraints are reasonable. In the highlands north of the Huygens landing site, topographic profiles show valleys ~90 m deep incised into a landscape with ~240 m of relief (Soderblom et al., 2007; Tomasko et al., 2005). Assuming that the ratio of valley depths to areally averaged erosion is comparable to that in our model runs, this translates to an average erosion of ~1.5-2% of the initial relief, consistent with the range of erosion shown in Fig. 9 for other areas of Titan.

6.2 Effects of SAR resolution

Although SAR resolution constitutes one of the major sources of uncertainty for mapping individual branches of Titan's drainage networks, small omissions do not significantly affect the measurement because ΔW is a measure of drainage shape, not density. The Huygens Descent Imager/Spectral Radiometer revealed fluvial features much smaller than the best resolution of the orbital SAR imagery (Soderblom et al., 2007; Tomasko et al., 2005), indicating that the finest scale features on Titan's surface are not resolved in SAR data. A comparison between terrestrial SAR and topographic data (Fig. 11) also underscores the limitations of SAR-based mapping. Any highly dissected areas on Titan that resemble the fine-scale valley networks in Fig. 11c and 11d may be difficult to delineate. Fluvial features on Titan's surface may be far more extensive than can be detected on the basis of the SAR images (Burr et al., submitted). Future missions to Titan may therefore reveal landscapes that are even more diverse than those we can see currently.

It is possible that all regions of Titan imaged with SAR have unresolved fine-scale fluvial dissection similar to that at the Huygens probe landing site (Tomasko et al., 2005). To evaluate the effects of mapping uncertainty related to radar instrument resolution, we experimented on a small dataset of four model runs. We tested the sensitivity of our results to image resolution by varying the drainage area threshold that we use to define a stream link when calculating ΔW (Fig. 12a). Even for large variations in the fine structure of the network, the overall trend in ΔW remains consistent, as do ΔW values for low values of E/H_0. However, for higher values of E/H_0, the inclusion of the lowest-order branches can shift the equilibrium value of ΔW. As a result, the percentiles for the upper limits on E/H_0 also shift (Fig. 12b). We interpret this shift to mean that the true certainty with which we know the upper limits may be moderately lower than the stated percentile values. The lower limits on erosion are robust and independent of resolution.

As discussed in section 3, we apply a threshold to the model topography such that only relatively deeply eroded valleys are analyzed. This threshold is important because otherwise our analysis would include fluvial networks that extend all the way to the drainage divides, whereas on Titan we have only mapped the networks that are visible in SAR imagery. Comparison of topography and SAR images (Fig.

11) supports the use of a relief threshold for identifying the portion of the fluvial network to be analyzed. As mentioned above, Fig. 11 clearly shows that many terrestrial fluvial features that are visible in the digital elevation models are invisible in the SAR images. We hypothesize that one factor that contributes to this discrepancy is the relief across the valleys. In southwestern Pennsylvania, the deepest and most easily visible valleys are ~150-200 meters deeper than the surrounding ridges, or >50% of the total relief in the landscape (Table 1). In Michigan, many of the features that disappear in the SAR imagery have relief of ~20-50 m, or 5-15% of the relief in the landscape. This effect is the basis for our relief filter for the model data; we analyze only the portions of the networks that we think would be visible in Titan's SAR imagery.

The effects on network shape that result from changing the relief filter are very similar to the effects of changing resolution (as described in the previous paragraph), and so it is unsurprising that these two experiments produce similar results on the modeled ΔW. Changing the sensitivity of this relief filter produces modest shifts in the model calibration curve for ΔW (a reduction of 25% in the relief threshold produces a shift of ~3-4% in the mean ΔW). The sensitivity of our erosion estimates to such shifts mirrors the response to variable resolution. Our estimates for the lower limits on Titan's erosion remain robust, but the percentiles at which we ascertain the upper limits on erosion may decrease from the values shown in Fig. 8.

6.3 Tectonics, spatial variability in erosion and ΔW

The similarity in our erosion estimates for equatorial, northern high-latitude, and southern high-latitude networks on Titan is interesting given the asymmetric distribution of lakes on Titan. *Aharonson et al.* (2009) suggest that the preponderance of lakes in the northern hemisphere may result from non-linear climate responses to the eccentricity of Saturn's orbit around the sun. Over timescales of ~45 Kyr, this asymmetry should reverse (Aharonson et al., 2009). The lack of asymmetry in our data may imply that the networks have developed over times much longer than 45 Kyr, which is reasonable given the constraints on Titan's surface age (Neish and Lorenz, 2012; Wood et al., 2010). Although clouds have been observed

most frequently at high latitudes on Titan (e.g. Rannou et al., 2006), *Schaller et al.* (2009) and *Turtle et al.* (2011) report storms in Titan's tropics. The networks in swath T13 are hundreds of kilometers across and are well developed (Fig. 1), with high ΔW. The similar lower limits on E/H_0 suggest that these large drainages near Xanadu may have eroded as deeply as networks close to the poles.

Within our study regions, the most distal branches of some networks appear to originate in mottled light-and-dark "crenellated" terrains that evoke the appearance of highly dissected regions in SAR imagery for Earth (Fig. 11). This observation does not necessarily conflict with our interpretation that in some areas there has been relatively little areally averaged erosion. Our ΔW populations for Titan span vast areas. If spatially non-uniform erosion has occurred within those areas, we may be averaging the ΔW statistics of networks with disparate histories. It is also possible to generate a spatially extensive imprint of fluvial erosion while only eroding through limited relief. For example, in our numerical simulations, there is no bedrock uplift or lowering of sinks, implying that the maximum vertical erosion is simply the initial relief. Yet the model drainage networks propagate throughout the landscape well before the relief is completely eroded. Finally, our results do not exclude the possibility that some regions on Titan may have experienced extensive erosion. Indeed, for two of our four study sites, including Xanadu, where there is abundant "crenellated" terrain, the ΔW statistic does not produce a reliable upper bound on erosion. Figure 6 demonstrates that the ΔW statistic is only sensitive to the early stages of landscape evolution, when drainage networks are invading previously undissected terrain. After most of the drainage area has been captured, basin shapes no longer change appreciably although erosion continues, and ΔW ceases to provide a unique upper limit on cumulative erosion. For two regions where we do provide upper bounds on erosion, our conclusion based on measurements of ΔW is that drainage networks in these areas appear to have caused relatively little exhumation.

Some drainage networks on Titan, including drainages from swaths T13 and T28 that are included in this study, have been classified as rectangular (Burr et al., 2009; Drummond et al., 2012). This geometry may suggest that these regions have been tectonically influenced (Burr et al., 2009; Drummond et al., 2012; Radebaugh et al., 2011). However, unless this tectonic control is extensive enough to alter the

shape of the entire drainage basin, it is unlikely to strongly affect measurements of ΔW or our estimates of cumulative erosion. Sub-basins in which tributaries have preferred orientations will not necessarily impart an elongated shape to the entire basin. *Drummond et al.* (2012) tabulate the geometric classification of all fluvial networks mapped through Cassini swath T71. Around half of the networks with more than 10 links in swaths T28/T29 and T39 are rectangular; all of the networks of that size in swath T13 are rectangular (Drummond et al., 2012). Given that the highest measured ΔW is for the rectangular T13 networks (Table 1), it is difficult to account for Titan's overall low ΔW values as a result of tectonic influences. Limited erosion provides a simpler explanation.

Several approaches could provide further insight into Titan's erosion rates, surface ages, and resurfacing history. Better constraints on precipitation rates during rain events, and the distribution and frequency of rain events, would permit better estimates of long-term erosion rates. Studies of non-fluvial resurfacing mechanisms such as aerosol deposition and tectonics would clarify the geologic controls on surface topography. Improved crater counting estimates would also contribute to our understanding of the chronology of landscape change on Titan.

7. Summary and Conclusions

We develop a statistic that relates the planform geometry of a fluvial network as it erodes into bedrock to the amount of cumulative erosion. We calibrate this statistic using a simple landscape evolution model, and show that the width function of a fluvial network (the frequency distribution of links in the network with respect to flow distance from the basin outlet) becomes systematically less uniform as fluvial erosion progresses. Comparisons of recently glaciated landscapes versus landscapes with a longer history of fluvial erosion on Earth are qualitatively consistent with our theoretical prediction. Using fluvial networks on western Kaua'i, where an initial topographic surface with a known age can be reconstructed, we demonstrate that the width function can be used to probabilistically assess upper and lower bounds on the ratio of cumulative erosion to initial relief.

We apply these methods to fluvial networks mapped in four regions on Titan, and find that Titan's north polar region has undergone a minimum of 0.4-0.6% of spatially averaged erosion of an initial surface, and for a subprovince with better constraints we suggest that there has been at most 9% erosion. Titan's Xanadu region has experienced at least 0.4% erosion of its initial relief, and the southern high latitudes show evidence for at least 0.5% erosion of the initial surface. Our upper limit on cumulative erosion in Titan's north polar region implies that, if estimates of Titan's surface age based on crater counting are correct, long-term erosion rates on Titan must be many times slower than typical continental erosion rates on Earth. Alternatively, some landscapes on Titan have been resurfaced in the geologically recent past.

Acknowledgments

The authors thank Trent Hare for providing GIS data and Tom Farr for processing the terrestrial SAR images in Fig. 11. We thank Ken Ferrier, Scott Miller, and Paul Richardson for valuable discussions. Comments from two anonymous reviewers improved the manuscript. Brenda Carbone and Kerin Willis provided administrative help. This work was supported by a NASA Cassini Data Analysis Program award to DMB and JTP.

Figures

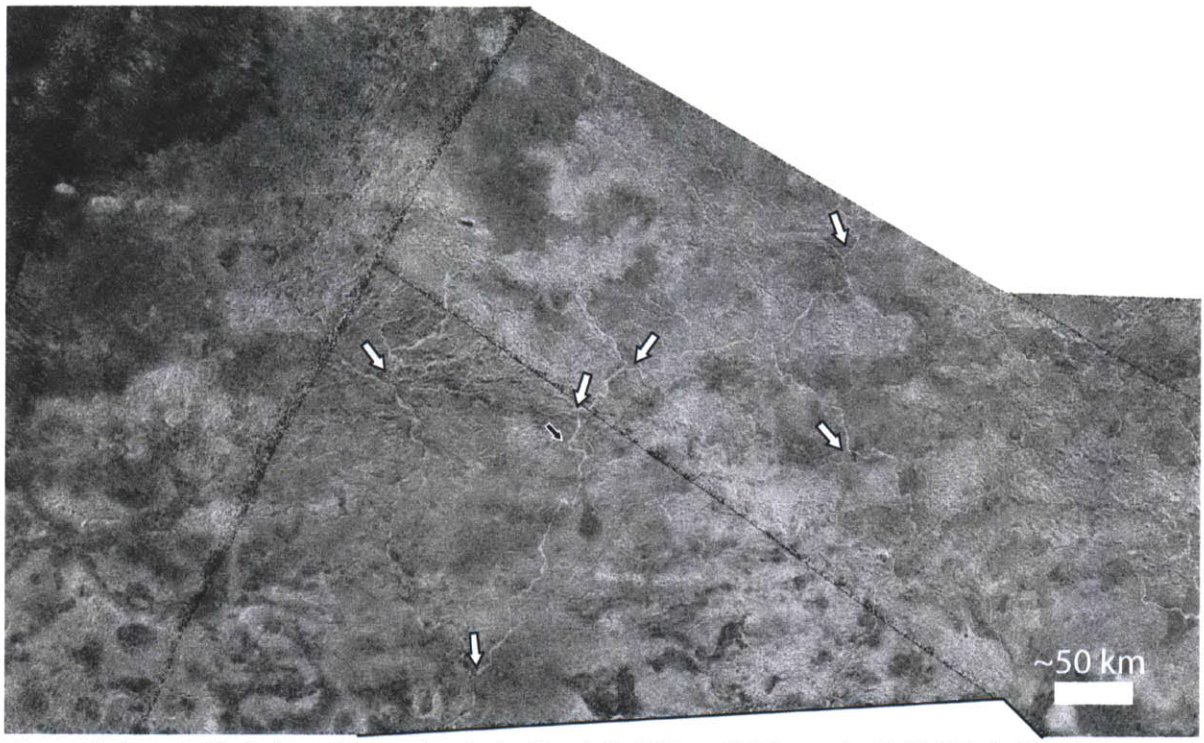

Figure 1: Low-latitude branching networks in Cassini's T13 and T43 swaths (249.5 E, 9.6 S).White arrows point to locations of visible valleys, and are oriented approximately parallel to flow direction. Black arrow points to perpendicular valley segments in a network that has been identified by Burr et al. (2009) as potentially reflecting tectonic influences.

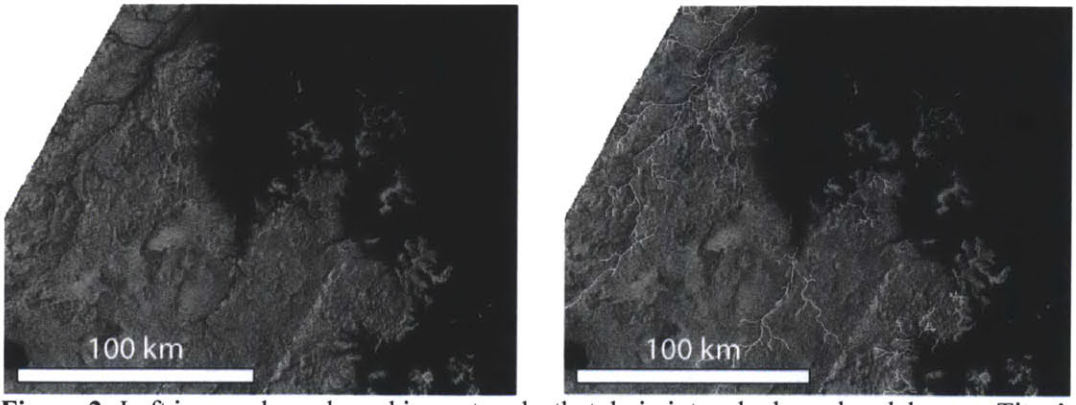

Figure 2: Left image shows branching networks that drain into a hydrocarbon lake near Titan's North Pole (Swath T28; image centered at 108.5E, 75N). Right image shows the same region after mapping fluvial networks (white lines).

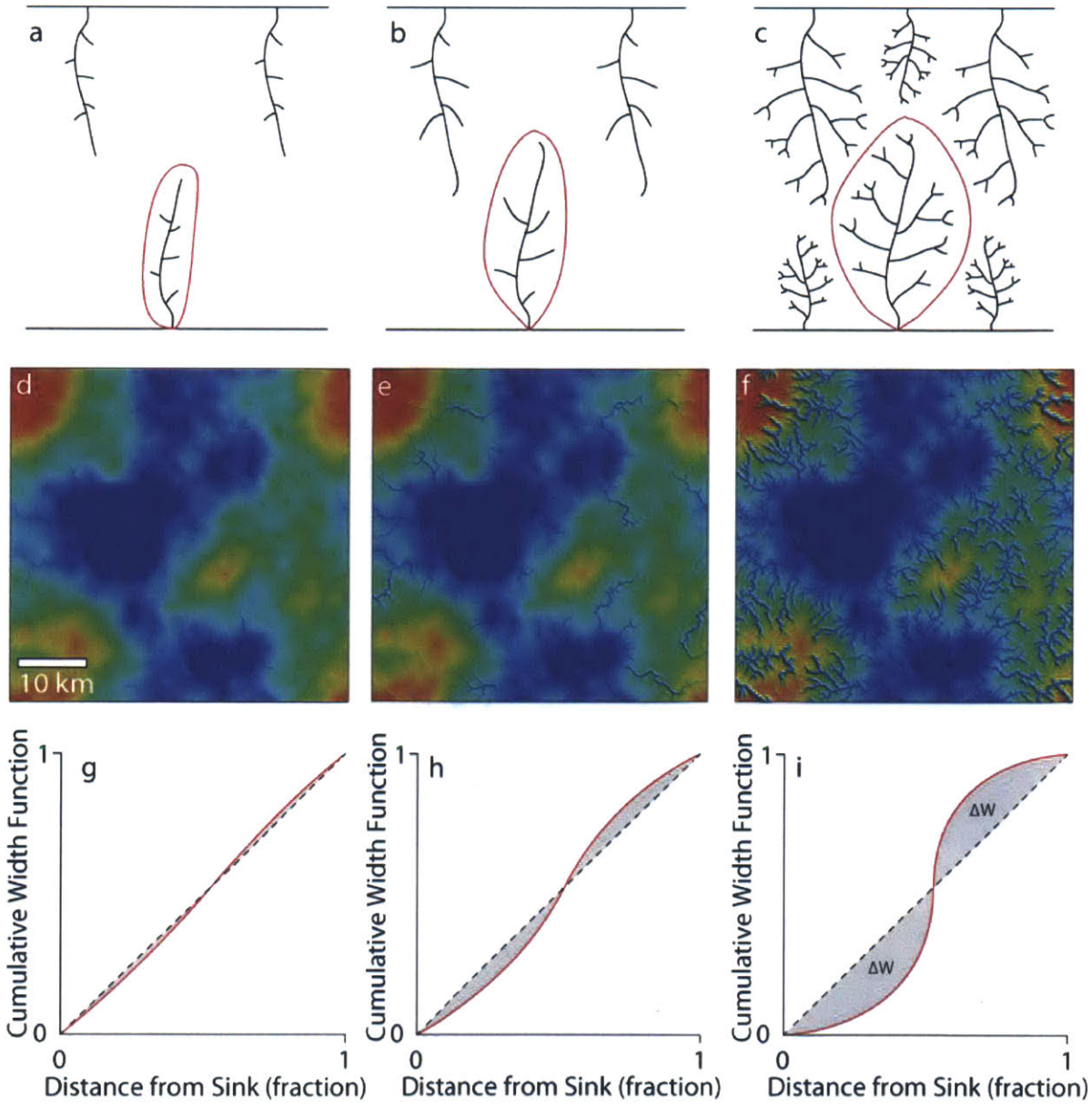

Figure 3: a-c: Schematic drawings illustrating the expected evolution of drainage networks in a landscape with sinks at the top and bottom of the frame. **(a)** Initially, headward advance dominates. Basins develop roughly uniform width. **(b)** Once upslope area is exhausted, lateral tributary growth causes widening. **(c)** Interaction among basins concentrates area at intermediate distances from outlet. **(d-f)**: Three frames from a landscape evolution model run illustrating the evolution predicted in frames a-c. Time increases by a multiple of five in each successive frame. Colors denote elevation, with blue to red showing lowest to highest elevations, respectively. Maximum initial elevations are ~400 meters, yielding average slopes of ~0.008. **(g-i):** Idealized illustration of the relationship between the cumulative width function (red line) and the ΔW statistic (shaded area) for the drainage networks shown in a-c. As shown in the figure, ΔW is proportional to the deviation of the cumulative width function from a uniform distribution of network links. Panels g-i are schematic; actual width functions may not be symmetric about their midpoints.

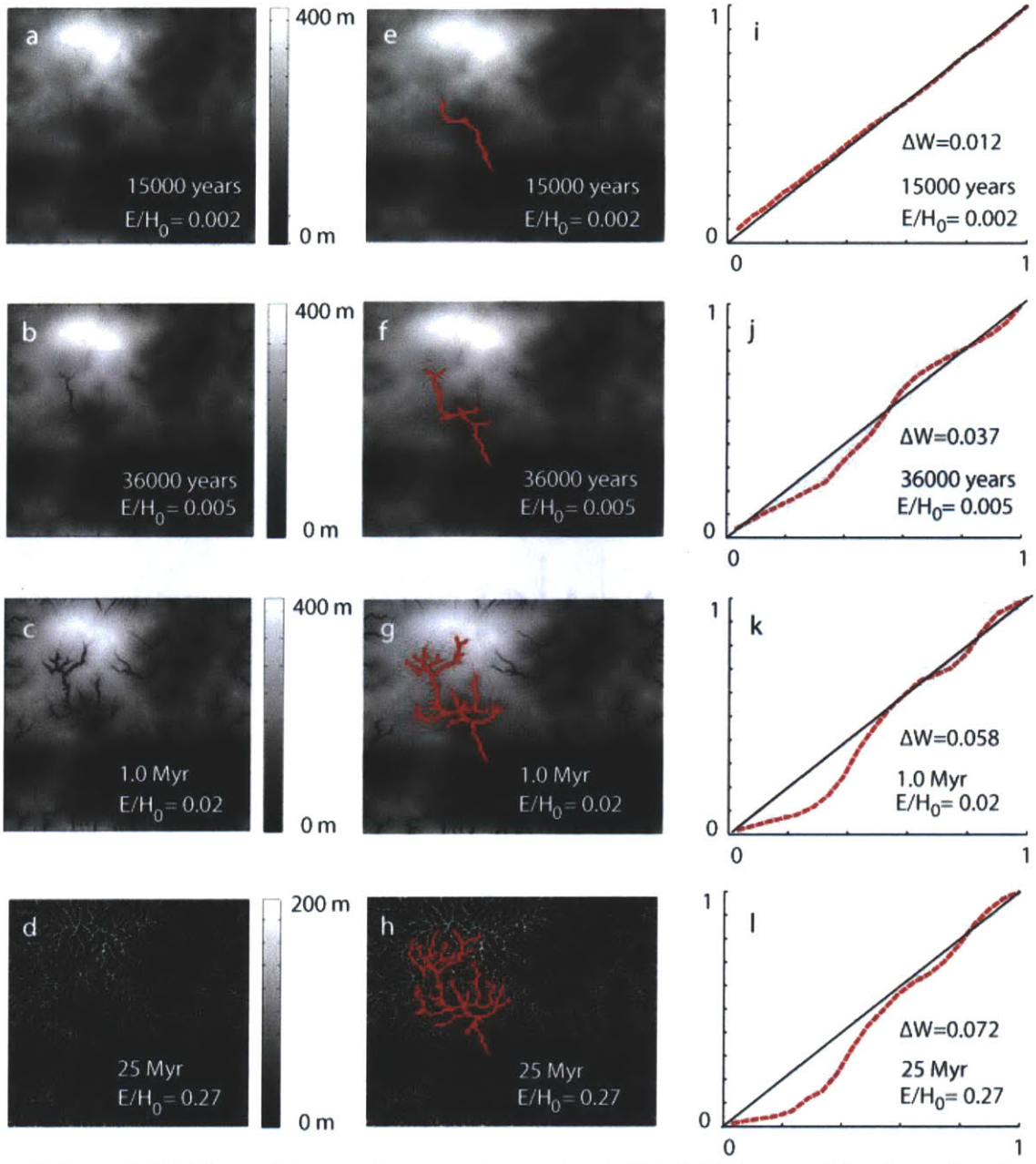

Figure 4: Example 25 Myr model run, with one drainage network highlighted in red. We only analyze the portion of the network that has eroded through >20% of the initial relief. The ΔW increases over time, eventually approaching a steady value for a given drainage network, even though the topography does not reach a steady state.

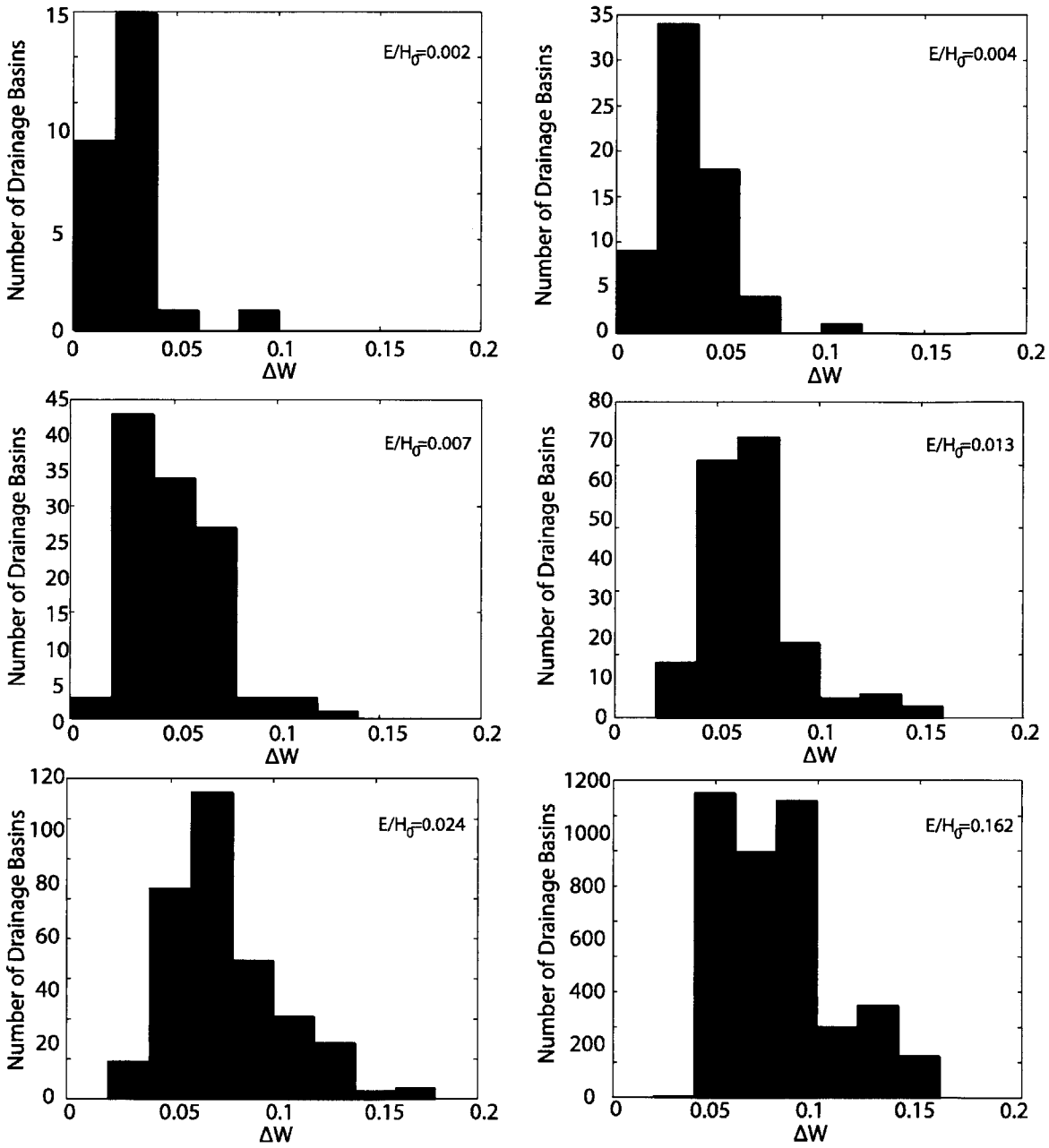

Figure 5: Six snapshots of the distribution of ΔW from an ensemble of 20 model runs. These histograms show that mean ΔW increases with increasing erosion relative to initial relief, eventually approaching a steady value of ΔW.

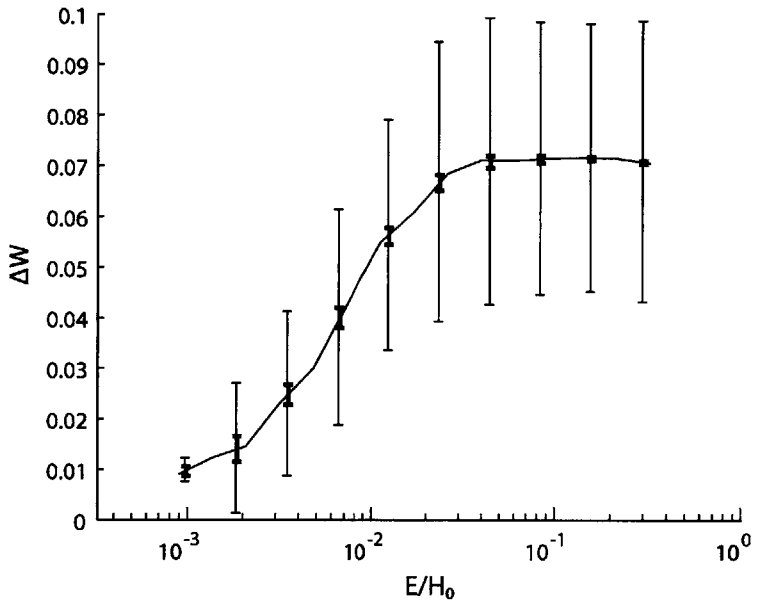

Figure 6: Compilation of binned ΔW as a function of E/H_0 for all twenty model runs. As erosion proceeds, drainages branch and become more equant, leading to higher values of ΔW. After erosion has reached approximately 10% of the initial relief, values of ΔW reach a steady-state. Large error bars represent one standard deviation; small bold error bars show one standard error.

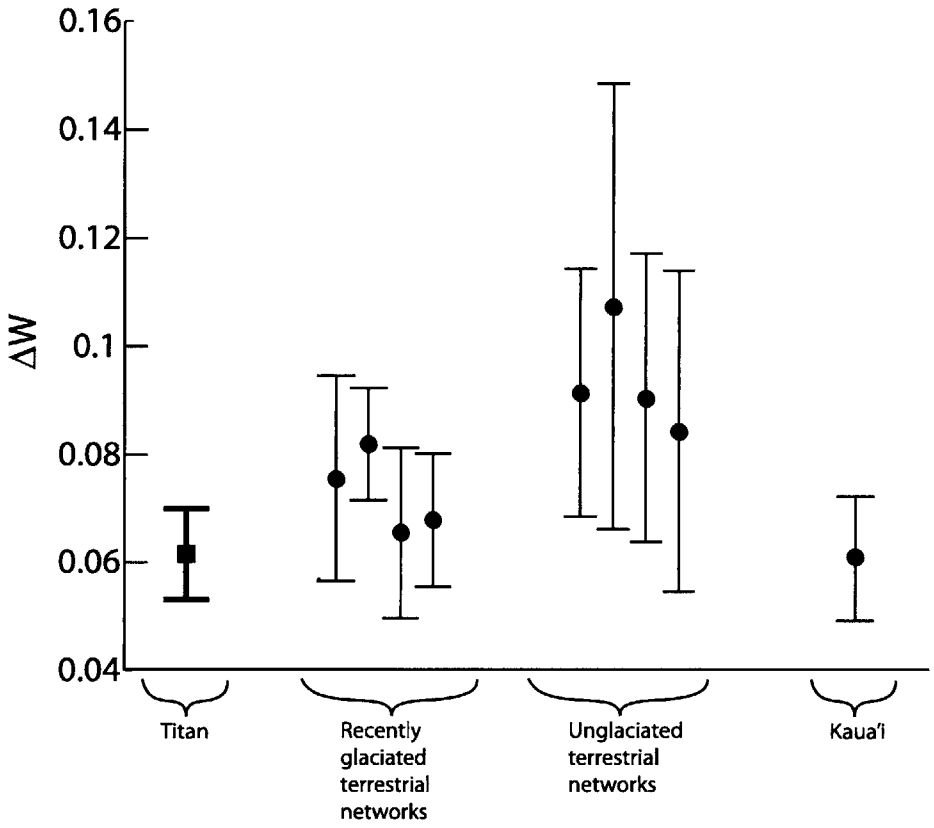

Figure 7: ΔW for regions on Titan and Earth. ΔW for Titan is averaged over all four study regions, with a total of 52 networks. Uncertainties represent two standard errors of the mean.

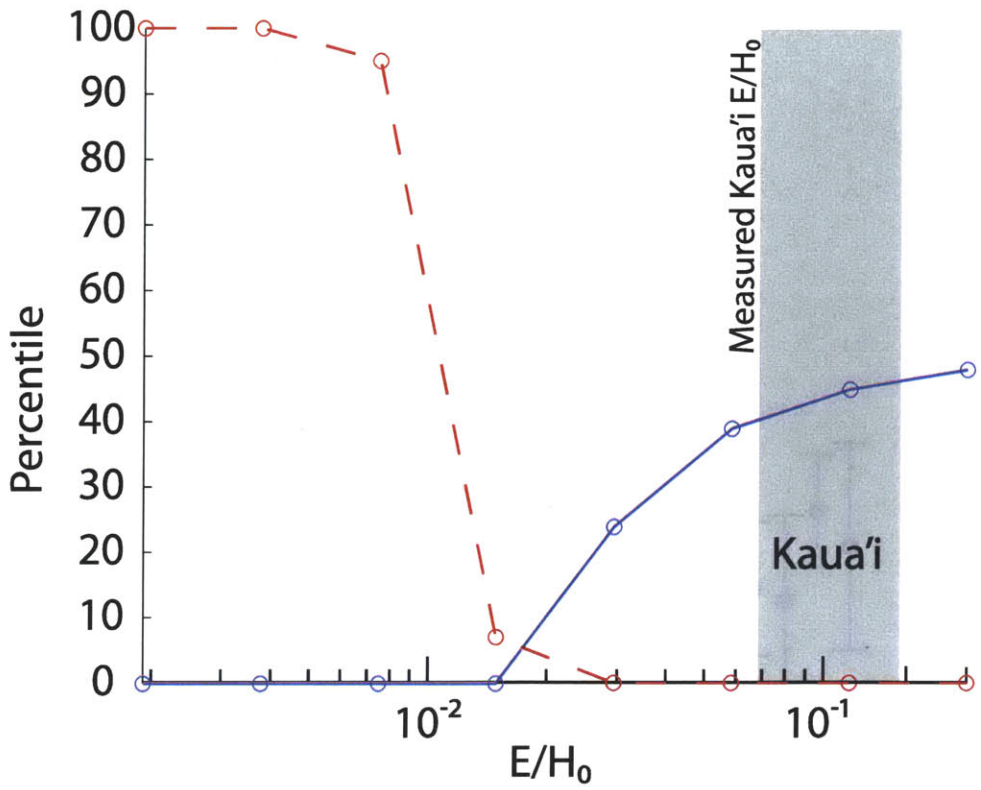

Figure 8: Monte Carlo simulations provide constraints on the likely lower (dashed red line) and upper (solid blue line) bounds on erosion relative to initial relief. For Kaua'i, the percentiles based on a measured ΔW of 0.061 ± 0.012 for twenty drainage networks are consistent with the actual E/H_0, shown by the gray bar. The width of the gray bar represents E/H_0 values within two standard errors of the mean erosion among our 20 Kaua'i basins.

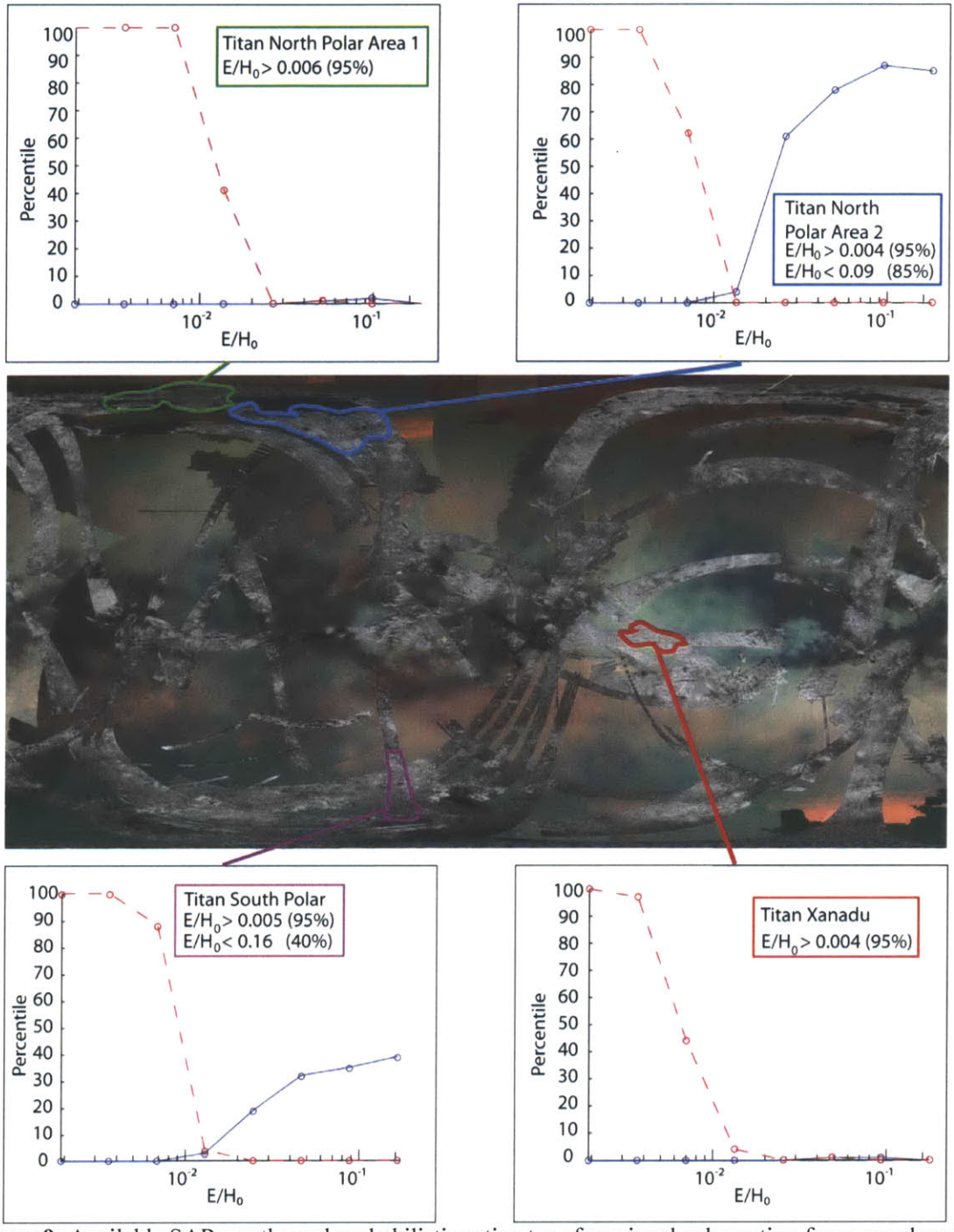

Figure 9: Available SAR swaths and probabilistic estimates of erosional exhumation for mapped regions of Titan. North Pole Area 1 is outlined in light green, North Pole Area 2 is blue, the Equatorial region is red, and T39 in the southern high latitudes is purple. Ligeia Mare, one of Titan's largest lakes, is visible next to the north polar networks. Four exterior panels show results of Monte Carlo calculations for each area. Dashed red curves show probability that E/H_0 for a particular region on Titan is greater than a given value on the x-axis, and solid blue curves show the probability that E/H_0 for Titan is less than a given value.

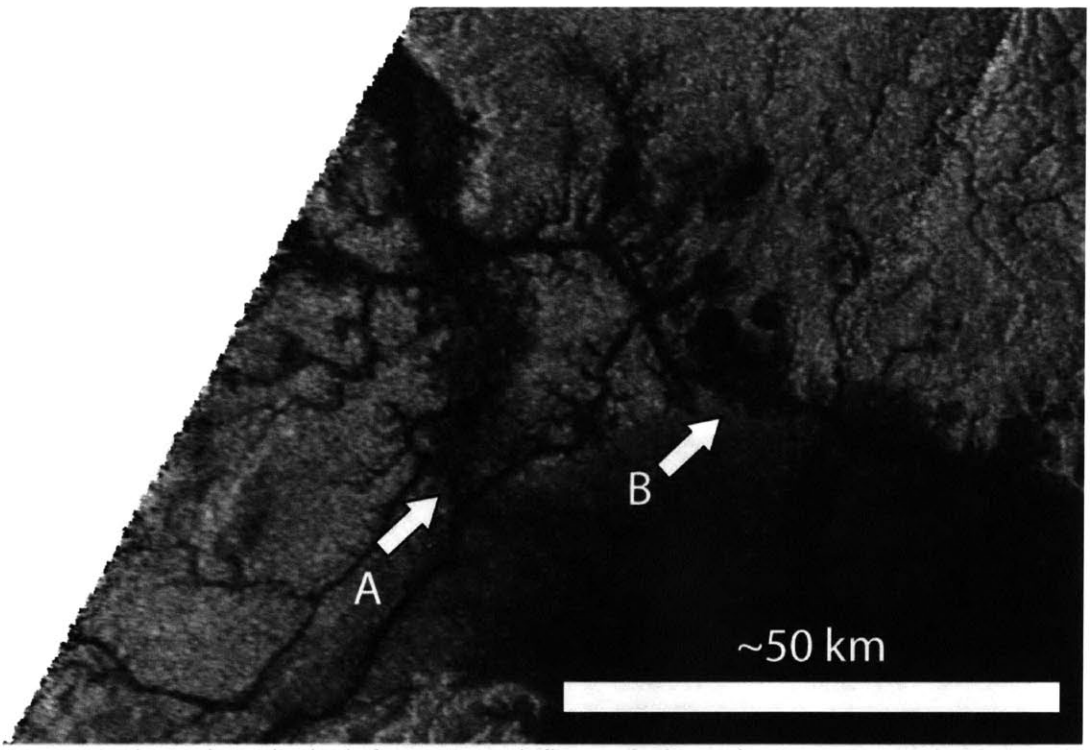

Figure 10: Apparent inconsistencies in drainage network flow paths located at 95E, 75N on the shores of Titan's Ligeia Mare (T28). **A**: Possible link between adjacent valleys via diffuse dark band could indicate stream capture. **B**: Junction angles suggest that the large network entering the image from the lower left does not drain into Ligeia Mare.

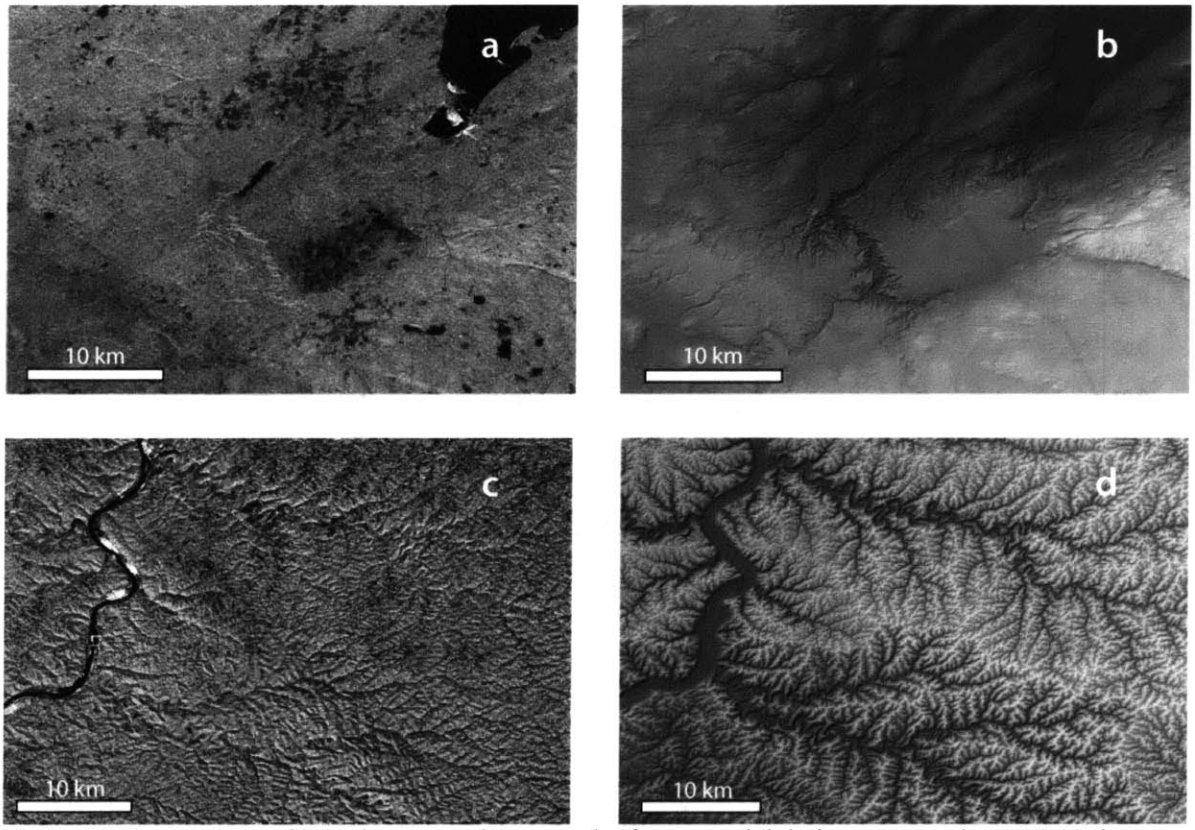

Figure 11. Comparison of SAR images and topography for terrestrial drainage networks. **(a)** SAR image and **(b)** shaded relief map of the region southwest of L'Anse Bay, Lake Superior, on Michigan's upper peninsula, centered at 46.57° N, 88.67° W. **(c)** SAR image and **(d)** shaded relief map of a section of the Allegheny Plateau east of the Ohio River in northern West Virginia and southwest Pennsylvania, centered at 39.67° N, 80.70° W. SAR images are from the C-band antenna on board the Shuttle RADAR Topography Mission *(Farr et al., 2007)*. Topography is from the USGS National Elevation Dataset. Map projections are transverse Mercator, with a pixel size of approximately 30 m.

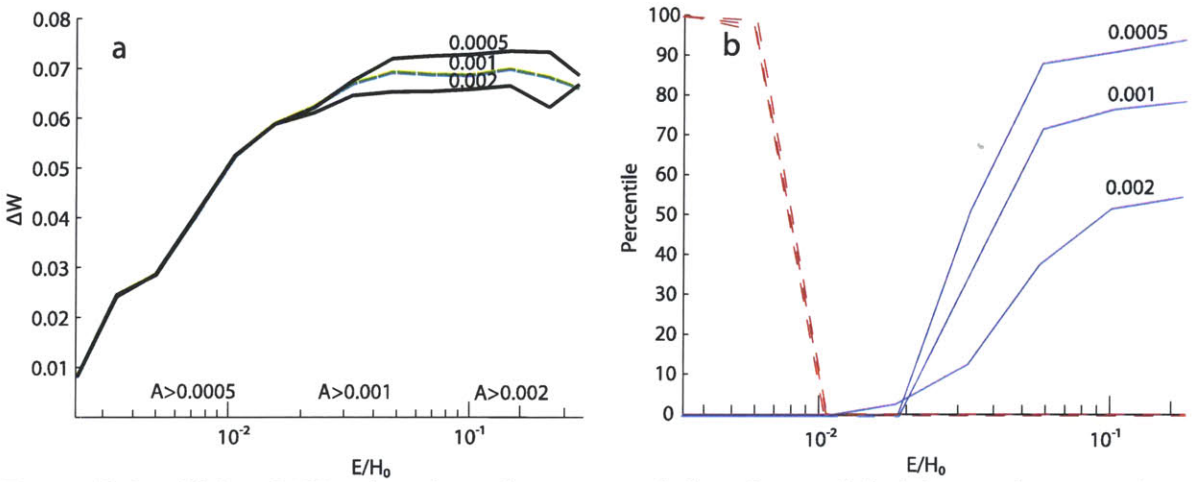

Figure 12. Sensitivity of ΔW and erosion estimates to resolution of mapped fluvial networks. **(a)** As the finest network links are excluded, the overall trend in measurements of ΔW is consistent. Curves are extracted from a set of four trial model runs. The effect on the steady value of ΔW at large cumulative erosion values is small but significant. Curves are labeled with the minimum contributing area (as a fraction of the total area of the grid) used as a threshold for delineating the drainage network. This is illustrated in the inset with an example channel network. The green dashed curve denotes the value used elsewhere in this study. **(b)**: Monte Carlo calculations for Titan's North Polar Area 2 using the synthetic data set in Panel A. Including or excluding the finest branches of the networks has a negligible effect on the predicted lower limits on exhumation. The magnitudes of the predicted upper limits on erosion are also relatively stable, but the percentiles shift, reflecting uncertainty in the specific percentiles for those estimates.

Tables

Location	Description [swaths]	Coordinates	Number of Networks	ΔW	Current Relief
Titan NP1	Titan Northern High-Latitude [T28/T29]	78.5 E, 80.1 N	19	0.07±0.016	> 300 m
Titan NP2	Titan Northern High-Latitude [T28/T29]	117.0 E, 74.0 N	21	0.05±0.012	> 300 m
Titan T13	Titan Low-Latitude [T13]	249.5 E, 9.6 S	4	0.07±0.035	~ 500 m
Titan T39	Titan Southern High-Latitude [T39]	328.0 E, 73.2 S	8	0.06±0.015	
SW Pennsylvania	Unglaciated	279.5 E, 39.5N	4	0.107±0.041	~ 300 m
NW Pennsylvania	Glaciated	280.0 E, 42.0 N	6	0.066±0.016	~ 200 m
NW Pennsylvania	South of LGM	280.5 E, 41.4 N	4	0.084±0.030	~ 200 m
Washington	Glaciated	237.9 E, 47.2 N	7	0.068±0.012	~ 600 m
Washington	South of LGM	237.6 E, 46.5 N	4	0.092±0.023	~ 1000 m
Oregon	Unglaciated	236.0 E, 43.4 N	8	0.091±0.026	~ 650 m
Michigan	Glaciated	271.4 E, 46.5 N	7	0.082±0.010	~ 350 m
Hudson Bay, Canada	Glaciated	262.5 E, 51.9N	5	0.076±0.019	~ 250 m
Western Kaua'i	Mana/Na'Pali Coast	200.3E, 22.06N	20	0.061±0.012	~1000 m

Table 1. ΔW measurements from Titan and Earth. Estimates of current relief for Titan are based on SAR topography from *Stiles et al.* (2009). "Glaciated" means that a given area was glaciated at the Last Glacial Maximum. Means for Titan are weighted by horizontal length of the networks. Uncertainties in ΔW are stated as 2 standard errors.

Supplementary Figure

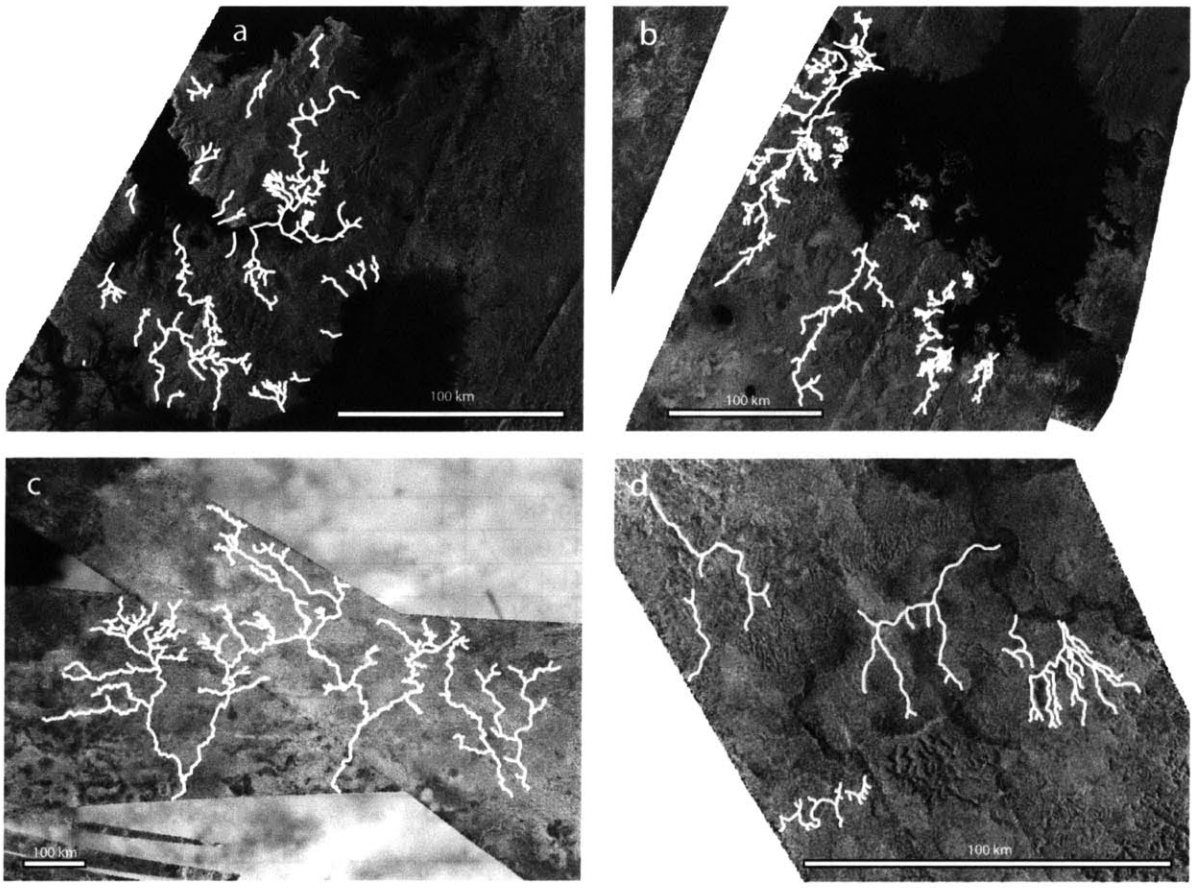

Figure S1. Maps of all networks analyzed in each area, overlain on synthetic aperture radar imagery. Center coordinates are given in Table 1. **(a)** Titan NP1, swaths T28 and T29. **(b)** Titan NP2, swaths T28 and T29. **(c)** Titan T13, near the equator. **(d)** Titan T39.

Chapter 7. Conclusions

In a controlled experiment, one can take a set of well-understood circumstances and introduce a perturbation. The effects of that perturbation yield information about how the whole system works.

The Permian-Triassic is a moment when the world as we know it was pushed to the brink. The trick is to understand the results from such a complicated experiment (which does not really qualify as controlled—it is more of an uncontrolled experiment). There are so many variables changing simultaneously that it is difficult to isolate the most important factors driving global change.

Quantitative data linking volatile release and climate change during the eruption of the Siberian Traps help to constrain the environmental effects of magmatism. While it may still be premature to formulate a comprehensive model for the relationship between the Siberian Traps and the end-Permian mass extinction, the results presented here provide a starting point for the integration of a range of scientific observations.

Paleontological evidence convincingly suggests that elevated CO_2 played a role in the marine mass extinction (Knoll et al., 2007). This CO_2 updraw may have originated directly from light carbon injection associated with Siberian Traps magmatism and the hallmark carbon isotopic excursion (Payne and Clapham, 2012a), in which case the carbon might derive from the crust or from recycled material in the mantle (Sobolev et al., 2011). Rapidly increasing CO_2 levels across the Permian Triassic boundary would also explain a drastic, coincident +20 °C shift in tropical sea surface temperatures (Sun et al., 2012).

In this thesis, I document a range of effects that would have exacerbated CO_2-driven climate change. I use melt inclusions to estimate the magmatic sulfur, chlorine, and fluorine budgets. Dominantly phreatomagmatic explosive volcanism lofted sulfur into the stratosphere, producing acid rain in the northern hemisphere and threatening terrestrial ecosystems. Metamorphic gases generated potentially

severe ozone depletion. The resulting combination of rapid changes in ultraviolet flux, environmental pH, CO_2 levels, and global temperatures may have proved fatal for Permian land plants and animals.

If sustained eruptive episodes generated prolonged sulfur release, the northern hemisphere may have experienced strong cooling. The effects on ocean circulation are unknown, but are potentially profound, and merit further investigation.

Counter-intuitively, in many ways Titan provides a better controlled experiment than the end-Permian Earth. Whereas Earth 252 million years ago was a world in flux, Titan is a portrait of Earth-like normalcy, with a number of strange twists. Our results show that for some regions of Titan, erosion has only superficially changed the surface. In the larger picture, this may imply that Titan's landscapes are either evolving slowly or have experienced recent resurfacing, which could hint at more dynamic events—ranging from possible tectonism to cryovolcanism—in Titan's past.

Titan shows us that in many ways, nature is robust. Even under very different environmental conditions, rain, erosion, and landscape evolution appear to occur just as they do on Earth. The message from the end-Permian is slightly more dire, especially given the current debate surrounding climate change: given the wrong circumstances, and a catastrophic push, the Earth is profoundly vulnerable.

Acknowledgments

My family members, who support and encourage me. My friends, who distract and advise me. My teachers, who guide me and help me learn from my mistakes. The administrative staff at MIT, who put up with me.

Most of all my wife, Carolyn, who loves me, and who always helps me to be better.

References

Aarnes, I., Fristad, K., Planke, S., and Svensen, H., 2011, The Impact of Host-Rock Composition on Devolatilization of Sedimentary Rocks During Contact Metamorphism around Mafic Sheet Intrusions: Geochemistry Geophysics Geosystems, v. 12, p. Q10019.

Aharonson, O., Hayes, A., Lopes, R., Lucas, A., Hayne, P., and Perron, J.T., 2012, Titan's Surface Geology, *in* I. Mueller-Wodarg, C.G., T. Cravens and E. Lellouch, ed., Titan: Surface, Atmosphere and Magnetosphere: Cambridge, UK., Cambridge University Press.

Aharonson, O., Hayes, A.G., Lunine, J.I., Lorenz, R.D., Allison, M.D., and Elachi, C., 2009, An Asymmetric Distribution of Lakes on Titan as a Possible Consequence of Orbital Forcing: Nature Geoscience, v. 2, p. 851-854.

Alt, J.C., Shanks, W.C., and Jackson, M.C., 1993, Cycling of Sulfur in Subduction Zones - the Geochemistry of Sulfur in the Mariana-Island Arc and Back-Arc Trough: Earth and Planetary Science Letters, v. 119, p. 477-494.

Anderson, A.T., 1974, Chlorine, Sulfur, and Water in Magmas and Oceans: Geological Society of America Bulletin, v. 85, p. 1485-1492.

Archibald, A., Lamarque, J.-F., Wild, O., Cionni, I., MacKenzie, I., Plummer, D., Skeie, R., and Strode, S., 2013, Pre-Industrial to End 21st Century Projections of Tropospheric Ozone from the Atmospheric Chemistry and Climate Model Intercomparison Project (Accmip): Atmospheric Chemistry and Physics, v. 13, p. 2063-2090.

Ariskin, A.A., Frenkel, M.Y., Barmina, G.S., and Nielsen, R.L., 1993, Comagmat - a Fortran Program to Model Magma Differentiation Processes: Computers & Geosciences, v. 19, p. 1155-1170.

Arndt, N., Chauvel, C., Czamanske, G., and Fedorenko, V., 1998, Two Mantle Sources, Two Plumbing Systems: Tholeiitic and Alkaline Magmatism of the Maymecha River Basin, Siberian Flood Volcanic Province: Contributions to Mineralogy and Petrology, v. 133, p. 297-313.

Arndt, N., Lehnert, K., and Vasilev, Y., 1995, Meimechites - Highly Magnesian Lithosphere-Contaminated Alkaline Magmas from Deep Subcontinental Mantle: Lithos, v. 34, p. 41-59.

Arndt, N.T., and Christensen, U., 1992, The Role of Lithospheric Mantle in Continental Flood Volcanism - Thermal and Geochemical Constraints: Journal of Geophysical Research-Solid Earth, v. 97, p. 10967-10981.

Artemieva, N., and Lunine, J., 2003, Cratering on Titan: Impact Melt, Ejecta, and the Fate of Surface Organics: Icarus, v. 164, p. 471-480.

Barnes, J.E., and Hofmann, D.J., 1997, Lidar Measurements of Stratospheric Aerosol over Mauna Loa Observatory: Geophysical Research Letters, v. 24, p. 1923-1926.

Becker, L., Poreda, R.J., Hunt, A.G., Bunch, T.E., and Rampino, M., 2001, Impact Event at the Permian-Triassic Boundary: Evidence from Extraterrestrial Noble Gases in Fullerenes: Science, v. 291, p. 1530-1533.

Beerling, D., Berner, R.A., Mackenzie, F.T., Harfoot, M.B., and Pyle, J.A., 2009, Methane and the Ch4 Related Greenhouse Effect over the Past 400 Million Years: American Journal of Science, v. 309, p. 97-113.

Beerling, D.J., Harfoot, M., Lomax, B., and Pyle, J.A., 2007, The Stability of the Stratospheric Ozone Layer During the End-Permian Eruption of the Siberian Traps: Philosophical Transactions of the Royal Society a-Mathematical Physical and Engineering Sciences, v. 365, p. 1843-1866.

Berner, R.A., 2002, Examination of Hypotheses for the Permo–Triassic Boundary Extinction by Carbon Cycle Modeling: Proceedings of the National Academy of Sciences, v. 99, p. 4172-4177.

Black, B., Elkins-Tanton, L., Weiss, B., Veselovskiy, R., Latyshev, A., and Pavlov, V., 2011, Emplacement Temperatures and Alteration Histories of Siberian Traps Volcaniclastic Deposits: AGU Fall Meeting Abstracts, v. 1, p. 1042.

Black, B.A., Elkins-Tanton, L.T., Rowe, M.C., and Peate, I.U., 2012, Magnitude and Consequences of Volatile Release from the Siberian Traps: Earth and Planetary Science Letters, v. 317–318, p. 363-373.
Black, B.A., Hauri, E., and Elkins-Tanton, L.T., submitted-a, Sulfur Isotopic Evidence for Sources of Siberian Traps Volatiles.
Black, B.A., Lamarque, J.-F., Shields, C., Elkins-Tanton, L.T., and Kiehl, J.T., submitted-b, Acid Rain and Ozone Depletion from Pulsed Siberian Traps Magmatism.
Blake, S., Self, S., Sharma, K., and Sephton, S., 2010, Sulfur Release from the Columbia River Basalts and Other Flood Lava Eruptions Constrained by a Model of Sulfide Saturation: Earth and Planetary Science Letters, v. 299, p. 328-338.
Bowring, S.A., Erwin, D.H., Jin, Y.G., Martin, M.W., Davidek, K., and Wang, W., 1998, U/Pb Zircon Geochronology and Tempo of the End-Permian Mass Extinction: Science, v. 280, p. 1039-1045.
Braun, D.D., Ehlers, J., and Gibbard, P.L., 2004, Quaternary Glaciations - Extent and Chronology, Part Ii, Elsevier.
Brown, R.H., Soderblom, L.A., Soderblom, J.M., Clark, R.N., Jaumann, R., Barnes, J.W., Sotin, C., Buratti, B., Baines, K.H., and Nicholson, P.D., 2008, The Identification of Liquid Ethane in Titan's Ontario Lacus: Nature, v. 454, p. 607-610.
Bryan, S.E., Peate, I.U., Peate, D.W., Self, S., Jerram, D.A., Mawby, M.R., Marsh, J.S., and Miller, J.A., 2010, The Largest Volcanic Eruptions on Earth: Earth-Science Reviews, v. 102, p. 207-229.
Buchl, A., and Gier, S., 2003, Petrogenesis and Alteration of Tuffs Associated with Continental Flood Basalts from Putorana, Northern Siberia: Geological Magazine, v. 140, p. 649-659.
Bureau, H., Keppler, H., and Metrich, N., 2000, Volcanic Degassing of Bromine and Iodine: Experimental Fluid/Melt Partitioning Data and Applications to Stratospheric Chemistry: Earth and Planetary Science Letters, v. 183, p. 51-60.
Burgisser, A., and Scaillet, B., 2007, Redox Evolution of a Degassing Magma Rising to the Surface: Nature, v. 445, p. 194-197.
Burr, D.M., Ádámkovics, M., Baker, V.R., Collins, G.C., Howard, A.D., III, R.P.I., Lamb, M.P., Moore, J.M., Perron, J.T., Sklar, L.S., Drummond, S.A., and Black, B.A., submitted, Fluvial Features on Titan.
Burr, D.M., Emery, J.P., Lorenz, R.D., Collins, G.C., and Carling, P.A., 2006, Sediment Transport by Liquid Surficial Flow: Application to Titan: Icarus, v. 181, p. 235-242.
Burr, D.M., Jacobsen, R.E., Roth, D.L., Phillips, C.B., Mitchell, K.L., and Viola, D., 2009, Fluvial Network Analysis on Titan: Evidence for Subsurface Structures and West-to-East Wind Flow, Southwestern Xanadu: Geophysical Research Letters, v. 36.
Butler, R.F., 1992, Paleomagnetism: Magnetic Domains to Geologic Terranes, Blackwell Scientific Publications Boston.
Büttner, R., Dellino, P., and Zimanowski, B., 1999, Identifying Magma–Water Interaction from the Surface Features of Ash Particles: Nature, v. 401, p. 688-690.
Caldeira, K., and Rampino, M.R., 1990, Carbon-Dioxide Emissions from Deccan Volcanism and a K/T Boundary Greenhouse-Effect: Geophysical Research Letters, v. 17, p. 1299-1302.
Campbell, I.H., Czamanske, G.K., Fedorenko, V.A., Hill, R.I., and Stepanov, V., 1992, Synchronism of the Siberian Traps and the Permian-Triassic Boundary: Science, v. 258, p. 1760-1763.
Campbell, I.H., and Griffiths, R.W., 1990, Implications of Mantle Plume Structure for the Evolution of Flood Basalts: Earth and Planetary Science Letters, v. 99, p. 79-93.
Cao, C.Q., Love, G.D., Hays, L.E., Wang, W., Shen, S.Z., and Summons, R.E., 2009, Biogeochemical Evidence for Euxinic Oceans and Ecological Disturbance Presaging the End-Permian Mass Extinction Event: Earth and Planetary Science Letters, v. 281, p. 188-201.
Carroll, M.K., and Rutherford, M.J., 1988, Sulfur Speciation in Hydrous Experimental Glasses of Varying Oxidation State--Results from Measured Wavelength Shifts of Sulfur X-Rays: American Mineralogist, v. 73, p. 845-9.

Carroll, M.R., and Webster, J.D., 1994, Solubilities of Sulfur, Noble-Gases, Nitrogen, Chlorine, and Fluorine in Magmas, Volatiles in Magmas, Volume 30: Reviews in Mineralogy, p. 231-279.
Clark, P.U., Dyke, A.S., Shakun, J.D., Carlson, A.E., Clark, J., Wohlfarth, B., Mitrovica, J.X., Hostetler, S.W., and McCabe, A.M., 2009, The Last Glacial Maximum: Science, v. 325, p. 710-714.
Claypool, G.E., Holser, W.T., Kaplan, I.R., Sakai, H., and Zak, I., 1980, The Age Curves of Sulfur and Oxygen Isotopes in Marine Sulfate and Their Mutual Interpretation: Chemical Geology, v. 28, p. 199-260.
Cocks, L.R.M., and Torsvik, T.H., 2007, Siberia, the Wandering Northern Terrane, and Its Changing Geography through the Palaeozoic: Earth-Science Reviews, v. 82, p. 29-74.
Coffin, M., and Eldholm, O., 1994, Large Igneous Provinces: Crustal Structure, Dimensions, and External Consequences: Reviews in Geophysics, v. 32, p. 1-36.
Cole, P., 1991, Migration Direction of Sand-Wave Structures in Pyroclastic-Surge Deposits: Implications for Depositional Processes: Geology, v. 19, p. 1108-1111.
Collins, G.C., 2005, Relative Rates of Fluvial Bedrock Incision on Titan and Earth: Geophysical Research Letters, v. 32.
Collins, G.C., Sklar, L.S., Litwin, K.L., and Polito, P.J., 2012, Do Titan's River Channels Carve into Ice Bedrock or Loose Regolith?, Titan Through Time 2: Houston, TX.
Cottrell, E., Spiegelman, M., and Langmuir, C.H., 2002, Consequences of Diffusive Reequilibration for the Interpretation of Melt Inclusions: Geochemistry Geophysics Geosystems, v. 3.
Crowe, B.M., and Fisher, R.V., 1973, Sedimentary Structures in Base-Surge Deposits with Special Reference to Cross-Bedding, Ubehebe Craters, Death Valley, California: Geological Society of America Bulletin, v. 84, p. 663-682.
Czamanske, G.K., Gurevitch, A., Fedorenko, V., and Simonov, O., 1998, Demise of the Siberian Plume: Paleogeographic and Paleotectonic Reconstruction from the Prevolcanic and Volcanic Record, North-Central Siberia: International Geology Review, v. 40, p. 95-115.
Dalrymple, G.B., Czamanske, G.K., Fedorenko, V.A., Simonov, O.N., Lanphere, M.A., and Likhachev, A.P., 1995, A Reconnaissance Ar-40/Ar-39 Geochronological Study of Ore-Bearing and Related Rocks, Siberian Russia: Geochimica Et Cosmochimica Acta, v. 59, p. 2071-2083.
Daniel, J.S., Solomon, S., Portmann, R.W., and Garcia, R.R., 1999, Stratospheric Ozone Destruction: The Importance of Bromine Relative to Chlorine: Journal of Geophysical Research-Atmospheres, v. 104, p. 23871-23880.
Danyushevsky, L.V., Della-Pasqua, F.N., and Sokolov, S., 2000, Re-Equilibration of Melt Inclusions Trapped by Magnesian Olivine Phenocrysts from Subduction-Related Magmas: Petrological Implications: Contributions to Mineralogy and Petrology, v. 138, p. 68-83.
Danyushevsky, L.V., Sokolov, S., and Falloon, T.J., 2002, Melt Inclusions in Olivine Phenocrysts: Using Diffusive Re-Equilibration to Determine the Cooling History of a Crystal, with Implications for the Origin of Olivine-Phyric Volcanic Rocks: Journal of Petrology, v. 43, p. 1651-1671.
Davis, M., Hut, P., and Muller, R.A., 1984, Extinction of Species by Periodic Comet Showers.
de Hoog, J.C.M., Taylor, B.E., and van Bergen, M.J., 2001, Sulfur Isotope Systematics of Basaltic Lavas from Indonesia: Implications for the Sulfur Cycle in Subduction Zones: Earth and Planetary Science Letters, v. 189, p. 237-252.
Devine, J.D., Sigurdsson, H., Davis, A.N., and Self, S., 1984, Estimates of Sulfur and Chlorine Yield to the Atmosphere from Volcanic-Eruptions and Potential Climatic Effects: Journal of Geophysical Research, v. 89, p. 6309-6325.
Ding, T., Valkiers, S., Kipphardt, H., De Bievre, P., Taylor, P., Gonfiantini, R., and Krouse, R., 2001, Calibrated Sulfur Isotope Abundance Ratios of Three Iaea Sulfur Isotope Reference Materials and V-Cdt with a Reassessment of the Atomic Weight of Sulfur: Geochimica Et Cosmochimica Acta, v. 65, p. 2433-2437.
Dixon, J.E., Clague, D.A., and Stolper, E.M., 1991, Degassing History of Water, Sulfur, and Carbon in Submarine Lavas from Kilauea Volcano, Hawaii: Journal of Geology, v. 99, p. 371-394.

Dixon, J.E., and Stolper, E.M., 1995, An Experimental Study of Water and Carbon Dioxide Solubilities in Mid-Ocean Ridge Basaltic Liquids. Part Ii: Applications to Degassing: Journal of Petrology, v. 36, p. 1633-1646.

Dixon, J.E., Stolper, E.M., and Holloway, J.R., 1995, An Experimental Study of Water and Carbon Dioxide Solubilities in Mid-Ocean Ridge Basaltic Liquids. Part I: Calibration and Solubility Models: Journal of Petrology, v. 36, p. 1607-1631.

Drummond, S.A., Burr, D.M., Cartwright, R., Black, B.A., and Perron, J.T., 2011, Global Mapping and Morphologic Classification of Titan Fluvial Features, LPSC, Volume 42: Houston, TX, p. 1919.

—, 2012, Morphologic Classification and Geologic Implications of Titan Fluvial Features, LPSC 43: Houston, TX.

Edmonds, M., and Gerlach, T.M., 2007, Vapor Segregation and Loss in Basaltic Melts: Geology, v. 35, p. 751-754.

Edmonds, M., Gerlach, T.M., and Herd, R.A., 2009, Halogen Degassing During Ascent and Eruption of Water-Poor Basaltic Magma: Chemical Geology, v. 263, p. 122-130.

Elachi, C., Allison, M.D., Borgarelli, L., Encrenaz, P., Im, E., Janssen, M.A., Johnson, W.T.K., Kirk, R.L., Lorenz, R.D., Lunine, J.I., Muhleman, D.O., Ostro, S.J., Picardi, G., Posa, F., Rapley, C.G., Roth, L.E., Seu, R., Soderblom, L.A., Vetrella, S., Wall, S.D., Wood, C.A., and Zebker, H.A., 2004, Radar: The Cassini Titan Radar Mapper: Space Science Reviews, v. 115, p. 71-110.

Elachi, C., Wall, S., Allison, M., Anderson, Y., Boehmer, R., Callahan, P., Encrenaz, P., Flamini, E., Franceschetti, G., Gim, Y., Hamilton, G., Hensley, S., Janssen, M., Johnson, W., Kelleher, K., Kirk, R., Lopes, R., Lorenz, R., Lunine, J., Muhleman, D., Ostro, S., Paganelli, F., Picardi, G., Posa, F., Roth, L., Seu, R., Shaffer, S., Soderblom, L., Stiles, B., Stofan, E., Vetrella, S., West, R., Wood, C., Wye, L., and Zebker, H., 2005, Cassini Radar Views the Surface of Titan: Science, v. 308, p. 970-974.

Elachi, C., Wall, S., Lopes, R., Soderblom, L., Lunine, J., Lorenz, R., Janssen, M., and Kirk, R., 2006, Titan's Surface by Radarlight: Bulletin of the American Astronomical Society, v. 38, Abstract 48.01.

Elkins-Tanton, L.T., 2007, Continental Magmatism, Volatile Recycling, and a Heterogeneous Mantle Caused by Lithospheric Gravitational Instabilities: Journal of Geophysical Research-Solid Earth, v. 112.

Elkins-Tanton, L.T., and Hager, B.H., 2000, Melt Intrusion as a Trigger for Lithospheric Foundering and the Eruption of the Siberian Flood Basalts: Geophysical Research Letters, v. 27, p. 3937-3940.

Elliott, S., 2009, Dependence of Dms Global Sea-Air Flux Distribution on Transfer Velocity and Concentration Field Type: Journal of Geophysical Research: Biogeosciences, v. 114, p. G02001.

Ellis, J., and Schramm, D.N., 1995, Could a Nearby Supernova Explosion Have Caused a Mass Extinction?: Proceedings of the National Academy of Sciences, v. 92, p. 235-238.

England, P., and Molnar, P., 1990, Surface Uplift, Uplift of Rocks, and Exhumation of Rocks: Geology, v. 18, p. 1173-1177.

Erwin, D.H., 1994, The Permo-Triassic Extinction: Nature, v. 367, p. 231-236.

Eshleman, V.R., Lindal, G.F., and Tyler, G.L., 1983, Is Titan Wet or Dry: Science, v. 221, p. 53-55.

Farley, K.A., Ward, P., Garrison, G., and Mukhopadhyay, S., 2005, Absence of Extraterrestrial He-3 in Permian-Triassic Age Sedimentary Rocks: Earth and Planetary Science Letters, v. 240, p. 265-275.

Farr, T.G., Rosen, P.A., Caro, E., Crippen, R., Duren, R., Hensley, S., Kobrick, M., Paller, M., Rodriguez, E., Roth, L., Seal, D., Shaffer, S., Shimada, J., Umland, J., Werner, M., Oskin, M., Burbank, D., and Alsdorf, D., 2007, The Shuttle Radar Topography Mission: Reviews of Geophysics, v. 45.

Fedorenko, V., 1994, Evolution of Magmatism as Reflected in the Volcanic Sequence of the Noril'sk Region, Proc Sudbury-Noril'sk Symp. Ontario Geological Survey Special, Volume 5, p. 171-184.

Fedorenko, V., Czamanske, G., Zen'ko, T., Budahn, J., and Siems, D., 2000, Field and Geochemical Studies of the Melilite-Rearing Arydzhangsky Suite, and an Overall Perspective on the Siberian Alkaline-Ultramafic Flood-Volcanic Rocks: International Geology Review, v. 42, p. 769-804.

Fedorenko, V.A., and Czamanske, G.K., 1997, Results of New Field and Geochemical Studies of the Volcanic and Intrusive Rocks of the Maymecha-Kotuy Area, Siberian Flood-Basalt Province, Russia: International Geology Review, v. 39, p. 479-531.
Fedorenko, V.A., Lightfoot, P.C., Czamanske, G.K., Hawkesworth, C.J., Wooden, J.L., and Ebel, D.S., 1996a, Petrogenesis of the Siberian Flood-Basalt Sequence at Noril'sk: International Geology Review, v. 38, p. 99-135.
Fedorenko, V.A., Lightfoot, P.C., Naldrett, A.J., Czamanske, G.K., Hawkesworth, C.J., Wooden, J.L., and Ebel, D.S., 1996b, Petrogenesis of the Flood-Basalt Sequence at Noril'sk, North Central Siberia: International Geology Review, v. 38, p. 99-135.
Fisher, R.V., and Schmincke, H.-U., 1984, Pyroclastic Rocks: Berlin, Springer-Verlag.
Foster, C.B., and Afonin, S.A., 2005, Abnormal Pollen Grains: An Outcome of Deteriorating Atmospheric Conditions around the Permian - Triassic Boundary: Journal of the Geological Society, v. 162, p. 653-659.
Foulger, G.R., 2011, Plates Vs Plumes: A Geological Controversy, Wiley-Blackwell.
Fulchignoni, M., Ferri, F., Angrilli, F., Ball, A.J., Bar-Nun, A., Barucci, M.A., Bettanini, C., Bianchini, G., Borucki, W., Colombatti, G., Coradini, M., Coustenis, A., Debei, S., Falkner, P., Fanti, G., Flamini, E., Gaborit, V., Grard, R., Hamelin, M., Harri, A.M., Hathi, B., Jernej, I., Leese, M.R., Lehto, A., Stoppato, P.F.L., Lopez-Moreno, J.J., Makinen, T., McDonnell, J.A.M., McKay, C.P., Molina-Cuberos, G., Neubauer, F.M., Pirronello, V., Rodrigo, R., Saggin, B., Schwingenschuh, K., Seiff, A., Simoes, F., Svedhem, H., Tokano, T., Towner, M.C., Trautner, R., Withers, P., and Zarnecki, J.C., 2005, In Situ Measurements of the Physical Characteristics of Titan's Environment: Nature, v. 438, p. 785-791.
Gaetani, G.A., O'Leary, J.A., Shimizu, N., Bucholz, C.E., and Newville, M., 2012, Rapid Reequilibration of H2o and Oxygen Fugacity in Olivine-Hosted Melt Inclusions: Geology, v. 40, p. 915-918.
Ganino, C., and Arndt, N.T., 2009, Climate Changes Caused by Degassing of Sediments During the Emplacement of Large Igneous Provinces: Geology, v. 37, p. 323-326.
Gerlach, T.M., and Graeber, E.J., 1985, Volatile Budget of Kilauea Volcano: Nature, v. 313, p. 273-277.
Gerlach, T.M., and Taylor, B.E., 1990, Carbon Isotope Constraints on Degassing of Carbon Dioxide from Kilauea Volcano: Geochimica Et Cosmochimica Acta, v. 54, p. 2051-2058.
Gilbert, J.S., and Lane, S.J., 1994, The Origin of Accretionary Lapilli: Bulletin of Volcanology, v. 56, p. 398-411.
Gill, A.E., 1982, Atmosphere-Ocean Dynamics.
Glaze, L.S., Baloga, S.M., and Wimert, J., 2011, Explosive Volcanic Eruptions from Linear Vents on Earth, Venus, and Mars: Comparisons with Circular Vent Eruptions: J. Geophys. Res., v. 116, p. E01011.
Gorbachev, N., and Grinenko, L., 1973, The Sulfur-Isotope Ratios of the Sulfides and Sulfates of the Oktyabr'sky Sulfide Deposit Noril'sk Region, and the Problem of Its Origin: Geokhimiya, v. 8, p. 1127-1136.
Griffith, C.A., Owen, T., Geballe, T.R., Rayner, J., and Rannou, P., 2003, Evidence for the Exposure of Water Ice on Titan's Surface: Science, v. 300, p. 628-630.
Grinenko, L.I., 1985, Sources of Sulfur of the Nickeliferous and Barren Gabbro-Dolerite Intrusions of the Northwest Siberian Platform: International Geology Review, v. 27, p. 695-708.
Grise, K.M., Thompson, D.W.J., and Birner, T., 2010, A Global Survey of Static Stability in the Stratosphere and Upper Troposphere: Journal of Climate, v. 23, p. 2275-2292.
Hageluken, C., 2006, Markets for the Catalyst Metals Platinum, Palladium and Rhodium: Metall, v. 60, p. 31.
Hamill, P., Jensen, E.J., Russell, P., and Bauman, J.J., 1997, The Life Cycle of Stratospheric Aerosol Particles: Bulletin of the American Meteorological Society, v. 78, p. 1395-1410.
Harfoot, M.B., Beerling, D.J., Lomax, B.H., and Pyle, J.A., 2007, A Two-Dimensional Atmospheric Chemistry Modeling Investigation of Earth's Phanerozoic O3 and near-Surface Ultraviolet Radiation History: Journal of Geophysical Research: Atmospheres (1984–2012), v. 112.

Hauri, E., 2002, Sims Analysis of Volatiles in Silicate Glasses, 2: Isotopes and Abundances in Hawaiian Melt Inclusions: Chemical Geology, v. 183, p. 115-141.
Hauri, E., Wang, J., Dixon, J.E., King, P.L., Mandeville, C., and Newman, S., 2002, Sims Analysis of Volatiles in Silicate Glasses: 1. Calibration, Matrix Effects and Comparisons with Ftir: Chemical Geology, v. 183, p. 99-114.
Hawkesworth, C.J., Lightfoot, P.C., Fedorenko, V.A., Blake, S., Naldrett, A.J., Doherty, W., and Gorbachev, N.S., 1995, Magma Differentiation and Mineralization in the Siberian Continental Flood Basalts: Lithos, v. 34, p. 61-88.
Hayes, A., Aharonson, O., Callahan, P., Elachi, C., Gim, Y., Kirk, R., Lewis, K., Lopes, R., Lorenz, R., Lunine, J., Mitchell, K., Mitri, G., Stofan, E., and Wall, S., 2008, Hydrocarbon Lakes on Titan: Distribution and Interaction with a Porous Regolith: Geophysical Research Letters, v. 35.
Head III, J.W., and Wilson, L., 1987, Lava Fountain Heights at Pu'u'o'o, Kilauea, Hawaii: Indicators of Amount and Variations of Exsolved Magma Volatiles: Journal of Geophysical Research, v. 92, p. 13715-13,719.
Head, J.W., and Wilson, L., 1987, Lava Fountain Heights at Pu'u'o'o, Kilauea, Hawaii: Indicators of Amount and Variations of Exsolved Magma Volatiles: Journal of Geophysical Research: Solid Earth (1978–2012), v. 92, p. 13715-13719.
Heiken, G., 1972, Morphology and Petrography of Volcanic Ashes: Geological Society of America Bulletin, v. 83, p. 1961-&.
Hoblitt, R.P., and Kellogg, K.S., 1979, Emplacement Temperatures of Unsorted and Unstratified Deposits of Volcanic Rock Debris as Determined by Paleomagnetic Techniques: Geological Society of America Bulletin, v. 90, p. 633-642.
Horton, R.E., 1945, Erosional Development of Streams and Their Drainage Basins - Hydrophysical Approach to Quantitative Morphology: Geological Society of America Bulletin, v. 56, p. 275-370.
Hotinski, R.M., Bice, K.L., Kump, L.R., Najjar, R.G., and Arthur, M.A., 2001, Ocean Stagnation and End-Permian Anoxia: Geology, v. 29, p. 7-10.
Howard, A.D., 1994, A Detachment-Limited Model of Drainage-Basin Evolution: Water Resources Research, v. 30, p. 2261-2285.
Howard, A.D., and Kerby, G., 1983, Channel Changes in Badlands: Geological Society of America Bulletin, v. 94, p. 739-752.
Howells, G.P., 1990, Acid Rain and Acid Waters, Ellis Horwood.
Huey, R.B., and Ward, P.D., 2005, Hypoxia, Global Warming, and Terrestrial Late Permian Extinctions: Science, v. 308, p. 398-401.
Iacono-Marziano, G., Gaillard, F., Scaillet, B., Pichavant, M., and Chiodini, G., 2009, Role of Non-Mantle Co2 in the Dynamics of Volcano Degassing: The Mount Vesuvius Example: Geology, v. 37, p. 319-322.
Isozaki, Y., 1997, Permo-Triassic Boundary Superanoxia and Stratified Superocean: Records from Lost Deep Sea: Science, v. 276, p. 235-238.
Jay, A.E., and Widdowson, M., 2008, Stratigraphy, Structure and Volcanology of the Se Deccan Continental Flood Basalt Province: Implications for Eruptive Extent and Volumes: Journal of the Geological Society, v. 165, p. 177-188.
Johnston, D.A., 1980, Volcanic Contribution of Chlorine to the Stratosphere - More Significant to Ozone Than Previously Estimated: Science, v. 209, p. 491-493.
Jugo, P.J., 2009, Sulfur Content at Sulfide Saturation in Oxidized Magmas: Geology, v. 37, p. 415-418.
Jump, A.S., and Peñuelas, J., 2005, Running to Stand Still: Adaptation and the Response of Plants to Rapid Climate Change: Ecology Letters, v. 8, p. 1010-1020.
Kamo, S.L., Czamanske, G.K., Amelin, Y., Fedorenko, V.A., Davis, D.W., and Trofimov, V.R., 2003, Rapid Eruption of Siberian Flood-Volcanic Rocks and Evidence for Coincidence with the Permian-Triassic Boundary and Mass Extinction at 251 Ma: Earth and Planetary Science Letters, v. 214, p. 75-91.

Katsura, T., and Nagashima, S., 1974, Solubility of Sulfur in Some Magmas at 1 Atmosphere: Geochimica Et Cosmochimica Acta, v. 38, p. 517-531.
Keller, H.U., Grieger, B., Kuppers, M., Schroder, S.E., Skorov, Y.V., and Tomasko, M.G., 2008, The Properties of Titan's Surface at the Huygens Landing Site from Disr Observations: Planetary and Space Science, v. 56, p. 728-752.
Kent, A.J.R., Clague, D.A., Honda, M., Stolper, E.M., Hutcheon, I.D., and Norman, M.D., 1999a, Widespread Assimilation of a Seawater-Derived Component at Loihi Seamount, Hawaii: Geochimica Et Cosmochimica Acta, v. 63, p. 2749-2761.
Kent, A.J.R., Norman, M.D., Hutcheon, I.D., and Stolper, E.M., 1999b, Assimilation of Seawater-Derived Components in an Oceanic Volcano: Evidence from Matrix Glasses and Glass Inclusions from Loihi Seamount, Hawaii: Chemical Geology, v. 156, p. 299-319.
Keszthelyi, L., Self, S., and Thordarson, T., 2006, Flood Lavas on Earth, Io and Mars: Journal of the Geological Society, v. 163, p. 253-264.
Khare, B.N., Sagan, C., Bandurski, E.L., and Nagy, B., 1978, Ultraviolet-Photoproduced Organic Solids Synthesized under Simulated Jovian Conditions - Molecular Analysis: Science, v. 199, p. 1199-1201.
Kiehl, J.T., and Shields, C.A., 2005, Climate Simulation of the Latest Permian: Implications for Mass Extinction: Geology, v. 33, p. 757-760.
Knoll, A.H., Barnbach, R.K., Payne, J.L., Pruss, S., and Fischer, W.W., 2007, Paleophysiology and End-Permian Mass Extinction: Earth and Planetary Science Letters, v. 256, p. 295-313.
Kobor, J.S., and Roering, J.J., 2004, Systematic Variation of Bedrock Channel Gradients in the Central Oregon Coast Range: Implications for Rock Uplift and Shallow Landsliding: Geomorphology, v. 62, p. 239-256.
Kontorovich, A.E., Khomenko, A.V., Burshtein, L.M., Likhanov, II, Pavlov, A.L., Staroseltsev, V.S., and Ten, A.A., 1997, Intense Basic Magmatism in the Tunguska Petroleum Basin, Eastern Siberia, Russia: Petroleum Geoscience, v. 3, p. 359-369.
Kouvaris, L.C., and Flasar, F.M., 1991, Phase-Equilibrium of Methane and Nitrogen at Low-Temperatures - Application to Titan: Icarus, v. 91, p. 112-124.
Koyaguchi, T., and Woods, A.W., 1996, On the Formation of Eruption Columns Following Explosive Mixing of Magma and Surface-Water: Journal of Geophysical Research-Solid Earth, v. 101, p. 5561-5574.
Krasnopolsky, V.A., 2009, A Photochemical Model of Titan's Atmosphere and Ionosphere: Icarus, v. 201, p. 226-256.
Kuiper, G.P., 1944, Titan: A Satellite with an Atmosphere: Astrophysical Journal, v. 100, p. 378-383.
Kump, L.R., 1991, Interpreting Carbon-Isotope Excursions: Strangelove Oceans: Geology, v. 19, p. 299-302.
Kump, L.R., Pavlov, A., and Arthur, M.A., 2005, Massive Release of Hydrogen Sulfide to the Surface Ocean and Atmosphere During Intervals of Oceanic Anoxia: Geology, v. 33, p. 397-400.
Lamarque, J.-F., Emmons, L., Hess, P., Kinnison, D.E., Tilmes, S., Vitt, F., Heald, C., Holland, E.A., Lauritzen, P., and Neu, J., 2012, Cam-Chem: Description and Evaluation of Interactive Atmospheric Chemistry in the Community Earth System Model: Geoscientific Model Development, v. 5, p. 369-411.
Lamarque, J.F., Kiehl, J., Shields, C., Boville, B., and Kinnison, D., 2006, Modeling the Response to Changes in Tropospheric Methane Concentration: Application to the Permian-Triassic Boundary: Paleoceanography, v. 21.
Lamarque, J.F., Kiehl, J.T., and Orlando, J.J., 2007, Role of Hydrogen Sulfide in a Permian-Triassic Boundary Ozone Collapse: Geophysical Research Letters, v. 34.
Langhans, M.H., Jaumann, R., Stephan, K., Brown, R.H., Buratti, B.J., Clark, R.N., Baines, K.H., Nicholson, P.D., Lorenz, R.D., Soderblom, L.A., Soderblom, J.M., Sotin, C., Barnes, J.W., and Nelson, R., 2012, Titan's Fluvial Valleys: Morphology, Distribution, and Spectral Properties: Planetary and Space Science, v. 60, p. 34-51.

Lavvas, P.P., Coustenis, A., and Vardavas, I.M., 2008, Coupling Photochemistry with Haze Formation in Titan's Atmosphere, Part I: Model Description: Planetary and Space Science, v. 56, p. 27-66.
Le Bas, M., Le Maitre, R., Streckeisen, A., and Zanettin, B., 1986, A Chemical Classification of Volcanic Rocks Based on the Total Alkali-Silica Diagram: Journal of petrology, v. 27, p. 745-750.
Lehrmann, D.J., Ramezani, J., Bowring, S.A., Martin, M.W., Montgomery, P., Enos, P., Payne, J.L., Orchard, M.J., Wang, H.M., and Wei, J.Y., 2006, Timing of Recovery from the End-Permian Extinction: Geochronologic and Biostratigraphic Constraints from South China: Geology, v. 34, p. 1053-1056.
Li, C., Ripley, E.M., and Naldrett, A.J., 2009a, A New Genetic Model for the Giant Ni-Cu-Pge Sulfide Deposits Associated with the Siberian Flood Basalts: Economic Geology, v. 104, p. 291-301.
Li, C., Ripley, E.M., Naldrett, A.J., Schmitt, A.K., and Moore, C.H., 2009b, Magmatic Anhydrite-Sulfide Assemblages in the Plumbing System of the Siberian Traps: Geology, v. 37, p. 259-262.
Li, C.S., Ripley, E.M., and Naldrett, A.J., 2009c, A New Genetic Model for the Giant Ni-Cu-Pge Sulfide Deposits Associated with the Siberian Flood Basalts: Economic Geology, v. 104, p. 291-301.
Lightfoot, P.C., Hawkesworth, C.J., Hergt, J., Naldrett, A.J., Gorbachev, N.S., Fedorenko, V.A., and Doherty, W., 1993, Remobilization of the Continental Lithosphere by a Mantle Plume - Major-Element, Trace-Element, and Sr-Isotope, Nd-Isotope, and Pb-Isotope Evidence from Picritic and Tholeiitic Lavas of the Norilsk District, Siberian Trap, Russia: Contributions to Mineralogy and Petrology, v. 114, p. 171-188.
Lightfoot, P.C., Naldrett, A.J., Gorbachev, N.S., Doherty, W., and Fedorenko, V.A., 1990, Geochemistry of the Siberian Trap of the Norilsk Area, Ussr, with Implications for the Relative Contributions of Crust and Mantle to Flood-Basalt Magmatism: Contributions to Mineralogy and Petrology, v. 104, p. 631-644.
Likens, G.E., Driscoll, C.T., and Buso, D.C., 1996, Long-Term Effects of Acid Rain: Response and Recovery of a Forest Ecosystem: Science-AAAS-Weekly Paper Edition, v. 272, p. 244-245.
Lindal, G.F., Wood, G.E., Hotz, H.B., Sweetnam, D.N., Eshleman, V.R., and Tyler, G.L., 1983, The Atmosphere of Titan - an Analysis of the Voyager-1 Radio Occultation Measurements: Icarus, v. 53, p. 348-363.
Lopes, R.M.C., Stofan, E.R., Peckyno, R., Radebaugh, J., Mitchell, K.L., Mitri, G., Wood, C.A., Kirk, R.L., Wall, S.D., Lunine, J.I., Hayes, A., Lorenz, R., Farr, T., Wye, L., Craig, J., Ollerenshaw, R.J., Janssen, M., LeGall, A., Paganelli, F., West, R., Stiles, B., Callahan, P., Anderson, Y., Valora, P., Soderblom, L., and Cassini, R.T., 2010, Distribution and Interplay of Geologic Processes on Titan from Cassini Radar Data: Icarus, v. 205, p. 540-558.
Lorenz, R.D., and Lunine, J.I., 1996, Erosion on Titan: Past and Present: Icarus, v. 122, p. 79-91.
Lorenz, R.D., Newman, C., and Lunine, J.I., 2010, Threshold of Wave Generation on Titan's Lakes and Seas: Effect of Viscosity and Implications for Cassini Observations: Icarus, v. 207, p. 932-937.
Lorenz, R.D., Wall, S., Radebaugh, J., Boubin, G., Reffet, E., Janssen, M., Stofan, E., Lopes, R., Kirk, R., Elachi, C., Lunine, J., Mitchell, K., Paganelli, F., Soderblom, L., Wood, C., Wye, L., Zebker, H., Anderson, Y., Ostro, S., Allison, M., Boehmer, R., Callahan, P., Encrenaz, P., Ori, G.G., Francescetti, G., Gim, Y., Hamilton, G., Hensley, S., Johnson, W., Kelleher, K., Muhleman, D., Picardi, G., Posa, F., Roth, L., Seu, R., Shaffer, S., Stiles, B., Vetrella, S., Flamini, E., and West, R., 2006, The Sand Seas of Titan: Cassini Radar Observations of Longitudinal Dunes: Science, v. 312, p. 724-727.
Lorenz, R.D., Wood, C.A., Lunine, J.I., Wall, S.D., Lopes, R.M., Mitchell, K.L., Paganelli, F., Anderson, Y.Z., Wye, L., Tsai, C., Zebker, H., and Stofan, E.R., 2007, Titan's Young Surface: Initial Impact Crater Survey by Cassini Radar and Model Comparison: Geophysical Research Letters, v. 34.
Lowenstern, J.B., 1995, Applications of Silicate-Melt Inclusions to the Study of Magmatic Volatiles: Magmas, fluids, and ore deposits, v. 23, p. 71-99.
Lunine, J.I., and Lorenz, R.D., 2009, Rivers, Lakes, Dunes, and Rain: Crustal Processes in Titan's Methane Cycle: Annual Review of Earth and Planetary Sciences, v. 37, p. 299-320.

Lunine, J.I., Stevenson, D.J., and Yung, Y.L., 1983, Ethane Ocean on Titan: Science, v. 222, p. 1229-1230.
Macdonald, G.A., Davis, D.A., and Cox, D.C., 1960, Geology and Ground-Water Resources of the Island of Kauai, Hawaii, Hawaii Division of Hydrography.
Madronich, S., McKenzie, R.L., Björn, L.O., and Caldwell, M.M., 1998, Changes in Biologically Active Ultraviolet Radiation Reaching the Earth's Surface: Journal of Photochemistry and Photobiology B: Biology, v. 46, p. 5-19.
Malaska, M., Radebaugh, J., Mitchell, K., Lopes, R., Wall, S., and Lorenz, R., 2011, Surface Dissolution Model for Titan Karst, First International Planetary Cave Research Workshop: Carlsbad, NM.
Malich, N.S., Mironyuk, E.P., and Tuganova, E.V., 1999, Geological Map of Siberian Platform and Adjoining Areas, Ministry of Natural Resources of the Russian Federation.
Malich, N.S., Tazihin, N.N., Tuganova, E.V., Bunzen, E.A., Kulikova, N.G., Safonova, I. V. et al., 1974, Map of Geological Formations of the Siberian Platform Cover (1:1,500,000).
Malitch, N.S., Mironyuk, E.P., and Tuganova, E.V., 1999, Geological Map of Siberian Platform and Adjoining Areas, Ministry of Natural Resources of the Russian Federation.
Mandeville, C., Shimizu, N., Kelley, K., and Cheek, L., 2008, Sulfur Isotope Variation in Basaltic Melt Inclusions from Krakatau Revealed by a Newly Developed Secondary Ion Mass Spectrometry Technique for Silicate Glasses, AGU Fall Meeting Abstracts, Volume 1, p. 07.
Maruoka, T., Koeberl, C., Hancox, P., and Reimold, W., 2003, Sulfur Geochemistry across a Terrestrial Permian–Triassic Boundary Section in the Karoo Basin, South Africa: Earth and Planetary Science Letters, v. 206, p. 101-117.
Mavrogenes, J.A., and O'Neill, H.S.C., 1999, The Relative Effects of Pressure, Temperature and Oxygen Fugacity on the Solubility of Sulfide in Mafic Magmas: Geochimica Et Cosmochimica Acta, v. 63, p. 1173-1180.
Mavrogenes, J.A., and O'Neill, H.S.C., 1999, The Relative Effects of Pressure, Temperature and Oxygen Fugacity on the Solubility of Sulfide in Mafic Magmas: Geochimica Et Cosmochimica Acta, v. 63, p. 1173-1180.
McClelland, E., Wilson, C.J.N., and Bardot, L., 2004, Palaeotemperature Determinations for the 1.8-Ka Taupo Ignimbrite, New Zealand, and Implications for the Emplacement History of a High-Velocity Pyroclastic Flow: Bulletin of Volcanology, v. 66, p. 492-513.
McClintock, M., and White, J.D., 2006, Large Phreatomagmatic Vent Complex at Coombs Hills, Antarctica: Wet, Explosive Initiation of Flood Basalt Volcanism in the Ferrar-Karoo Lip: Bulletin of Volcanology, v. 68, p. 215-239.
McCord, T.B., Hansen, G.B., Buratti, B.J., Clark, R.N., Cruikshank, D.P., D'Aversa, E., Griffith, C.A., Baines, E.K.H., Brown, R.H., Dalle Ore, C.M., Filacchione, G., Formisano, V., Hibbitts, C.A., Jaumann, R., Lunine, J.I., Nelson, R.M., and Sotin, C., 2006, Composition of Titan's Surface from Cassini Vims: Planetary and Space Science, v. 54, p. 1524-1539.
McDonough, W.F., and Sun, S.S., 1995, The Composition of the Earth: Chemical Geology, v. 120, p. 223-253.
McKay, C.P., Coustenis, A., Samuelson, R.E., Lemmon, M.T., Lorenz, R.D., Cabane, M., Rannou, P., and Drossart, P., 2001, Physical Properties of the Organic Aerosols and Clouds on Titan: Planetary and Space Science, v. 49, p. 79-99.
Melnikov, N.V., Khomenko, A.V., Kuznetsova, E.N., and Zhidkova, L.V., 1997, The Effect of Traps on Salt Redistribution in the Lower Cambrian of the Western Siberian Platform: Geologiya I Geofizika, v. 38, p. 1339-1345.
Metrich, N., and Wallace, P.J., 2008, Volatile Abundances in Basaltic Magmas and Their Degassing Paths Tracked by Melt Inclusions, *in* Putirka, K.D., and Tepley, F.J., eds., Minerals, Inclusions and Volcanic Processes, Volume 69: Reviews in Mineralogy & Geochemistry, p. 363-402.
Meyer, K., Yu, M., Jost, A., Kelley, B., and Payne, J., 2011, $\Delta^{13}c$ Evidence That High Primary Productivity Delayed Recovery from End-Permian Mass Extinction: Earth and Planetary Science Letters, v. 302, p. 378-384.

Meyerhoff, A.A., 1980, Geology and Petroleum Fields in Proterozoic and Lower Cambrian Strata, Lena-Tunguska Petroleum Province, Eastern Siberia, Ussr, *in* Halbouty, M.T., ed., Giant Oil and Gas Fields of the Decade 1968–1978. , American Association of Petroleum Geologists.

Michael, P.J., and Cornell, W.C., 1998, Influence of Spreading Rate and Magma Supply on Crystallization and Assimilation beneath Mid-Ocean Ridges: Evidence from Chlorine and Major Element Chemistry of Mid-Ocean Ridge Basalts: Journal of Geophysical Research-Solid Earth, v. 103, p. 18325-18356.

Michael, P.J., and Schilling, J.G., 1989, Chlorine in Mid-Ocean Ridge Magmas: Evidence for Assimilation of Seawater-Influenced Components: Geochimica Et Cosmochimica Acta, v. 53, p. 3131-3143.

Millard, G.A., Mather, T.A., Pyle, D.M., Rose, W.I., and Thornton, B., 2006, Halogen Emissions from a Small Volcanic Eruption: Modeling the Peak Concentrations, Dispersion, and Volcanically Induced Ozone Loss in the Stratosphere: Geophysical Research Letters, v. 33.

Miller, G.H., Geirsdóttir, Á., Zhong, Y., Larsen, D.J., Otto-Bliesner, B.L., Holland, M.M., Bailey, D.A., Refsnider, K.A., Lehman, S.J., and Southon, J.R., 2012, Abrupt Onset of the Little Ice Age Triggered by Volcanism and Sustained by Sea-Ice/Ocean Feedbacks: Geophysical Research Letters, v. 39.

Mitri, G., Showman, A.P., Lunine, J.I., and Lopes, R.M.C., 2008, Resurfacing of Titan by Ammonia-Water Cryomagma: Icarus, v. 196, p. 216-224.

Mitri, G., Showman, A.P., Lunine, J.I., and Lorenz, R.D., 2007, Hydrocarbon Lakes on Titan: Icarus, v. 186, p. 385-394.

Molina, M.J., 1996, Role of Chlorine in Stratospheric Chemistry: Pure and Applied Chemistry, v. 68, p. 1749-1756.

Moore, J.M., and Howard, A.D., 2010, Are the Basins of Titan's Hotei Regio and Tui Regio Sites of Former Low Latitude Seas?: Geophys. Res. Lett., v. 37, p. L22205.

Moore, J.M., and Pappalardo, R.T., 2011, Titan: An Exogenic World?: Icarus, v. 212, p. 790-806.

Nair, P.V.N., Joshi, P.V., Mishra, U.C., and Vohra, K.G., 1983, Growth of Aqueous-Solution Droplets of Hno3 and Hcl in the Atmosphere: Journal of the Atmospheric Sciences, v. 40, p. 107-115.

Naldrett, A.J., 1992, A Model for the Ni-Cu-Pge Ores of the Noril'sk Region and Its Application to Other Areas of Flood Basalt: Economic Geology, v. 87, p. 1945-1962.

Naldrett, A.J., Lightfoot, P.C., Fedorenko, V., Doherty, W., and Gorbachev, N.S., 1992, Geology and Geochemistry of Intrusions and Flood Basalts of the Norilsk Region, Ussr, with Implications for the Origin of the Ni-Cu Ores: Economic Geology and the Bulletin of the Society of Economic Geologists, v. 87, p. 975-1004.

Naumov, V.A., and Ankudimova, L.A., 1995, Palinological Complexes and Age of Volcanic Sediments of the Angara-Katanga District, Middle Angara Region: Geology and Geophysics, v. 36.

Neish, C.D., and Lorenz, R.D., 2012, Titan's Global Crater Population: A New Assessment: Planetary and Space Science, v. 60, p. 26-33.

Newman, S., and Lowenstern, J.B., 2002, Volatilecalc: A Silicate Melt-H2o-Co2 Solution Model Written in Visual Basic for Excel: Computers and Geosciences, v. 28, p. 597-604.

Niemann, H.B., Atreya, S.K., Bauer, S.J., Carignan, G.R., Demick, J.E., Frost, R.L., Gautier, D., Haberman, J.A., Harpold, D.N., Hunten, D.M., Israel, G., Lunine, J.I., Kasprzak, W.T., Owen, T.C., Paulkovich, M., Raulin, F., Raaen, E., and Way, S.H., 2005, The Abundances of Constituents of Titan's Atmosphere from the Gcms Instrument on the Huygens Probe: Nature, v. 438, p. 779-784.

Nilsson, K., and Peach, C.L., 1993, Sulfur Speciation, Oxidation-State, and Sulfur Concentration in Backarc Magmas: Geochimica Et Cosmochimica Acta, v. 57, p. 3807-3813.

Oman, L., Robock, A., Stenchikov, G., Schmidt, G.A., and Ruedy, R., 2005, Climatic Response to High-Latitude Volcanic Eruptions: Journal of Geophysical Research-Atmospheres, v. 110.

Parmentier, E.M., and Head, J.W., 1981, Viscous Relaxation of Impact Craters on Icy Planetary Surfaces: Determination of Viscosity Variation with Depth: Icarus, v. 47, p. 100-111.

Pavlov, V.E., Fluteau, F., Veselovskiy, R.V., Fetisova, A.M., and Latyshev, A.V., 2011, Secular Geomagnetic Variations and Volcanic Pulses in the Permian-Triassic Traps of the Norilsk and Maimecha-Kotui Provinces: Izvestiya-Physics of the Solid Earth, v. 47, p. 402-417.

Payne, J.L., and Clapham, M.E., 2012a, End-Permian Mass Extinction in the Oceans: An Ancient Analog for the Twenty-First Century?: Annual Review of Earth and Planetary Sciences, v. 40, p. 89-111.

—, 2012b, End-Permian Mass Extinction in the Oceans: An Ancient Analog for the Twenty-Firstcentury?: Annual Review of Earth and Planetary Sciences, v. 40, p. null.

Payne, J.L., and Kump, L.R., 2007, Evidence for Recurrent Early Triassic Massive Volcanism from Quantitative Interpretation of Carbon Isotope Fluctuations: Earth and Planetary Science Letters, v. 256, p. 264-277.

Payne, J.L., Lehrmann, D.J., Wei, J.Y., Orchard, M.J., Schrag, D.P., and Knoll, A.H., 2004, Large Perturbations of the Carbon Cycle During Recovery from the End-Permian Extinction: Science, v. 305, p. 506-509.

Peate, I.U., and Bryan, S.E., 2008, Re-Evaluating Plume-Induced Uplift in the Emeishan Large Igneous Province: Nature Geoscience, v. 1, p. 625-629.

Pelletier, J.D., 2004, Persistent Drainage Migration in a Numerical Landscape Evolution Model: Geophysical Research Letters, v. 31.

Perron, J.T., and de Pater, I., 2004, Dynamics of an Ice Continent on Titan: Geophysical Research Letters, v. 31.

Perron, J.T., Dietrich, W.E., and Kirchner, J.W., 2008, Controls on the Spacing of First-Order Valleys: Journal of Geophysical Research-Earth Surface, v. 113.

Perron, J.T., and Fagherazzi, S., 2012, The Legacy of Initial Conditions in Landscape Evolution: Earth Surface Processes and Landforms, v. 37, p. 52-63.

Perron, J.T., Kirchner, J.W., and Dietrich, W.E., 2009, Formation of Evenly Spaced Ridges and Valleys: Nature, v. 460, p. 502-505.

Perron, J.T., Lamb, M.P., Koven, C.D., Fung, I.Y., Yager, E., and Adamkovics, M., 2006, Valley Formation and Methane Precipitation Rates on Titan: Journal of Geophysical Research-Planets, v. 111.

Pinto, J.P., Turco, R.P., and Toon, O.B., 1989, Self-Limiting Physical and Chemical Effects in Volcanic-Eruption Clouds: Journal of Geophysical Research-Atmospheres, v. 94, p. 11165-11174.

Planke, S., 2013, Personal Communication.

Polozov, A., Svensen, H., and Planke, S., 2010, Formation of Phreatomagmatic Pipes in the Tunguska Basin (Siberia, Russia) During the End-Permian, EGU General Assembly Conference Abstracts, Volume 12, p. 13128.

Portenga, E.W., and Bierman, P.R., 2011, Understanding Earth's Eroding Surface with 10be: GSA Today, v. 21, p. 4-10.

Putirka, K., 1999, Clinopyroxene Plus Liquid Equilibria to 100 Kbar and 2450 K: Contributions to Mineralogy and Petrology, v. 135, p. 151-163.

Pyle, D.M., and Mather, T.A., 2009, Halogens in Igneous Processes and Their Fluxes to the Atmosphere and Oceans from Volcanic Activity: A Review: Chemical Geology, v. 263, p. 110-121.

Qin, Z.W., Lu, F.Q., and Anderson, A.T., 1992, Diffusive Reequilibration of Melt and Fluid Inclusions: American Mineralogist, v. 77, p. 565-576.

Radebaugh, J., Lorenz, R.D., Kirk, R.L., Lunine, J.I., Stofan, E.R., Lopes, R.M.C., Wall, S.D., and Cassini Radar, T., 2007, Mountains on Titan Observed by Cassini Radar: Icarus, v. 192, p. 77-91.

Radebaugh, J., Lorenz, R.D., Wall, S.D., Kirk, R.L., Wood, C.A., Lunine, J.I., Stofan, E.R., Lopes, R.M.C., Valora, P., Farr, T.G., Hayes, A., Stiles, B., Mitri, G., Zebker, H., Janssen, M., Wye, L., LeGall, A., Mitchell, K.L., Paganelli, F., West, R.D., and Schaller, E.L., 2011, Regional Geomorphology and History of Titan's Xanadu Province: Icarus, v. 211, p. 672-685.

Rampino, M.R., and Caldeira, K., 2005, Major Perturbation of Ocean Chemistry and a 'Strangelove Ocean'after the End-Permian Mass Extinction: Terra Nova, v. 17, p. 554-559.

Randel, W.J., and Wu, F., 2010, The Polar Summer Tropopause Inversion Layer: Journal of the Atmospheric Sciences, v. 67, p. 2572-2581.
Rannou, P., Montmessin, F., Hourdin, F., and Lebonnois, S., 2006, The Latitudinal Distribution of Clouds on Titan: Science, v. 311, p. 201-205.
Rees, P.M.A., 2002, Land-Plant Diversity and the End-Permian Mass Extinction: Geology, v. 30, p. 827-830.
Reichow, M.K., Pringle, M.S., Al'Mukhamedov, A.I., Allen, M.B., Andreichev, V.L., Buslov, M.M., Davies, C.E., Fedoseev, G.S., Fitton, J.G., Inger, S., Medvedev, A.Y., Mitchell, C., Puchkov, V.N., Safonova, I.Y., Scott, R.A., and Saunders, A.D., 2009, The Timing and Extent of the Eruption of the Siberian Traps Large Igneous Province: Implications for the End-Permian Environmental Crisis: Earth and Planetary Science Letters, v. 277, p. 9-20.
Reichow, M.K., Saunders, A.D., White, R.V., Al'Mukhamedov, A.L., and Medvedev, A.Y., 2005, Geochemistry and Petrogenesis of Basalts from the West Siberian Basin: An Extension of the Permo-Triassic Siberian Traps, Russia: Lithos, v. 79, p. 425-452.
Reichow, M.K., Saunders, A.D., White, R.V., Pringle, M.S., Al'Mukhamedov, A.I., Medvedev, A.I., and Kirda, N.P., 2002, Ar-40/Ar-39 Dates from the West Siberian Basin: Siberian Flood Basalt Province Doubled: Science, v. 296, p. 1846-1849.
Renne, P.R., and Basu, A.R., 1991, Rapid Eruption of the Siberian Traps Flood Basalts at the Permo-Triassic Boundary: Science, v. 253, p. 176-179.
Renne, P.R., Zhang, Z.C., Richards, M.A., Black, M.T., and Basu, A.R., 1995, Synchrony and Causal Relations between Permian-Triassic Boundary Crises and Siberian Flood Volcanism: Science, v. 269, p. 1413-1416.
Retallack, G.J., Veevers, J.J., and Morante, R., 1996, Global Coal Gap between Permian–Triassic Extinction and Middle Triassic Recovery of Peat-Forming Plants: Geological Society of America Bulletin, v. 108, p. 195-207.
Ries, G., Heller, W., Puchta, H., Sandermann, H., Seidlitz, H.K., and Hohn, B., 2000, Elevated Uv-B Radiation Reduces Genome Stability in Plants: Nature, v. 406, p. 98-101.
Ripley, E.M., Lightfoot, P.C., Li, C., and Elswick, E.R., 2003, Sulfur Isotopic Studies of Continental Flood Basalts in the Noril'sk Region: Implications for the Association between Lavas and Ore-Bearing Intrusions: Geochimica Et Cosmochimica Acta, v. 67, p. 2805-2817.
Robock, A., 2000, Volcanic Eruptions and Climate: Reviews of Geophysics, v. 38, p. 191-219.
Rodriguez-Iturbe, I., and Rinaldo, A., 1997, Fractal River Basins: Chance and Self-Organization: Cambridge, UK., Cambridge University Press.
Rodriguez, S., Le Mouélic, S., Sotin, C., Clénet, H., Clark, R.N., Buratti, B., Brown, R.H., McCord, T.B., Nicholson, P.D., and Baines, K.H., 2006, Cassini/Vims Hyperspectral Observations of the Huygens Landing Site on Titan: Planetary and Space Science, v. 54, p. 1510-1523.
Rose, W.I., Millard, G.A., Mather, T.A., Hunton, D.E., Anderson, B., Oppenheimer, C., Thornton, B.F., Gerlach, T.M., Viggiano, A.A., Kondo, Y., Miller, T.M., and Ballenthin, J.O., 2006, Atmospheric Chemistry of a 33-34 Hour Old Volcanic Cloud from Hekla Volcano (Iceland): Insights from Direct Sampling and the Application of Chemical Box Modeling: Journal of Geophysical Research-Atmospheres, v. 111.
Rosenbloom, N.A., and Anderson, R.S., 1994, Hillslope and Channel Evolution in a Marine Terraced Landscape, Santa-Cruz, California: Journal of Geophysical Research-Solid Earth, v. 99, p. 14013-14029.
Ross, P.S., Peate, I.U., McClintock, M.K., Xu, Y.G., Skilling, I.P., White, J.D.L., and Houghton, B.F., 2005, Mafic Volcaniclastic Deposits in Flood Basalt Provinces: A Review: Journal of Volcanology and Geothermal Research, v. 145, p. 281-314.
Rowe, M.C., and Lassiter, J.C., 2009, Chlorine Enrichment in Central Rio Grande Rift Basaltic Melt Inclusions: Evidence for Subduction Modification of the Lithospheric Mantle: Geology, v. 37, p. 439-442.

Rowe, M.C., Nielsen, R.L., and Kent, A.J., 2006, Anomalously High Fe Contents in Rehomogenized Olivine-Hosted Melt Inclusions from Oxidized Magmas: American Mineralogist, v. 91, p. 82-91.
Rudakova, A., and Krivolutskaya, N., 2009, Structural and Textural Specific Features of Rocks of Trap Rock Association in the Norilsk Trough (Nw of Siberian Platform): Moscow University Geology Bulletin, v. 64, p. 364-375.
Ryabov V.V., KONENKO V. F., and O.S., K., 1985, Rock-Forming Minerals of Picritic Basalts of the Norilsk Region: SOV. GEOL. GEOPHYS., v. 26, p. 77-84.
Saal, A.E., Hauri, E.H., Langmuir, C.H., and Perfit, M.R., 2002, Vapour Undersaturation in Primitive Mid-Ocean-Ridge Basalt and the Volatile Content of Earth's Upper Mantle: Nature, v. 419, p. 451-455.
Saal, A.E., Hauri, E.H., Van Orman, J.A., and Rutherford, M.J., 2013, Hydrogen Isotopes in Lunar Volcanic Glasses and Melt Inclusions Reveal a Carbonaceous Chondrite Heritage: Science.
Sagan, C., and Dermott, S.F., 1982, The Tide in the Seas of Titan: Nature, v. 300, p. 731-733.
Sakai, H., Casadevall, T.J., and Moore, J.G., 1982, Chemistry and Isotope Ratios of Sulfur in Basalts and Volcanic Gases at Kilauea Volcano, Hawaii: Geochimica Et Cosmochimica Acta, v. 46, p. 729-738.
Sakai, H., Marais, D.J.D., Ueda, A., and Moore, J., 1984, Concentrations and Isotope Ratios of Carbon, Nitrogen and Sulfur in Ocean-Floor Basalts: Geochimica Et Cosmochimica Acta, v. 48, p. 2433-2441.
Schaller, E.L., Roe, H.G., Schneider, T., and Brown, M.E., 2009, Storms in the Tropics of Titan: Nature, v. 460, p. 873-875.
Schilling, J.G., Bergeron, M.B., and Evans, R., 1980, Halogens in the Mantle beneath the North-Atlantic: Philosophical Transactions of the Royal Society of London Series a-Mathematical Physical and Engineering Sciences, v. 297, p. 147-178.
Schneider, T., Graves, S.D.B., Schaller, E.L., and Brown, M.E., 2012, Polar Methane Accumulation and Rainstorms on Titan from Simulations of the Methane Cycle: Nature, v. 481, p. 58-61.
Schumacher, R., and Schmincke, H.-U., 1991, Internal Structure and Occurrence of Accretionary Lapilli—a Case Study at Laacher See Volcano: Bulletin of Volcanology, v. 53, p. 612-634.
Schumacher, R., and Schmincke, H.U., 1995, Models for the Origin of Accretionary Lapilli: Bulletin of Volcanology, v. 56, p. 626-639.
Schwandner, F.M., Seward, T.M., Gize, A.P., Hall, P.A., and Dietrich, V.J., 2004, Diffuse Emission of Organic Trace Gases from the Flank and Crater of a Quiescent Active Volcano (Vulcano, Aeolian Islands, Italy): J. Geophys. Res., v. 109, p. D04301.
Seidl, M.A., and Dietrich, W.E., 1992, The Problem of Channel Erosion into Bedrock, *in* Schmidt, K.H., and Ploey, J.d., eds., Functional Geomorphology: Landform Analysis and Models, Volume 23, Catena Supplement, p. 101-124.
Seinfeld, J.H., and Pandis, S.N., 1997, Atmospheric Chemistry and Physics: From Air Pollution to Climate Change, John Wiley & Sons Inc.
Self, S., Blake, S., Sharma, K., Widdowson, M., and Sephton, S., 2008, Sulfur and Chlorine in Late Cretaceous Deccan Magmas and Eruptive Gas Release: Science, v. 319, p. 1654-1657.
Self, S., Thordarson, T., and Keszthelyi, L., 1997, Emplacement of Continental Flood Basalt Lava Flows: GEOPHYSICAL MONOGRAPH-AMERICAN GEOPHYSICAL UNION, v. 100, p. 381-410.
Self, S., Thordarson, T., Keszthelyi, L., Walker, G.P.L., Hon, K., Murphy, M.T., Long, P., and Finnemore, S., 1996, A New Model for the Emplacement of Columbia River Basalts as Large, Inflated Pahoehoe Lava Flow Fields: Geophysical Research Letters, v. 23, p. 2689-2692.
Sepkoski, J.J., Bambach, R.K., Raup, D.M., and Valentine, J.W., 1981, Phanerozoic Marine Diversity and the Fossil Record: Nature, v. 293, p. 435-437.
Sharma, M., 1997, Siberian Traps: GEOPHYSICAL MONOGRAPH-AMERICAN GEOPHYSICAL UNION, v. 100, p. 273-296.
Sharma, M., Basu, A.R., and Nesterenko, G.V., 1991, Nd-Sr Isotopes, Petrochemistry, and Origin of the Siberian Flood Basalts, Ussr: Geochimica Et Cosmochimica Acta, v. 55, p. 1183-1192.

Shen, S.-z., Crowley, J.L., Wang, Y., Bowring, S.A., Erwin, D.H., Sadler, P.M., Cao, C.-q., Rothman, D.H., Henderson, C.M., Ramezani, J., Zhang, H., Shen, Y., Wang, X.-d., Wang, W., Mu, L., Li, W.-z., Tang, Y.-g., Liu, X.-l., Liu, L.-j., Zeng, Y., Jiang, Y.-f., and Jin, Y.-g., 2011, Calibrating the End-Permian Mass Extinction: Science, v. 334, p. 1367-1372.

Sheridan, M.F., and Wohletz, K.H., 1981, Hydrovolcanic Explosions - the Systematics of Water-Pyroclast Equilibration: Science, v. 212, p. 1387-1389.

—, 1983, Hydrovolcanism: Basic Considerations and Review: Journal of Volcanology and Geothermal Research, v. 17, p. 1-29.

Sigurdsson, H., 1990, Evidence of Volcanic Loading of the Atmosphere and Climate Response: Global and Planetary Change, v. 89, p. 277-289.

Sigurdsson, H., Dhondt, S., and Carey, S., 1992, The Impact of the Cretaceous Tertiary Bolide on Evaporite Terrane and Generation of Major Sulfuric-Acid Aerosol: Earth and Planetary Science Letters, v. 109, p. 543-559.

Sisson, T.W., and Grove, T.L., 1993, Experimental Investigations of the Role of H2o in Calc-Alkaline Differentiation and Subduction Zone Magmatism: Contributions to Mineralogy and Petrology, v. 113, p. 143-166.

Sklar, L.S., and Dietrich, W.E., 2001, Sediment and Rock Strength Controls on River Incision into Bedrock: Geology, v. 29, p. 1087-1090.

Sobolev, A., Krivolutskaya, N., and Kuzmin, D., 2009, Petrology of the Parental Melts and Mantle Sources of Siberian Trap Magmatism: Petrology, v. 17, p. 253-286.

Sobolev, A.V., Kamenetsky, V.S., and Kononkova, N.N., 1991, New Data on Petrology of Siberia Meymechites: Geokhimiya, p. 1084-1095.

Sobolev, S.V., Sobolev, A.V., Kuzmin, D.V., Krivolutskaya, N.A., Petrunin, A.G., Arndt, N.T., Radko, V.A., and Vasiliev, Y.R., 2011, Linking Mantle Plumes, Large Igneous Provinces and Environmental Catastrophes: Nature, v. 477, p. 312-U80.

Soderblom, L.A., Tomasko, M.G., Archinal, B.A., Becker, T.L., Bushroe, M.W., Cook, D.A., Doose, L.R., Galuszka, D.M., Hare, T.M., Howington-Kraus, E., Karkoschka, E., Kirk, R.L., Lunine, J.I., McFarlane, E.A., Redding, B.L., Rizk, B., Rosiek, M.R., See, C., and Smith, P.H., 2007, Topography and Geomorphology of the Huygens Landing Site on Titan: Planetary and Space Science, v. 55, p. 2015-2024.

Sotin, C., Jaumann, R., Buratti, B.J., Brown, R.H., Clark, R.N., Soderblom, L.A., Baines, K.H., Bellucci, G., Bibring, J.P., Capaccioni, F., Cerroni, P., Combes, M., Coradini, A., Cruikshank, D.P., Drossart, P., Formisano, V., Langevin, Y., Matson, D.L., McCord, T.B., Nelson, R.M., Nicholson, P.D., Sicardy, B., LeMouelic, S., Rodriguez, S., Stephan, K., and Scholz, C.K., 2005, Release of Volatiles from a Possible Cryovolcano from near-Infrared Imaging of Titan: Nature, v. 435, p. 786-789.

Sparks, R.S.J., Bursik, M.I., Carey, S.N., Gilbert, J.S., Glaze, L.S., Sigurdsson, H., and Woods, A.W., 1997, Volcanic Plumes: Chichester, England, Wiley and Sons.

Stiles, B.W., Hensley, S., Gim, Y., Bates, D.M., Kirk, R.L., Hayes, A., Radebaugh, J., Lorenz, R.D., Mitchell, K.L., Callahan, P.S., Zebker, H., Johnson, W.T.K., Wall, S.D., Lunine, J.I., Wood, C.A., Janssen, M., Pelletier, F., West, R.D., Veeramacheneni, C., and Cassini, R.T., 2009, Determining Titan Surface Topography from Cassini Sar Data: Icarus, v. 202, p. 584-598.

Stofan, E.R., Elachi, C., Lunine, J.I., Lorenz, R.D., Stiles, B., Mitchell, K.L., Ostro, S., Soderblom, L., Wood, C., Zebker, H., Wall, S., Janssen, M., Kirk, R., Lopes, R., Paganelli, F., Radebaugh, J., Wye, L., Anderson, Y., Allison, M., Boehmer, R., Callahan, P., Encrenaz, P., Flamini, E., Francescetti, G., Gim, Y., Hamilton, G., Hensley, S., Johnson, W.T.K., Kelleher, K., Muhleman, D., Paillou, P., Picardi, G., Posa, F., Roth, L., Seu, R., Shaffer, S., Vetrella, S., and West, R., 2007, The Lakes of Titan: Nature, v. 445, p. 61-64.

Stolper, E., and Holloway, J.R., 1988, Experimental Determination of the Solubility of Carbon Dioxide in Molten Basalt at Low Pressure: Earth and Planetary Science Letters, v. 87, p. 397-408.

Stothers, R.B., Wolff, J.A., Self, S., and Rampino, M.R., 1986, Basaltic Fissure Eruptions, Plume Heights, and Atmospheric Aerosols: Geophysical Research Letters, v. 13, p. 725-728.
Strauss, H., 1997, The Isotopic Composition of Sedimentary Sulfur through Time: Palaeogeography Palaeoclimatology Palaeoecology, v. 132, p. 97-118.
Sun, Y., Joachimski, M.M., Wignall, P.B., Yan, C., Chen, Y., Jiang, H., Wang, L., and Lai, X., 2012, Lethally Hot Temperatures During the Early Triassic Greenhouse: Science, v. 338, p. 366-370.
Svensen, H., Planke, S., Polozov, A.G., Schmidbauer, N., Corfu, F., Podladchikov, Y.Y., and Jamtveit, B., 2009, Siberian Gas Venting and the End-Permian Environmental Crisis: Earth and Planetary Science Letters, v. 277, p. 490-500.
Symonds, R.B., Rose, W.I., Bluth, G.J.S., and Gerlach, T.M., 1994, Volcanic-Gas Studies; Methods, Results, and Applications: Reviews in Mineralogy and Geochemistry, v. 30, p. 1-66.
Tabazadeh, A., and Turco, R.P., 1993, Stratospheric Chlorine Injection by Volcanic-Eruptions - Hci Scavenging and Implications for Ozone: Science, v. 260, p. 1082-1086.
Taylor, B.E., 1986, Magmatic Volatiles; Isotopic Variation of C, H, and S: Reviews in Mineralogy and Geochemistry, v. 16, p. 185-225.
Textor, C., Graf, H.F., Herzog, M., and Oberhuber, J.M., 2003, Injection of Gases into the Stratosphere by Explosive Volcanic Eruptions: Journal of Geophysical Research-Atmospheres, v. 108.
Thode, H., 1991, Sulphur Isotopes in Nature and the Environment: An Overview: Stable isotopes: natural and anthropogenic sulphur in the environment. SCOPE, v. 43, p. 1-26.
Thordarson, T., Larsen, G., Steinthorsson, S., and Self, S., 2003, The 1783–1785 Ad Laki-Grímsvötn Eruptions Ii: Appraisal Based on Contemporary Accounts: Jökull, v. 53, p. 11-47.
Thordarson, T., Rampino, M., Keszthelyi, L., and Self, S., 2009, Effects of Megascale Eruptions on Earth and Mars, *in* Chapman, M.G., and Keszthelyi, L., eds., Preservation of Random Megascale Events on Mars and Earth: Influence on Geologic History, Volume 453, Geol Soc Am Spec Paper, p. 37-53.
Thordarson, T., and Self, S., 1993a, The Laki (Skaftar-Fires) and Grimsvotn Eruptions in 1783-1785: Bulletin of Volcanology, v. 55, p. 233-263.
—, 1993b, The Laki (Skaftár Fires) and Grímsvötn Eruptions in 1783–1785: Bulletin of Volcanology, v. 55, p. 233-263.
—, 1996, Sulfur, Chlorine and Fluorine Degassing and Atmospheric Loading by the Roza Eruption, Columbia River Basalt Group, Washington, USA: Journal of Volcanology and Geothermal Research, v. 74, p. 49-73.
—, 1998a, The Roza Member, Columbia River Basalt Group: A Gigantic Pahoehoe Lava Flow Field Formed by Endogenous Processes?: Journal of Geophysical Research-Solid Earth, v. 103, p. 27411-27445.
—, 1998b, The Roza Member, Columbia River Basalt Group: A Gigantic Pahoehoe Lava Flow Field Formed by Endogenous Processes?: Journal of Geophysical Research, v. 103, p. 27411-27,445.
—, 2003, Atmospheric and Environmental Effects of the 1783-1784 Laki Eruption: A Review and Reassessment: Journal of Geophysical Research-Atmospheres, v. 108.
Thordarson, T., Self, S., Oskarsson, N., and Hulsebosch, T., 1996, Sulfur, Chlorine, and Fluorine Degassing and Atmospheric Loading by the 1783-1784 Ad Laki (Skaftar Fires) Eruption in Iceland: Bulletin of Volcanology, v. 58, p. 205-225.
Timmreck, C., Graf, H.F., Lorenz, S.J., Niemeier, U., Zanchettin, D., Matei, D., Jungclaus, J.H., and Crowley, T.J., 2010, Aerosol Size Confines Climate Response to Volcanic Super-Eruptions: Geophysical Research Letters, v. 37.
Timmreck, C., Lorenz, S.J., Crowley, T.J., Kinne, S., Raddatz, T.J., Thomas, M.A., and Jungclaus, J.H., 2009, Limited Temperature Response to the Very Large Ad 1258 Volcanic Eruption: Geophysical Research Letters, v. 36.
Tomasko, M.G., Archinal, B., Becker, T., Bezard, B., Bushroe, M., Combes, M., Cook, D., Coustenis, A., de Bergh, C., Dafoe, L.E., Doose, L., Doute, S., Eibl, A., Engel, S., Gliem, F., Grieger, B., Holso, K., Howington-Kraus, E., Karkoschka, E., Keller, H.U., Kirk, R., Kramm, R., Kuppers, M.,

Lanagan, P., Lellouch, E., Lemmon, M., Lunine, J., McFarlane, E., Moores, J., Prout, G.M., Rizk, B., Rosiek, M., Rueffer, P., Schroder, S.E., Schmitt, B., See, C., Smith, P., Soderblom, L., Thomas, N., and West, R., 2005, Rain, Winds and Haze During the Huygens Probe's Descent to Titan's Surface: Nature, v. 438, p. 765-778.

Troll, V.R., Hilton, D.R., Jolis, E.M., Chadwick, J.P., Blythe, L.S., Deegan, F.M., Schwarzkopf, L.M., and Zimmer, M., 2012, Crustal Co2 Liberation During the 2006 Eruption and Earthquake Events at Merapi Volcano, Indonesia: Geophysical Research Letters, v. 39.

Tucker, G.E., and Bras, R.L., 1998, Hillslope Processes, Drainage Density, and Landscape Morphology: Water Resources Research, v. 34, p. 2751-2764.

Turtle, E.P., Perry, J.E., Hayes, A.G., Lorenz, R.D., Barnes, J.W., McEwen, A.S., West, R.A., Del Genio, A.D., Barbara, J.M., Lunine, J.I., Schaller, E.L., Ray, T.L., Lopes, R.M.C., and Stofan, E.R., 2011, Rapid and Extensive Surface Changes near Titan's Equator: Evidence of April Showers: Science, v. 331, p. 1414-1417.

Vasil'ev, Y.R., Zolotukhin, V.V., Feoktistov, G.D., and Prusskaya, S.N., 2000, Evaluation of the Volumes and Genesis of Permo-Triassic Trap Magmatism on the Siberian Platform: Geologiya I Geofizika, v. 41, p. 1696-1705.

Visscher, H., Brinkhuis, H., Dilcher, D.L., Elsik, W.C., Eshet, Y., Looy, C.V., Rampino, M.R., and Traverse, A., 1996, The Terminal Paleozoic Fungal Event: Evidence of Terrestrial Ecosystem Destabilization and Collapse: Proceedings of the National Academy of Sciences, v. 93, p. 2155-2158.

Visscher, H., Looy, C.V., Collinson, M.E., Brinkhuis, H., Cittert, J., Kurschner, W.M., and Sephton, M.A., 2004, Environmental Mutagenesis During the End-Permian Ecological Crisis: Proceedings of the National Academy of Sciences of the United States of America, v. 101, p. 12952-12956.

Walker, G.P.L., Self, S., and Wilson, L., 1984, Tarawera 1886, New Zealand -- a Basaltic Plinian Fissure Eruption: Journal of Volcanology and Geothermal Research, v. 21, p. 61-78.

Wall, S., Hayes, A., Bristow, C., Lorenz, R., Stofan, E., Lunine, J., Le Gall, A., Janssen, M., Lopes, R., Wye, L., Soderblom, L., Paillou, P., Aharonson, O., Zebker, H., Farr, T., Mitri, G., Kirk, R., Mitchell, K., Notarnicola, C., Casarano, D., and Ventura, B., 2010, Active Shoreline of Ontario Lacus, Titan: A Morphological Study of the Lake and Its Surroundings: Geophys. Res. Lett., v. 37, p. L05202.

Wallace, P., and Carmichael, I.S.E., 1992, Sulfur in Basaltic Magmas: Geochimica Et Cosmochimica Acta, v. 56, p. 1863-1874.

Wallace, P.J., and Anderson, A.T., 1998, Effects of Eruption and Lava Drainback on the H 2 O Contents of Basaltic Magmas at Kilauea Volcano: Bulletin of volcanology, v. 59, p. 327-344.

Ward, P.D., Montgomery, D.R., and Smith, R., 2000, Altered River Morphology in South Africa Related to the Permian-Triassic Extinction: Science, v. 289, p. 1740-1743.

Watson, G., 1956, A Test for Randomness of Directions: Geophysical Supplements to the Monthly Notices of the Royal Astronomical Society, v. 7, p. 160-161.

Webster, J.D., Kinzler, R.J., and Mathez, E.A., 1999, Chloride and Water Solubility in Basalt and Andesite Melts and Implications for Magmatic Degassing: Geochimica Et Cosmochimica Acta, v. 63, p. 729-738.

Wei, L.J., Mosley-Thompson, E., Gabrielli, P., Thompson, L.G., and Barbante, C., 2008, Synchronous Deposition of Volcanic Ash and Sulfate Aerosols over Greenland in 1783 from the Laki Eruption (Iceland): Geophysical Research Letters, v. 35.

Whipple, K.X., and Tucker, G.E., 1999, Dynamics of the Stream-Power River Incision Model: Implications for Height Limits of Mountain Ranges, Landscape Response Timescales, and Research Needs: Journal of Geophysical Research-Solid Earth, v. 104, p. 17661-17674.

White, J., Bryan, S., Ross, P., Self, S., and Thordarson, T., 2009, Physical Volcanology of Continental Large Igneous Provinces: Update and Review: Studies in Volcanology: The Legacy of George Walker. Special Publications of IAVCEI, v. 2, p. 291-321.

White, J.D.L., and Houghton, B.F., 2006, Primary Volcaniclastic Rocks: Geology, v. 34, p. 677-680.

White, J.D.L., and McClintock, M.K., 2001, Immense Vent Complex Marks Flood-Basalt Eruption in a Wet, Failed Rift: Coombs Hills, Antarctica: Geology, v. 29, p. 935-938.
White, R.V., 2002, Earth's Biggest 'Whodunnit': Unravelling the Clues in the Case of the End-Permian Mass Extinction: Philosophical Transactions of the Royal Society of London Series a-Mathematical Physical and Engineering Sciences, v. 360, p. 2963-2985.
Whitmire, D.P., and Jackson, A.A., 1984, Are Periodic Mass Extinctions Driven by a Distant Solar Companion?
Wignall, P.B., 2001, Large Igneous Provinces and Mass Extinctions: Earth-Science Reviews, v. 53, p. 1-33.
Willgoose, G., Bras, R.L., and Rodrigueziturbe, I., 1991, A Coupled Channel Network Growth and Hillslope Evolution Model .1. Theory: Water Resources Research, v. 27, p. 1671-1684.
Wohletz, K.H., 1983, Mechanisms of Hydrovolcanic Pyroclast Formation - Grain-Size, Scanning Electron-Microscopy, and Experimental Studies: Journal of Volcanology and Geothermal Research, v. 17, p. 31-63.
Wood, C.A., Lorenz, R., Kirk, R., Lopes, R., Mitchell, K., Stofan, E., and Cassini, R.T., 2010, Impact Craters on Titan: Icarus, v. 206, p. 334-344.
Wooden, J.L., Czamanske, G.K., Fedorenko, V.A., Arndt, N.T., Chauvel, C., Bouse, R.M., King, B.S.W., Knight, R.J., and Siems, D.F., 1993, Isotopic and Trace-Element Constraints on Mantle and Crustal Contributions to Siberian Continental Flood Basalts, Norilsk Area, Siberia: Geochimica Et Cosmochimica Acta, v. 57, p. 3677-3704.
Woods, A.W., 1993, Moist Convection and the Injection of Volcanic Ash into the Atmosphere: Journal of Geophysical Research-Solid Earth, v. 98, p. 17627-17636.
Wye, L.C., Zebker, H.A., and Lorenz, R.D., 2009, Smoothness of Titan's Ontario Lacus: Constraints from Cassini Radar Specular Reflection Data: Geophysical Research Letters, v. 36.
Yung, Y.L., Allen, M., and Pinto, J.P., 1984, Photochemistry of the Atmosphere of Titan - Comparison between Model and Observations: Astrophysical Journal Supplement Series, v. 55, p. 465-506.
Zebker, H.A., Gim, Y., Callahan, P., Hensley, S., and Lorenz, R., 2009, Analysis and Interpretation of Cassini Titan Radar Altimeter Echoes: Icarus, v. 200, p. 240-255.
Zharkov, M.A., 1984, Paleozoic Salt Bearing Formations of the World: Berlin, Springer-Verlag, 427 p.
Zolotukhin, V.V., and Almukhamedov, A.I., 1988, Traps of the Siberian Platform, *in* Macdougall, J.D., ed., Continental Flood Basalts: Dordrecht, Kluwer Academic Publishers.